Characterization of Heavy Ion Collisions with Photons and Hadrons at RHIC Energies

A THESIS SUBMITTED TO

JADAVPUR UNIVERSITY

FOR THE DEGREE OF

DOCTOR OF PHILOSOPHY IN SCIENCE

(PHYSICS)

By

DEBASISH DAS

VARIABLE ENERGY CYCLOTRON CENTRE

1/AF, BIDHANNAGAR, KOLKATA 700064

INDIA

June 2007

"To Thee My Noblest"

CERTIFICATE

This is to certify that the thesis entitled **"Characterization of Heavy Ion Collisions with Photons and Hadrons at RHIC Energies"** submitted by **Sri Debasish Das** who got his name registered on 08/11/2004 for the award of **Ph.D. (Science) degree of Jadavpur University**, is absolutely based upon his own work under the supervision of **Dr. Tapan K. Nayak** and that neither this thesis nor any part of its has been submitted for any degree/diploma or any other academic award anywhere before.

Dr. Tapan K. Nayak

Scientific Officer

Variable Energy Cyclotron Centre

Kolkata.

(Signature of the Supervisor and date with official seal)

Abstract

One of the definitive predictions of Quantum Chromodynamics (QCD) is that at sufficiently high density and/or temperature, strongly interacting matter will be in a deconfined state of the quarks and gluons, called the Quark-Gluon Plasma (QGP). The prime goal of the physics program with the relativistic heavy ion collisions is to study the nature of the transition from hadronic phase to QGP phase along with the properties of QCD matter created under such extreme conditions.

Among the large number of particles produced and emitted from the collision environment, photons do not interact strongly with the medium and hence carry information about the history of the collisions. Hadrons, however, provide an understanding of the evolutionary path of the system created in the collision at the time of freeze-out. In this thesis we explore and characterize the properties of heavy ion collisions at relativistic energies with photons and hadrons measured by the STAR experiment at Relativistic Heavy Ion Collider (RHIC). The detector details presented in this thesis include the photon measurements done at both forward and mid-rapidities along with the charged particles measured at mid-rapidity.

The dynamical evolution of the collision fireball and its space-time structure has been studied in this thesis using two-photon and two-pion correlation techniques at mid-rapidity. The invariant interferometric radii extracted from such correlations with direct photons and charged pions reveal comparative results. The multiplicity and transverse momentum dependence of three-dimensional pion interferometric radii in Au+Au and Cu+Cu collisions at different RHIC energies are studied. The freeze-out volume estimates with charged pions measured from such studies, show linear dependence as a function of charge particle multiplicity indicating consistent behaviour with a universal mean-free-path at freeze-out.

Acknowledgments

I wish express my deep reverence above all to God Almighty, for providing me mental strength and physical ability to pursue my studies and seeing me through the passage of time in all the ups and downs of life. The entire work presented in this thesis would not have been possible without the support, advice and encouragement which I received from many people during my research period.

First of all I would like to thank Dr. Tapan K Nayak, my thesis advisor at Variable Energy Cyclotron Centre, for his encouragement, support and guidance throughout my research period. I cherish the discussions I had with him and deeply acknowledge him for keeping me motivated to study heavy ion physics.

I would like to acknowledge the financial support from the Department Of Atomic Energy Govt. Of India which enabled me to take up this research work. I would like to convey my sincere thanks to Dr. Bikash Sinha, Director VECC and SINP for his support and encouragement in all respect.

I would I would like to convey my sincere thanks to Dr. Y.P Viyogi, Director IOP, Bhubaneswar, for his support, advice and encouragement during my research period. I wish to express my sincere thanks to Dr. D. K. Srivastava, Head Physics Group, VECC, for his support, advice and encouragement. I would like to sincerely thank Dr. R.K. Bhandari, Dr. S. Pal, Dr. S.K. Basu, Dr. A. Chaudhuri, Dr. D.N. Basu, Dr. A. Dhara, Dr. P. Barat, Dr. S. Bhattacharya, Dr. C. Bhattacharya, Dr. A. Chakrabarti, Dr. D. Bhowmick, Dr. T.K. Mukhopadhyay, Dr. S.R. Banerjee,

Dr. V.S.Pandit, Dr. D. Sarkar, Dr. A. Ray, Dr. U. De, Dr. P. Sen and many others of VECC group for their advice, support and words of encouragement. My sincere thanks to Dr. J. Alam and Dr. S. Sarkar for their suggestions, advice and constant encouragement. I wish to deeply acknowledge for the many thrilling moments of discussion I had with them.

I would like to express my sincere thanks to Dr. S. Chattopadhayay, Mr. M.R. DuttaMajumdar, Mr. G.S.N. Murthy and Mr. R.N. Singaraju for their support, advice and encouragement. I feel fortunate to have worked with them, to learn and understand the varied aspects of heavy ion physics, while being a research scholar in PMD Group at VECC. I sincerely keep in mind the nice experience of working with Dr. P. Ghosh, Mr. M.D. Trivedi, Dr. Z. Ahammed, Dr. B. Mohanty, Dr. A. K. Dubey, Mr. S. Pal, Mr. P. Bhaskar, Mr. V. Singhal, Mr. J. Saini, Mr. T. Samanta, Mr. T.K. Das, Ms. N. Mondal and Mr. P. Bhaduri of PMD group, VECC. I wish extend my gratitude of all my scholar friends in the collaboration, Mr. S. Das and Mr. P.K. Netrakanti, from VECC, Ms. M. Sharma from Panjab University, Mr. S. Bhardwaj from University of Rajasthan , Mr. D. Mishra, Mr. R. Sahoo and Ms. S. Dash from IOP, Bhubaneshwar and Mr. S.M. Dogra, Mr. S. Singh and Mr. N. Gupta from Jammu University for the help and exciting discussions I had with them.

I express my deep sense of gratitude to our spokesperson Dr. T. Hallman for the support and encouragement I received from him regarding my work, which immensely helped me to successfully collaborate with STAR BNL heavy ion physics group. I wish to express my sincere thanks to Dr. S.Y. Panitkin who has provided me constantly his advice and helped me all the way through the details of the HBT studies. The discussions which I had with him have enriched me and provided me strength to pursue the analysis with new vigour and zeal. I wish to thank every member of the STAR HBT group for the comments and suggestions which I

received from them regarding my analysis. My special thanks to Dr. M. A. Lisa, Dr. A. Kisiel, Dr. A.A. Suaide, Dr. J. Sandweiss, Mr. G. Lin, Dr. F. Retiere, Mr. P. Chaloupka, Mr. Z. Chajecki, Dr. J. Cramer and many others with whom I had the privilege to work and learn during my research period. I wish to thank Dr. J. Lauret for his help in understanding the critical details of data analysis and also wish to extend my deep acknowledgment to the RHIC operations Group, RHIC computing facility at BNL and NERSC LBL facility for their support. I wish to express my sincere thanks to Dr. W. Christie, Dr. R. Brown, Dr. Z. Xu, Dr. A. Lededev, Dr. B. Stringfellow, Dr. T. Ljubicic, Dr. W. Jacobs, Dr. D. Cebra and many others with whom I worked with during the PMD installation period and while taking shifts at STAR controls. I wish to thank each and every member of the STAR Collaboration for their dedicated effort towards the successful running of the experiment.

I had close and lively discussions with many members of the PMD Collaboration in India which include Dr. M. M. Aggarwal, Dr. A.K. Bhati and their group from Panjab University, Dr. S. Raniwala, Dr. R. Raniwala and their group from University of Rajasthan, Dr. L. K. Mangotra, Dr. S. K. Badyal, Dr. P.V.K.S. Baba, Dr. Anju Bhasin, Mr. A. Gupta, Dr. S. S. Sambyal and their group at Jammu University, Dr. D. P. Mohapatra, Dr. S. C. Phatak, Dr. P. K. Sahu and their group at IOP, Bhubaneswar, Dr. R. Varma, Dr. B. K. Nandi and their group at IIT Mumbai. I wish to thank each and every member of the PMD collaboration for their co-operation and comments which have helped me during my research period.

My special thanks to all my friends at VECC and their presence made my research period exciting and lively. Thanks to Damayanti, Kishan, Apu, Aparajita, Partha, Rupa, Mriganka, Sidharth, Provash, Prasun, Saikat, Jhelum, Arnomitra, Tapasi, Atanu, Jajati, Kaushik and many others with whom I shared such great

moments of friendship. I wish to thank the staff of VECC computer centre, library, canteen, administration, accounts, stores and security for their co-operation and help at every stage.

I wish to take this opportunity to thank many of my wonderful teachers at school and university who have inspired me in my studies. I wish to acknowledge all others who have silently motivated me during my research tenure.

I express my humble regards to my parents for their patience, love and continuous encouragement during my research period. Their inspiration and affection has helped me to overcome the many hurdles of life.

Date: **Debasish Das**

List of Publications

Publications in Conference Proceedings :

1. **"Identical Meson Interferometry in STAR Experiment"**,
   Debasish Das for the STAR Collaboration.
   Nineteenth International Conference on Ultra-Relativistic Nucleus-Nucleus Collisions (QM 2006), Shanghai, China, 2006. [arXiv: **nucl-ex/0702047**, Proceedings to be published in International Journal of Modern Physics E (World Scientific)]

2. **"Pion Interferometry in Au+Au and Cu+Cu collisions in STAR experiment at RHIC"**,
   Debasish Das for the STAR Collaboration.
   Proceedings of DAE-BRNS Symposium on Nuclear Physics, Baroda Vol **51** 2006 (524).

3. **"Preliminary Results on Direct Photon-Photon HBT Measurements in $\sqrt{s_{\rm NN}}$= 62.4 GeV and 200 GeV Au+Au Collisions at RHIC"** ,
   Debasish Das *et al.* for the STAR Collaboration.
   Eighteenth International Conference on Ultra-Relativistic Nucleus-Nucleus

Collisions (QM 2005), Budapest, Hungary, 2005. [arXiv: **nucl-ex/0511055** and Nukleonika,Vol 51, Suppl 3, Page : S55-S58]

4. **"Hadron and Photon Interferometry in STAR experiment at RHIC"**, **Debasish Das** for the STAR Collaboration.
   Proceedings of DAE-BRNS Symposium on Nuclear Physics, Mumbai Vol **50** 2005 (400).

5. **"Quality Assessment in Photon Multiplicity Detector fabrication"**, M.R.Dutta Majumder, **Debasish Das**, T.K.Nayak and Y.P.Viyogi
   Proceedings of DAE-BRNS Symposium on Nuclear Physics, Mumbai Vol **50** 2005 (437).

6. **"The STAR Photon Multiplicity Detector"** ,
   M.M. Aggarwal *et al.*
   Seventeenth International Conference on Ultra-Relativistic Nucleus-Nucleus Collisions (QM 2004), Oakland, USA, 2004.

7. **"Opto-Electronics in Large Array Gas Detector Systems"** ,
   M.R.Dutta Majumder, **Debasish Das**, Tapan K Nayak.
   Seventh International Conference on Opto-electronics, Fibre Optics and Photonics (Photonics 2004),India, 2004.
   arXiv: **physics/0512227**

8. **"Testing of Photon Multiplicity Detector for STAR experiment"**, **Debasish Das** *et al.*
   Proceedings of DAE-BRNS Symposium on Nuclear Physics, Mumbai Vol **46B** 2003 (520).

9. **"Integration of Photon Multiplicity Detector in STAR experiment at RHIC"**,

M.M. Aggarwal *et al.*

Proceedings of DAE-BRNS Symposium on Nuclear Physics, Mumbai Vol **46B** 2003 (486).

10. **"Development of an opto-coupler device for large array gas detector system"** ,

    M.R.Dutta Majumder and **Debasish Das**.

    Proceedings of DAE-BRNS Symposium on Nuclear Physics, Mumbai Vol **46B** 2003 (522).

11. **"The STAR Photon Multiplicity Detector"**,

    M.M. Aggarwal *et al.*

    Proceedings of DAE-BRNS Symposium on Nuclear Physics, Tirunelvelli Vol **45B** 2002 (426).

Publications in International Scientific Journals :

1. **"Global polarization measurement in Au + Au collisions"**,

   B. I. Abelev *et al.* [STAR Collaboration]

   arXiv:0705.1691 [nucl-ex] (Submitted to Phys.Rev.C)

2. **"Energy dependence of $\pi^{\pm}$, p and $\bar{p}$ transverse momentum spectrafor Au+Au collisions at $\sqrt{s_{\rm NN}}$ = 62.4 and 200 GeV"**,

   B. I. Abelev *et al.* [STAR Collaboration]

   arXiv:nucl-ex/0703040

3. **"Partonic flow and ϕ-meson production in Au + Au collisions at $\sqrt{s_{\rm NN}}$ = 200 GeV"**,

B. I. Abelev *et al.* [STAR Collaboration]
arXiv:nucl-ex/0703033 (Submitted to Phys.Rev.Lett.)

4. **"Charged particle distributions and nuclear modification at high rapidities in d+Au collisions at $\sqrt{s_{\rm NN}}$ = 200 GeV"**,
   B. I. Abelev *et al.* [STAR Collaboration]
   arXiv:nucl-ex/0703016 (Submitted to Phys.Lett.B)

5. **"Mass, quark-number, and $\sqrt{s_{\rm NN}}$ dependence of the second and fourth flow harmonics in ultra-relativistic nucleus nucleus collisions"**,
   B. I. Abelev *et al.* [the STAR Collaboration]
   arXiv:nucl-ex/0701010 (Submitted to Phys.Rev.C)

6. **"Rapidity and species dependence of particle production at large transverse momentum for d + Au collisions at $\sqrt{s_{\rm NN}}$ = 200 GeV"**,
   B. I. Abelev *et al.* [STAR Collaboration]
   arXiv:nucl-ex/0609021

7. **"Longitudinal double-spin asymmetry and cross section for inclusive jet production in polarized proton collisions at $\sqrt{s_{\rm NN}}$ = 200 GeV"**,
   B. I. Abelev *et al.* [STAR Collaboration]
   [arXiv:hep-ex/0608030] (Submitted to Phys.Rev.Lett.)

8. **"Neutral kaon interferometry in Au + Au collisions at $\sqrt{s_{\rm NN}}$ = 200 GeV"**,
   B. I. Abelev *et al.* [STAR Collaboration]
   Phys. Rev. C **74**, 054902 (2006) [arXiv:nucl-ex/0608012]

9. **"Strange particle production in p + p collisions at $\sqrt{s_{\rm NN}}$ = 200 GeV"**,
   B. I. Abelev *et al.* [STAR Collaboration]
   [arXiv:nucl-ex/0607033] (Submitted to Phys.Rev.C)

10. **"Transverse momentum and centrality dependence of high-p_T non-photonic electron suppression in Au+Au collisions at $\sqrt{s_{\rm NN}}$ = 200 GeV"**,
    B. I. Abelev *et al.* [STAR Collaboration]
    [arXiv:nucl-ex/0607012] (Submitted to Phys.Rev.Lett.)

11. **"$\Delta\phi\Delta\eta$ correlations in central Au + Au collisions at $\sqrt{s_{\rm NN}}$ = 200-GeV"**,
    J. Adams *et al.* [Star Collaboration]
    [arXiv:nucl-ex/0607003] (Submitted to Phys.Rev.C)

12. **"The multiplicity dependence of inclusive p_t spectra from p + p collisions at $\sqrt{s_{\rm NN}}$ = 200 GeV"**,
    J. Adams *et al.* [STAR Collaboration]
    Phys. Rev. D **74**, 032006 (2006) [arXiv:nucl-ex/0606028]

13. **"Scaling properties of hyperon production in Au + Au collisions at $\sqrt{s_{\rm NN}}$ = 200 GeV"**,
    J. Adams *et al.* [STAR Collaboration]
    [arXiv:nucl-ex/0606014] (Submitted to Phys.Rev.Lett.)

14. **"Identified baryon and meson distributions at large transverse momenta from Au + Au collisions at $\sqrt{s_{\rm NN}}$ = 200 GeV"**,
    B. I. Abelev *et al.* [STAR Collaboration]
    Phys. Rev. Lett. **97**, 152301 (2006) [arXiv:nucl-ex/0606003]

15. **"The energy dependence of p_t angular correlations inferred from mean-p_t fluctuation scale dependence in heavy ion collisions at the SPS and RHIC"**,
J. Adams *et al.* [STAR Collaboration]
[arXiv:nucl-ex/0605021]

16. **"Strange baryon resonance production in $\sqrt{s_{\rm NN}}$ = 200 GeV p + p and Au + Au collisions"**,
J. Adams *et al.* [STAR Collaboration]
Phys. Rev. Lett. **97**, 132301 (2006) [arXiv:nucl-ex/0604019]

17. **"Direct observation of dijets in central Au + Au collisions at $\sqrt{s_{\rm NN}}$ = 200 GeV"**,
J. Adams *et al.* [STAR Collaboration]
Phys. Rev. Lett. **97**, 162301 (2006) [arXiv:nucl-ex/0604018]

18. **"Forward neutral pion production in p + p and d + Au collisions at $\sqrt{s_{\rm NN}}$ = 200 GeV"**,
J. Adams *et al.* [STAR Collaboration]
Phys. Rev. Lett. **97**, 152302 (2006) [arXiv:nucl-ex/0602011]

19. **"Measurements of identified particles at intermediate transverse momentum in the STAR experiment from Au + Au collisions at $\sqrt{s_{\rm NN}}$ = 200-GeV"**
J. Adams *et al.* [STAR Collaborations]
[arXiv:nucl-ex/0601042] (Submitted to Phys.Rev.C)

20. **"Identified hadron spectra at large transverse momentum in p + p and d + Au collisions at $\sqrt{s_{\rm NN}}$ = 200 GeV"**,

J. Adams *et al.* [STAR Collaboration]
Phys. Lett. B **637**, 161 (2006) [arXiv:nucl-ex/0601033]

21. **"Strangelet search at RHIC"**
J. Adams *et al.* [STAR Collaboration]
[arXiv:nucl-ex/0511047] (Submitted to Phys.Rev.Lett.)

22. **"Multiplicity and pseudorapidity distributions of charged particles and photons at forward pseudorapidity in Au + Au collisions at $\sqrt{s_{\rm NN}}$ = 62.4 GeV"**,
J. Adams *et al.* [STAR Collaboration]
Phys. Rev. C **73**, 034906 (2006) [arXiv:nucl-ex/0511026]

23. **"Proton Λ correlations in central Au + Au collisions at $\sqrt{s_{\rm NN}}$ = 200 GeV"**,
J. Adams *et al.* [STAR Collaboration]
Phys. Rev. C **74**, 064906 (2006) [arXiv:nucl-ex/0511003]

24. **"Directed flow in Au + Au collisions at $\sqrt{s_{\rm NN}}$ = 62 GeV"**,
J. Adams *et al.* [STAR Collaboration]
Phys. Rev. C **73**, 034903 (2006) [arXiv:nucl-ex/0510053]

25. **"Transverse-momentum p_t correlations on (η, ϕ) from mean-p_t fluctuations in Au+Au collisions at $\sqrt{s_{\rm NN}}$ = 200 GeV"**,
J. Adams *et al.* [STAR Collaboration]
J. Phys. G **32**, L37 (2006) [arXiv:nucl-ex/0509030]

26. **"Incident energy dependence of p_T correlations at RHIC"**,
J. Adams *et al.* [STAR Collaboration]
Phys. Rev. C **72**, 044902 (2005) [arXiv:nucl-ex/0504031]

27. **"Multi-strange baryon elliptic flow in Au + Au collisions at $\sqrt{s_{\rm NN}}$ = 200 GeV"**,
J. Adams *et al.* [STAR Collaboration]
Phys. Rev. Lett. **95**, 122301 (2005) [arXiv:nucl-ex/0504022]

28. **"Multiplicity and pseudorapidity distributions of photons in Au + Au collisions at $\sqrt{s_{\rm NN}}$ = 62.4 GeV"**,
J. Adams *et al.* [STAR Collaboration]
Phys. Rev. Lett. **95**, 062301 (2005) [arXiv:nucl-ex/0502008]

29. **"Distributions of charged hadrons associated with high transverse momentum particles in p + p and Au + Au collisions at $\sqrt{s_{\rm NN}}$ = 200 GeV"**,
J. Adams *et al.* [STAR Collaboration]
Phys. Rev. Lett. **95**, 152301 (2005) [arXiv:nucl-ex/0501016]

30. **"Experimental and theoretical challenges in the search for the quark gluon plasma: The STAR collaboration's critical assessment of the evidence from RHIC collisions"**,
J. Adams *et al.* [STAR Collaboration]
Nucl. Phys. A **757**, 102 (2005) [arXiv:nucl-ex/0501009]

31. **"$K(892)^*$ resonance production in Au + Au and p + p collisions at $\sqrt{s_{\rm NN}}$ = 200 GeV at STAR"**,
J. Adams *et al.* [STAR Collaboration]
Phys. Rev. C **71**, 064902 (2005) [arXiv:nucl-ex/0412019]

32. **"Pion interferometry in Au + Au collisions at $\sqrt{s_{\rm NN}}$ = 200 GeV"**,
J. Adams *et al.* [STAR Collaboration]
Phys. Rev. C **71**, 044906 (2005) [arXiv:nucl-ex/0411036]

33. **"Minijet deformation and charge-independent angular correlations on momentum subspace (η, ϕ) in Au - Au collisions at $\sqrt{s_{\rm NN}} = 130$ GeV"**,
J. Adams *et al.* [STAR Collaboration]
Phys. Rev. C **73**, 064907 (2006) [arXiv:nucl-ex/0411003]

34. **"Azimuthal anisotropy in Au + Au collisions at $\sqrt{s_{\rm NN}} = 200$ GeV"**,
J. Adams *et al.* [STAR Collaboration]
Phys. Rev. C **72**, 014904 (2005) [arXiv:nucl-ex/0409033]

35. **"Pseudorapidity asymmetry and centrality dependence of charged hadron spectra in d + Au collisions at $\sqrt{s_{\rm NN}} = 200$ GeV"**,
J. Adams *et al.* [STAR Collaboration]
Phys. Rev. C **70**, 064907 (2004) [arXiv:nucl-ex/0408016]

36. **"Transverse momentum correlations and minijet dissipation in Au + Au collisions at $\sqrt{s_{\rm NN}} = 130$ GeV"**,
J. Adams *et al.* [STAR Collaboration]
[arXiv:nucl-ex/0408012]

37. **"Azimuthal anisotropy and correlations at large transverse momenta in p+p and Au+Au collisions at $\sqrt{s_{\rm NN}} = 200$ GeV"**,
J. Adams *et al.* [STAR Collaboration]
Phys. Rev. Lett. **93**, 252301 (2004) [arXiv:nucl-ex/0407007]

38. **"Open charm yields in d+Au collisions at s(NN)**(1/2) = 200-GeV"**,
J. Adams *et al.* [STAR Collaboration]
Phys. Rev. Lett. **94**, 062301 (2005) [arXiv:nucl-ex/0407006]

39. **"Measurements of transverse energy distributions in Au + Au collisions at $\sqrt{s_{\rm NN}}$ = 200 GeV"**,
J. Adams *et al.* [STAR Collaboration]
Phys. Rev. C **70**, 054907 (2004) [arXiv:nucl-ex/0407003]

40. **"Transverse-momentum dependent modification of dynamic texture in central Au + Au collisions at $\sqrt{s_{\rm NN}}$ = 200 GeV"**,
J. Adams *et al.* [STAR Collaboration]
Phys. Rev. C **71**, 031901 (2005) [arXiv:nucl-ex/0407001]

41. **"Hadronization geometry and charge-dependent number autocorrelations on axial momentum space in Au + Au collisions at $\sqrt{s_{\rm NN}}$ = 130 GeV"**,
J. Adams *et al.* [STAR Collaboration]
Phys. Lett. B **634**, 347 (2006) [arXiv:nucl-ex/0406035]

42. **"ϕ meson production in Au + Au and p + p collisions at $\sqrt{s_{\rm NN}}$ = 200 GeV"**,
J. Adams *et al.* [STAR Collaboration]
Phys. Lett. B **612**, 181 (2005) [arXiv:nucl-ex/0406003]

43. **"Centrality and pseudorapidity dependence of charged hadron production at intermediate p_T in Au + Au collisions at $\sqrt{s_{\rm NN}}$ = 130 GeV"**,
J. Adams *et al.* [STAR Collaboration]
Phys. Rev. C **70**, 044901 (2004) [arXiv:nucl-ex/0404020]

44. **"Production of e^+e^- pairs accompanied by nuclear dissociation in ultra-peripheral heavy ion collision"**,

J. Adams *et al.* [STAR Collaboration]
Phys. Rev. C **70**, 031902 (2004) [arXiv:nucl-ex/0404012]

45. **"Photon and neutral pion production in Au + Au collisions at $\sqrt{s_{\rm NN}}$ = 130-GeV"**,
J. Adams *et al.* [STAR Collaboration]
Phys. Rev. C **70**, 044902 (2004) [arXiv:nucl-ex/0401008]

46. **"Azimuthally sensitive HBT in Au + Au collisions at $\sqrt{s_{\rm NN}}$ = 200 GeV"**,
J. Adams *et al.* [STAR Collaboration]
Phys. Rev. Lett. **93**, 012301 (2004) [arXiv:nucl-ex/0312009]

47. **"Production of charged pions and hadrons in Au + Au collisions at $\sqrt{s_{\rm NN}}$ = 130 GeV"**,
J. Adams *et al.* [STAR Collaboration]
[arXiv:nucl-ex/0311017]

48. **"Cross sections and transverse single-spin asymmetries in forward neutral pion production from proton collisions at $\sqrt{s_{\rm NN}}$ = 200 GeV"**,
J. Adams *et al.* [STAR Collaboration]
Phys. Rev. Lett. **92**, 171801 (2004) [arXiv:hep-ex/0310058]

49. **"Azimuthal anisotropy at RHIC: The first and fourth harmonics"**
J. Adams *et al.* [STAR Collaboration]
Phys. Rev. Lett. **92**, 062301 (2004) [arXiv:nucl-ex/0310029]

50. **"Identified particle distributions in p + p and Au + Au collisions at $\sqrt{s_{\rm NN}}$ = 200 GeV"**,
J. Adams *et al.* [STAR Collaboration]
Phys. Rev. Lett. **92**, 112301 (2004) [arXiv:nucl-ex/0310004]

51. **"Pion, kaon, proton and anti-proton transverse momentum distributions from p + p and d + Au collisions at $\sqrt{s_{\rm NN}}$ = 200 GeV"**,
J. Adams *et al.* [STAR Collaboration]
Phys. Lett. B **616**, 8 (2005) [arXiv:nucl-ex/0309012]

52. **"Event-by-event fluctuations in Au + Au collisions at $\sqrt{s_{\rm NN}}$ = 130 GeV"**,
J. Adams *et al.* [STAR Collaboration]
Phys. Rev. C **71**, 064906 (2005) [arXiv:nucl-ex/0308033]

53. **"Pion kaon correlations in Au + Au collisions at $\sqrt{s_{\rm NN}}$ = 130-GeV"**,
J. Adams *et al.* [STAR Collaboration]
Phys. Rev. Lett. **91**, 262302 (2003) [arXiv:nucl-ex/0307025]

54. **"Multi-strange baryon production in Au + Au collisions at $\sqrt{s_{\rm NN}}$ = 130 GeV"**,
J. Adams *et al.* [STAR Collaboration]
Phys. Rev. Lett. **92**, 182301 (2004) [arXiv:nucl-ex/0307024]

55. **"ρ^0 production and possible modification in Au + Au and p + p collisions at $\sqrt{s_{\rm NN}}$ = 200 GeV"**,
J. Adams *et al.* [STAR Collaboration]
Phys. Rev. Lett. **92**, 092301 (2004) [arXiv:nucl-ex/0307023]

56. **"Multiplicity fluctuations in Au + Au collisions at $\sqrt{s_{\rm NN}}$ = 130-GeV"**,
J. Adams *et al.* [STAR Collaboration]
Phys. Rev. C **68**, 044905 (2003) [arXiv:nucl-ex/0307007]

57. **"Rapidity and centrality dependence of proton and anti-proton production from $^{197}Au + ^{197}Au$ collisions at $\sqrt{s_{\rm NN}}$ = 130 GeV"**,

J. Adams *et al.* [STAR Collaboration]

Phys. Rev. C **70**, 041901 (2004) [arXiv:nucl-ex/0306029]

58. **"Particle-Type Dependence of Azimuthal Anisotropy and Nuclear Modification of Particle Production in Au+Au Collisions at $\sqrt{s_{\rm NN}}$ = 200 GeV"**,

J. Adams *et al.* [STAR Collaboration]

Phys. Rev. Lett. **92**, 052302 (2004) [arXiv:nucl-ex/0306007]

Contents

List of Tables

List of Figures

Chapter 1

Introduction

Quantum Chromo-Dynamics (QCD) is the theory of the strong interactions which fundamentally describe hadronic matter. Hadron is a subatomic particle which experiences the strong nuclear force. Hadrons are not fundamental particles but are composed of fermions, called quarks and anti-quarks, and of bosons, called gluons. The basic constituents of QCD are quarks which interact through the exchange of gluons. It is believed that shortly after the creation of the universe in the "Big Bang" when the temperature was about a trillion degrees, all matter existed as quarks and gluons in a state called the Quark Gluon Plasma (QGP), along with some electrons and neutrinos. Conditions for creating this highly excited state of primordial matter under controlled laboratory environment using relativistic heavy ion collisions, enable to explore QCD matter that scientists think last existed one millionth of a second (a micro-second) after the "Big-Bang" which marked the beginning of the Universe about 14 billion years ago. As the infant universe expanded and cooled, this plasma went through a phase transition to form a variety of particles - most importantly nucleons - which constitute the building blocks of (nuclear) matter as we know it in present times. The investigation of QGP properties, such as its equation of state, by studying these particles with sophisticated

detectors will improve our understanding of the evolution of the early universe and the behaviour of QCD under extreme conditions. One of the important tasks in relativistic heavy-ion research is to find clear and unambiguous connections between the transient state of quark gluon plasma and the observable hadronic final state.

In this thesis we explore and characterize the properties of heavy ion collisions at relativistic energies with photons and hadrons. In this chapter we discuss QCD phase transition and properties of QGP which is expected to form in relativistic heavy ion collisions. The several signatures of QGP formation in such collision environment are discussed. We end the chapter with comparative studies of two-particle intensity interferometry correlations between photons and hadrons.

1.1 Quantum Chromo-Dynamics (QCD)

As far as we know, there are just four fundamental forces in nature : *strong*, *electromagnetic*, *weak* and *gravitational*. Quantum Chromo-Dynamics (QCD) is the theory of the strong interaction which describes how the coloured particles: *quarks* and *gluons* interact among themselves and with each other. The idea of colour plays a fundamental role in the interaction between quarks. Quarks interact strongly by exchanging colour [1]. Gluons are the quanta of the colour field that bind quarks in nucleons and also nucleons into nuclei. They are the particles that mediate the force (of the strong interaction) in QCD. All particles must contain all three colours or colour-anticolour combinations such that they are overall "white" or colourless [2].

Quarks have spin 1/2 and they are fermions. Quarks are characterized by their flavours and till the present time, these are six such flavours up, down, strange,

Table 1.1: Different quark flavours.

Quark	**Symbol**	**Mass(MeV)**	**Charge(Q)**	**Quantum Number**
Up	u	1.5 - 3.0	+2/3	Isospin(I_z)=+1/2
Down	d	3 - 7	-1/3	Isospin(I_z)=-1/2
Strange	s	95 ± 25	-1/3	Strangeness(S)=-1
Charm	c	1250 - 900	+2/3	Charm(C)=+1
Bottom	b	4200 - 700	-1/3	Bottom(B)=-1
Top	t	174200±3300	+2/3	Top(T)=+1

charm, bottom and top. The various other properties of quarks are listed in Table (1.1). In Table (1.1) [3, 4] I_z is the z-component of isospin, C is the charm quantum number, S is the strangeness, T is the topness, and B is the bottomness.

Since the quarks are confined inside nucleons and so to understand the nuclear structure we must first understand the proton and the neutron — hence study the hadron physics in greater detail. When a quark is confined in a hadron, the quark may acquire an effective mass which includes the effect of the zero-point energy of the quark in the confining potential. The effective mass of confined quark in a hadron is known as the *constituent mass* of the quark which is typically a few hundred MeV in magnitude.

QCD provides us with two important characteristics of quark-gluon dynamics [5, 6]: (i) at high energies the interaction becomes small, and quarks and gluons interact weakly (the asymptotic freedom), while (ii) at low energy the interaction becomes strong and leads to the confinement of colour. The interaction in QCD becomes stronger at long distances or at low energies, which is a signature of the confinement of colour [7].

The phenomenological potential between quark and an anti-quark increases linearly at large distances as :

$$V(r) = -\frac{4}{3}\frac{\alpha_s c\hbar}{r} + F_0 r \tag{1.1}$$

where α_s is the chromodynamic analog to the fine structure constant, and $\frac{4}{3}$ is the appropriate colour factor [2]. As seen from the first term of Eq. (1.1) which dominates for small r, whereas in the limit of $r \rightarrow 0$ the quarks can be considered non-interacting due to the property of asymptotic freedom [8, 9]. The Nobel Prize of physics (2004) was awarded to David J. Gross, H. David Politzer and Frank Wilczek "for the discovery of asymptotic freedom in the theory of the strong interaction".

Experimental estimation of F_0 (second term of Eq. (1.1)) is about 16 tons and so we can clearly understand why its next to impossible to remove a quark out of a hadron [2]. But in the last few decades particles have been made to collide with such extreme energies that the presence of quarks and gluons have been revealed very much in the same fashion "energetic" α-particles scattered from gold atoms have revealed the nucleus inside Rutherford atom. Although the hadrons are overall colourless they feel a residual strong force due to their coloured constituents.

1.1.1 QCD under extreme conditions

Quantum Chromo-Dynamics (QCD), in the extremes of temperature and baryon density, where the "extremes" [10, 11] means that temperatures of the order of 10^{12}K or 100 MeV and densities of a few times the nuclear matter density ($\sim 0.15\ /fm^3$). The calculations based on statistical QCD predict that strongly interacting systems at very high energy density and/or temperature are composed of weakly interacting quarks and gluons due to asymptotic freedom and Debye screening of colour charge [12]. On the other hand, at low temperature and density the quarks and gluons are confined inside the hadrons. Therefore a phase

transition from hadrons to quarks is expected at some intermediate temperature and density.

Based on the recipes for high temperature and density we can expect QGP formation: (i) at early Universe ,(ii) at the centre of compact stars and (iii) in the initial stage of colliding heavy nuclei at high energies. Heavy ion collisions studies attained importance as under the given conditions of temperature and density QCD lattice theory [13] predicts that hadronic matter undergoes a phase transition towards a "soup" of quarks and gluons in which quarks and gluons are deconfined. As the QCD coupling strength α_s, becomes large at long distances, we cannot adopt the perturbative method. Wilson's lattice gauge theory (Wilson, 1974) may be used to find a solution to this problem. It uses four-dimensional space-time not as a continuum, but as lattice, just as in the crystals, in which quarks occupy the lattice points while the gauge field occupies lattice links. By this method one can solve QCD utilizing Monte Carlo numerical simulations.

But whether quark matter can be formed in the collisions of hadrons needs deeper understanding, where the most promising technique involves in collision of heavy nuclei at relativistic energies. The coloured quarks under such extreme conditions are no longer confined to hadrons but can roam around the entire system. The hadronic system would then dissolve into its constituents, quarks and gluons such that the bulk properties of that hadronic system would be governed by these degrees of freedom [14].

1.2 Quark-Gluon Plasma (QGP)

QCD predicts a phase transition from a state formed by hadrons to a "plasma" of deconfined quarks and gluons [15], as the energy density exceeds a critical value. One of the earliest reviews by Shuryak in 1980 [16], where the first such proposition

was made to describe the deconfined state :

"When the energy density exceeds some typical hadronic value($\sim 1\ GeV/fm^3$), matter no longer consists of separate hadrons (protons, neutrons, etc.), but as their fundamental constituents, quarks and gluons. Because of the apparent analogy with similar phenomena in atomic physics we may call this phase of matter the QCD (or Quark-Gluon) Plasma."

The complicated structure of nuclear matter at low temperatures, where it is composed of a multitude of hadronic particles, baryons and mesons, is thus expected to give way at high temperatures to a plasma of weakly composed quarks and gluons, the $Quark\ -\ Gluon\ Plasma(QGP)$. A thermalized system where the properties of the system are governed by the quarks and gluons degrees of freedom is called the QGP.

1.2.1 The QGP Phase Diagram

To develop an understanding of the deconfining phase transition in hadronic matter and of the QGP properties has proven to be a challenging task. Lattice QCD predicts a phase transformation to a quark-gluon plasma at a temperature of approximately $T \approx 170MeV(1\ MeV \approx 1.1604 \times 10^{10}K)$ (as shown in (Figure. (1.1)) [17]) corresponding to an energy density $\epsilon \approx 1\ GeV/fm^3$, which is nearly an order of magnitude larger than normal nuclear matter.

The thermodynamics of quarks and gluons can be summarized as: statistical QCD predicts the hadron-quark deconfinement transition and the properties of QGP through the first principle calculations of ever increasing precision [18]. The thermodynamical information is presented in the form of a phase diagram, in which the different manifestations and phases of a substance occupy the different regions of a plot whose axes are calibrated in terms of the external conditions or control parameters [19]. The phase diagram of QCD is shown in (Figure. (1.2)) [20] where

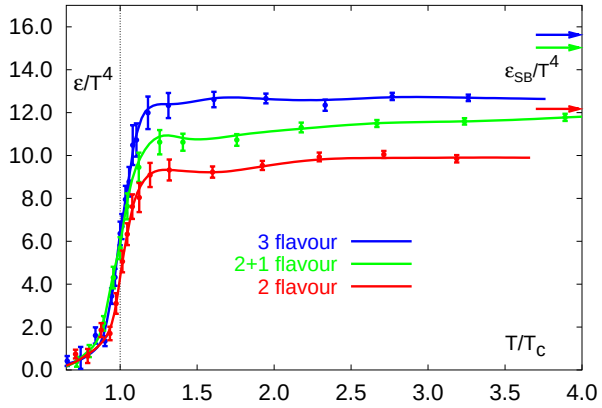

Figure 1.1: Lattice QCD results [17] for the energy density / T^4 as a function of the temperature scaled by the critical temperature T_C.

the the control parameters are the temperature T and the baryon chemical potential μ_B. The freeze-out points are determined from the thermal model analyses of heavy ion collision data at SIS, AGS and SPS energy.

The phase diagram in Figure. (1.2) suggests a possible occurrence of deconfined phases of quark matter at two extreme conditions [21]. The first situation occurs when the temperature is high and net baryon density is zero. The estimated critical temperature (at zero baryon density) is about 170 MeV [17]. The second situation occurs when the temperature is zero and the baryon density is about 5 times the equilibrium nuclear matter density. The astro-physics of neutron stars provides a good testing ground for the exploration of this very dense matter. Neutron stars are cold on the nuclear scale and have temperatures in the range of 10^5 to $10^9 K$ [11].

For a system in between these two limits, there is a pressure arising from the thermal motion of the particles and there is also a pressure arising from the degeneracy of the fermion gas. The total pressure is hence the sum of the two contributions. Thus, for a system whose temperature and net baryon density is

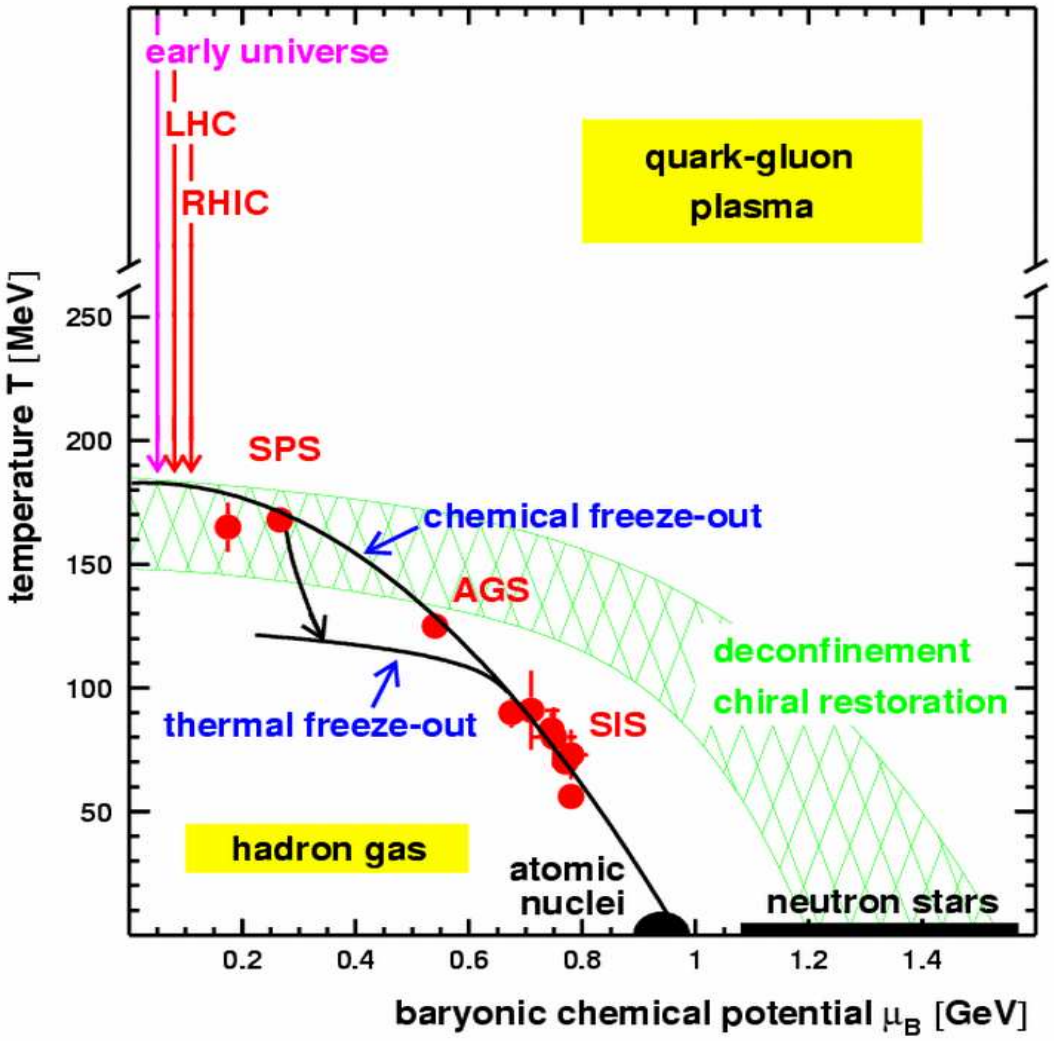

Figure 1.2: The QCD Phase diagram, temperature T vs. baryonic chemical potential μ_B [20]. The hadrochemical freeze-out points are determined from the thermal model analyses of heavy ion collision data at SIS, AGS and SPS energy. The hatched region represents the expectations of the transition region from a deconfined QGP state and a hadron gas state.

non-zero, the critical temperature at which the quark matter becomes deconfined shall be placed between the limits of T = 0 for a degenerate quark gas, and the other limit of critical temperature (T_C) for a pure plasma with no net baryon density. An important objective of modern nuclear physics is to explore the phase diagram of quark matter in the various temperatures and baryon density so as to confirm the existence of the new phase of quark matter [3].

The rise in the computational capabilities have provided the lattice simulations to probe into the properties of this dense matter and the predicted value of the transition is in the range of 160-190 MeV [17]. The results of these studies assert that around the critical temperature T_C, there is a significant rearrangement of the internal structure of the hadronic matter [22]. It has been found that near T_C the matter is strongly coupled [23].

1.3 Relativistic Heavy Ion Collisions

The aim of the relativistic heavy ion physics is the experimental study of the QCD nature of matter under the conditions of extreme temperature and high energy density. The discovery of the QGP can describe the system (governed by the quarks and gluons) in which the degrees of freedom are no more the colour neutral hadron states observed in isolation as particles and resonances [15, 24, 25, 26]. However this definition has its limitations as the high-energy proton-proton reactions cannot be described purely in terms of colour neutral hadrons, but on the other hand needs an analysis of partonic interactions [15]. The much needed difference in heavy ion collisions is the dominance of the partonic-level description for all momentum scales and over all nuclear sizes. To characterize the produced system, its essential to establish that these non-hadronic degrees of freedom form a statistical ensemble, so that the concepts of temperature, chemical

potential and flow velocity can be applied and the system can be characterized by an experimentally determined equation of state. The experimental measurements should further be able to determine the physical characteristics of the transition, for example the critical temperature, the order of the phase transition, and the speed of the sound along with the nature of the quasi-particles.

As discussed in Section 1.2.1, the transition from hadronic gas to a quark-gluon plasma should occur at a temperature of approximately 170 MeV. This value coincides with the "limiting" temperature of matter composed of hadrons first postulated by Hagedron [27]. The precise value of the transition temperature T_C, and how high the temperature must rise before the plasma can be considered as weakly coupled can be determined by accurate, non perturbative simulations of the equations of QCD. While at currently attained high temperatures $T \gg T_C$ the quark-gluon plasma may act as an weakly interacting gas of quarks and gluons but in the transition region near T_C the fundamental degrees of freedom may be much more complex [28].

1.3.1 Kinematic Variables

The initial information of the heavy ion collisions can be inferred from the observed particle distributions, both in transverse momentum (p_T) and rapidity (y) distributions. The particles can be characterized by the following kinematic variables:

- For the transverse direction the **transverse momentum (p_T)** or for the identified particles the **transverse mass (m_T)**,

$$m_T = \sqrt{p_T^2 + m^2} \tag{1.2}$$

  is used where m is the mass of the particle.

- The **rapidity** of a particle is defined in terms of its energy-momentum components E and p_z by

$$y = \frac{1}{2}\ln(\frac{E+p_z}{E-p_z}) \ . \tag{1.3}$$

  It is a dimensionless quantity related to the ratio of the forward light-cone momentum to the backward light-cone momentum. It can be either positive or negative. The rapidity variable depends on the frame of reference, but its simple. The rapidity of the particle in one frame of reference is related to the rapidity in another Lorentz frame of reference by an additive constant.

- In some experiments it maybe possible only to measure the angle of the detected particle relative to the beam axis. In that case it will be convenient to use the **pseudorapidity** variable called η, which is defined as,

$$\eta = -\ln[tan(\theta/2)] = \frac{1}{2}\ln(\frac{|\overrightarrow{p}|+p_z}{|\overrightarrow{p}|-p_z}), \tag{1.4}$$

  where θ is the angle between the particle momentum $\overrightarrow{p}$ and the beam axis.

Comparing Eq. (1.4) and Eq. (1.3) we can see that the pseudorapidity variable coincides with the rapidity variable when the momentum is large, where $|\overrightarrow{p}| \approx E$.

And using Eq. (1.4), we can express $|\overrightarrow{p}| = p_T \ cosh \ \eta$, where the magnitude of transverse momentum is $p_T = \sqrt{p^2 - p_z^2}$. So we obtain, $p_z = p_T \ sinh \ \eta$.

Using these results we can express the rapidity variable y in terms of pseudorapidity variable η as,

$$y = \frac{1}{2}\ln[\frac{\sqrt{p_T^2 \ cosh^2 \ \eta + m^2} + p_T \ sinh \ \eta}{\sqrt{p_T^2 \ cosh^2 \ \eta + m^2} - p_T \ sinh \ \eta}] \ , \tag{1.5}$$

m is the rest mass of the particle. Now expressing η in terms of y as,

$$\eta = \frac{1}{2}\ln[\frac{\sqrt{m_T^2\ cosh^2\ y - m^2} + m_T sinh\ y}{\sqrt{m_T^2\ cosh^2\ y - m^2} - m_T\ sinh\ y}]\ . \tag{1.6}$$

So if the particles have a distribution $dN/dydp_T$ in terms of the rapidity variable y, then the distribution in terms of the pseudorapidity variable η is

$$\frac{dN}{d\eta dp_T} = \sqrt{1 - \frac{m^2}{m_T^2\ cosh^2\ y}}\ \frac{dN}{dydp_T}\ . \tag{1.7}$$

In high energy experiments where dN/dy has a plateau shape, this transformation in Eq. (1.7) gives a small dip in $dN/d\eta$ around $\eta \approx 0$. In the center-of-mass frame, the peak value of $dN/d\eta$ is thus smaller than the peak value of dN/dy by approximately the factor $(1 - m^2/ < m_T^2 >)^{1/2}$. In the laboratory frame, the peak of the distribution is located around half the beam rapidity $\eta = y_b/2$ for which the factor $[1 - m^2/ < m_T^2 >)\ cosh^2(y_b/2)]^{1/2}$ is about unity. The peak value of $dN/d\eta$ is approximately equal to peak value of dN/dy. Hence the rapidity distribution remains unchanged as we move from center-of-mass frame to laboratory frame. The peak value of pseudorapidity distribution is lower in center-of-mass frame than laboratory frame [3].

1.3.2 Space-time evolution of the Collision

In any frame of reference where the incoming nuclei have very high energies the region when/where the nuclei overlap will be very thin in the longitudinal direction due to Lorentz contraction and very short in duration [29]. Now we consider the centre-of-mass frame where there is head-on collision of two equal nuclei. Because of Lorentz contraction the two colliding nuclei appear as two thin disks. When the beam "pancakes" recede after their initial overlap, the region between them is occupied by the secondaries at intermediate rapidities [15].

The Lorentz contracted nuclei [29] at extremely high energies produce particles at initial time t. At such high energies the nuclei are mostly transparent to nucleons and under such a central collision the nuclei pass through each other producing two excited fragmentation regions. The regions correspond to the target and to the projectile and are expected to be joined together by a central rapidity region with small net baryon number and high energy density [29, 30].

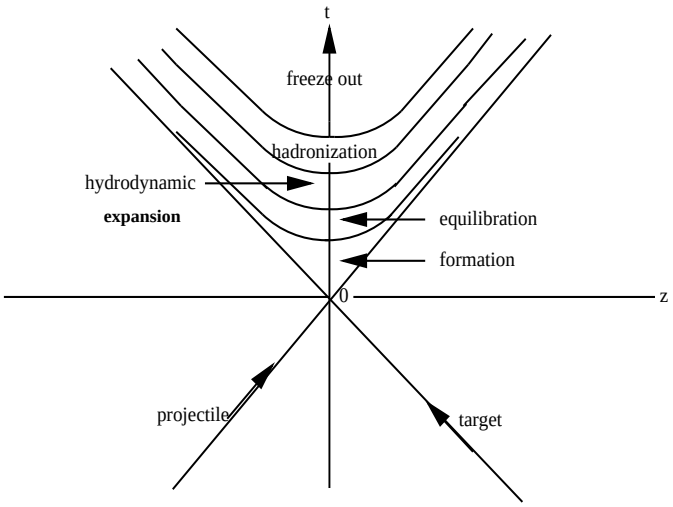

Figure 1.3: Space-time schematic in centre-of-mass frame of two colliding nuclei.

In the centre-of-mass frame in a head-on collision the nuclei follow trajectories close to the light cone, as shown in the t, z diagram of Figure. (1.3). Here z is the co-ordinate along the collision axis, with $z = t = 0$ the central point of the collision.

Using the rapidity y of the particle (from Eq. (1.3)) we can relate space-time as, $z = \tau\ sinh\ y$ and $t = \tau\ cosh\ y$, where τ is the proper time variable defined as:

$$\tau = \sqrt{t^2 - z^2}\ . \tag{1.8}$$

We can express the rapidity variable y in terms of t and z by

$$y = \frac{1}{2} \ln \frac{t+z}{t-z} \ . \tag{1.9}$$

Assuming thermalization at τ_0 the excitations are "free streaming" before and hydrodynamic after τ_0. Thus considering the initial boundary condition on the surface of constant $\tau = \tau_0$. Under such assumptions the energy density ϵ is a constant ϵ_0 and initial flow velocity v_z is z/t.

The various stages of a heavy ion (e.g gold-gold) collision is summarized as follows:

- The Initial state : The Lorentz contracted incoming nuclei contain a high density of "soft" gluons. The participating "pancakes", in gold-gold collisions may reach a saturated value in terms of high gluon density and hence their interaction marks the initial state of the collision.

- Impact of two nuclei : When the nuclei meet, the initial events are high-energy inelastic collisions between the individual nucleons in which many partons are liberated. The high energetic quarks and gluons formed produce "jets" of hadrons which propagate through the matter formed.

- Plasma phase : The released partons have the opportunity to re-scatter several times with the result that their momenta, initial highly correlated along the beam axis, are redistributed and a substantial amount of the incident kinetic energy. Thus the hot, dense matter, consisting of quarks, anti-quarks and gluons reach a state of equilibrium, with the dense matter expanding and cooling through very strong collective interactions.

- Final Freeze-out : The matter cools below QCD critical temperature and the quarks and anti-quarks coalesce to form hadrons, and such final state particles are sensed by detectors. But the hadronic properties revealed in

their spatial distributions along with the relative abundances of particles in terms of their quark constituents – retain an early picture at the time of freeze-out.

1.3.3 Initial Energy Density

In the centre-of-mass system, the region of small rapidity is known as the "central rapidity region". As introduced and explained in previous Section 1.3.2, the central region is related with the central spatial region around $z \sim 0$, and henceforth "central rapidity region" is associated with that.

The initial energy density of a fluid element is defined in the frame where the fluid element is at rest. In the centre-of-mass frame matter is at rest at z=0 [3]. The transverse overlapping area in the collision of two nuclei is denoted as A. So the initial energy density ϵ_0 averaged over the transverse area A at time τ_0 is thus,

$$\epsilon_0 = \frac{m_T}{\tau_0 A}\frac{dN}{dy}\Big|_{y=0} . \tag{1.10}$$

This relation was first derived and explained by Bjorken [29], which connects the initial energy density to the rapidity density. The Bjorken energy density of the central region estimated for different experiments is summarized in Chapter 2.

1.3.4 Particle Production

When the two nuclei strike each other with full speed, a superposition of nucleon-nucleon(NN) collisions occurs. The difference compared to individual NN collisions is that (i) each nucleon may re-scatter several times, and (ii) the produced partons from different NN collisions re-scatter with each other even before hadronization, as in the case of secondary hadrons produced in different NN collision. Both of

these items change the particle production per participating nucleon. The re-scatterings lead to a state of thermal equilibrium, resulting in thermodynamic pressure which acts against the outside vacuum, causing the reaction zone to expand collectively. Such expansion cools and makes the fireball below the critical energy density of quark-hadron transition. The resulting further interactions between these hadrons reduce as their average distance exceeds the range of strong interactions: "freeze-out" of hadrons. The heavy ion collision environment produces and emits huge number of particles [31] comprising of photons, leptons and various types of hadrons. The understanding and investigation of the hot and dense early stages of collision requires to exploit those features which happened early and was un-affected by re-scattering and collective expansion or which can be reliable back-extrapolated [32].

1.3.4.1 Photon Production

The photons are emitted all throughout the expansion, but their production is expected to be weighted towards the hot and dense early stages of the collision. The production of photons in heavy ion collisions is complex and can be summarized as four sets of mechanisms [33, 34]:

- (i) The photon is produced in the hard interaction of two partons in the incoming nuclei which is similar to the known QCD processes (QCD Compton, annihilation, bremsstrahlung) in the nucleon-nucleon collisions. Such rates can be calculated in perturbative QCD and falls off at large transverse momentum, p_T, as power law;

- (ii) When the nuclei collide the density of secondary hadrons is high that the quarks and gluons become unconfined and a bubble of QGP is formed. It is assumed that the plasma evolves hydro-dynamically. Photons are emitted in

the collisions of quarks and gluons in the plasma with an energy spectrum which is damped exponentially but that should extend upto several GeV;

- (iii) The QGP bubble expands and cools until a temperature of 150 to 200 MeV is reached and a hadronic phase appears. As they collide the neutral pions and other hot resonances (ρ, ω) emit photons until the freeze-out temperature is reached. The typical energy of such photon ranges from several hundred MeV to several GeV;

- (iv) Photons are also the decay products of the hadrons (like, π_0, η, etc) emerging at the end of the thermal evolution and have an energy of the range of few MeV. π_0 and η mesons can also be produced at higher p_T in hard parton scattering during the early stages of the collision, having the energy of the order of several GeV. These photons together with that mentioned in (i) are a background to thermal photons produced in (ii) and (iii).

1.3.4.2 Hadron Production

The hadrons made of quarks, are relatively produced and destroyed in all stages of the fireball expansion and hence provide only indirect information of the early collision stages. But they are very abundant and hence can be accurately measured.

The particle source produced in these relativistic heavy ion collisions possess a very high energy density and therefore high temperature which immediately begins to expand and cool. After the expansion reaches to a certain extent, eventually the temperature decreases at a point where hadrons stop interacting with each other [35]. The particle ratios are fixed at this point and we refer to this state of particle source as a "chemical freeze-out"(i.e when the hadron abundances freeze-out) [35, 36, 37], which provides information in particular about the degree of chemical equilibration.

There is another type of freeze-out, that is, after further expansion and cooling, the temperature goes down to a point where the final state interactions between hadrons are no longer effective. This is referred to as a "thermal freeze-out" (i.e along the last-scattering hyper-surface which indicates the decoupling of the momenta) [35, 38].

1.3.5 Particle Correlations

The parton interactions in relativistic heavy ion collisions lead to the build up of pressure as the colliding system undergoes longitudinal and transverse expansion, where the latter cause an increase in final transverse momenta of the produced particles. The subsequent transverse radial expansion of the system creates strong position-momentum correlations and leads to characteristic rapidity, transverse momentum and azimuthal correlations among the produced particles [39, 40, 41].

The *correlation techniques (of two and many particle)* are powerful tools in the present quest to understand multi-particle production in nuclear collision [42]. The evidence of QGP phase transition must come from studying the particles that are emitted from the region after it has entered the normal hadronic phase. A promising phenomena which survives hadonization and freeze-out is based on the expectation that the larger number of degrees of freedom is associated with the deconfined state with manifestation of increased system entropy. The increase in entropy will cause the system to expand more and/or interact for a longer time and produce more particles, which can be revealed with the help of two-particle correlations [43, 44].

1.3.6 QGP Signatures

Experimental investigations of the quark-gluon plasma require the identification of appropriate experimental tools for observing its formation and studying its properties. One serious problem is that the size and the lifetime of the plasma are expected to be small, at most a few fermi in diameter and perhaps 5 to 10 fm/c in duration [23, 45]. Furthermore, signals of the quark-gluon plasma compete with the backgrounds emitted from the hot hadronic gas phase that follows the hadronization of the plasma, and are modified by the final state interactions in the hadronic phase.

Different experimental probes examine different stages of the matter as it expands and evolves back to normal matter. *Hard probes* created in the initial collisions before thermalization of the medium probe the medium through their final-state interactions. *Soft probes* come from the medium itself and provide a picture of its thermalization and spatial evolution [45].

1.3.6.1 Soft probes

The soft probes [18] test the equilibration and the presence of collective effects at freeze-out. The spectra and relative abundances of "light" hadrons produced in nuclear collisions provide direct information on the system state at the end of the strong interaction period. The basic concepts behind this class of signatures [45] is the determination of the energy density ϵ, pressure P, and entropy density s of the superdense hadronic matter as a function of the temperature T and the baryochemical potential μ_B. The measurable observables that are related to the variables T, s, and ϵ, are customarily identified with the *average transverse momentum* $\langle p_T \rangle$, the hadron rapidity (or pseudo-rapidity) distribution, and the transverse energy dE_T/dy respectively. The transverse momentum of the emitted hadrons have been

measured to infer about the collision system at freeze-out.

1.3.6.1.1 Multiplicity : The *multiplicity* of the produced particles [46] is the first and most fundamental observable which characterizes the heavy ion interactions. The studies of the global shapes of the multiplicity distribution implies a wide η acceptance experiment. It also exhibits a "bell" shape where the central region is sensitive to the details of hadro-production mechanism and the side regions are related to the fragmentation of the projectile and target. Furthermore, the multiplicity information allows one to constrain the hadro-production models. Thus, in the phenomenological approach, the measured pseudorapidity density $dN_{ch}/d\eta$ is expressed as the sum of a term proportional to the number of participants N_{part} (soft component) and the number of binary collisions N_{coll} (hard component). Measuring $dN_{ch}/d\eta$ as a function of N_{part}, one can estimate the relative number of particles produced in hard and soft scatterings.

1.3.6.1.2 Flow : A high degree of collective behaviour displayed by the medium produced in such relativistic heavy ion collisions, is termed as *flow* [47]. The high pressure of the quark-gluon plasma leads to the formation of a collective outward flow during the expansion of the dense matter. By characterizing the non-central collisions we can understand the extent of this outward pressure and under such conditions the overlap region is not circular in the transverse plane, but on the other-hand elliptically shaped. So the density distribution if decomposed into azimuthal angle Fourier components has many non-zero coefficients, with the second coefficient(called v_2 or elliptic flow) as the largest [48]. This Fourier decomposition really measures particle emission directly correlated with the orientation of the density gradients as shown by the fact that v_2 for all charged particles at low transverse momenta scales linearly with the eccentricity of the nuclear overlap

region (which is the exact shape of the ellipse) [49].

1.3.6.1.3 Fluctuations : Another set of global observables are related to *fluctuations* [23], which are of fundamental importance for studying perturbation of a thermodynamic system. Several thermodynamic quantities show varying fluctuation patterns when the system undergoes a phase transition [50]. In the study of phase transitions the measurements of particle number and energy fluctuations become relevant. Event-by-event fluctuations of thermodynamic quantities measured in high energy heavy-ion collisions provide a reasonable framework for studying the nature of the QGP phase transition in the laboratory.

1.3.6.1.4 Hanbury-Brown - Twiss (HBT) effect : The lattice simulations of QCD state that the speed of sound (c_s), is expected to reach a minimum near T_C, and then increase in the hadronic gas domain. If matter is produced near this point, the expansion is minimal, leading to an increase in lifetime of the emission source or fireball. Identical particle correlations (or interferometry) yields information on the reaction geometry, thus providing important information about the space-time dynamics and system lifetime of nuclear collisions. The information about the space-time structure of the emitting source created in elementary particle and heavy ion collisions from the measured particle momenta can be extracted by the method of "two-particle intensity interferometry techniques" also called the $Hanbury - Brown - Twiss (HBT) effect$ [51, 52] which was initially developed to measure the angular size of distant stars [53].

The two particle correlations arises from the interference of particle wave-functions where interference is defined as a phenomenon associated with the superposition of two or more waves. Such correlation depends on whether the particles are bosons or fermions. Also the degree of interference depends on the degree of

coherence of the emitting source of particles (produced in such collisions), and turns a maximum for a totally incoherent source. HBT is a useful method to understand the crucial reaction mechanisms and equation of state of the particle emitting source [54] in relativistic heavy ion collisions, where the Quark-Gluon Plasma (QGP) is expected to be formed.

The information of the QCD equation of state(EoS) can be extracted from the collective dynamics studies of heavy ion collisions. EoS is especially soft near the QCD phase transition ($T_C = 173 \pm 15$ MeV) where the speed of sound $c_s^2 (= dp/d\epsilon) \approx 1/20$ steeply drops from the region T $> 2T_C$ where $c_s^2 \approx 1/3$ [55]. A key goal of flow studies in relativistic heavy ion collisions is to understand the "softest point" in the data [56], and it was shown [57] that the transition to the QGP softens the EoS in the transition region. It thus reduces the tendency of matter to expand on account of internal pressure, which in turn delays the expansion prolonging the system lifetime considerably [58].

The prolongation of the lifetime can be measured and observed via the ratio of the inverse widths of the two-particle correlation functions in the outward and side-ward directions. Thus interferometry can provide the important signature of the phase transition from the enhanced ratio relative to that value obtained from the ideal gas case without such a transition [58]. Such a time delay provides a crucial signature to the QGP formation and helps in the characterization of the "soft region" in EoS of dense matter formed in relativistic heavy ion collisions. The correlation function with pions (as they are most abundantly produced) and direct photons (as they are produced at all stages of the collision system) will provide an estimate of the volume and hence infer the EoS of the emitting source.

1.3.6.2 Electromagnetic probes

Photons and *lepton pairs* [59] provide probes of the interior of the quarks-gluon

plasma during the earliest and hottest phase of the evolution of the fireball since they are not affected by the final state interactions.

1.3.6.2.1 Leptons: The produced lepton l^- and its anti-particle partner l^+ carry the information of thermodynamical state of the medium at the moment of their production, since the production rate and momentum distribution of the l^+l^- pairs depend on the momentum distribution of quarks and anti-quarks in the plasma, which in turn are governed by the thermodynamic condition of the plasma [3]. But in a high energy nucleus-nucleus collision, the possible formation of the QGP is not the only source of the production of l^+l^- pairs. There are other processes like for example the Drell - Yan process which is important for large values of the invariant mass of the l^+l^- pair [3, 60, 61]. In the Drell - Yan process in a nucleus-nucleus collision, we have a valence quark of a nucleon of one of the nuclei can interact with a sea anti-quark of a nucleon of the other nucleus. They annihilate to form a virtual photon which subsequently decays into a l^+l^- pair.

A large fraction of the dilepton yield arises from the decay of long lived states, such as the neutral pions, eta, or the omega. These resonances decay well outside the hot and compressed region and henceforth detailed analysis of the dilepton spectra is needed in order to extract the information about the properties of the hot and dense matter, such as the possible in medium changes of hadrons. In the low mass region, below the phi-meson, the most important production channels are: (i) Dalitz decays of η, Δ, ω, a_1; (ii) Direct decays of the vector mesons, such as ρ, ω and Φ. To separate out the portion due to QGP, it is essential to analyze the contribution from all other sources of dilepton production [60, 61].

1.3.6.2.2 Photons: The several production mechanisms of photons in heavy ion collisions are discussed in Section 1.3.4.1 and the investigation using photon is

advantageous in following aspects :

- Photons are electro-magnetically interacting particles and hence while traversing through the nuclear matter the mean free path of the photons is found to be large and the photons may not suffer a collision after it is produced in dense medium;

- The energy distribution of photons will allow to measure the temperature of the plasma, if the rate of the production in plasma is more than the various backgrounds. The expected range of such photons are in GeV range and at lower energy values the rate is dominated by the large background from hadronic decays which hinder such probes. The higher values can be calculated from perturbative QCD methods [59];

- Photons are emitted at all stages of the collision and hence they provide valuable information about the collision history and also about the hot and dense matter formed. This provides an important advantage unlike the hadrons which serve the physics information after the plasma has cooled down.

When we define the "inclusive" photon spectrum : it is the unbiased photon spectrum observed in a collision of two hadrons or a hadron and a nucleus or two nuclei. Such a spectrum constitute of a cocktail of many components as follows:

- "Prompt" photons are those that are produced in the early stages of the collision in the hard QCD processes. They are directly associated with the hard process or produced by bremsstrahlung in a hard QCD process. The associated power spectrum is power behaved and dominates at large transverse momentum;

- "Thermal" photons which are emitted in the collisions of the quarks and gluons in the QGP phase or in the scattering of the hadronic resonances

in hot and dense matter. Their spectrum is exponentially damped at large energy;

- "Direct" photons are the sum of the "prompt" and "thermal" photons. They can be obtained experimentally by subtracting from the inclusive spectrum the contribution from the "decay" photons which constitute a reducible background.

To measure the direct photons in heavy ion collisions is a difficult task due to the large background of decay photons produced in electromagnetic decays like $\pi_0 \rightarrow \gamma + \gamma$ and $\eta \rightarrow \gamma + \gamma$. The interest for direct photons arises from the fact that they traverse the hot dense nuclear matter formed in such relativistic heavy ion collisions with almost without any further interaction [62, 63, 64]. They thus convey information about the early stages of the nucleus-nucleus collision. It is expected that during the early stages of the collision with sufficiently high energy a thermalized medium is formed in which quarks and gluons are the relevant degrees of freedom.

The electric charges in such a quark-gluon plasma (QGP) are expected to radiate photons whose momentum reflects the temperature of the system. The production of thermal photons is a suggested signature of QGP formation and the main contribution to "thermal direct photons" is expected from the early hot phase after thermalization. So by measuring the "thermal direct photons" one can understand the initial temperature of the fireball [65].

In the heavy ion collisions the aim is to extract the "thermal" signal which can be done by subtracting the "prompt" photon contribution (calculated from theory) from the "direct" photon spectrum. So except for the photons from QGP all the photons originating from other sources are to be considered as background. In the context of thermal production the "soft" photons have an energy much less

than the temperature of the medium while the "hard" ones have an energy of the order of the temperature or larger. Only hard thermal assume importance for phenomenological studies as the soft ones are overwhelmed by the background.

1.3.6.3 Hard probes

In QGP which is a dense system of deconfined quarks and gluons, the long range forces become screened and only the short range interactions remain. For the understanding of the medium we need hard probes to penetrate the medium and resolve the sub-hadronic scales causing a distinction between confined and deconfined quarks and gluons. The colour structure of QCD matter can be probed by its effects on the propagation of a fast parton. The mechanisms are similar to those responsible for the electromagnetic energy loss of a fast charged particle in matter where energy may be lost either by excitation of the penetrated medium or by radiation.

There are two types of hard probes:

— hard quarks and gluons (jets) [66], and

— heavy quark-antiquark resonances(charmonium, bottomonium) [67].

Partons with large transverse momentum in the high-density system result from the initial scattering of nucleon constituents. After the hard scattering occurs, the parton fragments create a high energy cluster(jet) of particles. The propagation of partons through a dense partonic medium modifies the parton transverse momentum due to induced radiative energy loss or jet quenching [68]. High transverse momentum (p_T) particles and jets have been used to probe the QGP to study its properties and gain a better understanding of high density QCD and hadronization.

The production of heavy flavour states in p+p, p+A and A+A collisions provides an important tool to study the properties of QGP [69]. The larger production

cross-sections for charmonium [70] states compared to bottomonium states have initiated the studies of charmonium along with the observation of charmonium suppression [71, 72] in relativistic heavy ion collisions. As the bottomonium is massive ($\sim 10GeV/c^2$) its decay leptons have sufficiently large momenta and bottomonium spectroscopy requires large multiplicities. Its decay leptons have sufficiently large momenta above the background processes which helps in high-level triggering.

1.3.6.4 Quarkonium suppression

In a QGP, the string tension is zero. The only interaction between c and $\overline{c}$ is the Coulomb type interaction. If a J/Ψ particle is placed in QGP, the colour charge of the charm quark c will be screened by the quarks, anti-quarks and the gluons on the plasma. The basic mechanism for deconfinement in the dense QGP is the Debye screening of the quark colour charge. The effect of Debye screening will modify the the long-range Coulomb potential into a short-range Yukawa potential with the range given by Debye screening length, λ_D.

When the screening radius becomes less than the binding radius of the quark system, which means that it becomes less than the hadron radius, the confining force can no longer hold the quarks together and hence deconfinement sets in. The J/Ψ has a radius of about 0.2 fm which is much smaller than the normal hadronic scale $\Lambda_{QCD}^{-1} \approx 1$ fm; having a binding energy of 0.6 GeV which is larger than $\Lambda_{QCD} \approx 0.2$ GeV. Λ_{QCD} is called the QCD scale parameter to be determined from experiments.

In nucleus-nucleus collisions the J/Ψ particles are produced in the initial stage of hard scattering. The suppression of J/Ψ production in a quark-gluon plasma occurs because a $c\overline{c}$ pair formed by fusion of two gluons from the colliding nuclei cannot bind inside the quark-gluon plasma. Hence the effect of plasma will make the J/Ψ unbound, thus the suppression of J/Ψ production is a possible signature

of QGP formation [71].

1.3.6.5 Strangeness enhancement

The production of hadrons containing strange quarks is normally suppressed in hadronic reactions compared with the production of hadrons containing only up and down valence quarks. This suppression increases with growing strangeness content of the produced hadrons. The theoretical studies have shown that strangeness is produced rapidly in the collisions of thermalized gluons, within the deconfined state, formed in heavy ion collisions [73, 74].

When a quark-gluon plasma is formed, the production of hadrons carrying strange quarks is expected to be saturated because of strange quark content of the plasma is rapidly equilibrated by $s\overline{s}$ pair production in the interactions of two gluons [75]. So the yield of multi-strange baryons and strange antibaryons is predicted to be strongly enhanced [76] in the presence of a quark-gluon plasma.

The deconfined state of QGP breaks up in a fast hadronization process: with the enhancement of strange hadrons hadrons and strange anti-baryons, along with the rise of valence quark content of hadrons produced as the predicted property of deconfined phase [75]. This occurs due to the breakup of strangeness rich deconfined states (or hadronization), where several strange quarks are formed before and the independent reactions can combine into a multi-strange hadron.

1.3.6.6 Probes of Chiral symmetry restoration

The approximate chiral symmetry of QCD is spontaneously broken by the existence of a quark condensate in vacuum [23]. Due to large energy deposit in the collision zone of the relativistic collisions, a hot, chirally symmetric QGP is formed. But the rapid expansion at earlier times, the system is suddenly reduced down to

lower temperatures, where chiral symmetry is spontaneously broken [77]. Lattice simulations predict a very rapid drop of the scaler quark condensate $\langle q\overline{q}\rangle$ from its vacuum value to almost zero in a narrow temperature region around T_C. The temporary restoration of chiral symmetry in nuclear collisions may result in the formation of domains of disoriented chiral condensate (DCC) [45].

1.4 Photon and Hadron Interferometry

The two-particle intensity interferometry techniques (or HBT correlations explained in Sections 1.3.5 and 1.3.6.1) have been successfully used in nuclear and particle physics for a broad energy domain to measure the space-time extent of a variety of particle sources. The particles used are pions and kaons initially and later extended to protons, neutrons and other heavier particles.

Photons, which provide a natural probe for interference, was a difficult initial choice because of the low production cross-section at intermediate energies. We have summarized photon and hadron production in Section 1.3.4. At relativistic energies measuring such direct photons is largely hindered due to the large background of hadron decays such as $\pi_0 \rightarrow \gamma\gamma$ or $\eta \rightarrow \gamma\gamma$. The direct photons, which are emitted during all the stages of the collision, serve as a deep probe of the hot and dense matter.

However the two-photon momentum correlations are not very much affected as the correlations of photons coming from decay of two different hadrons are confined to extremely small relative momenta. This makes photon interferometry a promising tool which can provide the system sizes at all stages of heavy ion collisions [78, 79, 80].

Despite the difficulties in measurements due to decay background of π^0's and η's, the photon intensity interferometry can provide the essential information about

the early reaction stages of the relativistic heavy ion collisions where the high temperature phase of QCD, the Quark Gluon Plasma(QGP) comes within experimental reach.

The Table 1.2 shows an enumeration of differences between photons and hadrons which appear to be relevant from the intensity interferometry point of view.

Table 1.2: Comparative analogy of Photon and Hadron Interferometry

Photon Interferometry	**Hadron Interferometry**
(1)Direct photons provide information of the system at all stages of the collision.	(1)Hadrons (mesons and baryons) provide information of the collision system at freeze-out.
(2)Very Small yields of direct photons making the measurement difficult.	(2)Large yields of hadrons.
(3)Very few experimental measurements.	(3)Large experimental results.

1.5 Thesis layout

In this thesis, photon and hadron production and correlation studies are discussed and presented. These measurements are used to understand the space-time structure of the particle emitting source. The remainder of the thesis is organized as follows: In Chapter 2 the experimental facilities at Brookhaven National Laboratory, i.e mainly the Relativistic Heavy Ion Collider (RHIC) and the experimental setup of the STAR detector systems are discussed. Further detector details regarding the photon and hadron measurements in STAR experiment are explained in Chapter 3. The challenging studies of photon multiplicity measurements at forward rapidity with STAR Photon Multiplicity Detector (PMD) are presented in Chapter 3, along with the description of STAR Barrel Electro-Magnetic Calorimeter (BEMC) and STAR Time Projection Chamber (TPC). In Chapter 4 we discuss the basics of the

method of two-particle correlations (also known as intensity interferometry). In Chapter 5, development of analyses cuts for two-photon intensity interferometry measurements in Au+Au collisions at $\sqrt{s_{\rm NN}} = 62.4$ GeV using STAR BEMC are discussed. In Chapter 6, systematic analyses of two-pion intensity interferometry in Au+Au collisions at $\sqrt{s_{\rm NN}} = 62.4$ GeV and Cu+Cu collisions at $\sqrt{s_{\rm NN}} = 62.4$ and 200 GeV using STAR TPC, are presented and compared with previous RHIC results and lower energies. A summary and outlook is presented in Chapter 7.

Chapter 2

Experimental Facilities

The search of Quark-Gluon Plasma (QGP) will be by characterizing its experimentally observed properties, using the experimental facilities like accelerators and sophisticated detectors. A collaboration was setup in 1984 with researchers from Berkeley Laboratory, USA, and Gesellschaft für Schwerionenforschung (GSI), Germany, working in BEVALAC (the accelerator configuration when the Bevatron was coupled to the SuperHILAC). They observed the first evidence that nuclear matter can be compressed to high temperature and density which marked the first major milestone in the search for QGP in laboratory. The evidence discovered was a phenomenon called *collective flow* [47] which is described in Section 1.3.6.1.2.

The collisions between heavy nuclei at relativistic energies provide the only possibility to study the properties of dense matter in the laboratory. The experimental search for Quark-Gluon Plasma (QGP) is the most fundamental and challenging task in modern nuclear physics and this triggered a series of experimental searches during the past two decades at CERN and BNL.

Many observed effects in the field of heavy ions have been provided by the Schwer Ionen Synchrotron (SIS), GSI and Alternating Gradient Synchrotron (AGS)

of the Brookhaven National Laboratory (BNL), USA. Also in recent past the Super Proton Synchrotron (SPS) accelerated particles upto the size of lead. Various experiments with AGS and SPS opened a new era in the search of Quark-Gluon Plasma. Presently the Relativistic Heavy Ion Collider (RHIC) at Brookhaven National Laboratory was constructed to investigate the properties of nuclear matter at ultra-high energy densities. In 2007 the Large Hadronic Collider(LHC) at CERN will be commissioned. Other searches for future facilities are being set-up at the Facility for Antiproton and Ion Research (FAIR) in Gesellschaft für Schwerionenforschung (GSI), Darmstadt to arrange heavy ion experiments at low energy and high luminosity.

The Table (2.1) presents an overview of ultra-relativistic heavy ion accelerators which summarizes the last 30 years of heavy ion collision experiments from 2 GeV (1975) to 5500 GeV(2007). It shows the maximum energy-per-nucleon in centre-of-mass frame and whether the set-up is fixed target or collider.

Table 2.1: Experimental facilities for heavy ion collisions.

Experimental Facility (time period)	**Laboratory**	$\sqrt{s_{\rm NN}^{max}}$	**Type**
BEVLAC(1975 - 1986)	LBNL	2.0 GeV	Fixed target
SIS(1989 -)	GSI	2.4 GeV	Fixed target
AGS(1986 - 1998)	BNL	4.8 GeV	Fixed target
SPS(1986 - 2003)	CERN	17.3 GeV	Fixed target
RHIC(2000 -)	BNL	200 GeV	collider
LHC(2007 -)	CERN	5500 GeV	collider
FAIR(2014 -)	GSI	8 GeV	Fixed target

The Bjorken energy density of the central region (described in Section 1.3.3) from the estimated central event samples is $\sim$ 0.5 GeV/fm^3 for SIS energies, $\sim$ 1.5 GeV/fm^3 in Au+Au collisions at AGS energies ($\sqrt{s_{\rm NN}}$ = 5 GeV), $\sim$ 2.9 GeV/fm^3 in Pb+Pb collisions at SPS energies ($\sqrt{s_{\rm NN}}$ = 17 GeV), to about 5.4

GeV/fm^3 in Au+Au collisions at full RHIC energy ($\sqrt{s_{\rm NN}}$ = 200 GeV) [15]. In this chapter the experimental facilities at Brookhaven National Laboratory, i.e mainly the Relativistic Heavy Ion Collider (RHIC) and the experimental setup of the STAR detector systems are discussed.

2.1 Relativistic Heavy Ion Collider (RHIC)

The Relativistic Heavy Ion Collider(RHIC) which was completed in 1999 and started its operation from 2000 is a unique heavy ion collider/accelerator [81]. The scope of the RHIC design and construction which began in 1990 included the superconducting hadron collider with the beam injection lines from the existing Alternating Gradient Synchrotron(AGS) to the collider. It was thought that the already existing facilities like the Tandem Van de Graff, the Booster and the AGS would be used as the heavy ion injector for the RHIC rings. The proton linac would be used for the source of polarized protons.

The circumference of RHIC ring is 3.8 km and is composed of two identical quasi-circular rings of superconducting magnets which are oriented to intersect at six interaction points (IPs) supporting four experiments (STAR, PHENIX, BRAHMS, PHOBOS) as shown in Figure. (2.1). The RHIC machine [82] is capable of accelerating and maintaining beams of ions – with heavy ions (like gold) upto a momenta of 100 GeV per nucleon and protons upto 250 GeV, along with the smaller mass nuclei upto the intermediate momenta depending on their mass to charge ratio. The primary objective of RHIC is to investigate the phase transition and study the formation and property of QGP.

RHIC also has the unique capability of colliding polarized protons beams, making possible experiments that are important for studying the spin structure of nucleons [83]. The addition of Siberian Snakes for such spin studies was made

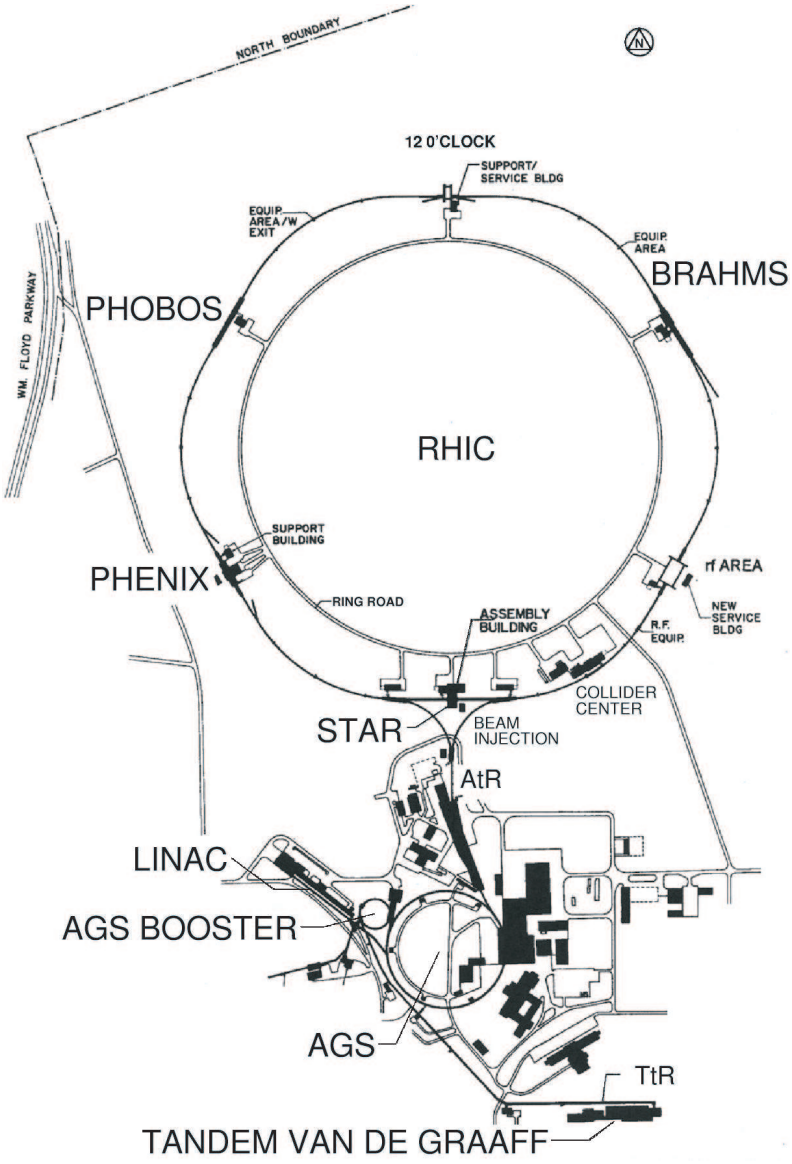

Figure 2.1: The Relativistic Heavy Ion Collider, Brookhaven National Laboratory, USA [82].

Table 2.2: A summary of the colliding species at RHIC.

Year (Run)	System/Species	$\sqrt{s_{NN}}$(GeV)
2000 (Run-1)	Au+Au	56 (one day), 130
2001-2 (Run-2)	Au+Au, p+p	200
	Au+Au	20 (one day)
2002-3 (Run-3)	d+Au, p+p	200
2003-4 (Run-4)	Au+Au, p+p	200
	Au+Au	62.4
2004-5 (Run-5)	Cu+Cu, p+p	200
	Cu+Cu	62.4, 22.5 (one day)
	p+p	410 (< one day)
2006 (Run-6)	p+p	200
	p+p	62.4
2007 (Run-7)	Au+Au	200

possible by the Spin Physics Collaboration with the RIKEN Laboratory of Japan.

Using the suitable ion source the heavy ion collisions can be achieved. However two completely independent superconducting rings and using as a particle sources two Tandems Van de Graaf and a proton linac, the facility permits the study of both symmetrical (like gold-gold, copper-copper, proton-proton) and also the asymmetrical colliding systems (like deuteron-gold). The particles that can be accelerated, stored and collided in RHIC from the range of A=1 (protons) to A $\sim$ 200 (gold). In order to understand the properties of the nuclear matter obtained in central gold-gold collisions, (at $\sqrt{s_{NN}}$= 200 GeV) systems of smaller size (like Cu+Cu, d+Au) and lower energies (like $\sqrt{s_{NN}}$ = 62.4 , 22.5 and 20 GeV) were also experimented and studied. Table 2.2 shows a brief summary of all these RHIC runs along with the colliding species, starting with the first day (March 10, 2000) until the present (2007).

The ultimate goal of the physics program at RHIC is to study the properties of strongly interacting matter under extreme conditions of high energy density

with ultra-relativistic nucleus-nucleus collisions. By colliding heavy ions at ultra-relativistic energies one expects to create matter under conditions that are sufficient for de-confinement. RHIC facility at Brookhaven National Laboratory provides collision environment of different heavy ion species such as Au+Au, Cu+Cu, d+Au etc. in varied centre-of-mass energies ranging from 20 to 200 GeV per nucleon.

For the RHIC collisions, the ions (like gold, copper, etc) originate in the Tandem Van de Graff accelerator and proceed to the Booster and the AGS, thus getting accelerated to more and more higher energies. As the collider consists of two quasi-circular concentric accelerator/storage rings on a common horizontal plane, the "Blue Ring" for clockwise, while the "Yellow Ring" for counter clock-wise beams. The rings are oriented in such a manner that they intersect with each other at six locations. Each of the rings have six arc sections (each $\sim$ 356m long) and six insertion sections (each $\sim$ 277m long), with the collision point at the centre.

Colliding ions in RHIC is a multi-step process which starts with the injector chain comprising of three accelerators successively boosting the energy and thus stripping the electrons from atoms. The negatively charged gold ions from a pulsed sputter ion source at the Tandems Van de Graaf are partially stripped of their electrons with the foil at the Tandem's high voltage terminal, thus accelerating to the energy of 1 MeV/u in the second stage of the Tandem. After further stripping (for gold ions which corresponds to the charge state of +32) at the exit of the Tandem, the ions are delivered to the Booster Synchrotron where they are accelerated more to 95 MeV/u. The ions are stripped again at the exit of the Booster after reaching a +77 charge state at this stage and injected to the AGS for acceleration to the RHIC injection energy. Fully stripped state (+79 for gold ions) is reached at the exit of the AGS. In p+p collisions, the protons are injected into the Booster synchrotron directly from the LINAC (LINear ACcelerator), accelerated in the AGS and finally injected in the RHIC. For polarized proton beams it is

difficult to maintain with the increased energy. It is due to the increased density and strength of the spin resonances. The Siberian Snakes make the acceleration possible for polarized proton beams which provide an unique opportunity for the spin physics program at RHIC.

There are two major detector facilities (STAR and PHENIX) and two smaller experiments (PHOBOS and BRAHMS). Each of the experiment is designed to look into different aspects of particle interactions and have unique capabilities, but with significant overlap to provide essential cross-checks.

The BRAHMS (Broad RAnge Hadron Magnetic Spectrometer) experiment [84] is composed of two move-able spectrometer arms and was created to measure charged hadrons over a wide rapidity range and transverse momentum. It consists of two magnetic spectrometers to study the different experimental conditions, momenta, and particle densities at the forward and the other the central region of the collision phase-space. The global information for event characterization is provided by detectors like Beam-Beam counters, a multiplicity detector along with a Zero Degree Calorimeter(ZDC).

The PHENIX experiment (Pioneering High Energy Nuclear Interaction eXperiment) is one of the two large experiments currently taking data at RHIC. The PHENIX Experiment [85] consists of a collection of detectors, each of which perform a specific role in the measurement of the results of a heavy ion collision. The detectors are grouped into two central arms, which measure particles like pions, protons, kaons, deuterons, photons, and electrons, along with the two muon arms (one on the north side and another on south side) which focus on the measurement of muon particles. There are also additional event characterization detectors that provide additional information about such relativistic collisions, and a set of three huge magnets that bend the trajectories of the charged particles. A high speed trigger and data acquisition system allow for nearly dead-timeless running.

The PHOBOS detector [86] consists of four major subsystems like a multiplicity array, a vertex detector, a two-arm magnetic spectrometer including a time-of-flight wall, and several trigger detectors which also determine the centrality of the collision. PHOBOS is capable of measuring charged particle densities over the full 4π solid angle using a multiplicity detector, and measures identified charged particles near mid-rapidity in two spectrometer arms. PHOBOS comprises of many silicon detectors surrounding the interaction region which helps to provide detailed information with the detection of charged particles with very low transverse momenta.

2.2 Solenoidal Tracker At RHIC (STAR)

The Solenoidal Tracker at RHIC (STAR) detector [87, 88] is located at the 6 o'clock position in the RHIC complex as shown in Figure. (2.1). It has been built to study Nucleus-Nucleus collisions at RHIC and comprises of 51 institutions from 12 countries, with a total of $\sim$ 544 collaborators. The STAR detector is capable of measuring hadron production over a large solid angle, using detector systems [89] for high precision tracking, momentum analysis, and particle identification in a region surrounding the center-of-mass rapidity. The large acceptance of STAR with full azimuthal coverage and large acceptance makes it suited for event-by-event characterization of heavy ion collisions and for the detection of hadron jets. Figures (2.2) and (2.3) show a cross-sectional side view of the STAR detector. Its main components are a large Time Projection Chamber (TPC), a Silicon Vertex Tracker (SVT), two smaller radial Forward and Backward TPCs (FTPCs), a Time of Flight (TOF) patch, a Barrel ElectroMagnetic Calorimeter (BEMC), an EndCap ElectroMagnetic Calorimeter(EEMC), a Silicon Strip Detector(SSD), a Photon Multiplicity Detector(PMD) and a Forward Pion Detector(FPD) inside a room temperature solenoidal magnet [90] with a maximum magnetic field of 0.5 T which

provides a uniform magnetic field for charged particle momentum analysis.

2.2.1 Central Detectors

The charge particle tracking close to the interaction region is provided by the SVT whereas the main three-dimensional tracking capability is provided by the radial-drift TPC.

2.2.1.1 Silicon Vertex Tracker (SVT)

The SVT [91] is mainly for improving the primary vertex position, and also the two- track resolution, and the energy-loss measurement resolution for particle identification. The SVT also enables the reconstruction of very short-lived particles like Λ, Ξ, Ω which have their decay vertex close to the primary vertex. SVT consists of 216 silicon drift detectors(equivalent to a total of 13 million pixels) [92] arranged in three cylindrical layers at distances of approximately 7, 11 and 15 cm from the beam axis. The silicon detectors cover a pseudo-rapidity range $|\eta| \leq 1.0$ with complete azimuthal coverage.

2.2.1.2 Time Projection Chamber (TPC)

The TPC [93] is the primary tracking device of the STAR detector. It records the tracks of particles, thus helping determine their momenta from their curvature in the magnetic field. It also identifies the particles by measuring their ionization energy loss (dE/dx) [94]. The momentum resolution of the SVT and TPC reach a value of δp/p = 0.02 for a majority of tracks in the TPC and will be discussed in detail in Section 3.3.

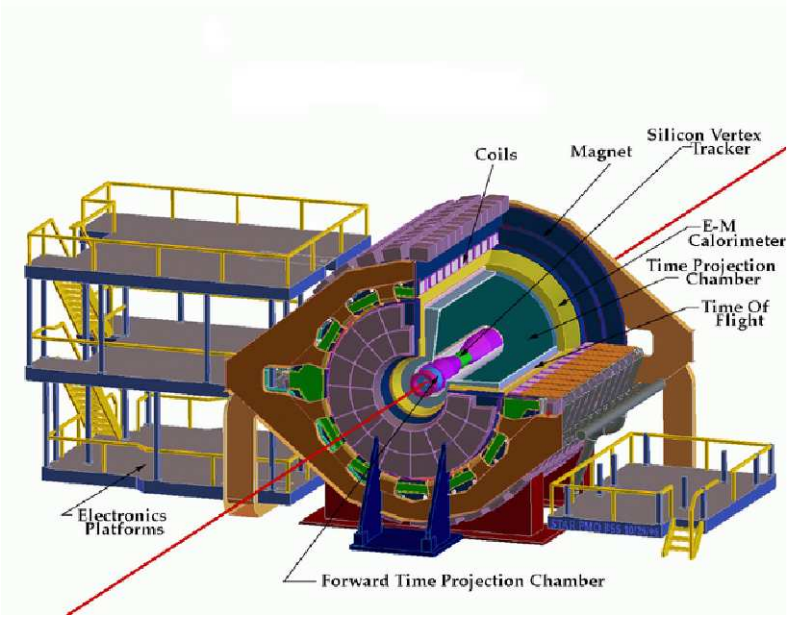

Figure 2.2: The STAR detector [87].

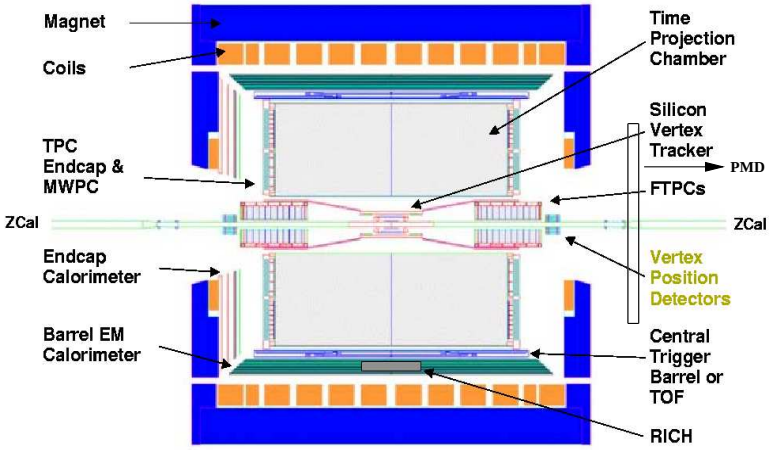

Figure 2.3: The cross-sectional view of STAR detector [87].

2.2.1.3 Time Of Flight (TOF)

The TOF [95] was introduced in the STAR experiment to extend particle identification to larger momenta over a small solid angle. The detectors consist of two separate STAR subsystems. The electronic signals from these detectors define the time intervals of interest for particle time of flight measurements - the Pseudo Vertex Position Detector (pVPD) is the start detector and the Time-Of-Flight Patch (TOFp) is the stop detector. The pVPD consists of two identical detector assemblies that are positioned very close to the beam pipe and outside the STAR magnet. The TOFp is positioned inside the STAR magnet immediately outside the TPC. The signals from these detectors are carried to electronics racks on the so-called South Platform next to STAR for digitization and interfacing with the STAR data stream.

Each detector is based on conventional scintillator/phototube technology and includes custom high-performance front-end electronics and a common CAMAC-based digitization and read-out. The start resolution attained by the pVPD was 24 ps, implying a pVPD single-detector resolution of 58 ps. The total time resolution of the system averaged over all detector channels was 87 ps, allowing direct π/K/p discrimination for momenta up to 1.8 GeV/c, and direct (π+K)/p discrimination up to $\sim$ 3 GeV/c.

2.2.1.4 Barrel Electro-Magnetic Calorimeter (BEMC)

The Barrel Electro-Magnetic Calorimeter (BEMC) and Endcap Electro-Magnetic Calorimeter (EEMC) make a good system in STAR, which allows the measurement of transverse energy of events, and trigger on and measure high transverse momentum photons, electrons and electromagnetically decaying hadrons.

BEMC [96] which is one of the major detector sub-system in STAR is used

to trigger and study rare and high P_T processes like jets, leading hadrons, direct photons and heavy quarks. It also provides large acceptance for photons, electrons along with neutral pions and eta mesons in both polarized p+p and heavy ion systems like Au+Au, Cu+Cu collisions. With this calorimeter on can reconstruct neutral pions at relatively high $P_T \approx$ 25-30 GeV/c and also capable of identifying single electrons and pairs in dense hadron backgrounds from the heavy vector mesons and W and Z decays. All these measurements require precise electromagnetic shower reconstruction along with high spatial resolution. Two layers of shower maximum detectors which are essentially gas wire pad chambers are placed within the BEMC lead/scintillator stack to provide the high spatial resolution measurements of shower distributions in two mutually orthogonal dimensions. The detailed discussion is done in Section 3.2.

2.2.2 Forward Detectors

The study of particle production at forward rapidity is important and so in STAR detector sub-systems we have detectors to measure charged particles, neutral pions and photons in the forward region.

2.2.2.1 Forward Time Projection Chamber (FTPC)

The two cylindrical FTPCs [97] were constructed to extend the acceptance of the STAR detector. FTPCs were constructed to extend the phase space coverage of the STAR experiment to the region $2.5 < |\eta| < 4.0$. They measure momenta and production rates of positively and negatively charged particles as well as strange neutral particles. The increased acceptance also improves the general event characterization of STAR and also helps in the study of asymmetric collision systems like p+A (eg. d+Au).

2.2.2.2 Endcap Electro-Magnetic Calorimeter (EEMC)

The EEMC [98] is situated on the west pole-tip of the STAR detector and covers the region between 1 and 2 in pseudorapidity and full azimuthal coverage. The EEMC is also a lead-scintillator sampling electromagnetic calorimeter. With its different acceptance than BEMC, it provides the capability to detect photons and electro-magnetically decaying mesons (π_0, η).

2.2.2.3 Forward Pion Detector (FPD)

The FPD [99] consists of electromagnetic calorimeters mounted on the east tunnel platform extension of STAR. This detector detects forward neutral pions and also it is used as a local polarimeter for the polarized proton running. The detector consists of lead-glass calorimeters and a prototype FPD was earlier installed at STAR, 750 cm from the IR to identify neutral pions. The basic calorimeter module is a light box consisting of 7 x 7 matrix of existing lead-glass detectors, FEU-84 photomutiplier tubes and resistive voltage dividers.

2.2.2.4 Photon Multiplicity Detector (PMD)

A photon multiplicity detector has been installed in the forward region of the STAR experiment to measure the photon multiplicity, where the high particle density prevent the use of a calorimeter. PMD [100] is a gas based detector consisting of preshower and charge particle veto planes. The details of the principle and construction is described in Section 3.1.

2.2.3 Trigger Detectors

Trigger [101] in STAR is a pipelined system in which based on the digitized signals from the fast detectors are examined at the RHIC crossing rate($\sim$ 10 MHz). The

STAR data acquisition system [102] receives data from multiple detectors which have a wide range of readout rates, and the fast and flexible setup processes event sizes of 200 MB at input rates of 100 Hz. The STAR trigger system is a multi-level trigger system and is based on digitized input from fast detectors which are analyzed at the RHIC crossing rate (10 MHz). The relatively slow detectors provide the momentum and particle identification for the physics analysis.

The trigger system is functionally divided into different layers with level 0 being the fastest while levels 1 and 2 are slower. STAR has also a third level trigger (L3) [103], which bases its decision on the complete, online reconstruction of the event. This particular trigger includes also a display which allows the visual inspection of the events almost in real time.

The STAR trigger detectors are: Central Trigger Barrel (CTB), Beam Beam Counter (BBC), Zero Degree Calorimeter (ZDC), Barrel Electromagnetic Calorimeter (BEMC), Endcap Electromagnetic Calorimeter (EEMC) and Forward Pion Detector (FPD).

2.2.3.1 Zero Degree Calorimeter (ZDC)

The Zero Degree Calorimeters [104, 105] operate as fast detectors for STAR trigger and are used for determining the energy in neutral particles remaining in the forward directions. The two ZDCs are located at the first bending magnets in the collider line. Each is split into 3 modules, and each module consists of layers of lead and scintillator fibers going to a PMT and ADCs. These devices determine the number of spectator neutrons, for use as a minimum bias trigger, and act as an intra-RHIC normalizing detector.

2.2.3.2 The Central Trigger Barrel (CTB) and Beam Beam Counter (BBC)

The Central Trigger Barrel [101] consists of 240 scintillator slats arranged in 4 cylindrical bands around the TPC. Each slat is viewed by one PMT. The CTB covers a region from -1 to +1 in η and 0 to 2π in ϕ. It measures charged multiplicity in this region of phase space.

There are two Beam-Beam Counters [105] wrapped around the beam-pipe, one on either side of the TPC. Each counter consists of two rings of hexagonal scintillator tiles where an outer ring is composed of large tiles and an inner ring composed of small tiles. Internally, each ring is itself divided into two separate sub-rings of 6 and 12 tiles each. The timing difference between the two counters will provide the primary vertex position.

Chapter 3

Detectors for Photon and Hadron measurements in STAR

In high energy heavy ion collisions, large number of particles are produced and emitted from the collision environment. These consist of photons, leptons and various types of hadrons. Among the various signatures of QGP, photons have an advantage over other signals as they participate only in electromagnetic interactions and practically do not loose energy by scattering and re-scattering from free quarks or hadrons (as discussed in Sections 1.3.4.1 and 1.3.6.2.2). The studies of hadrons (discussed in Section 1.3.4.2) provide an understanding of the evolutionary path of the system created in the collision at the time of freeze-out. Hadron multiplicities and their correlations provide information on the nature, composition, and size of the medium from which they originate. Henceforth photon multiplicity and correlations provide important complementary tools to the hadronic measurements.

The STAR detector (discussed in Section 2.2) is a large coverage and highly granular detector. It is one of the two large heavy ion experiments (where the other one is PHENIX) at RHIC. STAR searches for signatures of the quark-gluon

plasma by investigating the global observables of nuclear collisions over a wide rapidity (y) and azimuthal (ϕ) range.

The details of STAR Photon Multiplicity Detector (PMD) is explained in Section 3.1, where-as Sections 3.2 and 3.3 describe STAR Barrel Electro - Magnetic Calorimeter (BEMC) and STAR Time Projection Chamber (TPC) respectively.

3.1 Photon Multiplicity Detector (PMD)

The photon multiplicity measurements provide an additional opportunity to study the changes in relative population of the electromagnetic and hadronic components of the multi-particle final state [106, 107]. The inclusive photon production is dominated by photons from hadron decays such as $\pi_0 \rightarrow \gamma\gamma$ and henceforth provide a complementary basis to charged pion measurements. Such multiplicity measurements of photons have been done in WA93 and WA98 experiments at CERN SPS [108, 109].

A preshower Photon Multiplicity Detector (PMD) is installed in the east wall of the wide angle hall which encompasses the STAR Experiment [110]. This detector is designed to measure photon multiplicity in the forward region (with pseudo-rapidity from -2.3 to -3.8) where the environment is such that it precludes the use of a calorimeter due to the hindrance of high level overlap of fully developed showers [100, 111]. The basic principle of photon multiplicity measurements with PMD is similar to the detectors used in WA93 and WA98 experiments at CERN SPS [108, 109] and also for the ALICE experiment being commissioned at present in CERN LHC [112].

By measuring the multiplicity and spatial distribution of photons on an event-by-event basis and by combining the information from other detectors, investigations on the following broad topics of physics can be pursued with PMD :

- determination of the reaction plane and the probes of thermalization via studies of azimuthal anisotropy and flow;
- critical phenomena near the phase boundary leading to fluctuations in global observables like multiplicity and pseudorapidity distributions;
- signals of chiral-symmetry restoration (e.g DCC) through the measurement of charged-particle multiplicity (N_{ch}) in a common part of phase space and study of the observables N_γ and N_γ/N_{ch} with full azimuthal coverage and with momentum selection of particles.

3.1.1 Basic Principle

The PMD is a highly segmented preshower detector placed behind a lead converter plate of 3 radiation length thickness as shown in Figure (3.1). The lead acts as a photon converter and a photon produces an electromagnetic shower on passing through the converter. These shower particles produce signals in several cells of the sensitive volume of the detector [111, 113].

The charged hadrons usually affect only one cell and produce a signal which resembles that from Minimum Ionizing Particles (MIPs). The converter thickness is optimized such that the conversion probability is high for photons without excessively blowing up the shower and to reduce shower overlap in a high multiplicity environment by simultaneously keeping the interaction probability of hadrons to a low value. For achieving better hadron rejection capability, another plane of the detector of identical dimension as that of the preshower part is placed before the lead plate as shown in Figure (3.1), which acts as veto for charged particles. The principle of photon counting presented in Figure (3.2) shows that a photon passing through the converter produces an electromagnetic shower in the preshower plane of the PMD leading to a larger signal spread over several cells as compared to the

charged particle which is essentially confined to one cell. Photons can be separated from hadrons by summing the energies of the connected cells after which a suitable cut is applied on the deposited energy and cluster size.

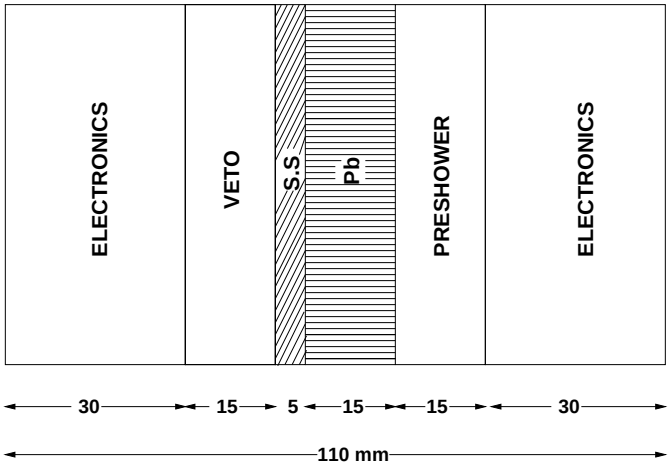

Figure 3.1: Cross-sectional schematic of the PMD [113] showing the veto plane, lead converter and preshower plane. SS is the support plane on which the lead plates and gas chambers are mounted.

3.1.2 Detector Fabrication

The detector is based on a honeycomb proportional chamber design using the $Ar + CO_2$ gas mixture in the ratio of 70% : 30% by weight [100, 111]. Such gaseous mixture is preferred as it is insensitive to neutrons and also aging free. For proper handling of optimized high particle density in the forward region, the detector technology has been optimized with the considerations that (i) multi-hit probability should be less,(ii) MIP should be contained in one cell and (iii) low energy δ-electrons (which remain responsible for causing cross-talk with the adjacent cells), should be prevented from traveling to nearby cells. The copper honeycomb body forms the common cathode and is kept at a large negative potential.

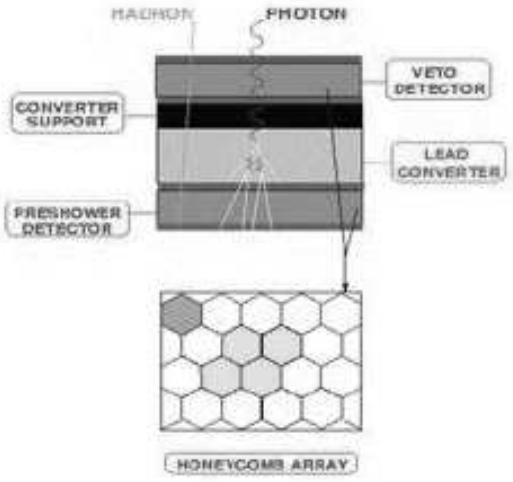

Figure 3.2: Principle of photon counting.

The PMD consists of the following mechanical parts :

- the modular honeycomb chambers (identical for preshower and charged particle veto);
- lead converter plates;
- support assembly.

The PMD is designed in two halves with a vertical split axis, and the two halves can be independently assembled and installed. Both have independent movements to open on the two sides of the beam pipe.

3.1.2.1 Unit Cell

The detector consists of an array of shallow hexagonal cells. In a normal cylindrical proportional counter the long wire length compared to the diameter minimizes the

edge effects. But in the present case we have the gas thickness comparable to the cell size.

The choice of the material and the thickness for the honeycomb cells were influenced by the following considerations :

- the material should help to reduce the transverse size of the preshower by containing the low energy δ electrons moving at large angles;
- the thickness should be kept low to avoid large amount of material and reduce shower blowup in the detector medium.

The schematic view of a unit cell is shown in Figure (3.3) along with a longitudinal section illustrating the use of extended cathode for field shaping, where such design was finalized after extensive prototype tests to ensure uniform charged particle detection efficiency throughout the cell [112].

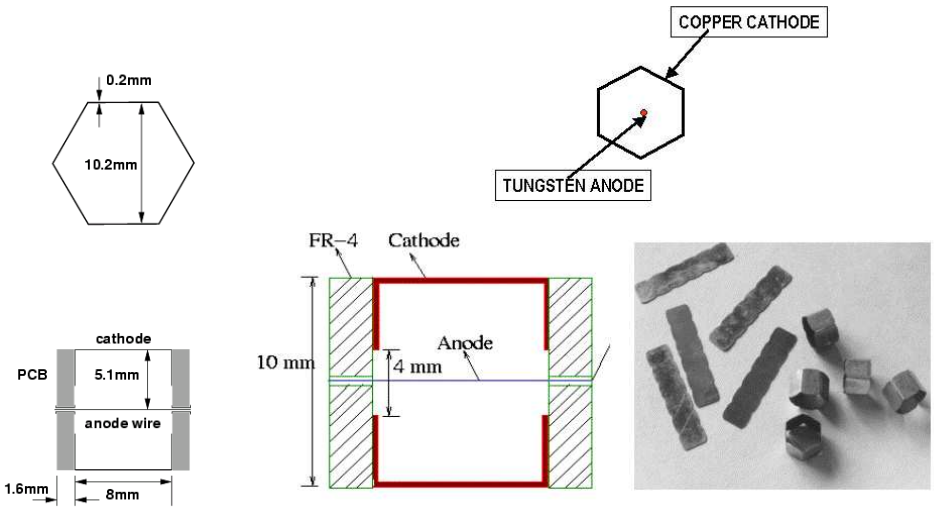

Figure 3.3: Unit Cell schematic with cross-section.

3.1.2.2 Unit Module

A honeycomb of 24×24 cells constitute a unit module. This is a rhombus of side $\sim$ 254 mm having identical boundary shape on all the four sides. Cell walls at the boundary are kept half as thick as those for the inside ones so that adjacent unit modules can join seamlessly.

The components of a unit module are shown in Figure (3.4). It consists of a custom-built copper honeycomb array of cells sandwiched between two PCBs which hold the anode wire along the axis of each cell. The inner face of the PCBs are metalized except for a small annular region near the wire. This metalization is in contact with the cathode and acts like an extension of the cathode on the ends of the cell. The gold-plated tungsten wires (20 μm diameter), which serve as anodes, are inserted through the holes on the Printed Circuit Boards (PCB), using a needle and a tensioning jig. The top PCB, which contains the electronics boards, has solder-islands at the centre of each cell with a 0.5 mm diameter gold-plated through-hole. The wires are soldered under a controlled tension of about 25 gm. The signal tracks from a cluster of 64 cells are brought to a 70-pin connector. The PCBs on the bottom side have only soldering islands without signal tracks, serving as the anchor points.

A copper unit cell is the building block of the honeycomb. It is fabricated using 0.2 mm thick copper sheets which are solder-coated on one side. The sheet is die stamped to precise dimensions along with notches and bent in hexagonal form with precision dies. These are then arranged in a 24×24 matrix in a high precision jig of rhombus shape as shown in Figure (3.5). Hexagonal Stainless Steel inserts, having dimensions matching the inner dimensions of the cell, are inserted in each cell. The assembly is clamped tight and heated so that soldered surfaces join to form a rigid honeycomb [100].

Quality assessment for the fabrication of the unit module is done in several

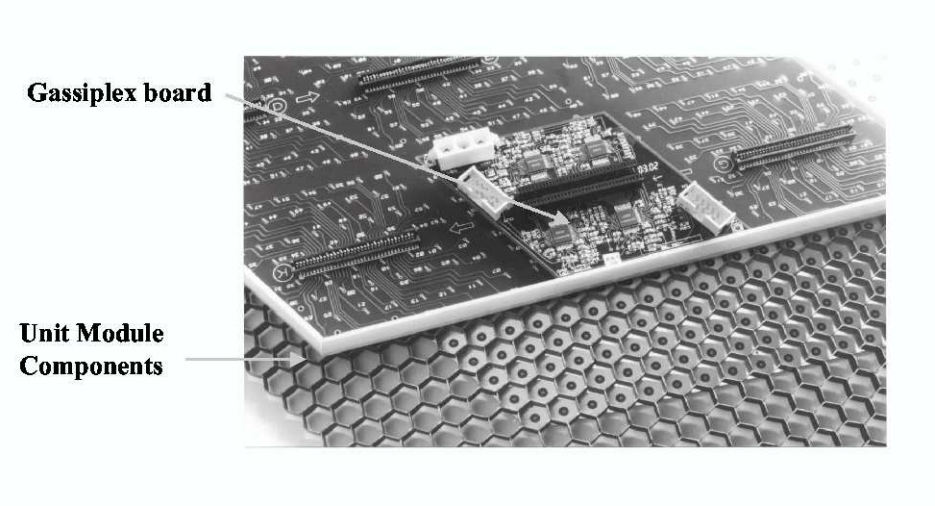

Figure 3.4: The components of the unit module showing the honeycomb between the top and bottom PCB along with the front end electronics board.

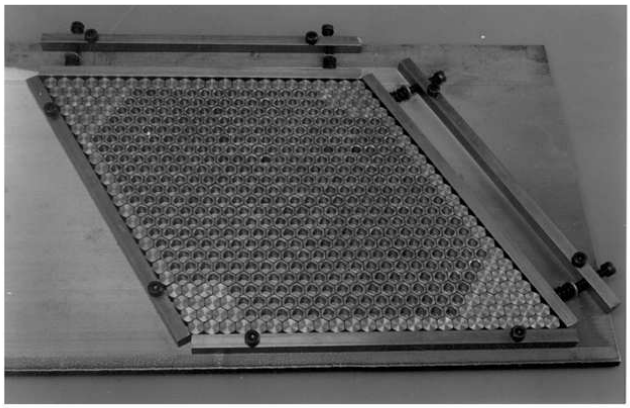

Figure 3.5: The jig for unit module fabrication.

ways, *viz*, visual inspection of the solder joints and measurement of resistance of each wire to monitor dry-soldering contacts, along with PCB leakage current measurement [114]. Resistance measurement distribution shows that the Root Mean Square (RMS) is within 5% for one unit module. The flow chart for unit module fabrication is shown in Figure (3.6). In addition, High Voltage(HV) tests (discussed in Section 3.1.3) are also performed after connecting the front-end electronics boards (described in Section 3.1.4) and the pedestals of chips are monitored to test stable operation of the detector. The tests with HV are done after the unit modules are assembled into a supermodule.

3.1.2.3 Supermodule

A set of unit modules are enclosed in a gas-tight chamber called supermodules. The number of unit modules varies from 4 to 9 within a supermodule. The STAR PMD consists of 24 supermodules arranged in the form of a hexagon as shown in Figure (3.7). This geometry ensures full azimuthal coverage with minimum number of supermodules.

Supermodule is a gas-tight chamber made of 3 mm thick FR4 grade glass epoxy sheet as the base plate and a 7 mm thick and 25 mm high aluminium boundary wall. A schematic cross-section of a supermodule is shown in Figure (3.8). The boundary walls are made of custom extruded aluminium channels with a hollow cross-section to facilitate gas flow into the modules. The opposite sides of the boundary walls have gas-feed channels. Each channel has 24 openings into the chamber. This scheme, along with the notches in the cells, keep the gas flow impedance low. A set of assembled unit modules are placed to fill the inner area of the supermodule enclosure, leaving a gap of 1 mm on all sides to accommodate general assembly tolerance and to provide insulation between the honeycomb cathode and the boundary. One such assembled supermodule with 9 unit modules is

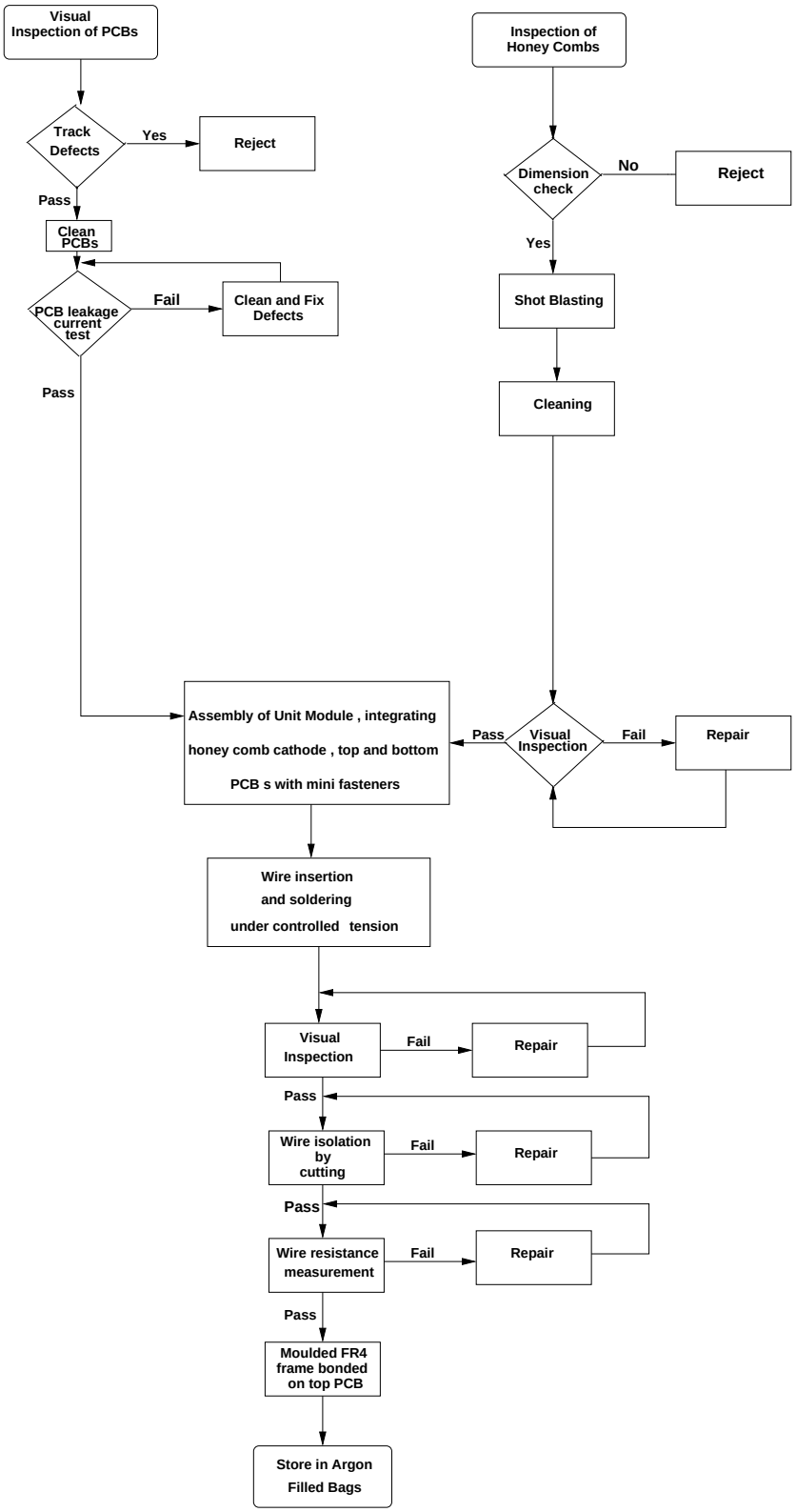

Figure 3.6: The flow-chart for unit module assembly.

shown in Figure (3.9).

The flow chart for supermodule assembly is shown in Figure (3.10). For the application of HV to supermodules (discussed in Section 3.1.3), an aluminum enclosure containing one SHV connector, a HV limiting resistor and decoupling capacitor is fixed at one corner of each supermodule very close to the HV tapping point.

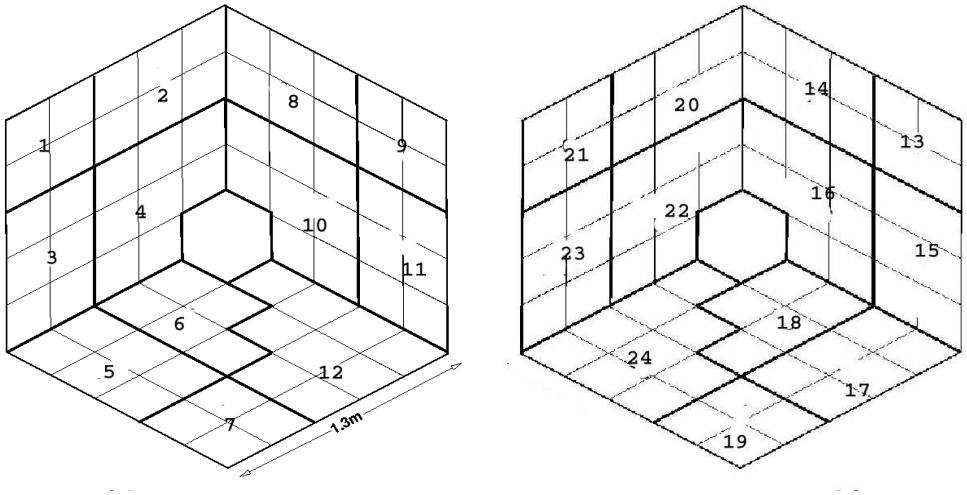

Figure 3.7: The layout of the STAR PMD where the thick lines indicate the supermodule boundaries. There are 12 such supermodules each in the preshower ("right figure" view from tunnel side) and veto plane ("left figure" view from interaction region). The divisions inside a supermodule indicate the unit modules.

3.1.3 Testing of PMD

Before dispatching the supermodules for installation in STAR experiment, the following tests have been carried out in the laboratory [115]:

- Test the gas leak in the supermodules, if any, using a sniffer probe.
- Test of High Voltage (HV) stability by measuring leakage current and monitoring discharge if any.

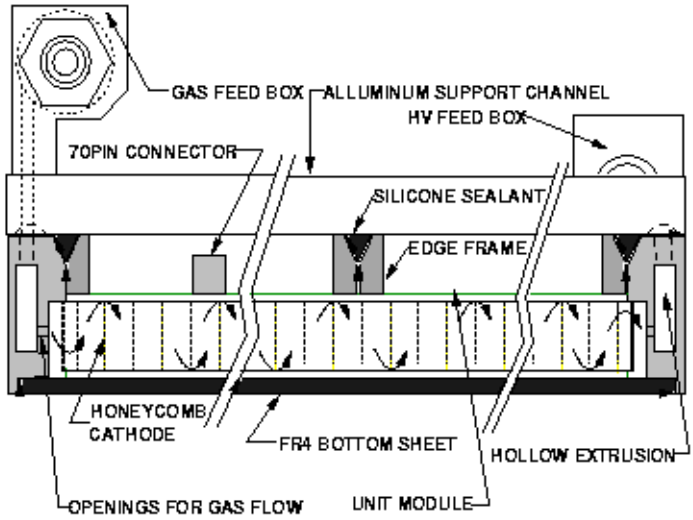

Figure 3.8: The schematic view of supermodule.

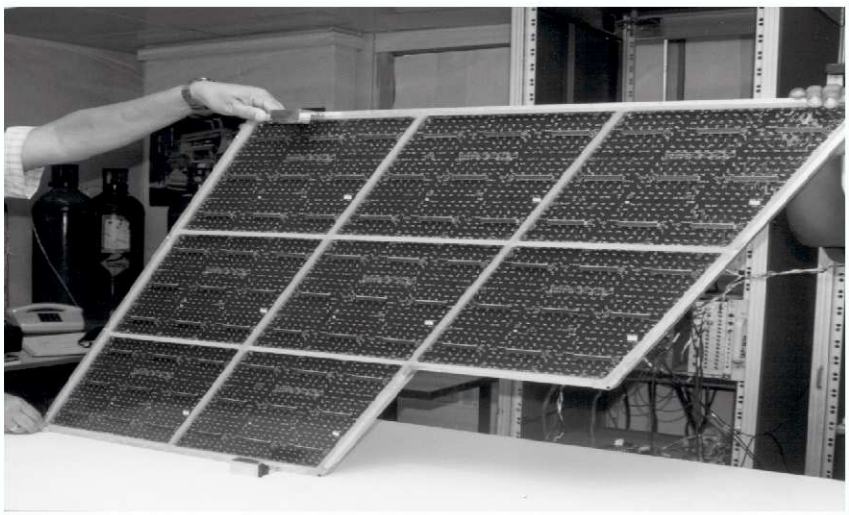

Figure 3.9: A supermodule with nine unit modules.

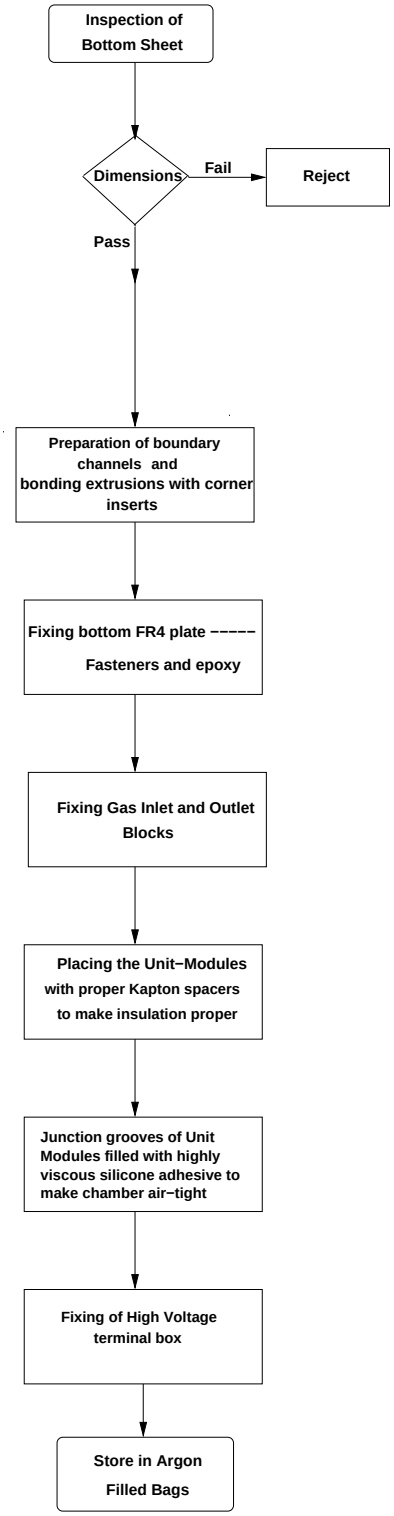

Figure 3.10: The flow-chart for supermodule assembly.

- Test of channel by channel pedestal and its variation at the operating voltage using FEE and a PC-based Data Acquisition System.
- Test to observe the pulse signal with strong radioactive source.

Gas leaks if found anywhere, were sealed using epoxy resin. Testing of HV stability was started after about 24 to 48 hours of gas flushing depending on the size of supermodule. For test with high voltage, the 9 connector groups on a unit module were shorted with shorting connectors and the leakage current was monitored for -1600V, much higher than the operating voltage value. The set trip current limit was 2 μA for a supermodule. Groups of 9 connectors were sequentially added till the entire supermodule was covered with shorting connectors as shown in Figure (3.11). Leakage current was measured using the setup shown in Figure (3.12).

It was observed that a group (64 cells) shorted with shorting connectors showed occasional tripping in presence of HV showing high current. The current was $\geq$ 5 μA both at lower (50V-400V) and higher voltages, indicating one or more bad channels in that group. In presence of HV the board with DIP switches to isolate channels helped in the identification of the faulty channels. Subsequently the corresponding bad channel numbers were marked on the PCB and signal track is cut off. Also proper spark monitoring was done with an opto-coupler circuit [116] and an oscilloscope. An estimate of bad channels eliminated is shown in Figure (3.13) for the entire detector consisting of 144 unit modules in 24 supermodules.

The testing procedure is summarized in the flow-chart diagram of Figure (3.14). Following precautions were taken while testing the HV stability : (i) If the leakage current was less than 200 nA for one unit module then only we added unit modules one by one till the total supermodule was covered with shorting connectors. (ii) For each supermodule the leakage current as a whole was not allowed to be more

than 2 μA with shorting connectors.

The pedestal spread and mean values with front-end electronics were monitored to crosscheck the collective performance of the cells with HV. The pulse signal of an individual cell was monitored across 1 MΩ using voltage probe with an oscilloscope in the presence of a strong radioactive source as shown in Figure (3.15).

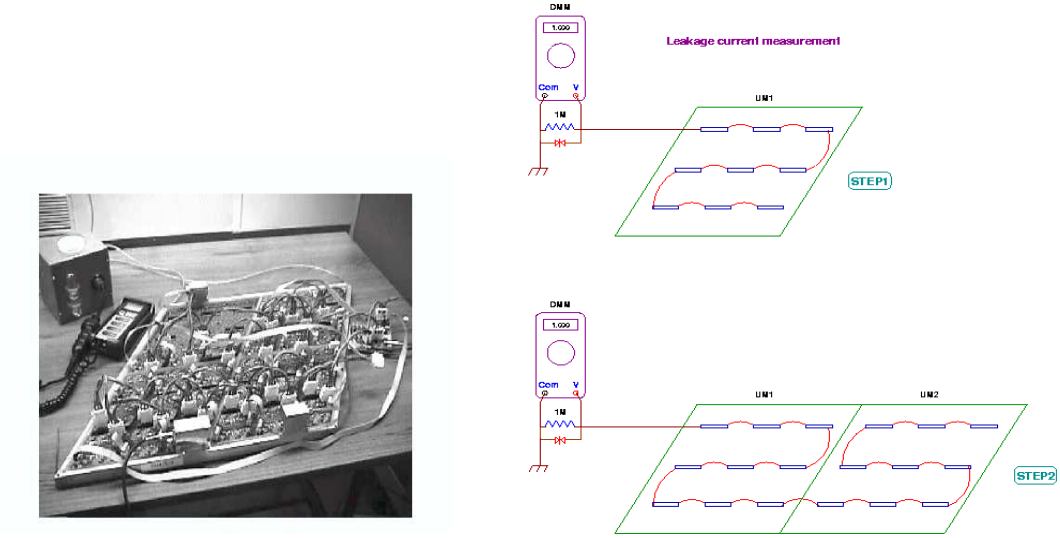

Figure 3.11: Supermodule High Voltage tests.

3.1.4 Front End Electronics

The Front-End Electronics (FEE) for processing the STAR PMD signals is based on the use of 16-channel Gassiplex chips developed at CERN [117] which provide analog multiplexed signals and readout using the custom built ADC board (C-RAMS). C-RAMS can handle a maximum of 2000 multiplexed signals. Considering the symmetry requirements of the detector hardware, the readout of the entire PMD has been divided into 48 chains. Each chain covers three unit modules and has 1728 channels.

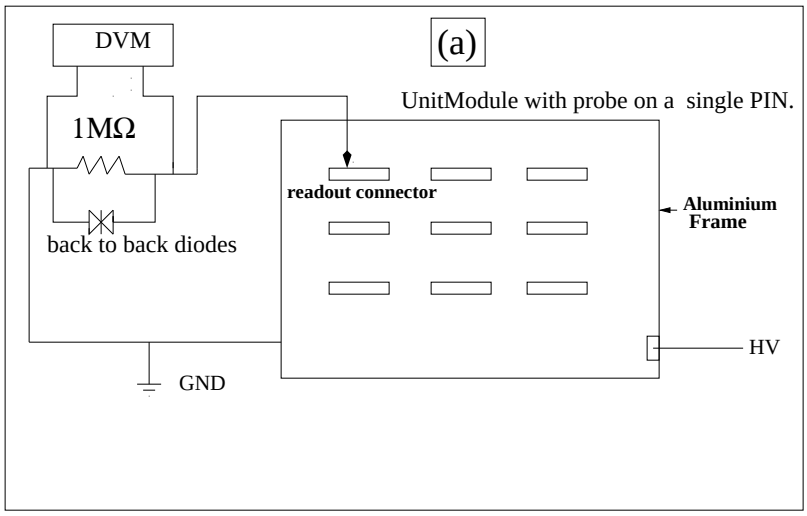

Figure 3.12: Digital Voltmeter (DVM) connected across 1MΩ resistance and using an additional probe via dip switch board which has one side grounded to short the channels one by one in that group for identifying the bad one.

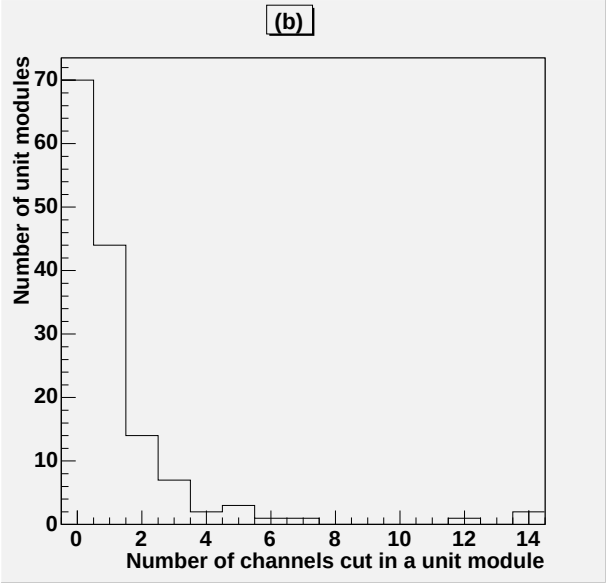

Figure 3.13: The Histogram plot of Unit Module vs. Number of Channels cut in each. The number of bad channels in a unit module was found to be much less than 5 %.

3.1.4.1 Gassiplex chip

Gassiplex, a 16-channel low noise signal processor is a flexible ASIC (Application Specific Integrated Chip) for a very wide range of detector applications. The functional blocks of the chip are [118]:

(i) Charge-sensitive amplifier (CSA)

This low-noise amplifier is characterized by a long decay time constant of 20 μs which makes it sensitive to the largest amount of the detector current. The linear output range of the CSA can be symmetrized.

(ii) Deconvolution filter and shaping amplifier

After the CSA, the deconvolution filter compensates the logarithmic shape of the charge signal and provides the shaper with a quasi-step function with one pole provided by the Rf.Cf time constant of the CSA.

The shaper provides a Semi-Gaussian signal with 1.2 μs peaking-time and a return to the baseline better than 1 % after 5 μs.

(iii) Track/Hold (T/H)

The track-and-hold circuit stores the analog information at the peaking time and finally the 16 channels are multiplexed to one output.

The Gassiplex chips have a dynamic range [1] of 2V for a input signal of 560 fC. The negative range is limited to -1.1 V, namely 300 fC [117]. Placing an injection capacitance of 1.8pF on one particular channel of Gassiplex chip the dynamic range as shown in Figure (3.16) is tested in laboratory, the negative range of which will be required for the PMD. We have also tested in laboratory by injecting pulse of different amplitude to sweep and see the plots for a single FEE board with respect to 64 channels. The Gassiplex has a input capacitance of 1pF per channel [117] and so when we plot the calibration we find that slowly the channel wise fluctuation become small with the rise of higher pulse input indicating saturation.

[1] The ratio of the largest to the smallest signal which can be accurately processed by a module.

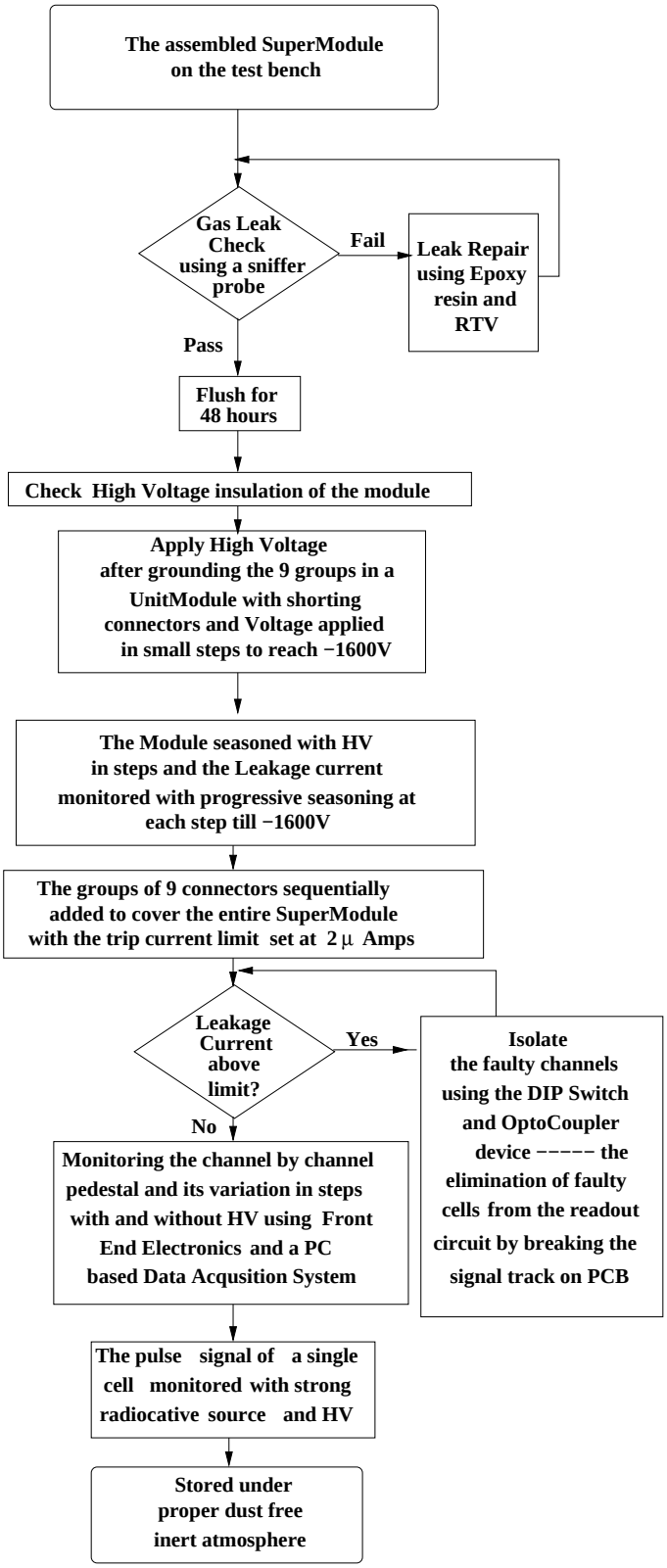

Figure 3.14: The PMD testing flow-chart.

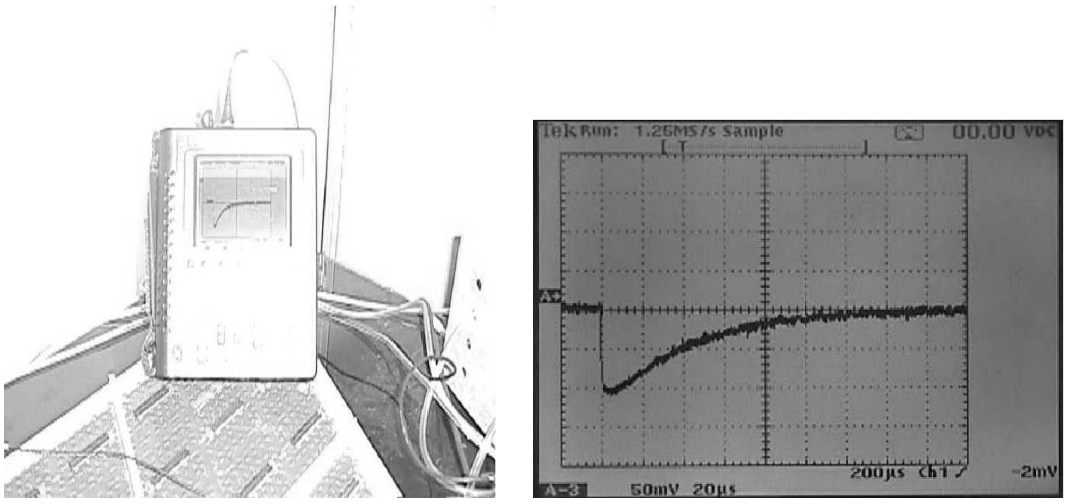

Figure 3.15: The pulse signal of an individual cell in the presence of a strong radioactive source.

For proper quality control in the assembly of FEE boards, each of the 10,000 Gassiplex chips have been tested for full functionality of each channel. The chip test-board is shown in Figure (3.17). Initially after the chip is placed in the test-board and connected to LV power supply. The average current drawn by a healthy chip is $\sim$ 25-30 mA. If the chip drew excess current the chip is rejected at an initial level. The full functionality of all the channels are tested for each chip, along with the pedestal measurement and checking of CLK OUT signals. The minimum pedestal as well as the spread in pedestal has been determined for each chip.

Besides the manual check, described above, a PC-based data acquisition (DAQ) system is made where the CAEN sequencer module V551B is used to generate clocks and the required control signals (e.g Track/Hold, BUSY and CLEAR) for Gassiplex chips. A software trigger is generated and fed into the sequencer and once the signal is digitized in C-RAMS V550, it is read in a PC through a PCI-VME interface [119]. The pedestal measurements done manually and with the

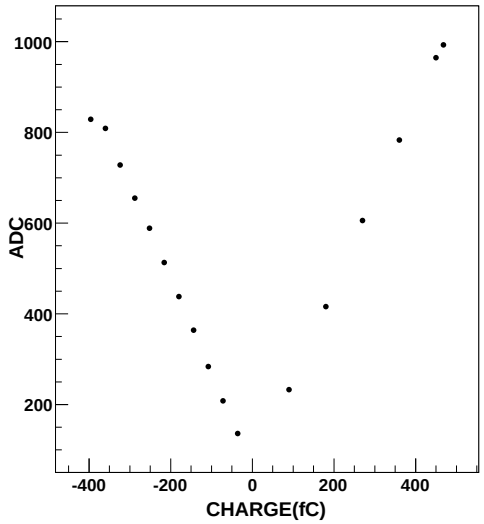

Figure 3.16: Gassiplex chip dynamic range plot.

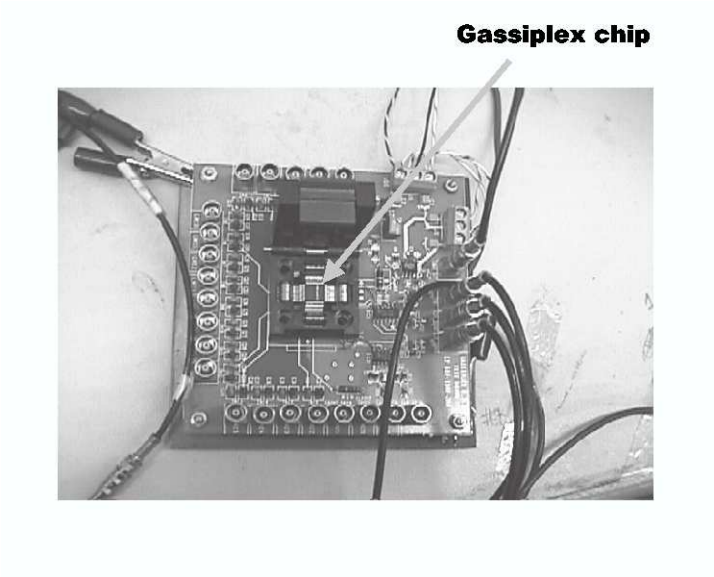

Figure 3.17: Gassiplex chip test-board.

DAQ system are compared in Figure (3.18).

The scatter plot of pedestal minima vs. pedestal spread for 5000 chips is shown in Figure (3.19) where it is seen that we can select chips of four categories having close ranges of pedestal minima and pedestal spreads. The narrow width of the distribution shows that the number of chips used in FEE is a large fraction of the total number of chips tested in laboratory, both with DAQ and chip test set-up.

3.1.4.2 Readout chain

Each readout chain is driven by (i) a translator board (ii) 27 FEE boards each consisting of 4 Gassiplex chips and (iii) a buffer amplifier board.

(i) Translator Board: It converts fast NIM levels of all control signals into the level required for the operation of Gassiplex chips. Operating voltage for these chips is ±2.75V and hence all the NIM signals are to be translated to 0 to 2.75 V levels.

(ii) FEE board: The cells in the unit modules are arranged in clusters consisting of 8×8 cells connected to a 70-pin connector. This cluster of 64 cells is read out by a FEE having four Gassiplex chips. One such board is shown in Figure (3.20). For geometrical considerations the FEE board is also made in rhombus shape. When all the boards are placed on the detector, they almost fully cover the detector area. This arrangement helps to reduce the material and also provides a ground shield for the detector. To reduce voltage drops over a long chain of 1728 channels, a bus-bar like design has been adopted to provide power to the FEE boards. To protect the input channels against high voltage spikes, a provision has been made on the board layout to connect a diode protection circuit. Each of such FEE board requires two such diode protection boards consisting of 32 twin diodes as seen in Figure (3.20).

(iii) Buffer amplifier board: The buffer amplifier is used for the transmission

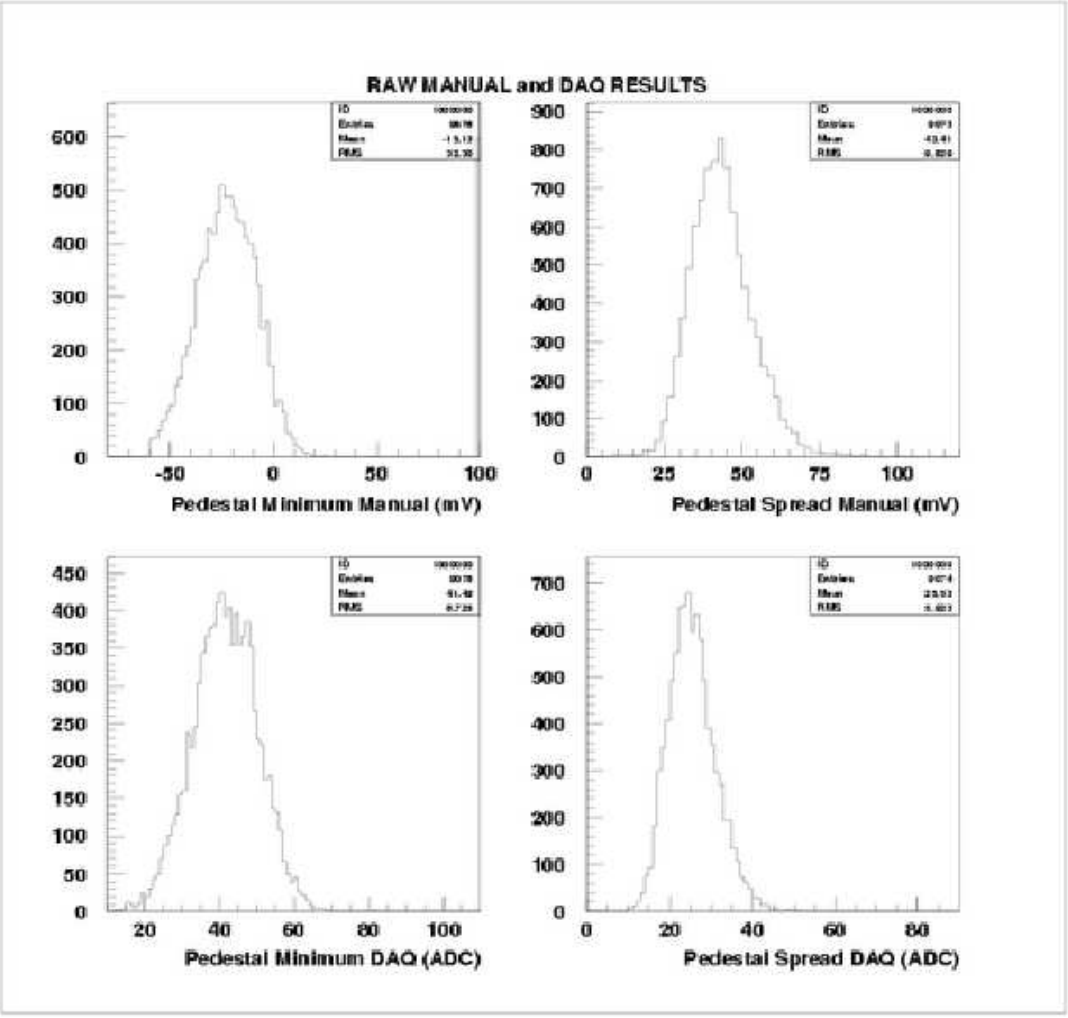

Figure 3.18: Gassiplex chip test results using manual methods and data acquisition systems.

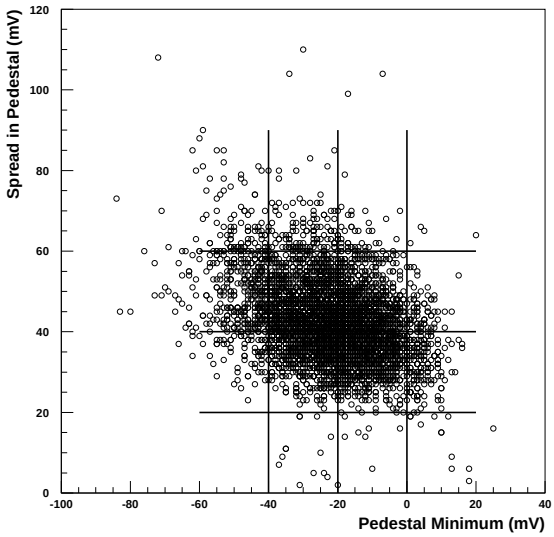

Figure 3.19: Pedestal Minimum vs. pedestal spread for Gassiplex chips [100].

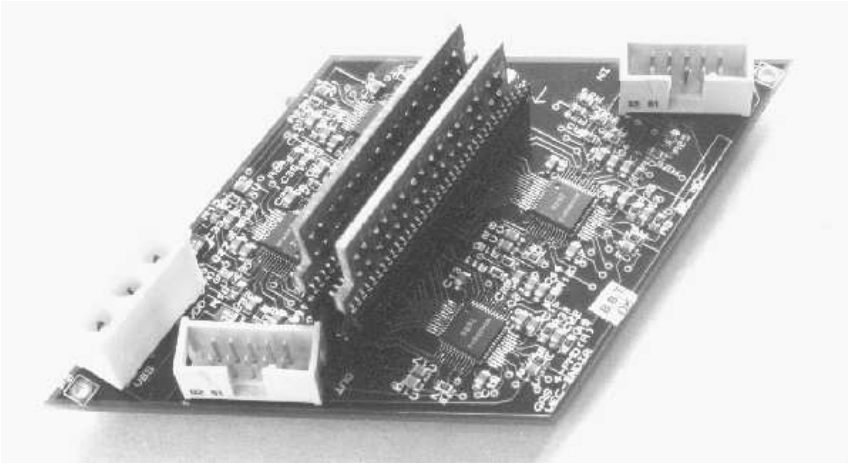

Figure 3.20: A FEE board with four Gassiplex chips.

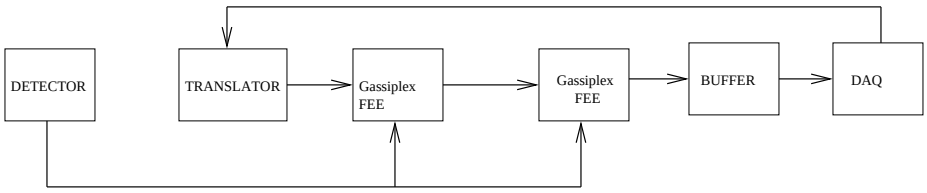

Figure 3.21: Readout chain schematic for STAR PMD.

of a train of analog multiplexed signals to the readout through a low impedence cable. Readout chain schematic for STAR PMD is presented in Figure (3.21).

Digitization using C-RAMS requires that all multiplexed pulses within a chain should have the same polarity. In order to read the full chain, the pedestals in the chain need to be adjusted to the minimum value. This shifting of the pedestal effectively reduces the dynamic range. To minimize the reduction in dynamic range due to pedestal adjustment, we need to select the chips for a chain having minimum pedestals in very close range as described in the earlier part of this section.

3.1.4.3 Trigger for PMD

The Level 0 (L0) trigger in STAR arrives at ~ 1.5 μs after the interaction but the peaking of the Gassiplex is 1.2 μs (as discussed in Section 3.1.4.1). The pretrigger to PMD is issued from the ZDC coincidences. This is generated within 500 ns of the interaction before the Gassiplex chip peaking time. The PMD trigger scheme is shown in Figure (3.22) [113].

When the pretrigger arrives at the PMD trigger system, the sequencer sends a T/H signal to the FEE which remains till the arrival of the validation of L0 to continue with digitization and data transfer. All the data is stored in the buffer memory within 10 ms, and the transfer of data from the buffer memory to the STAR DAQ starts with the arrival of L2.

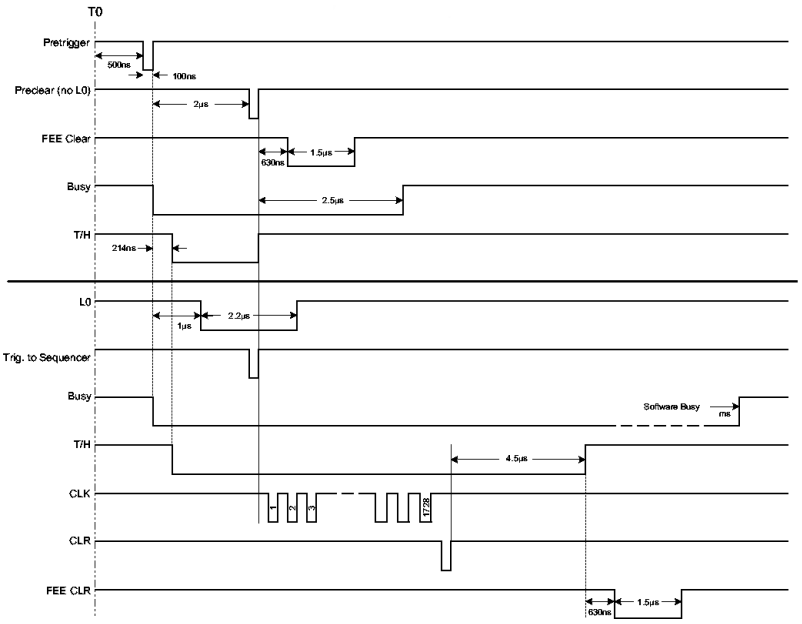

Figure 3.22: Timing diagram for PMD trigger scheme.

3.1.5 Integration of PMD in STAR

The two halves of the PMD are supported on the girders and hang freely in a vertical position. The support structure allows both x- and z- movements of the detector. Each half of the PMD can be separated for access by a smooth independent movement controlled by limit switches. The services of the two halves are independent and when fully open, the two halves provide sufficient clearance for the pole-tip support of the STAR magnet to move in.

The integration of PMD as presented in Figure (3.23) [120] started from 2002. As a test of its FEE functionality and HV stability of supermodules a brief data taking period followed in 2003 with p+p and d+Au collisions at $\sqrt{s_{\rm NN}} = 200$ GeV. The PMD actively took data in 2004 for Au+Au collisions at $\sqrt{s_{\rm NN}} = 62.4$ and 200 GeV and again in 2005 for Cu+Cu collisions at $\sqrt{s_{\rm NN}} = 22$, 62.4 and 200 GeV.

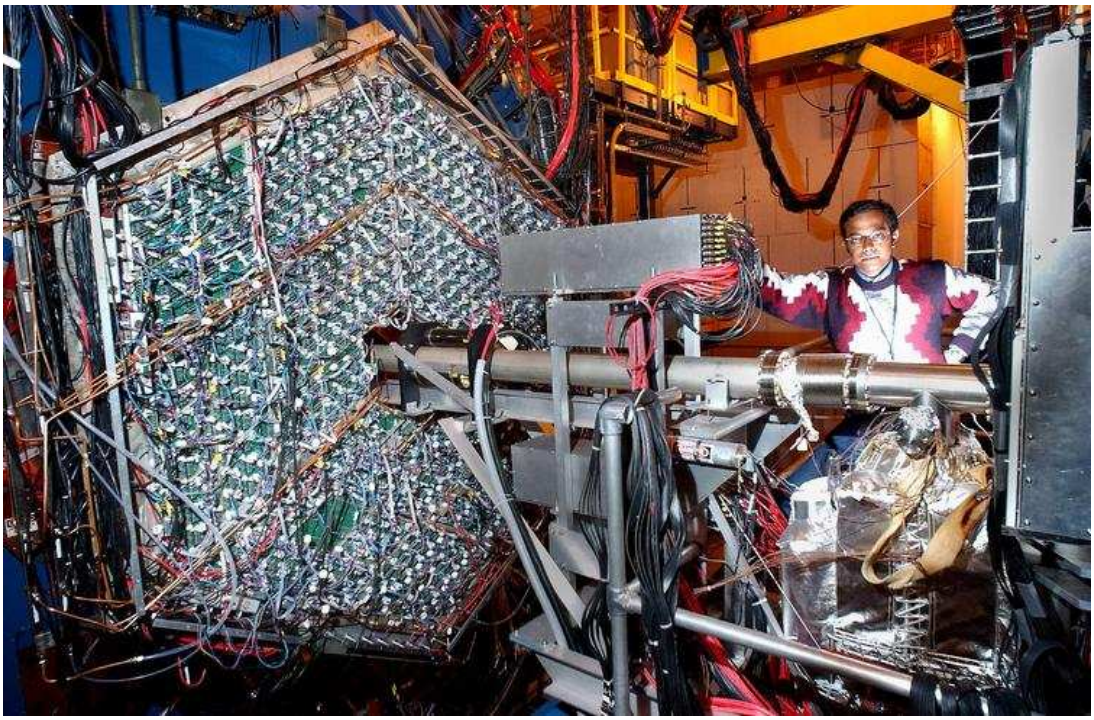

Figure 3.23: PMD in STAR experiment at RHIC [120].

3.1.6 Online Monitoring and Quality Assurance

A fast, efficient and comprehensive monitoring system is a vital part of any particle and heavy ion physics experiment. The online monitoring of a large collaborative physics experiment like STAR has to full-fill a series of requirements. The status of the experiment has to be known in great detail at all times during the data taking process. These status data have to be recorded in a format that can be combined easily with the data taken by the experiment for later offline analysis. At the same time they have to be presented to the shift crew in a way that allows for quick and efficient problem identification and that points at possible problems and solutions.

It is desirable and important to incorporate expert knowledge about the different detectors of the experiment into the monitoring software. It is equally desirable to make the online monitoring information readily available to the experts. We had one such monitoring software which was efficiently devised for the PMD data taking [Figure (3.24)]. Mainly handled by detector experts this online software provided successful inputs to the shift crew, for smooth running of the PMD. The basic architecture of PMD online is shown in Figure (3.25).

3.1.6.1 PMD performance studies

The preshower plane and some supermodules of veto plane were operational in 2004 for Au+Au collisions at $\sqrt{s_{\rm NN}}$ = 62.4 and 200 GeV and also in 2005 for Cu+Cu collisions at $\sqrt{s_{\rm NN}}$ = 22, 62.4 and 200 GeV. Brief tests were also carried with p+p collisions at $\sqrt{s_{\rm NN}}$ = 200 GeV in 2004.

The full functionality of the run-time slow control tools (both hardware and software) and physics analysis algorithms were tested for PMD with Au+Au data for the first time in 2004 and then with Cu+Cu data in 2005.

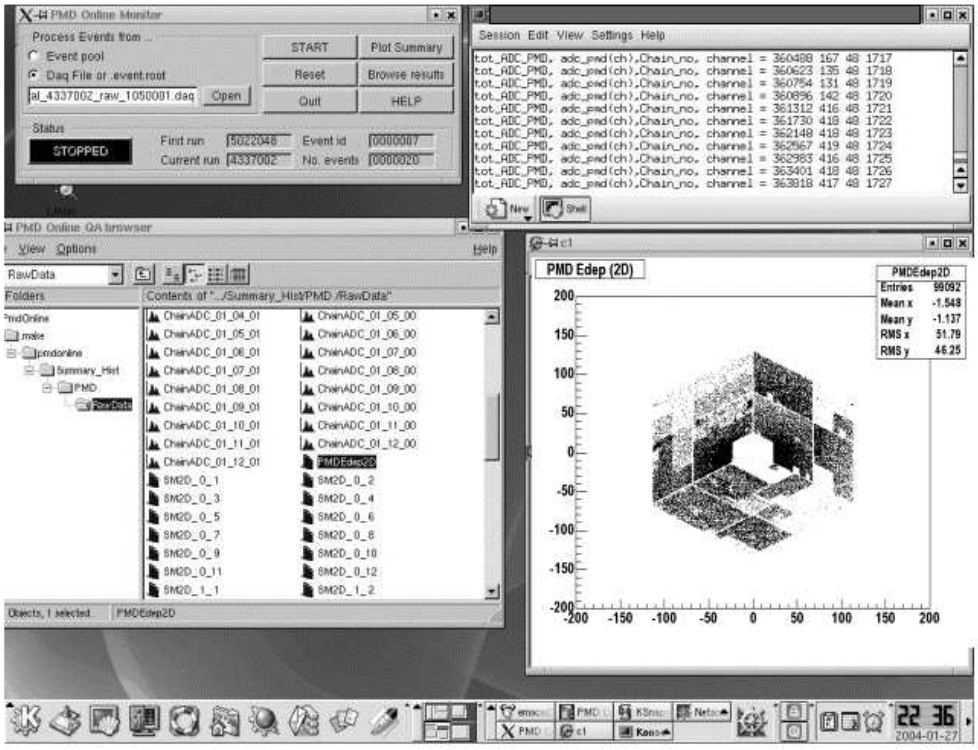

Figure 3.24: Online monitoring screen view.

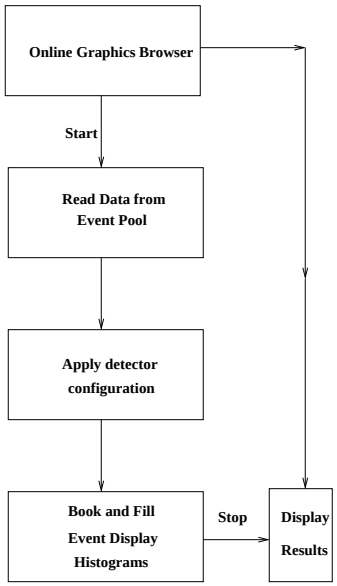

Figure 3.25: Online architecture.

The requirements for run-time control included :

- the Slow Control of Low Voltage for PMD FEE;
- the Slow Control of High Voltage for PMD supermodules;
- the Slow Control for NIM crates;
- the Online monitoring of data and quality assurance (QA) plots;
- the periodic checking of gas;
- the DAQ monitoring for PMD.

As shown in Figure (3.7), there are 12 supermodules on each of the preshower and veto plane of PMD. Each plane of PMD has 24 FEE chains. The preliminary QA plots to understand the behaviour of chains and supermodules from control

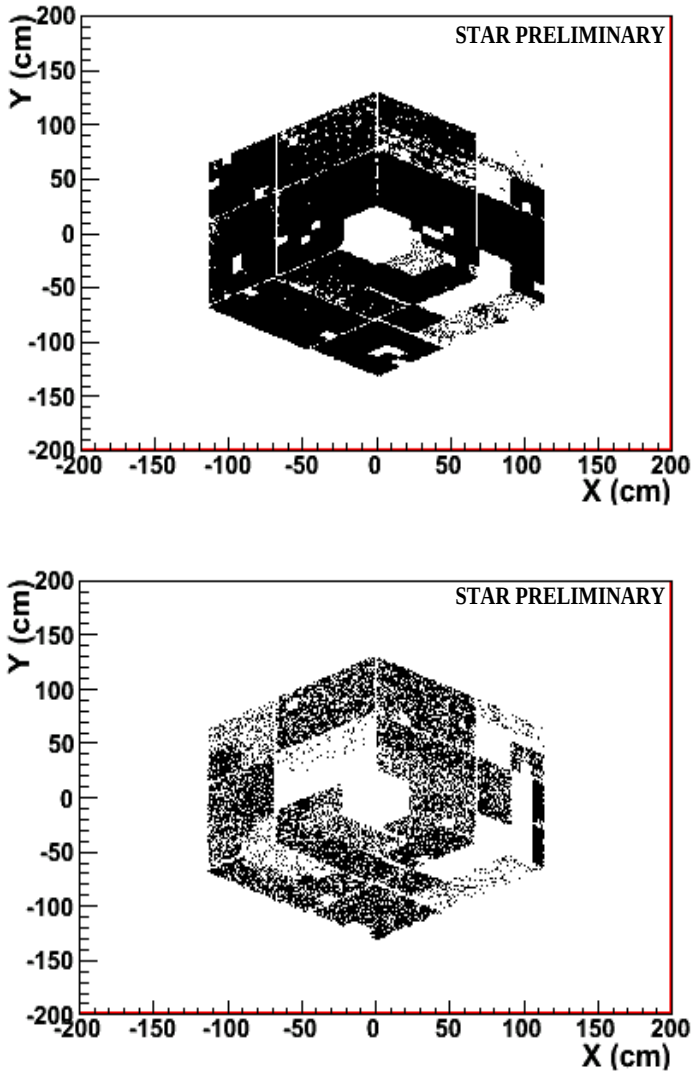

Figure 3.26: Typical X-Y hit display of preshower plane where the top panel is for Au+Au data at $\sqrt{s_{\rm NN}}$ = 200 GeV and the bottom panel for p+p data $\sqrt{s_{\rm NN}}$ = 200 GeV, both taken in 2004.

room during beam-time, were the two-dimensional Y vs. X hit distribution histograms. The pedestal subtracted hits distributions are shown for clearly shown for p+p and Au+Au (as presented in Figure (3.26)) ensuring the working condition of electronics and detector sub-parts, providing assurance on the quality of data taken. Such plots can be monitored from the STAR control room with Online software.

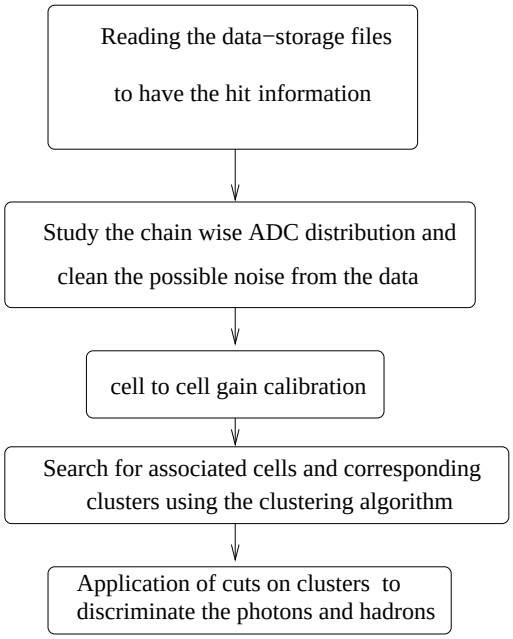

Figure 3.27: PMD data analysis procedure.

The PMD data analysis procedure is shown in Figure (3.27), and before further QA checks, a smaller data subset for the necessary global information based on similar run-time conditions is produced. The choice of the data to be taken for physics analysis from the whole accumulated dataset is based on the stability of the supermodules in terms of HV, the information which is maintained in online logbook. Further information of the data quality can be interpreted from the ADC distribution of the read-out chains. ADC distribution of a readout chain

comprising of 1728 cells is shown in Figure (3.28). A bump is seen in the ADC spectra which indicates the saturation reached in the Gassiplex chip.

Sometimes it has been observed that some chains and a few channels signal large number of times ($\sim$ 10 to 50 times) compared to other chains for similar multiplicity dataset. We can visualize and understand the effect by studying the frequency distribution of the channels accumulated over a large number of events. Such rise is shown in Figure (3.29) and also observed in the chain ADC distributions (at low ADC values) shown in the top panel of Figure (3.30).

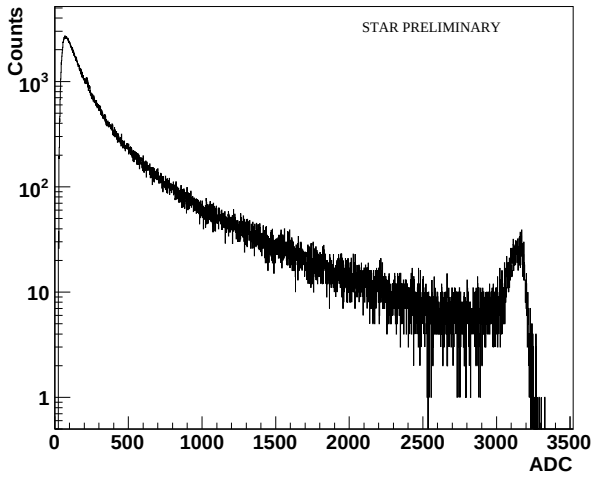

Figure 3.28: The ADC distribution for a group of 1728 cells in a chain showing a saturation around 3000 ADC for Au+Au collisions at $\sqrt{s_{\rm NN}}$ = 200 GeV taken in 2004.

The low ADC noisy channels are removed after a 10 ADC cut is applied uniformly on the cell level. In the next step the frequency of channel hit is analysed for each chain over a large number of events. After that, we get the distribution of the number of times each channel is fired in a chain and store the mean and RMS values for all chains. A channel is marked bad if it is beyond 5 times the RMS

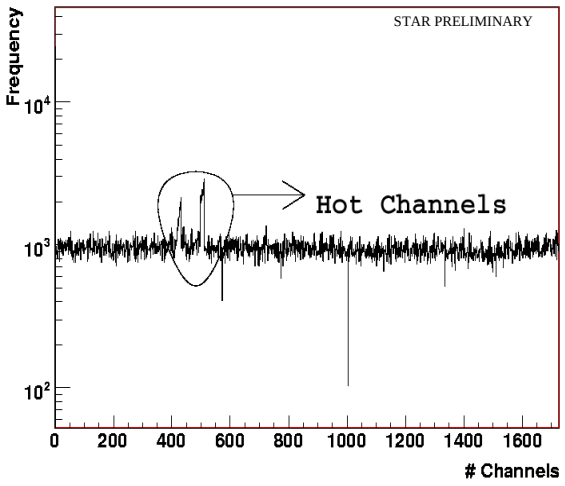

Figure 3.29: The frequency of channels hit over a large number of events and the encircled part showing the rise due to hot and noisy channels, for Au+Au data at $\sqrt{s_{\rm NN}}$ = 200 GeV taken in 2004.

from the mean of the distribution. To ensure proper quality control all channels for each chain are again passed through the set cut value of 6 times the RMS which provides a clean ADC distribution shown in the bottom panel of Figure (3.30). The ADC distribution of bad and noisy channels is shown in the middle panel of Figure (3.30). The 2-dimensional distribution of TPC track multiplicity with PMD hits after the application of clean up procedure is presented in Figure (3.31).

3.2 Barrel Electro - Magnetic Calorimeter (BEMC)

The BEMC is a lead-scintillator sampling electromagnetic calorimeter [96] which is located inside the aluminium coil of the STAR solenoid and covers $|\eta| \leq 1.0$ and 2π in azimuth and thus matches in acceptance with the TPC tracking. Figure (3.32) shows the cross-sectional view of the STAR detector with BEMC.

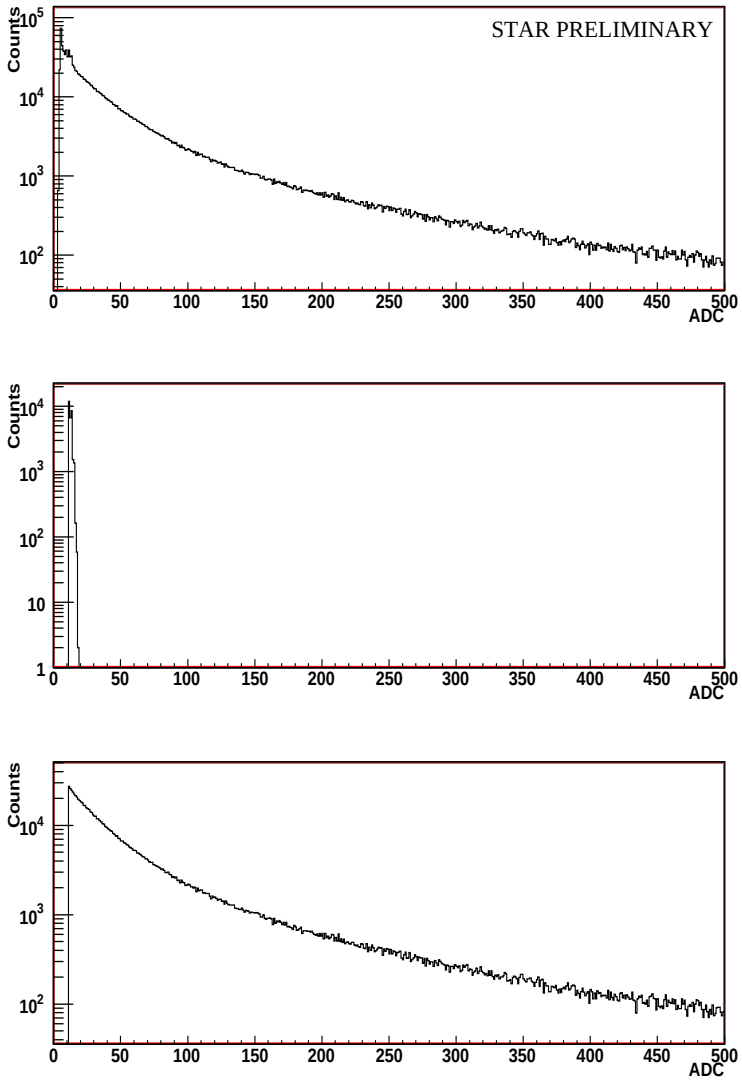

Figure 3.30: Typical cell ADC distribution for a group of 1728 cells in a chain for Cu+Cu collisions at $\sqrt{s_{\rm NN}} = 62.4$ GeV taken in 2005. The top panel shows the ADC distribution before the data clean-up, the bump at the low ADC region is due to hot channels. We see them in the middle panel. The bottom panel shows the ADC distribution after the removal of the hot and noisy channels.

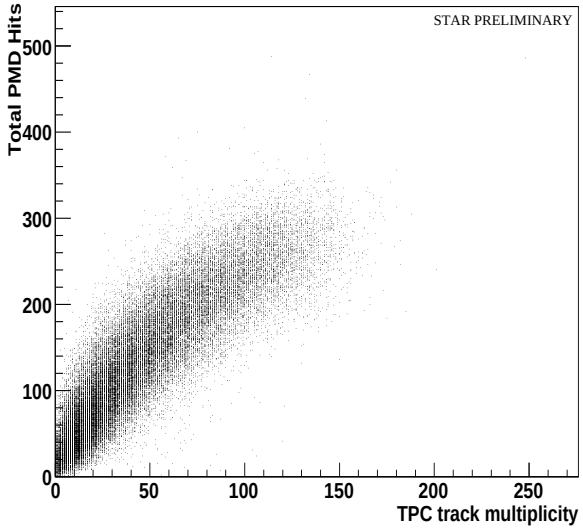

Figure 3.31: Correlation of total PMD hits with TPC track multiplicity for Cu+Cu collisions at $\sqrt{s_{\rm NN}} = 62.4$ GeV taken in 2005.

The calorimeter has a depth of 20 radiation lengths at η=0 and an inner radius of 220 cm. The BEMC includes a total of 120 calorimeter modules, each subtending an angle of 6^0 in ϕ direction ($\sim$ 0.1 radian) and 1.0 unit in η direction as shown in Figure (3.33). These calorimeter modules are mounted 60 in ϕ and 2 in η. Each module is divided into 40 towers with granularity ($\Delta\eta$,$\Delta\phi$) = (0.05, 0.05). A Preshower detector is integrated into each of the 4800 towers of the BEMC. The calorimeter is a sampling calorimeter, and the core of each module consists of a lead-scintillator stack and the shower maximum detectors are situated approximately 5 radiation lengths from the front of the stack. There are 20 layers of 5 mm thick lead, 19 layers of 5 mm thick scintillator and 2 layers of 6 mm thick scintillator. The latter, thicker scintillator layers are used in the preshower portion of the detector. The first and second scintillating layers of the calorimeter

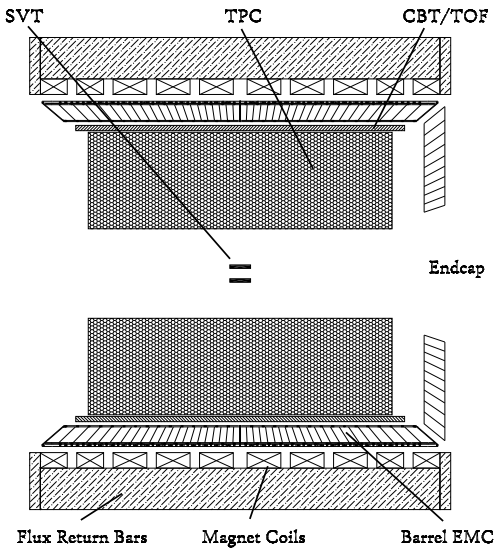

Figure 3.32: The cross-sectional view of the STAR detector with BEMC [96].

comprise the preshower detector. Two layers of gaseous Shower Maximum Detectors with two-dimensional readout are located at 5 radiation length($X0$) inside the calorimeter module.

The STAR Barrel Shower Maximum Detector (BSMD) is a wire proportional counter - strip readout detector using gas amplification [96]. While the BEMC towers provide precise energy measurements for isolated electromagnetic showers, the high spatial resolution of ($\Delta\eta$,$\Delta\phi$) = (0.007, 0.007) provided by the SMDs is essential for direct γ identification, π^0 reconstruction and electron identification. The electromagnetic energy resolution of the calorimeter is δE/E $\sim$ 16% / $\sqrt{E}$ (GeV).

The detector strips sense the induced charge from the charge amplification near the wire. There are 50 μm gold plated tungsten wires in the centre of the extrusion channels. A total of 36000 strips are present in the full detector and 120 ganged

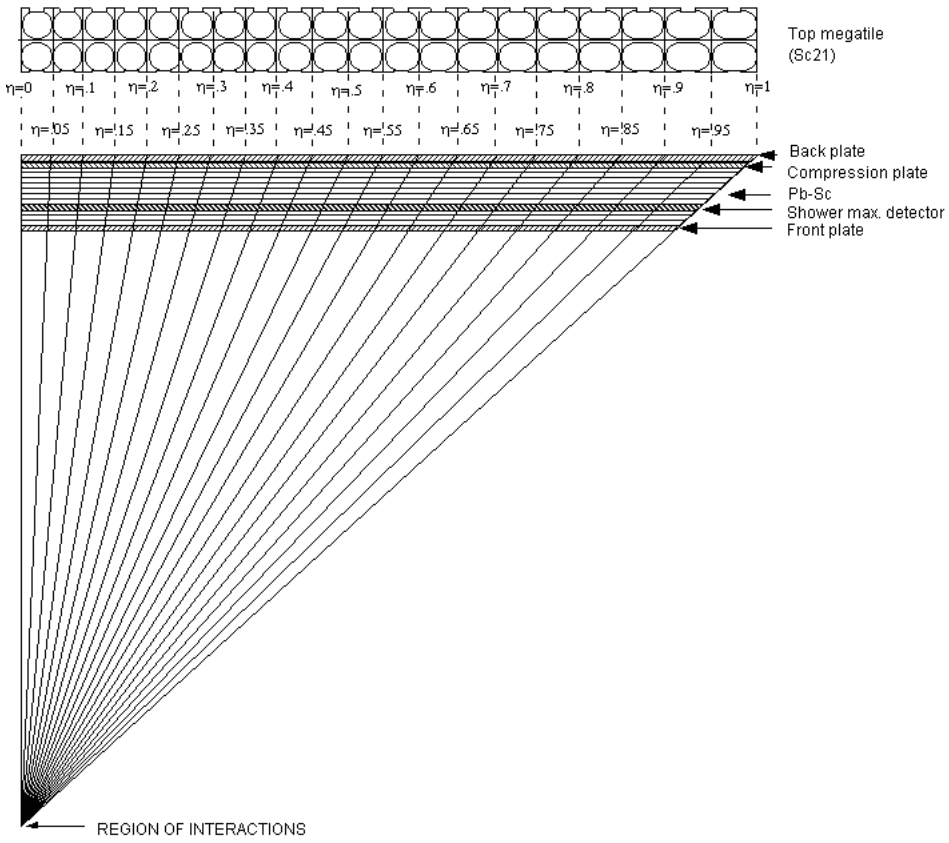

Figure 3.33: The side view of a BEMC module [96].

wire channels in the full BEMC. Each of the 1200 distinct areas have $\approx$ 0.1 X 0.1 in $\eta - \phi$, with 15η and 15ϕ strips. The wires in the BSMD in each of the 120 EMC modules have a length 1.0 in η. The signals can be used to provide 120 independent shower max trigger signals from the BEMC, each spanning $\Delta\eta$ x $\Delta\phi$ = 1.0 x 0.1. As the detector is inside the lead-scintillator stack, the SMD is under a fixed pressure of 15 psi.

The BEMC electronics [96] includes trigger, readout of photo-tubes and SMD, high-voltage system for photo-tubes, low voltage power, slow controls functions, calibration controls, and interfaces to the STAR trigger, DAQ and slow controls. The bulk of the front end electronics including signal processing, digitization, buffering, formation of trigger primitives, and the first level of readout is located in the BEMC crates situated outside the magnet iron. The exceptions are the preamplifiers and switched capacitor array's which form the analog pipeline for the SMD wire chambers. They are situated in the BEMC modules inside the STAR magnet.

The BEMC tower data is processed via a separate path. The photo-tube signals from the towers are integrated and digitized in the front-end cards on every RHIC crossing. These data are pipelined until level-0 trigger time, and if a trigger occurs they are transferred to a token-addressable memory in the tower data collector located on the STAR electronics platform to await readout. The signals from the pads of the SMD are amplified with a simple trans-impedence amplifier and driver on the front end processing cards before entering an analog pipeline composed of switched capacitor arrays to await the level-0 trigger. When the level-0 trigger arrives, the SMD analog signals are queued with the multiplexing ratio of 80:1 to the 10-bit SMD digitizers. SMD digitized signals are first available in STAR's level-2 trigger processors in $\sim$ 200 μs, still ahead of digital information from the TPC.

BEMC is at present running and taking data in STAR and later on (in Chapter

5) we shall describe the detailed analysis software and photon reconstruction with BEMC. The study of photon correlations and its physical implications in the search for QGP will also be discussed in Chapter 5.

3.3 Time Projection Chamber (TPC)

The Time Projection Chamber (TPC) [93] provide complete azimuthal coverage around the beam line and tracking for charged particles within ± 1.8 units in pseudo-rapidity. With a length of 4.2 m and has a diameter of 4 m.

It is situated in a solenoidal magnet that provides a uniform magnetic field of maximum strength 0.5 T (important for charged particle momentum analysis). The TPC volume is filled with P10 gas (10% methane and 90% argon) [93, 94], in a uniform electric field of 135 V/cm. The trajectories of primary ionizing particles passing through the gas volume are reconstructed with high precision from the released secondary electrons which drift in the electric field to the readout end caps of the chamber. The uniform electric field which is required to drift the electrons is defined by a thin conductive Central Membrane (CM) at the centre of TPC, concentric field cage cylinders and the read out end caps. The electric field must be uniform since it requires the track precision in sub mm and electron drift paths upto 2 meters. The schematic picture of STAR TPC is presented in Figure (3.34).

The uniform electric field of the TPC is defined by having the correct boundary conditions with the parallel disks of the central membrane (CM) and the end caps with the concentric field cage cylinders. The CM is operated at 28 KV while the end caps are at ground. The field cage cylinders provide a series of equi-potential rings that divide the space between the CM and the anode planes into 182 equally spaced segments.

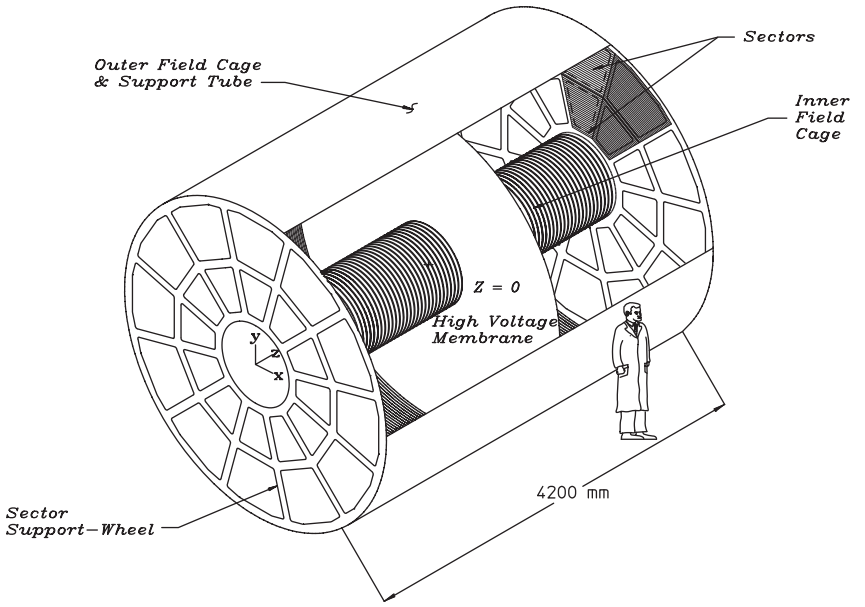

Figure 3.34: Schematic picture of STAR TPC which surrounds a beam-beam interaction region at RHIC [93].

Each endcap of the TPC is radially divided into 12 sectors which are further partitioned in an inner and an outer sub-sector. The inner sub-sector consists of 13 pad-rows and the outer of 32 pad-rows. The pads size were chosen so that they provide good two-track spatial resolution. To understand the efficiency of finding 2 hits with the distance separating them, studies have been done taking the ratio of the distributions of distance separating 2 hits in the same event and 2 hits from different events. Studies show that the two hits can be completely resolved when they are separated in the padrow direction (i.e along the local x axis) by at least 0.8 cm in the inner sector and 1.3 cm in the outer sector. In a similar manner the two hits are completely resolved when they are separated in the drift direction (i.e along the z axis) by 2.7 cm in the inner sector and 3.2 cm in the outer sector.

Additionally, the pads are closely packed to maximize the amount of charge collected by each of them, thus optimizing the dE/dx resolution. The spacing between pad rows is larger in the inner sector to cope with the higher hit density. The readout system is based on Multi Wire Proportional Chambers (MWPC) with readout pads. The drifting electrons avalanche in the high fields at the 20 μm anode wires providing an amplification of 1000 to 3000. The positive ions created in the avalanche induce a temporary charge on the pads which disappears as the ions move away from the anode wire. The image charge is measured by the preamplifier/shaper/waveform digitizer system. The induced charge from an avalanche is shared over several adjacent pads, so the original track position can be reconstructed to a small fraction of a pad width. There are a total of 136,608 pads in the readout system.

The track of an infinite momentum particle passing through the TPC is sampled by 45 pad rows, but a finite momentum track may not cross all 45 rows. It depends on the radius of curvature of the track, the track pseudo-rapidity, fiducial cuts near sector boundaries, and other details about the particle trajectory. The wire

chambers are sensitive to almost 100% of the secondary electrons arriving at the pad plane, the overall tracking efficiency is lower (80 - 90%) due to fiducial cuts, track merging, and to lesser extent bad pads and dead channels. There are at most a few percent dead channels in each run cycle. The acceptance of TPC is 96% for high momentum tracks traveling perpendicular to the beamline. The 4% inefficiency is caused by the spaces between the sectors which are required to mount the wires on the sectors.

The TPC raw data is firstly calibrated and the event reconstruction consists of next following four steps: cluster finding, global track-finding and fitting, primary vertex fitting, and primary track re-fitting. The cluster finder gathers the TPC data into clusters in 2 dimensional space and time direction. They are subsequently converted into three dimensional space-points in the global STAR co-ordinate system, where the drift velocity and trigger-time offset are taken into account. Their integrated and gain calibrated charge is used for particle identification via the dE/dx measurement as shown in Figure (3.35) [93]. The track of a primary particle passing through the TPC is reconstructed by finding ionization clusters along the track. The clusters are found separately in x,y and in z space.(The local x axis is along the direction of the pad row while the local y axis extends from the beamline outward through the middle of, and perpendicular to the padrows. The z axis lies along the beamline.) For example, the x position cluster finder looks for ionization of adjacent pads, within a pad row, but with comparable drift times. For simple clusters, the energy from all pads is summed up to provide the total ionization of the cluster. The x and y co-ordinates of a cluster are determined by the charge measured on adjacent pads in a single pad row. The z co-ordinate of a point inside TPC is determined by measuring the time of drift of a cluster of secondary electrons from the point of origin to the anodes on the endcap and dividing by the average drift velocity.

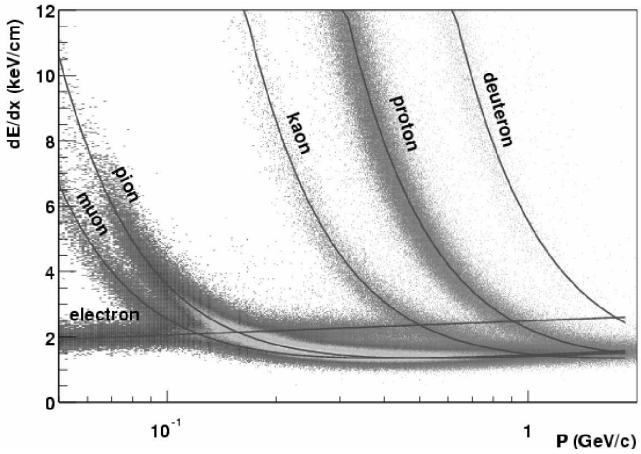

Figure 3.35: The energy loss distribution for all measured particles with STAR TPC [93].

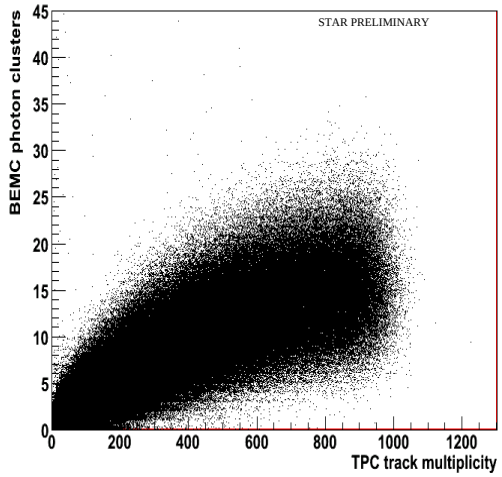

Figure 3.36: Correlation of BEMC photon clusters with TPC track multiplicity for Au+Au collisions at $\sqrt{s_{\rm NN}} = 62.4$ GeV.

Operating on these space points for proper reconstruction a track is required to have hits on at least 10 pad rows because shorter tracks are likely to be broken track fragments. After this the tracks are passed through a Kalman filter, with the calculation of track parameters taking into account the energy loss and multiple scattering in the beam pipe. These tracks are called *global tracks* which are extrapolated towards the beam-axis in the centre of TPC and a common origin is calculated which is identified as the *primary vertex*. The vertex resolution of high multiplicity events is approximately 150 μm, both parallel and perpendicular to the beam axis. After the primary vertex is found, all the global tracks which point back to the newly found primary vertex within 3 cm or less, undergo a second pass through the Kalman filter where the primary vertex is now taken into account. These are labelled as *primary tracks*.

The exciting physics with TPC has provided STAR with many important results and understanding of ultra-relativistic collisions. Figure (3.36) shows the correlation plot between BEMC photon clusters and TPC tracks. The study of hadron correlations using TPC primary tracks is described in Chapter 6.

Chapter 4

Two-Particle Correlations

The experimental search for evidence of Quark Gluon Plasma (QGP) is the most fundamental and challenging task in modern nuclear physics. Numerous experimental observables were proposed as signatures of QGP creation in heavy-ion collisions. One of the predictions is based on expectation that larger number of degrees of freedom associated with deconfined state manifest itself in an increased entropy of the system which should survive subsequent hadronization and freeze-out. This increase in entropy is expected to lead to an increased radius and duration of particle emission, which can be revealed with the help of two-particle correlations.

In this chapter we discuss the basics of the method of two-particle correlations (also known as intensity interferometry). We also discuss the method to decompose the space-time geometry which can be assessed by the experimental measurements and also the ways to make proper Coulomb corrections for charged particles. We end the chapter with a preview of HBT puzzle along with comparative studies of model calculations and experimental data.

4.1 Two-Particle Intensity Interferometry

The two-particle correlations arise from the interference of the particle wave functions, and depend on whether the particles are bosons or fermions. Interference is a phenomenon associated with the superposition of two or more waves.

Intensity interferometry which is also known as two-identical particle correlation, was formulated in a pioneering experiment in 1956 by Robert Hanbury-Brown and Richard Q. Twiss [53] as a method of measuring the stellar radii through the angle subtended by nearby stars, as seen from earth's surface, using the correlation between two photons. When one of the photon is detected by one detector, the probability for detection of the second photon in coincidence is found to correlate with respect to the relative transverse separation between the two detectors. Intensity interferometry differs from ordinary amplitude interferometry in that it does not compare amplitudes (as done in Young's double-slit experiment) but compares the intensities of two different points. The information about the space-time structure of the emitting source created in elementary particle and heavy-ion collisions from the measured particle momenta can be extracted by the method of two-particle intensity interferometry techniques also called the $Hanbury - Brown - Twiss (HBT) effect$.

In particle physics, the HBT effect was independently discovered by G. Goldhaber, S. Goldhaber, W.Y. Lee and A. Pais in 1960 [51], where they studied at Bevatron the angular correlations of identical pions in $p\overline{p}$ annihilations. The enhancement of pion pairs at small relative momenta was explained as a simple refinement of the statistical model by taking into account the Bose-Einstein(BE) statistics for like charged pions. It was also gradually realized that such correlations of identical particles emitted by excited nuclei are sensitive to the geometry of the system and also its lifetime [121, 122].

The study of small relative momentum correlations, is one of the most powerful tools at our disposal to study the complicated space-time dynamics of heavy ion collisions. It provides crucial information which helps to improve our understanding of the reaction mechanisms and to interpret theoretical models of heavy-ion collisions [123].

Historically most of the HBT measurements in heavy-ion experiments have been done with the pions [124] and later on extended to kaons, protons and other heavier particles. Hadron correlations reflect the properties of the hadronic source, i.e. size of the system at the freeze-out time. The direct photons, which are emitted during all the stages of the collision, serve as a deep probe of the hot and dense matter. Hence direct photon HBT correlations can provide the system sizes at all stages of heavy-ion collisions.

4.2 A Simple Model of Intensity Interferometry

A simple example of HBT interference is shown in Figure. (4.1) where a particle of momentum p_1 is detected at x_A and another identical particle p_2 is detected at x_B. They are emitted from the point sources x_1 and x_2 of an extended source. The solid and dashed lines joining point sources I and II with the detectors A and B are the possible trajectories of the particles.

The degree of correlation using the simple description [123, 125, 126, 127], is given by single particle distribution function :

$$\frac{dN^1}{d^3p_1} \tag{4.1}$$

and the two-particle distribution function :

$$\frac{dN^{1,2}}{d^3p_1 d^3p_2} \ . \tag{4.2}$$

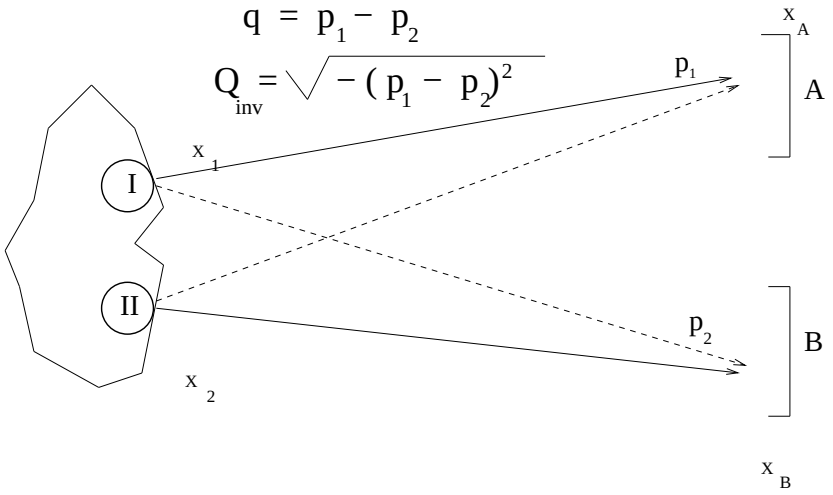

Figure 4.1: Schematic representation of two indistinguishable particles of momentum p_1 and p_2 being detected respectively at x_A and x_B. They are emitted from the point sources x_1 and x_2 of an extended source. The solid and dashed lines joining point sources I and II with the detectors A and B are the possible trajectories of the particles.

The two-particle correlation functions are constructed as the ratio of the measured two-particle inclusive and single-particle inclusive spectra [124, 125],

$$C(p_1, p_2) = \frac{dN^{1,2}/(d^3p_1 d^3p_2)}{(dN^1/d^3p_1)(dN^2/d^3p_2)} \ . \tag{4.3}$$

The single-inclusive distribution is expressed as

$$\frac{dN^1}{d^3p_1} = P_1(p_1) = \langle |A(p_1)|^2 \rangle \tag{4.4}$$

where $P_1(p_i)$ is the single particle momentum distribution and $A(p_i)$ is production probability amplitude expressed as,

$$A(p_i) = \frac{1}{\sqrt{2}}\beta(p_i)[e^{-ip_i.(x_A - x_1)}e^{i\phi_1} \pm e^{-ip_i.(x_A - x_2)}e^{i\phi_2}] \ . \tag{4.5}$$

Thus the single-inclusive distribution can be written as:

$$\frac{dN^1}{d^3p_1} = \langle |A(p_1)|^2 \rangle = \frac{\beta(p_1)^2}{2}[2 \pm e^{ip_1.(x_1-x_2)}\langle e^{\pm i(\phi_1-\phi_2}\rangle + c.c] \tag{4.6}$$

where $\beta(p_1)$ in the above equation is a real function which characterizes the source strength, which is taken equal for the two sources and $c.c$ is the *complex conjugate*. The phases ϕ are taken to be different between the two sources, and we neglect the p dependence of the phases.

As these are for identical particles and hence cannot be distinguishable the $\pm$ sign ambiguity infers +ve or symmetric for bosons, and $-$ve or anti-symmetric for fermions.

When there is incoherent emission, we have

$$\langle e^{\pm i(\phi_1-\phi_2)}\rangle = 0 \ , \tag{4.7}$$

and hence,

$$\frac{dN^1}{d^3p_1} = \beta(p_1)^2 \ . \tag{4.8}$$

The amplitude for the two-particle emission is given by

$$\frac{dN^{1,2}}{d^3p_1 d^3p_2} = P_2(p_1,p_2) = \langle |A(p_1,p_2)|^2 \rangle \tag{4.9}$$

and thus we have,

$$\begin{aligned} \frac{dN^{1,2}}{d^3p_1 d^3p_2} &= \frac{\beta(p_1)^2\beta(p_2)^2}{2}[2 \pm e^{i(p_1-p_2).(x_1-x_2)}\langle e^{\pm i(\phi_1+\phi_2-\phi_1^{'}-\phi_2^{'})}\rangle \qquad (4.10) \\ &\quad + c.c \ ] \\ &= \beta(p_1)^2\beta(p_2)^2(1 \pm \cos[(p_1-p_2).(x_1-x_2)]) \qquad (4.11) \end{aligned}$$

which is independent of ϕ and $\phi^{'}$.

The correlation function which is defined in Eq. (4.3) can be expressed as

$$C(p_1, p_2) = (1 \pm \cos[(p_1 - p_2).(x_1 - x_2)]) \ . \tag{4.12}$$

In reality instead of two discrete points we have extended sources in space and time. For such extended sources described by $\rho(x)$, the normalized space-time distribution, we have,

$$\begin{aligned} P_2(p_1, p_2) &= P_1(p_1)P_1(p_2) \int d^4x_1 \int d^4x_2 |A(p_1, p_2)|^2 \rho(x_1)\rho(x_2) & (4.13) \\ &= P_1(p_1)P_1(p_2)[1 \pm |\tilde{\rho}(q)|^2] \ , & (4.14) \end{aligned}$$

where

$$|\tilde{\rho}(q)| = \int d^4x e^{iq.x} \rho(x) \tag{4.15}$$

is the Fourier transform of $\rho(x)$.

So the resulting two-particle intensity correlation function (with +ve sign for bosons and −ve sign for fermions) is

$$C(p_1, p_2) = \frac{P_2(p_1, p_2)}{P_1(p_1)P_1(p_2)} = (1 \pm |\tilde{\rho}(q)|^2) \tag{4.16}$$

where we denote the momentum difference of the pair by $q = p_1 - p_2$.

The two-particle correlation function is also written as,

$$C(p_1, p_2) = (1 \pm \lambda |\tilde{\rho}(q)|^2) \tag{4.17}$$

where the λ parameter is called the incoherence or chaoticity parameter which was introduced for the analysis of experimental data [126, 127]. So this correlation function now interpolates between the case of a coherent source $\lambda = 0$ and the case of a completely chaotic source with $\lambda = 1$.

4.2.1 Emission Function and Space-time structure of Collisions

The two-particle correlations in momentum space and the source distribution in co-ordinate space can be derived [52, 122, 128, 129, 130] if the particles are emitted independently ("chaotic source") and travel freely from the source to the detector.

So the relations for single-particle spectrum :

$$E_p \frac{dN}{d^3p} = \int d^4x S(x,p) \tag{4.18}$$

and for the correlator :

$$C(\overrightarrow{q},\overrightarrow{K}) = 1 \pm \frac{|\int d^4x S(x,K) e^{iq.x}|^2}{\int d^4x S(x,K+\frac{1}{2}q) \int d^4y S(y,K-\frac{1}{2}q)} \tag{4.19}$$

where the emission function $S(\mathrm{x},K)$ explained above is the single-particle *Wigner Phase − space density* of the particles (with +ve sign for bosons and −ve sign for fermions) in the source.

For the single particle spectrum Eq. (4.18) this Wigner function must be evaluated on-shell, *i.e* at $p^0 = E_p = (m^2 + \overrightarrow{p}^2)^{1/2}$. The correlation function Eq. (4.19) is expressed in terms of the relative momentum $\overrightarrow{q} = \overrightarrow{p_1} - \overrightarrow{p_2}$, $q^0 = E_1 - E_2$, and the average (pair) momentum $\overrightarrow{K} = (\overrightarrow{p_1} + \overrightarrow{p_2})/2$, $K^0 = (E_1 + E_2)/2$. As the two measured particles are on-shell, $p^0_{1,2} = E_{1,2} = (m^2 + \overrightarrow{p}^2_{1,2})^{1/2}$, the 4-momenta q and K are *off − shell*. They satisfy the orthogonality relation [129, 130],

$$q.K = 0 \ . \tag{4.20}$$

This infers that three among the four relative momentum components are kinematically independent. The principal focus of two-particle intensity interferometry is to extract as best information as possible from the emission function

S(x,K) [52, 129, 130], which characterizes the particle emitting source created under such extreme conditions in heavy-ion collisions.

Using the smoothness approximation which assumes that the emission function has a sufficiently smooth momentum dependence such that one can replace

$$S(x, K - \frac{1}{2}q)S(y, K + \frac{1}{2}q) \approx S(x, K)S(y, K) \tag{4.21}$$

and hence from Eq. (4.19) we have,

$$C(\overrightarrow{q}, \overrightarrow{K}) \approx 1 \pm \left| \frac{\int d^4x S(x, K) e^{iq.x}}{\int d^4x S(x, K)} \right|^2 \equiv 1 \pm |\langle e^{iq.x} \rangle(K)|^2 \ . \tag{4.22}$$

Since S(x,K) is always real the reconstruction of its phase not the issue. The mass-shell constraint relation in Eq. (4.20) removes one of the 4-components of the relative momentum q and it can be formulated as,

$$q^0 = \overrightarrow{\beta} . \overrightarrow{q}, \qquad\qquad \overrightarrow{\beta} = \overrightarrow{K}/K^0 \approx \overrightarrow{K}/E_K \tag{4.23}$$

where the energy difference is q^0 and $\overrightarrow{\beta}$ is the pair-velocity.

With only the 3-independent $\overrightarrow{q}$-components, the Fourier transform in Eq. (4.22) cannot be inverted and which means that the spatial-temporal structure of S(x,K) cannot be fully recovered from the measured correlator :

$$C(\overrightarrow{q}, \overrightarrow{K}) - 1 \approx \pm \left| \frac{\int_x e^{i \overrightarrow{q} . (\overrightarrow{x} - \overrightarrow{\beta} t)} S(x, K)}{\int_x S(x, K)} \right|^2 = \pm \left| \frac{\int_x e^{i . \overrightarrow{q} . \overrightarrow{x}} S(t, \overrightarrow{x} + \overrightarrow{\beta} t; \overrightarrow{K})}{\int_x S(x, K)} \right|^2 . \tag{4.24}$$

Henceforth we can conclude that the space and time components of the source need further unavoidable model assumptions about S(x,K). Such dependences can be removed by additional information not included in the identical two-particle correlations.

Reformulating the correlator in terms of the normalized relative distance distribution,

$$d(x,K) = \int_x s(X + \frac{x}{2}, K)s(X - \frac{x}{2}, K), \qquad s(x^{'}, K) = \frac{S(x^{'}, K)}{\int_{x^{'}} S(x^{'}, K)}, \qquad (4.25)$$

where d(x,K) = d(-x,K) is an even function of x. So the correlator can be expressed as,

$$C(\overrightarrow{q}, \overrightarrow{K}) - 1 \approx \pm \int d^4x \;\; cos(q.x)d(x,K) = \pm \int d^3x \;\; cos(\overrightarrow{q}, \overrightarrow{x})S_{\overrightarrow{K}}(\overrightarrow{x}) \quad (4.26)$$

using the relations in Eq. (4.23) along with the introduction of relative source function

$$S_{\overrightarrow{K}}(\overrightarrow{x}) = \int dt \; d(t, \overrightarrow{x} + \overrightarrow{\beta}t; \overrightarrow{K}, E_K) \quad . \qquad (4.27)$$

In the particle-pair rest frame where $\overrightarrow{\beta} = 0$, the relative source function $S_{\overrightarrow{K}}(\overrightarrow{x})$ is the integral over the time part of the relative source distribution d($\overrightarrow{x}$,t;K), and the time structure of the source is integrated out. $S_{\overrightarrow{K}}(\overrightarrow{x})$ which is for each pair momentum $\overrightarrow{K}$, can be constructed back from the measured correlator $C(\overrightarrow{q}, \overrightarrow{K})$ by inversion of the Fourier Transform in Eq. (4.26).

4.3 Final State Interactions

In the calculations so far we have considered only the effect of symmetry on two-particle correlations. But the correlations can also arise from two-particle final state interactions even if the symmetry-based correlations are absent [131, 132, 133, 134, 135]. The experimental analysis of interferometry assumes a bigger challenge due to the presence of strong and Coulomb final state interactions(FSI). For

small relative momenta the effects of strong interactions maybe neglected for pions but for the proton-proton interactions they cannot be neglected [136]. The pion correlation functions on the other-hand are severely affected by the long range Coulomb interactions. The discussion will be exclusively for bosons since pion correlations are later discussed in Chapter 6.

4.3.1 Coulomb Interactions

The effect of Coulomb interactions distorts the experimental correlation functions hence causing a suppression (enhancement) of the measured correlation function at very small relative momenta for like-sign (unlike-sign) pairs. So we need to correct them to subtract such final state interaction effects. The earlier presumption of the final state interactions [137] used the thought that particle production occurs within the range of their interactions, but such concepts were refuted by the Bose-Einstein enhancement features.

To understand the Coulomb interaction effects [138] let us solve the Schrödinger equation for the Coulomb wave-function [139] Ψ_{coul} :

$$(-\frac{\nabla^2}{2\mu} - E + V_{coul})\Psi_{coul} = 0, \tag{4.28}$$

where μ is the reduced mass and E is the energy of the particle in the centre of mass system.

Solving Eq. (4.28) in terms of the confluent hyper-geometric function F [52, 140],

$$\Psi_{coul}(\overrightarrow{r}) = \Gamma(1+i\eta)e^{-\frac{1}{2}\pi\eta}e^{-\frac{i}{2}(\overrightarrow{q}.\overrightarrow{r})}F(-i\eta;1;z_-), \tag{4.29}$$

$$z_\pm = \frac{1}{2}(q.r \pm \overrightarrow{q}.\overrightarrow{r}) = \frac{1}{2}qr(1 \pm cos\theta), \tag{4.30}$$

where $r = |\overrightarrow{r}|$ and θ is the angle between the vectors $\overrightarrow{r}$ and $\overrightarrow{q}$.

The Sommerfeld parameter η expressed in terms of the particle mass "m" and electromagnetic coupling strength "e" :

$$\eta_{\pm} = \pm\frac{e^2}{4\pi}\frac{\mu}{q/2} = \pm\frac{me^2}{4\pi q} \tag{4.31}$$

where the plus (minus) sign is for unlike-sign (like-sign) particle pairs.

For identical particle-pairs the wave-function should be properly symmetrized as, $\Psi_{coul}(\overrightarrow{r}) \mapsto \frac{1}{\sqrt{2}}[\Psi_{coul}(\overrightarrow{r}) + \Psi_{coul}(\overrightarrow{-r})]$ and the corresponding correlation function from Eq. (4.26) is

$$C(\overrightarrow{q}, \overrightarrow{K}) = \int d^3r S_{\overrightarrow{K}}(\overrightarrow{r})|\Psi_{coul}(\overrightarrow{r})|^2 \quad . \tag{4.32}$$

The correlator is expressed in terms of the relative source function explained in Eq. (4.26), which describes the probability that a particle pair with pair-momentum $\overrightarrow{K}$ is emitted from the source at initial relative distance $\overrightarrow{r}$ in the pair rest frame.

For a point-like source $S_{\overrightarrow{K}}(\overrightarrow{r}) = \delta^{(3)}(\overrightarrow{r})$, the correlator in Eq. (4.32) as given from the Gamow factor $G(\eta)$ which is the square of the Coulomb wave-function $\Psi_{coul}(\overrightarrow{r})$ at the vanishing pair separation $\overrightarrow{r} = 0$,

$$G(\eta) = |\Psi_{coul}(\overrightarrow{r} = 0)|^2 = |\Gamma(1 + i\eta)\ e^{-\frac{1}{2}\pi\eta}|^2 = \frac{2\pi\eta}{e^{2\pi\eta} - 1} \quad . \tag{4.33}$$

The Gamow factor is found to significantly over estimate the FSI effects. The dependence of Coulomb correlations on the size R of the source can be estimated from Eq. (4.32) using $S_{\overrightarrow{K}}(\overrightarrow{r}) \propto exp[-\overrightarrow{r}^2/4R^2]$ [52, 129, 138]. The experimental application and inferences will be done in Chapter 6.

4.4 Parametrization of Correlation Functions

For the physical understanding of the spatial and temporal nature of the source, it is essential to characterize it in terms of some source parameters. Generally the two-particle correlation function is usually parametrized by Gaussian approximation, which elucidates the interpretation of HBT radii in terms of the space-time dependence of the emission function $S(\mathrm{x},K)$ [44, 52, 128, 129, 130, 141]. However at times such extracted parameters may become solely dependent on the fitting methods. Such dependencies can be avoided using imaging methods [142] and three-dimensional analysis where the correlation functions are decomposed in Cartesian or spherical harmonics [143, 144].

4.4.1 Gaussian Parametrization

The Gaussian parameterization in relative momentum components, of the correlation and source functions provide the basic understanding of experimental data. The effective source of particles of momentum K understood in terms of space-time variances ("RMS widths") are [129],

$$\langle \tilde{x}_\mu \tilde{x}_\nu \rangle (\overrightarrow{K}) \equiv \langle (x-\bar{x})_\mu (x-\bar{x})_\nu \rangle \tag{4.34}$$

where $\langle ... \rangle$ denotes the (K-dependent) space-time average over the emission function in Eq. (4.22). The effective source centre is $\bar{x}(K) = \langle x \rangle$ and from Eq. (4.22) the correlator can be written as,

$$C(\overrightarrow{q}, \overrightarrow{K}) = 1 \pm exp[-q_\mu q_\nu \langle \tilde{x}_\mu \tilde{x}_\nu \rangle (\overrightarrow{K})] \quad . \tag{4.35}$$

Here we have considered the smoothness and on-shell approximations discussed in Section 4.2.1. Henceforth we can express the space-time variances $\langle \tilde{x}_\mu \tilde{x}_\nu \rangle$ as functions of $\overrightarrow{K}$. The absolute space-time position $\bar{x}(\overrightarrow{X})$ of the source centre is not

apparent and thus cannot be measured. The width of the correlation function is expressed in terms of RMS widths of S(x,K), which we see in Eq. (4.34) [129].

These width parameters do not in general characterize the total extension of the collision system but rather measure the size of the system through a filter of wavelength $\overrightarrow{K}$. As introduced and explained in [145], the observer sees the "region of homogeneity" from where the particle pairs of momentum $\overrightarrow{K}$ are likely to be emitted. The direction of $\overrightarrow{K}$ corresponds to the direction from which the collision region is viewed. The modulus of $\overrightarrow{K}$ provides the central velocity $\overrightarrow{\beta}$ [Eq. (4.23)] of that part of the collision region seen through the wavelength filter [52, 129, 141, 146]. Only under special cases where the emission function without showing any spatial-momentum correlations factorizes as S(x,K) = f(x)g(K), these variances $< \tilde{x}_\mu \tilde{x}_\nu >$ coincide with such widths of the total source.

We have introduced in [Eq. (4.17)] the chaoticity parameter λ, which is dependent on $\overrightarrow{K}$ and parameterizes the intercept of the correlation function for q=0. This $\lambda(\overrightarrow{K})$ is unity for a completely chaotic source and it lies between zero and unity for a partially chaotic (or coherent) source. So from [Eq. (4.17)], taking account this deviation from complete chaoticity where C(q=0)=2, for bosons (*e.g* pions), the correlator is expressed as,

$$C(\overrightarrow{q}, \overrightarrow{K}) = 1 + \lambda(\overrightarrow{K}) exp[-q_\mu q_\nu \langle \tilde{x}_\mu \tilde{x}_\nu \rangle (\overrightarrow{K})] \quad . \tag{4.36}$$

In identical pion-interferometry, many of the measured pions are from long-lived decays. Pions from the weak decays have their decay vertices typically a few centimeters from the reaction center. Contributions from such weak decays can be identified, however the decays from η and $\eta^{'}$ are hard for experimental identification as they occur a few thousand fm away from the center of the collision. Such contributions mainly from long-lived resonances along with the particle misidentification can cause reduction in $\lambda(\overrightarrow{K})$. Besides that Coulomb corrections for

FSI also influence the values of $\lambda(\overrightarrow{K})$.

4.4.2 Bertsch-Pratt(Cartesian) parametrization

While relating Eq. (4.36) with experimental analysis we need to remove one of the four q-components using the mass-shell relation in Eq. (4.20). Based on the choice of the three independent components different Gaussian parameterizations exist. The discussions here are done for bosons as we shall later discuss photon correlations in Chapter 5 and pion correlations in Chapter 6.

The simplest parameterization is,

$$C(\overrightarrow{q}, \overrightarrow{K}) = 1 + \lambda(\overrightarrow{K})\ exp\ [-Q_{inv}^2 R_{inv}^2(\overrightarrow{K})] \tag{4.37}$$

where Q_{inv} is the invariant momentum dependence of the two particles and R_{inv} is the invariant radius parameter. R_{inv} is not a direct measure of the size of effective density as it contains also the time component [3]. A detailed three-dimensional characterization of the emitting source can be possible by decomposing the relative momentum vector $\overrightarrow{q}$ according to the Cartesian or Bertsch-Pratt ("out-side-long") convention [44, 124, 129, 147].

As shown in Figure. (4.2) the relative momenta $\overrightarrow{q}$ are decomposed into the variables q_{long}, along the beam direction, q_{out}, parallel to the transverse momentum of the pair $\overrightarrow{k_T} = (\overrightarrow{p_{1T}} + \overrightarrow{p_{2T}})/2$, and q_{side}, perpendicular to q_{long} and q_{out}. The time-component is removed by the mass-shell constraint in Eq. (4.20) and so from Eq. (4.23) the pair velocity is expressed as

$$\overrightarrow{\beta} = (\beta_T, 0, \beta_\ell)\ . \tag{4.38}$$

The correlator using the Bertsch-Pratt(Cartesian) parametrization is expressed as,

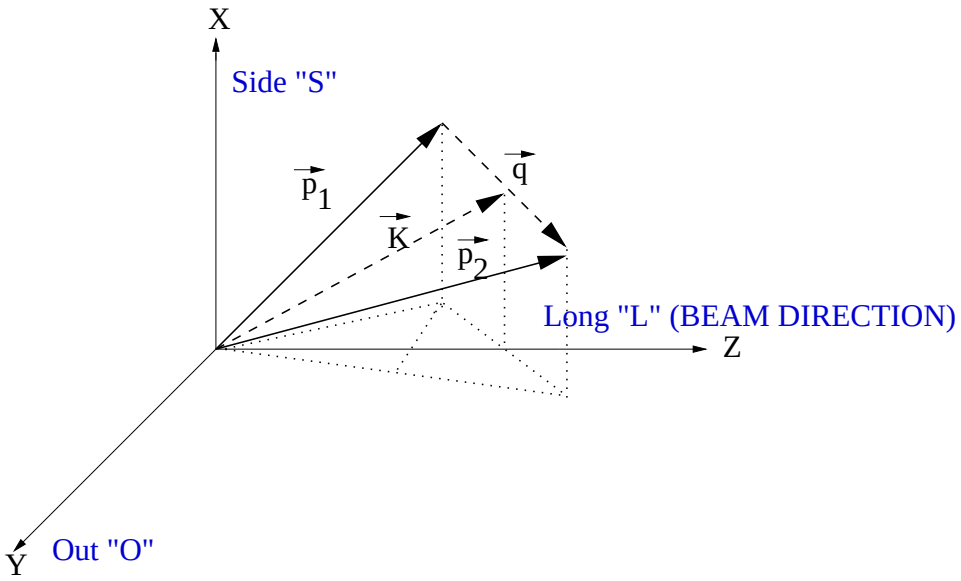

Figure 4.2: The Bertsch-Pratt ("out-side-long") parametrization

$$C(\overrightarrow{q},\overrightarrow{K}) = 1 + \lambda(\overrightarrow{K}) exp(-\sum_{i,j=o,s,l} R_{ij}^2(\overrightarrow{K}) q_i q_j) \ . \tag{4.39}$$

The Gaussian width parameters R_{ij} of this Cartesian parametrization can be expressed as space-time variances [Eq. (4.34)] by

$$R_{ij}^2(\overrightarrow{K}) = \langle(\tilde{x}_i - \beta_i\tilde{t})(\tilde{x}_j - \beta_j\tilde{t})\rangle, i,j = o,s,l \ . \tag{4.40}$$

The correlator $C(\overrightarrow{q},\overrightarrow{K})$ is dependent on k_T, k_ℓ and also on the azimuthal orientation Φ of the transverse pair momentum $|\overrightarrow{k_T}|$. Φ is defined with respect to some pair-independent direction in the laboratory system, e.g. relative to the impact parameter $\overrightarrow{b}$ [148],

$$\Phi = \angle(\overrightarrow{k_T}, \overrightarrow{b}) \ . \tag{4.41}$$

The emission function has a reflection symmetry $x_s \rightarrow -x_s$ for azimuthally

symmetric collision analysis [123, 147, 149], where the correlator becomes symmetric under $q_s \rightarrow -q_s$. Using these relations we have $R^2_{os} = R^2_{sl} = 0$ and the correlator can be expressed as :

$$C(\overrightarrow{q}, \overrightarrow{K}) = 1+\lambda(\overrightarrow{K})\, exp(-R^2_o(\overrightarrow{K})q^2_o - R^2_s(\overrightarrow{K})q^2_s - R^2_l(\overrightarrow{K})q^2_l - 2R^2_{ol}(\overrightarrow{K})q_o q_l)\ . \quad (4.42)$$

These HBT radii have both the space and time information of the source and hence their interpretation depends on the frame in which the relative momenta $\overrightarrow{q}$ are specified. Choosing the longitudinal co-moving system (LCMS) with the condition that the source is symmetric under $x_l \rightarrow -x_l$, the cross-term R^2_{ol} vanishes [123, 147] and so Eq. (4.42) is expressed in terms of "out-side-long" as:

$$C(\overrightarrow{q}, \overrightarrow{K}) = 1+\lambda(\overrightarrow{K})\, exp(-R^2_{out}(\overrightarrow{K})q^2_{out} - R^2_{side}(\overrightarrow{K})q^2_{side} - R^2_{long}(\overrightarrow{K})q^2_{long})\ . \quad (4.43)$$

The HBT radii parameters $R^2_{ij}(\overrightarrow{K})$ [52, 149] which characterize the correlator in Eq. (4.43) are,

$$\begin{aligned} R^2_{out}(\overrightarrow{K}) &=< (\tilde{x} - \beta_T \tilde{t})^2 > (\overrightarrow{K}) \\ R^2_{side}(\overrightarrow{K}) &=< \tilde{y}^2 > (\overrightarrow{K}) \\ R^2_{long}(\overrightarrow{K}) &=< \tilde{z}^2 > (\overrightarrow{K}) \end{aligned} \quad (4.44)$$

where the transverse velocity β_T is defined in Eq. (4.38) .

Azimuthally sensitive HBT measurements for non-central collisions which involves measurements at different Φ angles also provides a measure of the source shape [52, 150, 151, 152].

4.4.3 Probing beyond Gaussian parametrizations

The shape of the correlation functions explained in section 4.2.1 are characterized in the form of "source parameters", from the Gaussian parametrizations described

in sections 4.4.1 and 4.4.2. But the measured correlation functions deviate from the Gaussian shape more or less significantly, but, often remain ignored in most experimental analyses. There are two such consequences due to non-Gaussian behavior: (a) the corresponding space-time variances deviate from the fitted source parameters and (b) the Gaussian radius parameters do not provide all the information of the correlator[Eq. (4.22)]. Non-Gaussianness of the experimental correlation functions can be understood from the associated measurements using edgeworth expansion studies [153, 154, 155, 156] and spherical harmonics [143, 144].

4.5 Results of Model studies and Data

4.5.1 Hydrodynamic studies

Hydrodynamics is the theoretical framework (proposed by Landau [157]) in a continuous fluid like medium. It is the most suitable approach to study the signals of dense matter formation, since it is the only dynamical model which provides a direct link between the collective observables and Equation of State(EoS) [158]. The equation of motion can be described from the kinetic equations [159]. It considers that a hot and dense thermal gas of particles at the initial point which expand hydro-dynamically till the picture of continuous medium is destroyed [160].

At RHIC the hydrodynamic simulations of elliptic flow start to overshoot the data above $p_T > 2$GeV [159]. This indicates that the main contribution of elliptic flow originates at early stages of the collision, where the system is dense and mean free path close to hydrodynamic limit zero. However the later stage, called the freeze-out happens when the mean free path of particles become comparable with the smallest of the system dimensions: its mean free path or hydrodynamic length [160].

The two-particle pion correlations are measured at freeze-out, where the mean free path is large and hence that maybe the reason of the limited applicability of hydrodynamic model predictions on interferometric measurements at RHIC [146]. As the matter expands and dynamic evolution occurs, the lifetime of the produced fireball determines phase space density and particle reaction rates, necessitating any dynamic model for these measurements to be consistent with HBT results [123]. A detailed discussion on hydrodynamic models for heavy ion collisions is found in Reference [159] and a current status of HBT in hydrodynamical context is discussed in Reference [123].

A brief summary of the salient descriptions for different hydro-inspired models with the HBT data is given below:

- The HBT data have been compared with the three-dimensional hydrodynamic model of Hirano et al. where the EoS is for hadronic matter which is in partial chemical equilibrium [161].

- Also the data have been compared with two-dimensional model of Heinz and Kolb [162] and a two-dimensional chiral model by Zseische et al. [163].

- The comparative results of these above mentioned models and HBT data [123] still show a large deviation with significant over prediction for R_{long} and R_{out}/R_{side} ratio. In general these models use EoS that are softer than those used for cascades and Boltzmann calculations, and they often have latent heat during the transition from partonic phase [123].

- The comparisons with hybrid hydrodynamic models like Ultra-relativistic Quantum Molecular Dynamics(UrQMD) do not have agreement with the data for R_{out} and R_{long} [164].

4.5.2 Boltzmann or Cascade Models

A brief summary of the salient descriptions for other dynamic models (Boltzmann/cascade) with the HBT data :

- Relativistic Quantum Molecular Dynamics(RQMD) model [165] over predicts the R_{out}/R_{side} and under predicts multiplicities. The Hadronic Re-scattering Model(HRM) [166, 167] in fact provides a closer semblance to the data. Another cascade model which models the collision of light partons to an eventual one-to-one hadronization to pions is Molnar Parton Cascade(MPC) [168]. But MPC also underestimates source radii [123];

- A Multi-Phase Transport(AMPT) model [169] is a hybrid model that uses minijet partons from the hard processes in the HIJING Model [170] as the initial condition of modeling the collisions dynamics. AMPT provides a better fit to the experimental data and shows that the two-pion correlation function is sensitive to the parton-scattering cross section, which controls the density at which the parton-to-hadron transition occurs in this model [169]. However the fall of HBT radii with k_T is more in AMPT than in data, which fall off $\sim m_T^{1/2}$ [123].

4.5.3 HBT Puzzle

The predictions from hydrodynamic results show that the emitting source evolving through a quark-gluon to hadronic phase transitions will emit pions over a long period of time causing an enhancement in R_{out}/R_{side} ratio [58, 158]. On the contrary the experimental results show $R_{out}/R_{side} \approx 1$ [123] and this has been termed as "the RHIC HBT puzzle" [162]. The most puzzling aspect is that the models which have a phase transition fails to reproduce experimental data.

However an alternative model using relativistic quantum mechanical treatment of opacity and refractive index is done which reproduces the HBT radii and pion spectrum for central Au+Au collisions at RHIC [171]. The work initially compared with STAR data [171] was extended later by the PHOBOS collaboration [172]. The interpretations of RHIC HBT results done with a theoretical model [171] (using the hydrodynamic parameterization of the source) requires the application of quantum wave mechanics along with the nuclear optical model to the medium produced by the colliding systems. The formulated new relativistic quantum mechanical description of the collision medium also included collective flow along with the absorption and refraction in a complex potential. Klein-Gordon wave equations for pions in medium has been solved and the calculated overlap integrals with these wave-functions have been used to obtain the predictions of pion spectra and HBT radii.

The effects of including the pionic interactions for successful description of measured spectra and radii is done by putting the effects of pion-medium final state interactions (FSI) while solving the relevant relativistic wave equation. Due to the attractive strength of these interactions the pions act as massless objects inside the medium. The medium also acts as if it is free of the chiral condensate which is the source of the pion mass, and henceforth acting as a system with a restored chiral symmetry [173]. A hydro-based multidimensional Gaussian emission function is used to describe the probability of pion emission as a function of position and momentum in medium. This assumption is combined with the optical model wave-functions to obtain the emission function. A distorted-wave emission function (DWEF) is what is used to calculate the pion correlation function and spectrum [171].

Numerical calculations using the above discussed formalism [171] were used with a minimization program which included upto 12 model parameters to obtain

the best fit to STAR $\sqrt{s_{\rm NN}} = 200$ GeV Au+Au pion spectrum and HBT radii [171, 173]. The model comparisons with HBT data suggest good agreement. Based on the assumption of the properties of matter formed in Cu+Cu collisions to be of the same type as in Au+Au collisions along with a simple scaling of the model parameters $\propto A^{1/3}$, the predictions for Cu+Cu collisions are also provided.

Initial calculations [174] however predict another possibility of the deviation between the data and model (which lead to the HBT puzzle to) calculations which is viscosity, subsequently included and reproduced in some recent calculations [175]. The recent studies with a granular source model [176] also reproduce better matching with experimental measurements of pion HBT radii. But detailed calculations are needed which can ensure systematic understanding of assumed model parameters and experimental data.

Chapter 5

Photon Correlations

Direct photons emitted from the early hot phase of the relativistic heavy ion collisions and their correlations serve as important signatures of the quark gluon plasma and its properties. Due to their electromagnetic nature of interaction, the photons have a clear advantage in such correlation studies [177, 178, 179, 180, 181, 182, 183, 184, 185] as they weakly interact with the system and are free from Coulomb interactions (which one needs to correct for hadronic measurements).

The Bose-Einstein correlations of the direct photons provide information about the various stages of heavy ion collisions [78, 186, 187]. However, it is difficult to extract the small yield of direct photons due to the large background of photons produced by electromagnetic decay of the hadrons (especially π^0's and η's). It has been proposed that one can obtain the direct photon HBT signal using all produced photons [187]. The correlations of direct photons can be decoupled from the residual correlations of decay photons. The decay photon correlations do not contribute to the region of small invariant momenta where the effects of the direct photon interferometry assume significance, as discussed in this chapter.

Intensity correlations between photons produced in heavy ion collisions had

been measured for $E_\gamma \geq 25$ MeV in the reaction $^{86}Kr +^{nat} Ni$ at 60A MeV energy [188, 189]. The ^{86}Kr beam was delivered by the GANIL accelerators at an average intensity of 10 electrical nA. The hard photons were detected by the 320 hexagonal BaF_2 scintillation detectors of Two Arms Photon Spectrometer (TAPS) and the rise seen in the invariant relative momentum distribution of photon pairs from 40 MeV to 5 MeV was attributed due to the expected interferometric effects. The other studies done at GANIL are with Multi Element DEtector Array (MEDEA) for $^{36}Ar +^{27} Al$ reaction at 95A MeV [188, 190] and for lower beam energies of 40A MeV [191].

At ultra-relativistic energies the first measurement studies with the two-photon correlations in central $^{208}Pb +^{208} Pb$ collisions at 158A GeV [192] were carried out by the WA98 collaboration at CERN using the LEad-glass photon Detector Array (LEDA). The extracted invariant photon radii of 6 fm at low momenta was found comparable to that measured for pions of similar momenta.

The two-photon interferometry measurements in Au+Au collisions at $\sqrt{s_{\rm NN}}$ = 62.4 GeV using the STAR Barrel Electro-Magnetic Calorimeter (BEMC) are presented in the following sections of this Chapter. The development of analyses cuts for photon studies and comparative estimates with charged pions are also discussed.

5.1 Experimental Setup and Trigger details

The Barrel Electro-Magnetic Calorimeter (BEMC) is the main detector in STAR for photon measurements [96]. For the RHIC Run-IV, 50% of the BEMC was installed and operational, covering an acceptance of $0<\eta<1$ and full azimuth. The BEMC is a lead-scintillator sampling electromagnetic calorimeter with equal volumes of lead and scintillator. The STAR Barrel Shower Maximum Detector

(BSMD) is a wire proportional counter - strip readout detector using gas amplification. The details of BEMC are discussed in Section 3.2.

The minimum bias trigger is obtained using the charged particle hits from an array of scintillator slats arranged in a barrel, called the Central Trigger Barrel, surrounding the TPC, two zero degree hadronic calorimeters at ±18 m from the detector center along the beam line, and two Beam-Beam Counters (described in detail in Section 2.2.3). In this analysis for Au+Au collisions (at $\sqrt{s_{\rm NN}} = 62.4$ GeV) using BEMC, the minimum-bias trigger settings using ZDCs and BBCs were used, along with the threshold cut on CTB.

The global characteristics of the event (e.g vertex and energy distributions) have been studied to ensure the selection of good event sample for further physics analysis. For this analysis we selected events with a collision vertex within ± 30 cm measured along the beam axis from the centre of the Time Projection Chamber(TPC). The event selection criteria based on the photon energy distributions are discussed in the next section.

5.2 Details of Photon Analysis

When a particle strikes the BEMC, it deposits a fraction (possibly all) of its energy in the various sub-parts of the Calorimeter, like the lead-scintillator sampling towers, preshower and SMDs. The hits generated from the particle, if produced from the same one are grouped as clusters. Here clustering is done separately for the sampling towers and two SMD planes in η and ϕ directions. Further matching of the clusters is done to reconstruct the BEMC "points", which are used in the analysis for the energy and spatial positions(η , ϕ) of the photon candidates.

The photons and electrons after traversing through the TPC, hit the BEMC towers and generate electro-magnetic showers thereby depositing their energies in

the BEMC. The BEMC is used for obtaining the energy of the shower because of the better energy resolution and higher depth. The spatial position and shower-sizes are provided by the BSMDs which are placed at 5 radiation length ($X0$) inside the calorimeter module.

5.2.1 Photon Selection

The flow-chart schematic for BEMC point reconstruction chain is shown in Figure (5.1). At the start of the chain the raw ADC values of towers and strips are read out. After getting the ADC values for all EMC sub-detectors, calibration constants along-with the status tables from the run to run database are applied to get the proper energy values.

The next step is to find clusters from the data which is done module by module. Clustering is done on three detectors: BEMC towers, BSMD η strips and BSMD ϕ strips. During the analysis the following parameters are set: (i) the the minimum seed energy, (ii) minimum add-on energy and (iii) maximum size of a cluster. The minimum seed energy is the energy threshold required to start a new cluster. Besides that a tower and strip must have a minimum add-on energy to be included as a part of the existing cluster. The details of the chosen parameter values for analysis will be discussed later in this chapter.

The final step is to match the clusters of the BEMC towers, BSMD η strips and BSMD ϕ strips to make the stage of reconstruction in order to get the BEMC points. For the cases where we have one cluster in BEMC, one cluster in BSMD η and one cluster in BSMD ϕ in a given module, we assign the BEMC cluster energy to the (η, ϕ) pairs. But for the cases when the number of matched pairs is more than one, then we need to split the BEMC cluster energy and such energy sharing is dependent only on the BSMD cluster energies.

From these reconstructed BEMC points the energy and co-ordinates of the

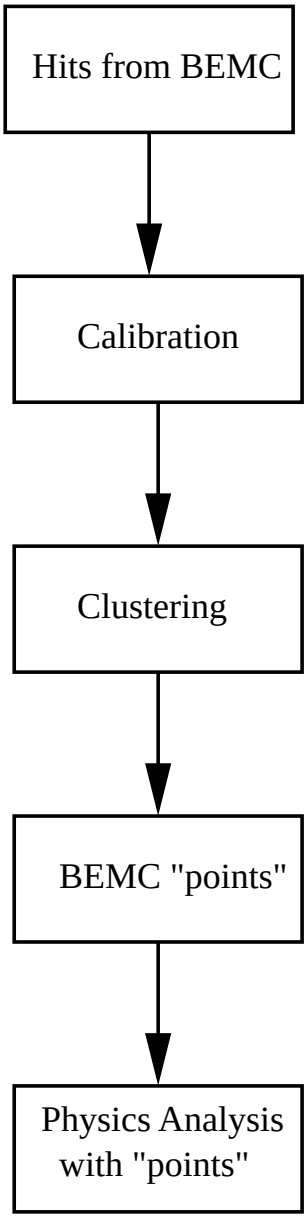

Figure 5.1: The Offline BEMC reconstruction schematic.

photon candidates are determined. We have seen that some events have high spurious energy measurements (possibly due to noisy towers and event pile-up). Such large energy values of the all the added point (cluster) energies accumulated over a number of events show up on the x-axis in the top and middle panels of Figure (5.2). We see that the distribution is fairly proper till 300 GeV. Henceforth a cut is applied to remove such spurious events having total energy > 300 GeV, from the analysed event-sample as shown in the bottom panel of Figure (5.2). The selected events after they successfully pass the vertex and energy cuts are chosen for the present analysis. In BEMC, points are required to have clusters from both the BSMD η and BSMD ϕ planes to achieve better co-ordinate resolution.

As the charged hadrons have a finite probability to shower and deposit energy, we need to suppress the hadronic contributions to make a better sample of photon candidates for the analysis. So the track-to-point positional associations are made with the projected charged particle tracks from TPC on the BEMC. The photon-like clusters in the calorimeter are taken in this analysis which do not have a TPC track pointing at them within the proximity of single tower $(\Delta\eta,\Delta\phi) = (0.05,0.05)$. The schematic presented in Figure (5.3) show one such projected TPC track (with co-ordinates $= (\eta_2, \phi_2)$) situated from a BEMC point (with co-ordinates $=(\eta_1, \phi_1)$) with the proximity of a single tower and hence rejected from the analysis.

The sample of photon-candidates after hadron suppression is used for the construction of the correlation functions. Also the conditions of using those clusters which have both BSMD η and ϕ information provide a more accurate spatial information required in the reconstruction of photon correlations functions. The BEMC cluster seed energy taken is 0.4 GeV while both the BSMD η and ϕ chosen seed energy is 0.2 GeV. Also the BSMD maximum cluster size is chosen to be of 4 strips for η and ϕ.

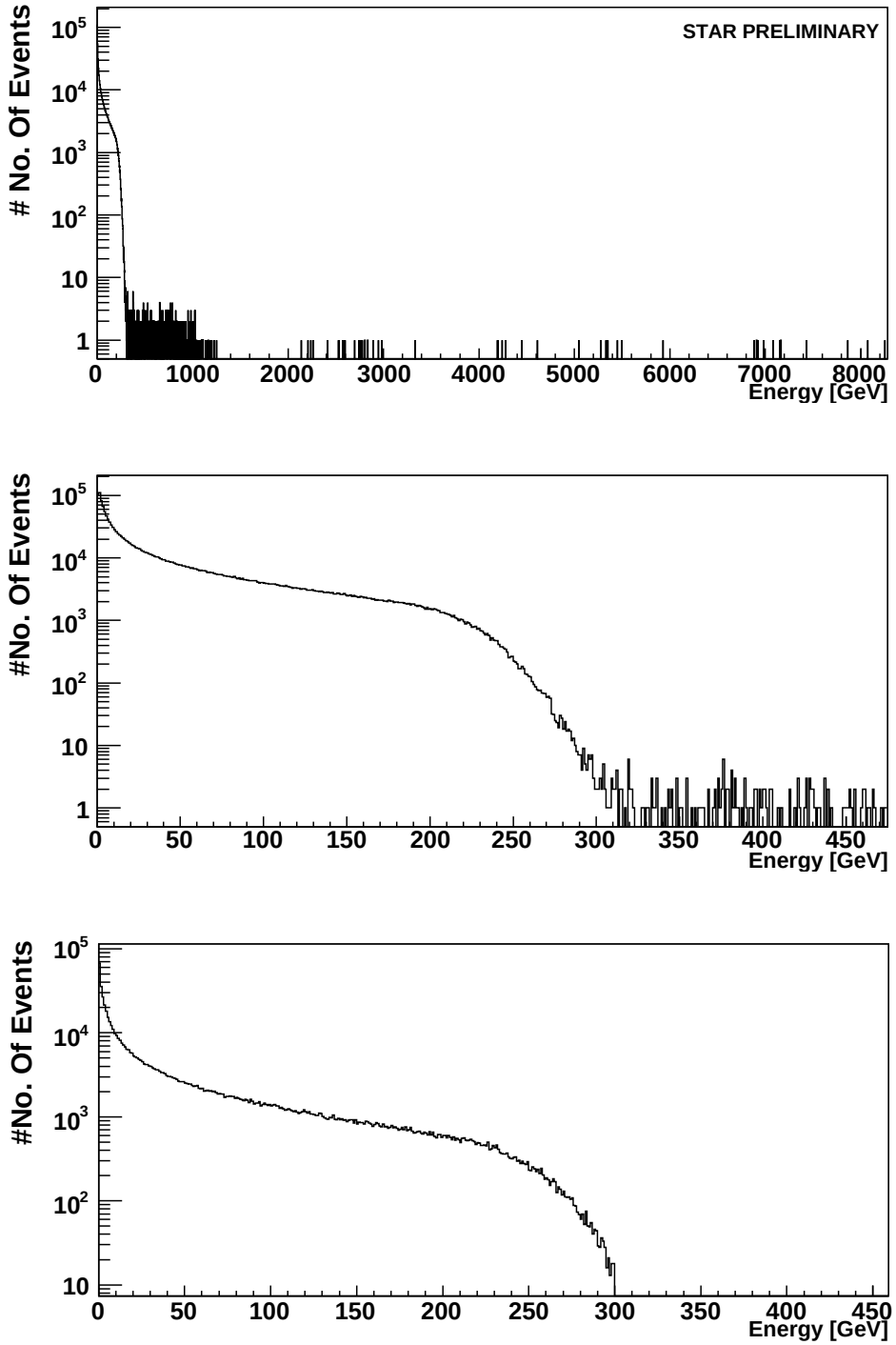

Figure 5.2: The total energy measurement distribution on the top and middle panel without any cuts. The high energy measurements show up in the distribution presented in top and middle panel. The bottom panel shows with cuts applied to reject events with total energy > 300 GeV.

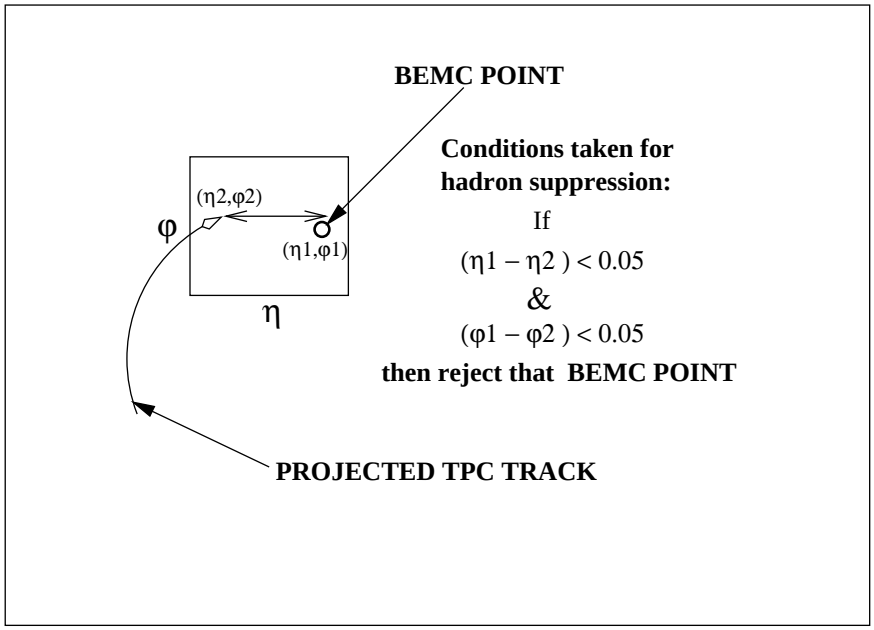

Figure 5.3: Hadron suppression schematic in the photon analysis.

5.3 Construction of the Correlation Function

The energy E and 3-momentum $\overrightarrow{p}$ of a particle of mass m form a 4-vector $p^{\mu} = (E, \overrightarrow{p})$ whose square, using the natural units with $c = 1$, is

$$p^2 \equiv E^2 - |\overrightarrow{p}|^2 = m^2 \ . \tag{5.1}$$

The scalar product of 4-momenta,

$$p_1^{\mu}.p_2^{\mu} = E_1E_2 - \overrightarrow{p_1}.\overrightarrow{p_2} = E_1E_2 - |\overrightarrow{p_1}|.|\overrightarrow{p_2}|cos(\theta_{12}) \tag{5.2}$$

is invariant (frame independent), where θ_{12} is the angle between the particles.

From the experimental point of view it is easier to calculate the correlation function distribution over the invariant relative four-momentum,

$$Q_{inv} = \sqrt{-(p_1^\mu - p_2^\mu)^2} = \sqrt{-m_1^2 - m_2^2 + 2[E_1E_2 - |\overrightarrow{p_1}|.|\overrightarrow{p_2}|cos(\theta_{12})]} \tag{5.3}$$

which is equivalent to the invariant mass for photons [189, 188]. The square of the invariant mass of two-photons is given by

$$M_{inv}^2 = 4E_1E_2Sin^2\frac{\theta_{12}}{2} = 2E_1E_2(1 - cos(\theta_{12})), \tag{5.4}$$

where E_1 and E_2 are the corresponding photon energies, while θ_{12} their angular separation.

Experimentally, the correlation function (normalized to unity at large Q_{inv}) is obtained from the ratio,

$$C(Q_{inv}) = A(Q_{inv})/B(Q_{inv}), \tag{5.5}$$

where A(Q_{inv}) is the pair distribution in invariant momentum for photon-pairs from the same event(correlated distribution), and B(Q_{inv}) is the corresponding distribution for pairs of photons taken from different events (uncorrelated distribution) [52, 187].

As explained in Eq.(5.5) to construct the photon correlation function we need two types of distributions, the A(Q_{inv})(real) and B(Q_{inv})(mixed). To construct the "real" distribution we take both the photons of the photon pair from the same event, whereas for the "mixed" distribution we take the first photon of the pair from one event and second photon from another event. Each particle in one event is mixed with all the particles in a collection of events which in our case consists of 10 events. While constructing the "real" distribution the photon pair combinations are chosen in such a manner that there is no double counting in the pair numbers.

All the additional cuts are implemented on the photon pair, e.g like minimal cluster distance (opening angle cut), excluding clusters from the same tower, the

energy asymmetry (or α) cut etc., in the "real" and "mixed" distributions are constructed with the same conditions.

The reconstruction of photon correlation functions are prone to errors of two major kinds : (i) one cluster can get splitted into several and (ii) close clusters can merge into one. The cluster splitting (case-(i)) produces pairs with small relative momenta and henceforth affect the small momenta region which have small statistics due to geometrical reasons. Cluster merging (case-(ii)) on the other-hand reduces the total number of pairs.

The direct way to estimate the strength of the merging effect is to introduce a cut on the minimal distance between the two clusters (implemented in terms of the opening angle θ_{12}) as explained in Eq. (5.3). The opening angle measurements are done using the spatial positions of the BEMC points and the positional co-ordinates of the primary vertex.

5.3.1 Cluster Splitting

The opening angle "ratio" distribution of "real" and "mixed" events is presented with various cuts in Figure (5.4). The effects of cluster splitting have been studied with opening angle "ratio" distribution along with its effect with cluster energy cuts. The four separate cases presented in Figure (5.4) are :

(i) Without any cuts;

(ii) Energy cut > 0.4 GeV;

(iii) Excluding clusters from same tower;

(iv) Energy cut > 0.4 GeV and excluding clusters from same tower.

During BEMC point reconstruction, for the cases when the number of matched BSMD pairs is more than one, we need to divide the BEMC cluster energy according to the ratio of the strengths of (η , ϕ) pair energies. However considering

the individual photon energy > 0.4 GeV (which is cluster seed energy taken for BEMC as discussed in Section 5.2.1) of the pair, removes the cases where 2 such BSMD clusters can cause such a sharing in BEMC (case(ii) shown with "squares" in Figure (5.4)). We see the the maximum rise in the angle "ratio" distribution with case (i) in Figure (5.4) shown with "circles".

Since the split photons are spatially close we rejected all photon clusters from the same tower. This has been presented as case (iii) with "triangles" in Figure (5.4)). The application of both such energy cuts along with the exclusion of clusters present in same tower effectively reduces the splitting cases, showing the least rise at lower opening angles, which we see as case (iv) in Figure (5.4) plotted with "stars". Henceforth we can say that the conditions of case (iv) is the most effective cut which can be applied on BEMC points to remove splitting under the applied cluster conditions.

5.3.2 Cluster Merging

Figure (5.4) shows that in the region below ~ 0.02 radians it is difficult to separate two BEMC points and the opening angle "ratio" distribution drops down for all the 4-cases discussed earlier. So we can conclude from this observation that to remove cluster merging such minimal opening angle separation cut is needed on the BEMC points. However the detailed study of the effects on such opening angle separation cut on the photon correlation functions will be discussed in next section.

5.3.3 Effect of opening angle cut

The photon correlation distribution as a function of Q_{inv} using Eq.(5.5) are presented in Figure (5.5) with different minimal cluster separation cut in terms of the opening angle (θ_{12}). The opening angle (θ_{12}) of the photon pairs are chosen to be

greater than 0.012, 0.016, 0.020 and 0.024 radians respectively. Here the photon correlation functions are constructed with individual photon energy > 0.4 GeV and rejecting all photon clusters from the same tower (as described in case(iv) of Figure (5.4)).

The inset plot in Figure (5.5) at low Q_{inv} shows that $\theta_{12} > 0.02$ radians is the optimum cut to remove cluster merging discussed in Section. 5.3.2. But even after we have reduced splitting and removed merging we still have an enhancement below 0.1 GeV/c which is clearly seen in Figure (5.5). So the study of the low Q_{inv} region with further cuts is essential.

5.3.4 Effect of Alpha Cut

Figure (5.6) shows the correlation distribution as a function of Q_{inv} with the following cut (called the energy asymmetry or α cut defined as):

$$\alpha = \frac{|E_1 - E_2|}{E_1 + E_2} \tag{5.6}$$

with individual photon energy > 0.4 GeV. The α cut used here is $< 10\%$. The α cut helps in selecting those pairs which participate in the symmetric decay and reduce un-even sharing of cluster energies where one cluster possess more energy share than the other. We see very little difference with and without α cuts for energy > 0.4 GeV as presented in Figure (5.6).

The photon correlation distribution as a function of Q_{inv}, with and without α cuts for two different energy parameters (0.4 GeV and 0.8 GeV) are presented in Figure (5.7). The inset plot in Figure (5.7) also show very little difference with and without α cuts even for different energies. The photon correlation functions presented in Figure (5.6) and (5.7) are constructed with opening angle (θ_{12}) $>$ 0.02 radians and rejecting all photon clusters from the same tower.

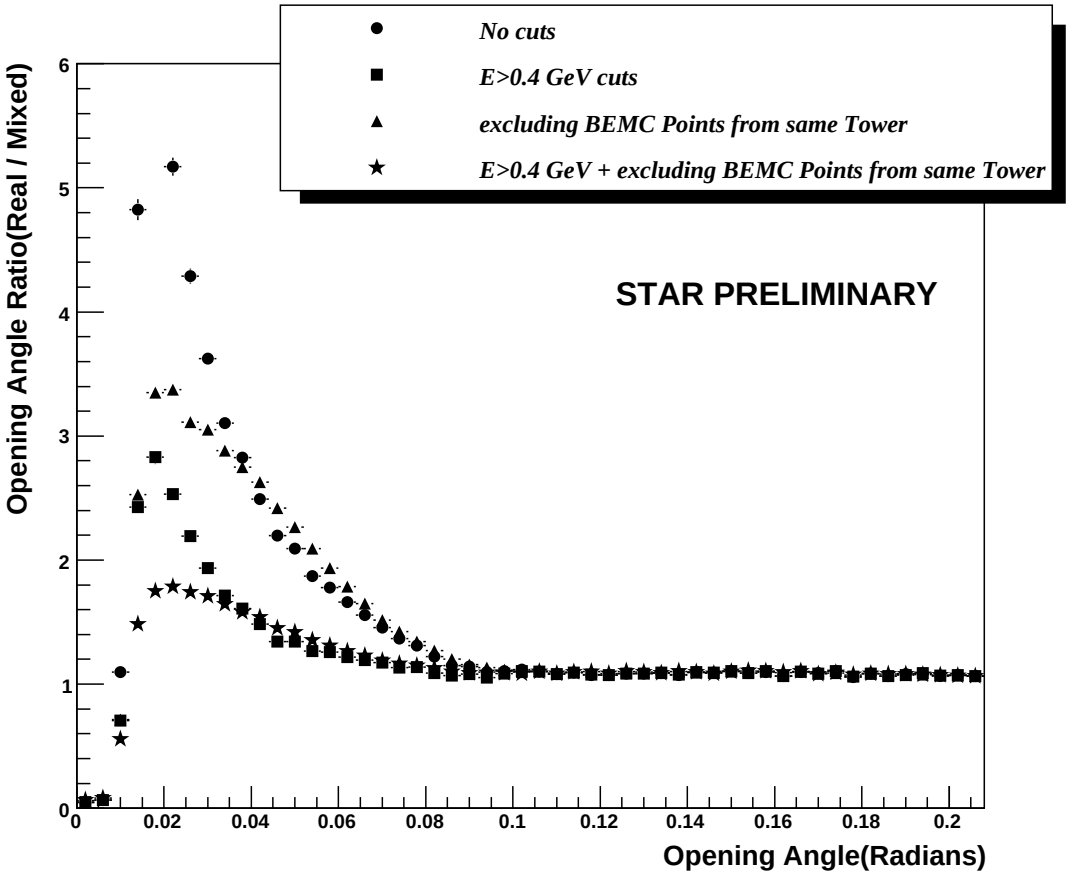

Figure 5.4: The opening angle ratio distribution without cuts and comparison of distribution behaviour with energy and same tower rejection cuts. The 4-cases in descending order presented are: (i) Without any Cuts (shown with "circles");(ii) Energy cut > 0.4 GeV (shown with "squares"); (iii) Excluding clusters from same tower (shown with "triangles"); (iv) Energy cut > 0.4 GeV and excluding clusters from same tower (shown with "stars").

However with the application of higher energy cut of 0.8 GeV applied on individual BEMC points we see a major reduction in the photon correlation functions at low Q_{inv}. It can be seen from Figure (5.7) that the choice of higher individual photon energy cut helps to reduce large enhancement below 0.1 GeV/c. This plot also indicates that we need to study the photon correlation functions with higher energy cuts.

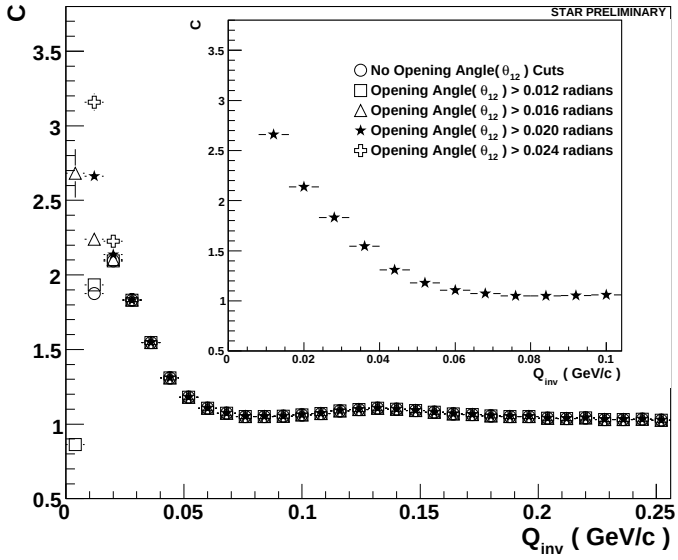

Figure 5.5: Correlation function of photons with different opening angle cuts. The inset plot with opening angle (θ_{12}) > 0.02 radians. Here the photon correlation functions are constructed with individual photon energy > 0.4 GeV and rejecting all photon clusters from the same tower.

5.3.5 Effect of Energy Cut

The energy cuts applied on the photon pairs reduce splitting but such cuts also require optimization as the correlation strength for direct photons is small with the dominant part of the final photons produced from π^0 decay. However such cuts can

be optimized after comparing the photon correlation functions at low Q_{inv} with different energy cuts applied on BEMC point pairs as presented in Figure (5.8). The photon correlation distribution as a function of Q_{inv} with different energy cuts of 0.4, 0.6 and 0.8 GeV are studied in Figure (5.8), where the inset plot shows the effect of cuts at low Q_{inv}. The correlation function with the optimized cut of 0.8 GeV is shown in Figure (5.9). The photon correlation functions presented in Figure (5.8) and (5.9) are constructed with opening angle (θ_{12}) > 0.02 radians and rejecting all photon clusters from the same tower.

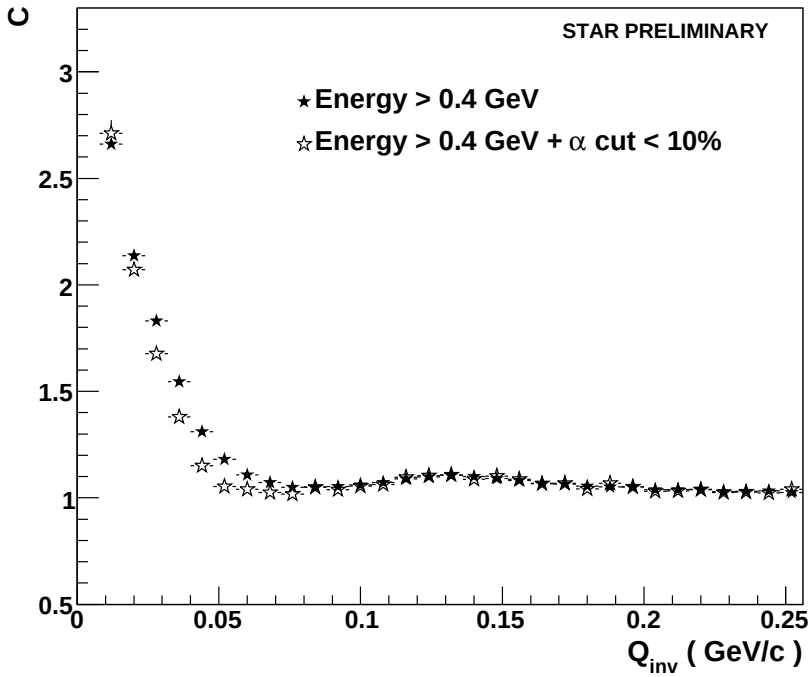

Figure 5.6: Correlation function of photons with and without α cuts and energy cut > 0.4 GeV. All photon clusters from the same tower are rejected along with opening angle (θ_{12}) > 0.02 radians.

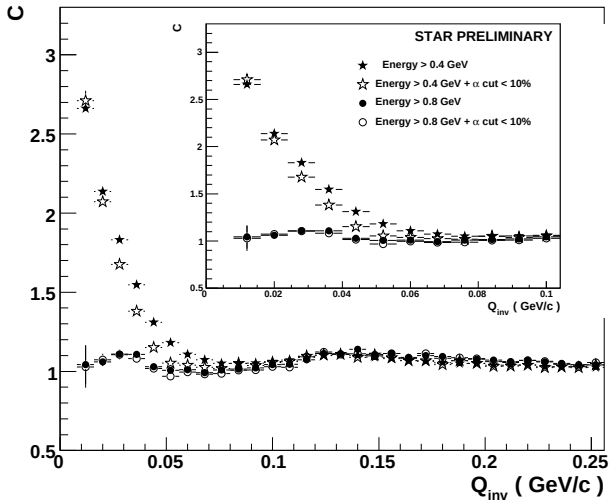

Figure 5.7: Correlation function of photons with different energy cuts with and without α cuts. All photon clusters from the same tower are rejected along with opening angle (θ_{12}) > 0.02 radians.

5.4 Photon Correlation Function

The large production of decay photons from neutral pions and η mesons are possible hindrances which affect the inclusive photon spectrum. However since the residual correlations of decay photons appear at larger relative momenta compared to direct photon correlations, we can disentangle the effects of decayed ones [187].

The detailed apparatus and analysis effects are described in the previous Section 5.3, which can modify the shape, hence produce a rise at low Q_{inv} in the two-photon correlation functions. The minimal angle (or distance) between the showers are introduced and also the energy limit applied on the individual photon candidates (after hadron suppression) show a significant change at low Q_{inv} region.

Such two-photon correlation function [193] using 1.8 million minimum-bias events of Au+Au collisions at $\sqrt{s_{\rm NN}} = 62.4$ GeV is presented in Figure (5.10).

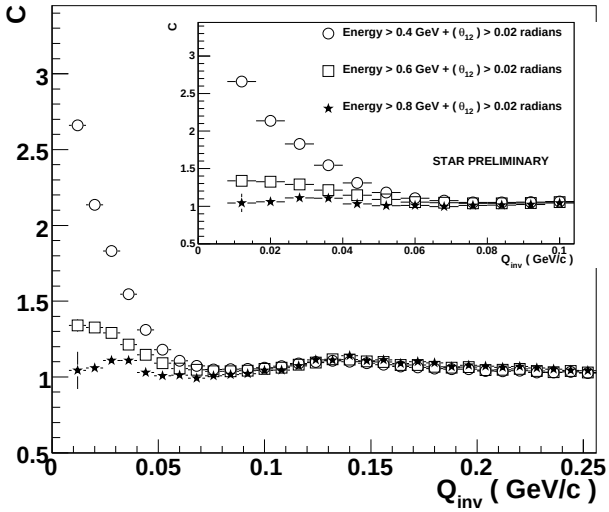

Figure 5.8: Correlation function of photons with different energy cuts. All photon clusters from the same tower are rejected along with opening angle (θ_{12}) > 0.02 radians.

Figure (5.10) shows the two-photon correlation distribution as a function of Q_{inv} which is constructed with opening angle (θ_{12}) > 0.02 radians, individual photon cluster energy greater than 0.8 GeV and rejecting all photon clusters from the same tower.

The correlation function defined in Eq.(5.5) has been fitted with the following Gaussian parametrization (described in Section 4.4.1):

$$C(Q_{inv}) = Norm\ [\ 1 + \lambda\ exp(-R_{inv}^2 Q_{inv}^2)\ ], \tag{5.7}$$

with a normalization parameter "Norm", the chaoticity parameter λ and the radius parameter R_{inv}. The invariant radius (R_{inv}) of photon source estimated from the fit is 6.80 $\pm$ 0.82 fm.

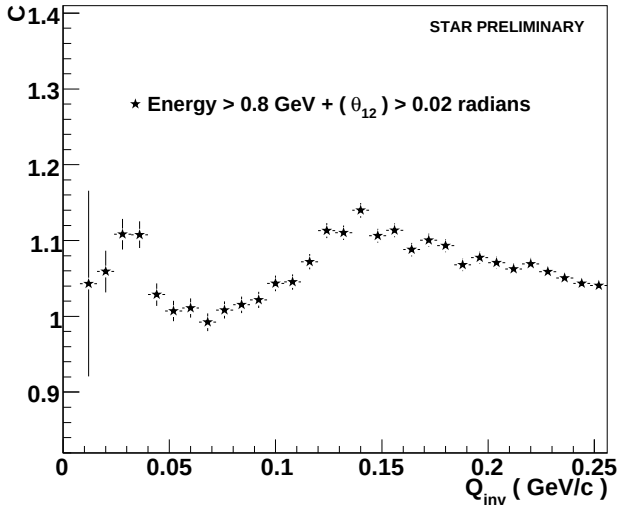

Figure 5.9: Correlation function of photons with energy cut of 0.8 GeV. All photon clusters from the same tower are rejected along with opening angle (θ_{12}) > 0.02 radians.

5.5 Comparisons with charged particles

The correlation function of charged pions analysed for 2 million minimum-bias events of Au+Au collisions at $\sqrt{s_{\rm NN}} = 62.4$ GeV is shown in Figure (5.11). The two-pion correlation distribution as a function of Q_{inv} is also fitted with same Gaussian parametrization described in Eq. (5.7). In Figure (5.10) for photons we have chosen the low Q_{inv} fit region excluding the π_0 peak clearly visible at $Q_{inv} = mass_{\pi_0}$. However the fitted $C(Q_{inv})$ for charged pions have no such resonance peak effects and hence fitted for large Q_{inv} which is presented in Figure (5.11).

The invariant radius of photon source ($R_{inv} = 6.80 \pm 0.82$ fm) reveal comparable results (in *Fermi* units) with the correlation radii ($R_{inv} = 5.45 \pm 0.01$ fm) extracted for charged pions as shown by the fit results in Figure (5.10) and Figure (5.11). The details of charged pion correlations for Au+Au and Cu+Cu

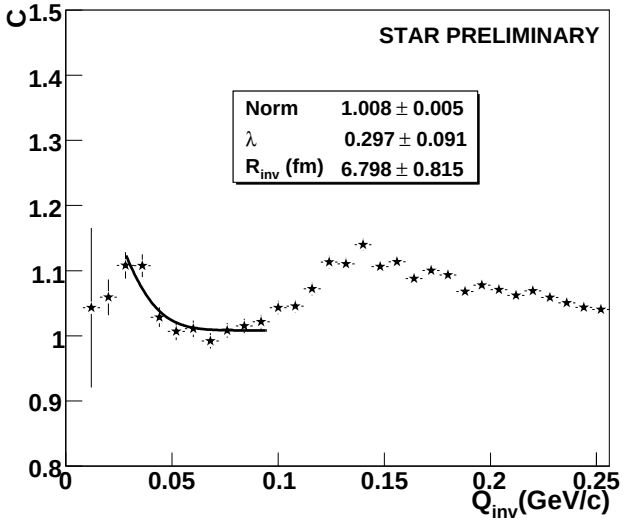

Figure 5.10: Correlation function of photons fitted with Eq. (5.7) for minimum-bias Au+Au collisions at $\sqrt{s_{\rm NN}} = 62.4$ GeV.

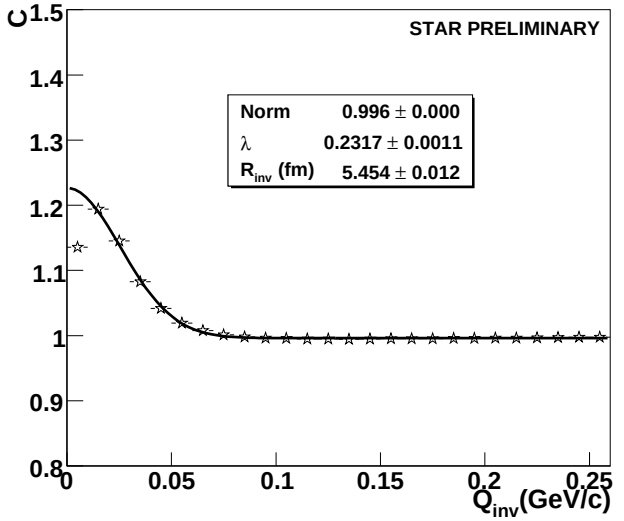

Figure 5.11: Correlation function of charged pions fitted with Eq. (5.7) for minimum-bias Au+Au collisions at $\sqrt{s_{\rm NN}} = 62.4$ GeV.

datasets at different RHIC energies are described next in Chapter 6.

Chapter 6

Hadron Correlations

Numerous experimental observables have been proposed as signatures of QGP creation in heavy-ion collisions which we have summarized in Section 1.3.6. One of the predictions is based on the expectation that large number of degrees of freedom associated with deconfined state, manifests itself in an increased entropy of the system which should survive subsequent hadronization and freeze-out. This is expected to lead to an increased dimension and duration of particle emission, thus manifesting as one of the significant probes for QGP phase transition.

The information about the space-time structure of the emitting source can be extracted by the method of intensity interferometry techniques [51] popularly known as Hanbury-Brown Twiss (HBT) correlations [53], which we have discussed in detail in Chapter 4. The primary goal of such correlations mostly performed at mid-rapidity and low transverse momentum, with pions (the most abundantly produced hadron) is to study the space-time sizes of the emitting source and freeze-out processes of the dynamically evolving collision fireball. The HBT measurements have been successfully studied in most of the heavy-ion experiments (see [123] for a recent review).

The systematic analyses of two-pion interferometry in Au+Au collisions at

$\sqrt{s_{\rm NN}}$ = 62.4 GeV and Cu+Cu collisions at $\sqrt{s_{\rm NN}}$ = 62.4 and 200 GeV using STAR Time Projection Chamber (TPC) are discussed in this Chapter. We have discussed both the one dimensional invariant relative momentum distributions and three-dimensional decompositions using Bertsch-Pratt formalism.

6.1 Identical Hadron Correlation Function

Experimentally the two-particle correlation function is constructed as,

$$C(\overrightarrow{q},\overrightarrow{K}) = \frac{A(\overrightarrow{q},\overrightarrow{K})}{B(\overrightarrow{q},\overrightarrow{K})} \quad , \tag{6.1}$$

where A($\overrightarrow{q},\overrightarrow{K}$) is the pair distribution for particles with relative momentum $\overrightarrow{q} = \overrightarrow{p_1} - \overrightarrow{p_2}$ and average momentum $\overrightarrow{K} = (\overrightarrow{p_1} + \overrightarrow{p_2})/2$ from the same event (called "real" or "true" pairs), and B($\overrightarrow{q},\overrightarrow{K}$) is the corresponding distribution for pairs of particles taken from different events [121, 129] (called "background" or "mixed" pairs). The correlation function is normalized to unity at large $\overrightarrow{q}$.

The comparative invariant source radii (R_{inv}) for photons and charged particles are discussed in Section 5.5 (of previous Chapter 5). Fitting the one dimensional correlation functions (constructed in invariant relative momenta) with the same Gaussian parametrization described in Eq. (5.7), the invariant pion source sizes for Au+Au and Cu+Cu collisions at $\sqrt{s_{\rm NN}}$ = 62.4 GeV and 200 GeV are described later in Section 6.6.

Previous pion HBT measurements at RHIC in Au+Au collisions at $\sqrt{s_{\rm NN}}$ = 130 GeV [194, 195] and 200 GeV [153, 196] show the extracted source size to be qualitatively similar. However detailed comparisons with smaller colliding systems and energies is required to understand the dynamical information of the source during freeze-out. The crucial information provided from such Bose-Einstein correlation studies with pions help to improve our understanding

of the reaction mechanisms and to constrain theoretical models of heavy ion collisions [52, 122, 125, 126, 127, 128, 130, 146].

6.2 Experimental Setup and Trigger details

The STAR detector described in Section 2.2 is a solenoidal detector which has large acceptance and is azimuthally symmetric. The detector subsystems relevant for the present analysis are a large TPC explained in detail in Section 3.3 along with the trigger detectors like the two Zero-Degree Calorimeters (ZDCs), a central trigger barrel (CTB) and two Beam-Beam Counters (BBCs). The latter three subsystems were used for online triggering only and we have summarized the details about the STAR Trigger in Section 2.2.3.

In this analysis for Au+Au and Cu+Cu collisions the minimum bias trigger settings using ZDC and BBCs were used. A threshold cut of CTB multiplicity greater than 15 is used for 62.4 GeV Au+Au dataset only.

6.3 Event and Centrality Selection

For this analysis we selected events with a collision vertex within $\pm$ 30 cm measured along the beam axis from the center of the Time Projection Chamber(TPC). This event selection was applied to all the data sets discussed here.

The events are binned according to the collision centrality, where the centrality was characterized according to the measured multiplicity of charged hadrons from the TPC, within the pseudo-rapidity ($|\eta|$ <0.5). The centrality selection for 62.4 GeV Au+Au collisions is presented in Figure (6.1) (where the lines marking the charged hadron multiplicity value in % cross-section) show the centrality classes taken for the analysis. The 6 centrality bins for Au+Au collisions at $\sqrt{s_{\rm NN}} = 62.4$

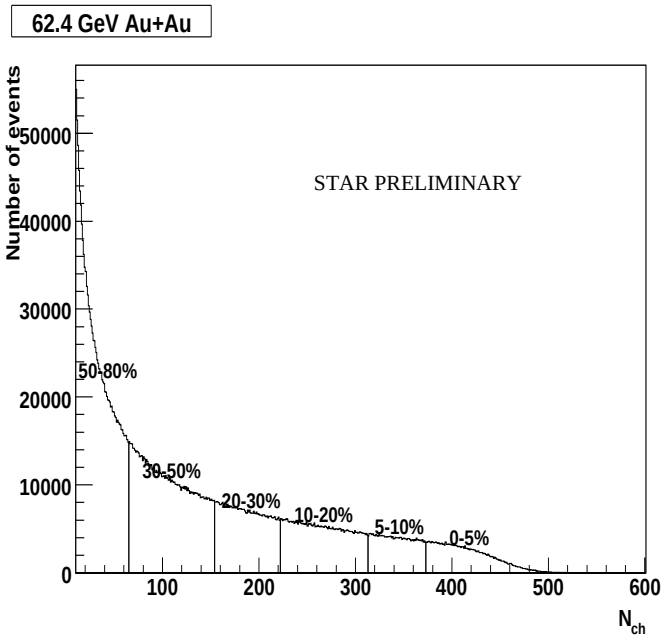

Figure 6.1: The multiplicity distributions of charged hadrons from the TPC within the pseudo-rapidity $|\eta|$ <0.5, for Au+Au collisions at $\sqrt{s_{\rm NN}}$ = 62.4 GeV.

GeV used for the analysis correspond to 0-5%, 5-10%, 10-20%, 20-30%, 30-50%, 50-80% of the total hadronic cross-section. In Table 6.1, we give the centrality bins for Au+Au at $\sqrt{s_{\rm NN}}$ = 62.4 GeV along with the multiplicity bin, average number of participating nucleons and average number of binary collisions. The number of participating nucleons and the number of binary collisions have been obtained from Glauber calculations [197]. A dataset of 2 million events was used for this analysis.

Figure (6.2) show the centrality selection (where the lines mark the charged hadron multiplicity value in % cross-section) for Cu+Cu collisions at $\sqrt{s_{\rm NN}}$ = 62.4 GeV. Table 6.2 represent the 6 centrality bins for Cu+Cu collisions at $\sqrt{s_{\rm NN}}$ = 62.4 GeV corresponding to 0-10%, 10-20%, 20-30%, 30-40%, 40-50%, 50-60% of the total hadronic cross-section. In Table 6.2 along with the multiplicity bin the

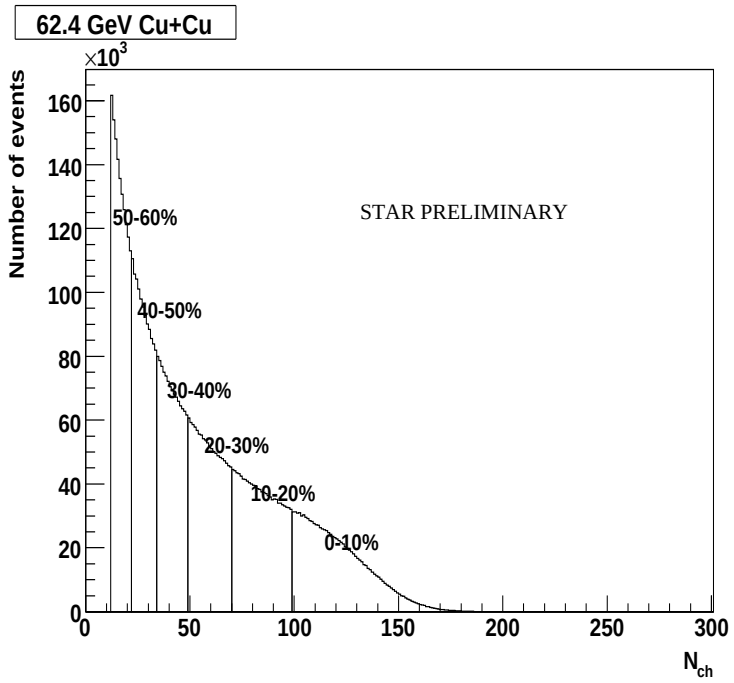

Figure 6.2: The multiplicity distributions of charged hadrons from the TPC within the pseudo-rapidity $|\eta|$ <0.5, for Cu+Cu collisions at $\sqrt{s_{\rm NN}}$ = 62.4 GeV.

average number of participating nucleons and average number of binary collisions obtained from Glauber calculations [197] are also presented. The number events taken were 9.0 million.

Figure (6.3) show the centrality selection (where the lines mark the charged hadron multiplicity value in % cross-section) for Cu+Cu collisions at $\sqrt{s_{\rm NN}}$ = 200 GeV respectively. Table 6.3 represent the 6 centrality bins for Cu+Cu collisions at $\sqrt{s_{\rm NN}}$ = 200 GeV corresponding to 0-10%, 10-20%, 20-30%, 30-40%, 40-50%, 50-60% of the total hadronic cross-section. In Table 6.3 along with the multiplicity bin the average number of participating nucleons and average number of binary collisions obtained from Glauber calculations [197] are also presented. The number events taken were 4.2 million.

Table 6.1: Centrality Selection, number of participating nucleons and number of binary collisions for Au+Au at $\sqrt{s_{\rm NN}} = 62.4$ GeV

% cross-section	N_{ch}^{TPC}	$< N_{part} >$	$< N_{coll} >$
0-5	>373	$347.3^{+4.3}_{-3.7}$	$904^{+67.7}_{-62.4}$
5-10	373-313	$293.3^{+7.3}_{-5.6}$	$713.7^{+63.7}_{-54.8}$
10-20	312-222	$229.0^{+9.2}_{-7.7}$	$511.8^{+54.9}_{-48.2}$
20-30	221-154	$162.0^{+10.0}_{-9.5}$	$320.9^{+43.0}_{-39.2}$
30-40	153-102	$112.0^{+9.6}_{-9.1}$	$193.5^{+30.4}_{-31.4}$
40-50	101-65	$74.2^{+9.0}_{-8.5}$	$109.3^{+22.1}_{-21.8}$
50-60	64-38	$45.8^{+7.0}_{-7.1}$	$56.6^{+15.0}_{-14.3}$
60-70	37-20	$25.9^{+5.6}_{-5.6}$	$26.8^{+8.8}_{-9.0}$
70-80	19-9	$13.0^{+3.4}_{-4.6}$	$11.2^{+3.7}_{-4.8}$

Table 6.2: Centrality Selection, number of participating nucleons and number of binary collisions for Cu+Cu at $\sqrt{s_{\rm NN}} = 62.4$ GeV

% cross-section	N_{ch}^{TPC}	$< N_{part} >$	$< N_{coll} >$
0-10	>99	$95.59^{+1.06}_{-1.06}$	$160.64^{+5.45}_{-5.39}$
10-20	99-70	$72.06^{+2.50}_{-2.17}$	$109.82^{+6.31}_{-6.14}$
20-30	69-49	$52.27^{+3.06}_{-2.79}$	$71.42^{+6.19}_{-6.08}$
30-40	48-34	$37.04^{+2.89}_{-3.17}$	$45.24^{+5.23}_{-4.81}$
40-50	33-22	$25.43^{+2.02}_{-2.68}$	$27.71^{+3.15}_{-3.75}$
50-60	21-12	$16.92^{+2.09}_{-2.96}$	$16.50^{+2.68}_{-3.25}$

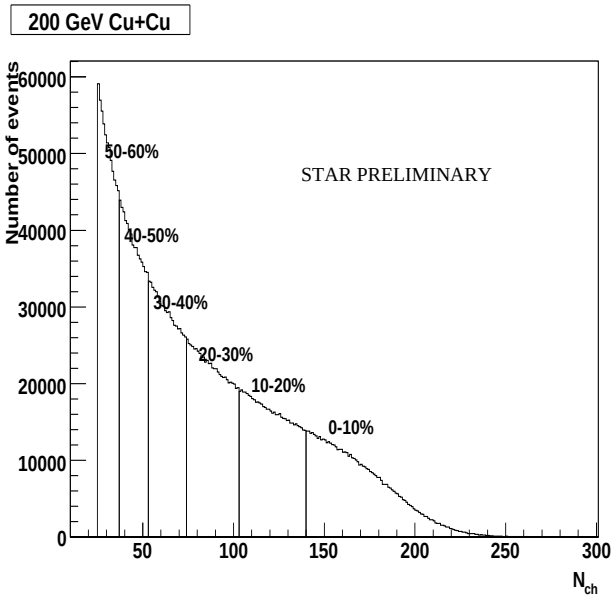

Figure 6.3: The multiplicity distributions of charged hadrons from the TPC within the pseudo-rapidity $|\eta|$ <0.5, for Cu+Cu collisions at $\sqrt{s_{\rm NN}}$ = 200 GeV.

Table 6.3: Centrality Selection, number of participating nucleons and number of binary collisions for Cu+Cu at $\sqrt{s_{\rm NN}}$ = 200 GeV

% cross-section	N_{ch}^{TPC}	$< N_{part} >$	$< N_{coll} >$
0-10	>138	$98.34^{+1.13}_{-1.13}$	$185.64^{+6.12}_{-5.63}$
10-20	138-98	$74.47^{+2.14}_{-2.46}$	$125.92^{+6.80}_{-6.65}$
20-30	97-69	$54.10^{+2.59}_{-2.86}$	$80.95^{+5.82}_{-6.99}$
30-40	68-47	$38.56^{+2.47}_{-2.78}$	$51.07^{+4.77}_{-5.60}$
40-50	46-30	$26.29^{+3.00}_{-2.34}$	$30.61^{+3.87}_{-3.96}$
50-60	29-17	$17.61^{+2.64}_{-3.10}$	$18.16^{+3.54}_{-3.48}$

6.4 Particle Selection

We have selected tracks in the rapidity region $|y| < 0.5$. The particle identification was done by correlating the specific ionization of particles in the TPC gas with their measured momenta. For this analysis pions are selected by requiring the specific ionization to be within 2 standard deviations from their theoretical Bethe-Bloch value. For the removal of kaons and protons which could satisfy this condition, particles were also required to be further than 2 standard deviations from the Bethe-Bloch value for kaons and protons.

For the removal of non-primary (decay) pions we applied a cut of 3 cm to each track on the distance of closest approach (DCA) of the extrapolated track to the primary vertex. Charged particle tracks reconstructed on the TPC used for this analysis were accepted, if they satisfied the requirements to have hits on at least 15 pad rows, as the shorter tracks maybe from other broken track fragments.

6.5 Pair Cuts

The two track reconstruction defects which can affect HBT analysis are merging and splitting: (1) where in splitting of tracks we have one single particle reconstructed as two tracks and (2) for merging of tracks two particles with similar momenta reconstructed as one track. The splitting and merging of tracks needs to be understood and studied at pair level.

6.5.1 Track splitting

The track splitting causes an enhancement of pairs in the low relative momentum and to address this problem we have a assigned pair parameter called the Splitting Level (SL), defined in Ref [153] as:

$$\mathrm{SL} \equiv \frac{\sum_i S_i}{\mathrm{Nhits}_1 + \mathrm{Nhits}_2} \quad \text{where} \quad \mathrm{S}_i = \tag{6.2}$$

$$\begin{cases} +1 & \text{one track leaves a hit on pad-row} \\ -1 & \text{both tracks leave a hit on pad-row} \\ 0 & \text{neither track leaves a hit on pad-row,} \end{cases}$$

where i is the pad-row number, and Nhits_1 and Nhits_2 are the total number of hits associated to each track in the pair.

As explained in Eq. (6.2), if only one track has a solitary hit in a pad-row +1 is added to the running quantity, whereas, if both tracks have a hit in the same pad-row, a sign of separate tracks, -1 is added to this quantity. After the sum is done, it is divided by the sum of hits in both tracks, this normalizes SL to a value between -0.5 (where both the tracks have hits in exactly same pad-rows) and 1.0 (where tracks do not have any hit in same pad-row).

The 2-dimensional plots of Q_{inv} *vs* average track separation at entrance is presented in Figure (6.4) for "real" pairs in Cu+Cu collisions at $\sqrt{s_{\mathrm{NN}}} = 200$ GeV. The top panel of Figure (6.4) shows without any SL applied for pairs with $Q_{inv} <$ 100 MeV/c and the bottom panel with SL chosen from -0.5 to 0.6 which clearly show the removal of split tracks.

However the value of SL is required to be smaller than a certain value which can be estimated from the study of the one-dimensional correlation distributions as a function of Q_{inv} for different values of SL, presented in Figure (6.5). Figure (6.5) shows that with the increase of the allowed value of SL the correlation function becomes stable till we reach SL = 0.6. Since the correlation function does not change for lower values of SL, the pairs used for the correlation functions are required to have SL < 0.6. We have already studied the effects of SL cut on "real" pairs in Figure (6.4) where we observe that such a cut also removes some real pairs.

So SL cut is applied throughout the currently used Au+Au and Cu+Cu datasets, on both "real" and "mixed" pairs as defined by the numerator and denominator of the correlation function in Eq. (6.1).

6.5.2 Track merging

Merging is caused at low momentum and the particles with similar momentum have higher merging probability. To understand the merging effect we have studied the Q_{inv} "correlation functions" for charged pions as a function of the Fraction Of Merged Hits (FMH). Two hits are considered to be merged if the probability to separate them is less than 99% according to the two-track resolution in the TPC. When we apply this cut to the "real" and "mixed" pairs we introduce in the denominator the effect of reduction of low "momentum" pairs which occurs in the numerator. Figure (6.6) show the one-dimensional correlation functions as a function of Q_{inv}, for different values of Fraction Of Merged Hits (FMH) allowed. Applying the condition that the fraction of merged hits to be less than 10% for every pair entering the correlation function throughout the currently used Au+Au and Cu+Cu datasets, the track merging was found to be optimally reduced. But the introduction of these cuts also affect the fits to the source parameters described in Section 6.6.3.1.

In the present analysis with Au+Au collisions at $\sqrt{s_{\rm NN}} = 62.4$ GeV and Cu+Cu collisions at $\sqrt{s_{\rm NN}} = 62.4$ and 200 GeV, we have studied and verified the cut parameter values used to remove splitting and merging for Au+Au collisions at $\sqrt{s_{\rm NN}} = 200$ GeV [153]. Since the detector setup is identical, the splitting and merging cuts used are similar to the previous STAR analysis.

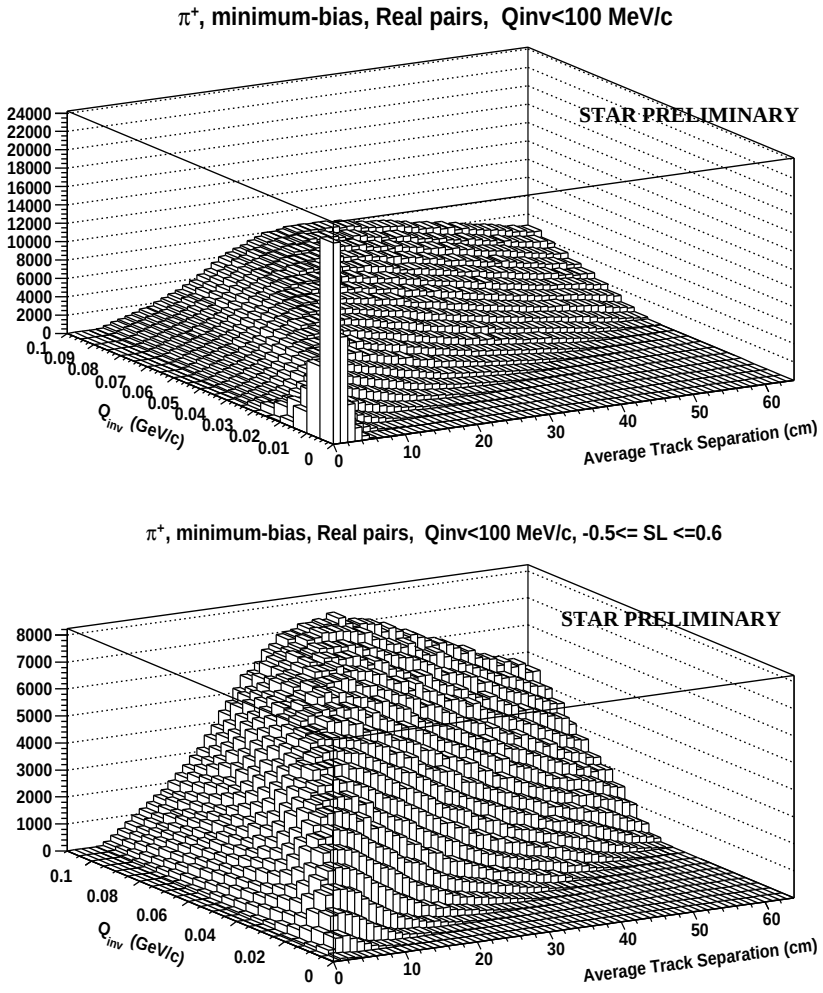

Figure 6.4: The 2-dimensional plots for real pairs with $Q_{inv} < 100$ MeV/c with average track separation at entrance for Cu+Cu collisions at $\sqrt{s_{\rm NN}} = 200$ GeV. The top panel shows without SL cuts and the bottom panel with SL cuts from -0.5 to 0.6, clearly showing the split tracks removed.

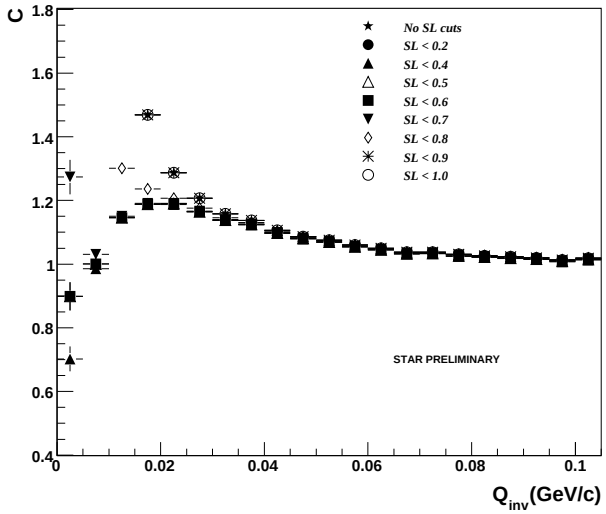

Figure 6.5: The 1-dimensional Q_{inv} distribution plots (for Cu+Cu collisions at $\sqrt{s_{\rm NN}} = 200$ GeV) with varied SL (anti-splitting cut). From this plot the selected cut is SL < 0.6.

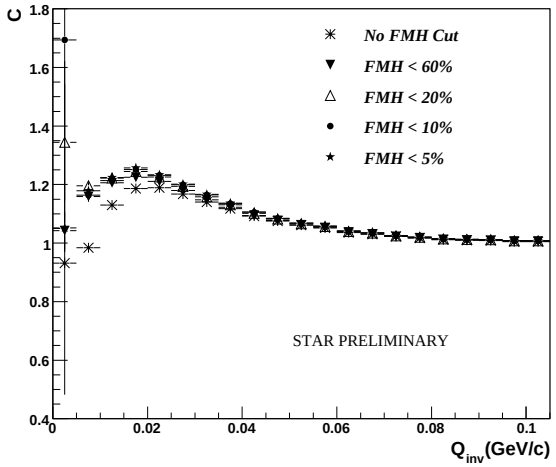

Figure 6.6: The 1-dimensional Q_{inv} distribution plots with different values of the maximum fraction of merged hits for Cu+Cu collisions at $\sqrt{s_{\rm NN}} = 200$ GeV. The applied cut is FMH $< 10\%$.

6.5.3 k_T cuts

No p_T cut was applied to single tracks but the pairs were required to have an average transverse momentum ($k_T = (|\overrightarrow{p_{1T}} + \overrightarrow{p_{2T}}|)/2$) in 4 bins that correspond to [150,250] MeV/c, [250,350] MeV/c, [350,450] MeV/c and [450,600] MeV/c. The results are presented and discussed as a function of average k_T (or $m_T = \sqrt{k_T^2 + m_\pi^2}$) in each of those bins.

6.6 The Analysis Method

6.6.1 Construction of the Correlation Function

The two particle correlation function is constructed based on Eq. (6.1) with the measured distribution in numerator from pairs of the same event whereas the denominator is obtained from mixed events. The background pairs [121] are constructed from the mixed events, where each particle in a given event is mixed with all particles for a collection of ten similar events. The similar events were taken within each centrality bin and further enforced to possess a relative z position of primary vertex within 10 cm.

Figure (6.7) shows the one-dimensional two-pion correlation distribution as a function of Q_{inv} and the corresponding fits (described in Eq.(5.7), to the minimum-bias datasets for Au+Au and Cu+Cu collisions at $\sqrt{s_{\rm NN}}$ = 62.4 GeV and 200 GeV. The correlation functions are calculated for the corresponding k_T bin of [150 - 600] MeV/c. The extracted invariant radii from Gaussian parametrization for the different datasets, ($R_{inv} \approx 6.45 \pm 0.60$ fm for Au+Au collisions at $\sqrt{s_{\rm NN}}$ = 200 GeV; $R_{inv} \approx 4.12 \pm 0.01$ fm for Cu+Cu collisions at $\sqrt{s_{\rm NN}}$ = 200 GeV; $R_{inv} \approx 5.45 \pm 0.01$ fm for Au+Au collisions at $\sqrt{s_{\rm NN}}$ = 62.4 GeV; $R_{inv} \approx 3.98 \pm 0.01$ fm for Cu+Cu collisions at $\sqrt{s_{\rm NN}}$ = 62.4 GeV) provide us with a rough

estimate of the space-time extent of the source. However with the availability of high statistics data and development of new techniques, it has become possible to have a three-dimensional decomposition [44, 124, 147] of $\overrightarrow{q}$, providing better insights to the collision geometry. The details of such decomposition are discussed in Section 4.4.2 (of Chapter 4) and will be done later in next Section 6.6.2.

6.6.2 Bertsch-Pratt Parametrizations and Coulomb interactions

As introduced and explained in [145], the observer sees the "region of homogeneity" from where the particle pairs of momentum $\overrightarrow{K}$ are likely to be emitted. The direction of $\overrightarrow{K}$ corresponds to the direction from which the collision region is viewed [52, 129, 141, 146].

A detailed characterization of the emitting source can be possible by decomposing the relative momentum $\overrightarrow{q}$ according to the Bertsch-Pratt (or "out-side-long") convention [44, 124, 147]. The relative momenta $\overrightarrow{q}$ are decomposed into the variables q_{long}, along the beam direction, q_{out}, parallel to the transverse momentum of the pair $\overrightarrow{k_T} = (\overrightarrow{p_{1T}} + \overrightarrow{p_{2T}})/2$, and q_{side}, perpendicular to q_{long} and q_{out}. The details of Bertsch-Pratt Parametrizations are explained in Section 4.4.2 (of Chapter 4).

We have discussed only the effect of symmetrization on correlations of two identical particles. But the correlations can also arise from two-particle final state interactions even if the symmetry-based correlations are absent [131, 132]. For pions the effects of strong interactions are negligible but the long range Coulomb repulsion effects cause a suppression of the measured correlation function at small $\overrightarrow{q}$ (discussed in Section 4.3, of Chapter 4). Different procedures have been suggested to take into account the Coulomb effects, namely the so called standard [194], dilution [198] and Bowler-Sinyukov [133, 135, 153, 199]. In the presented analyses,

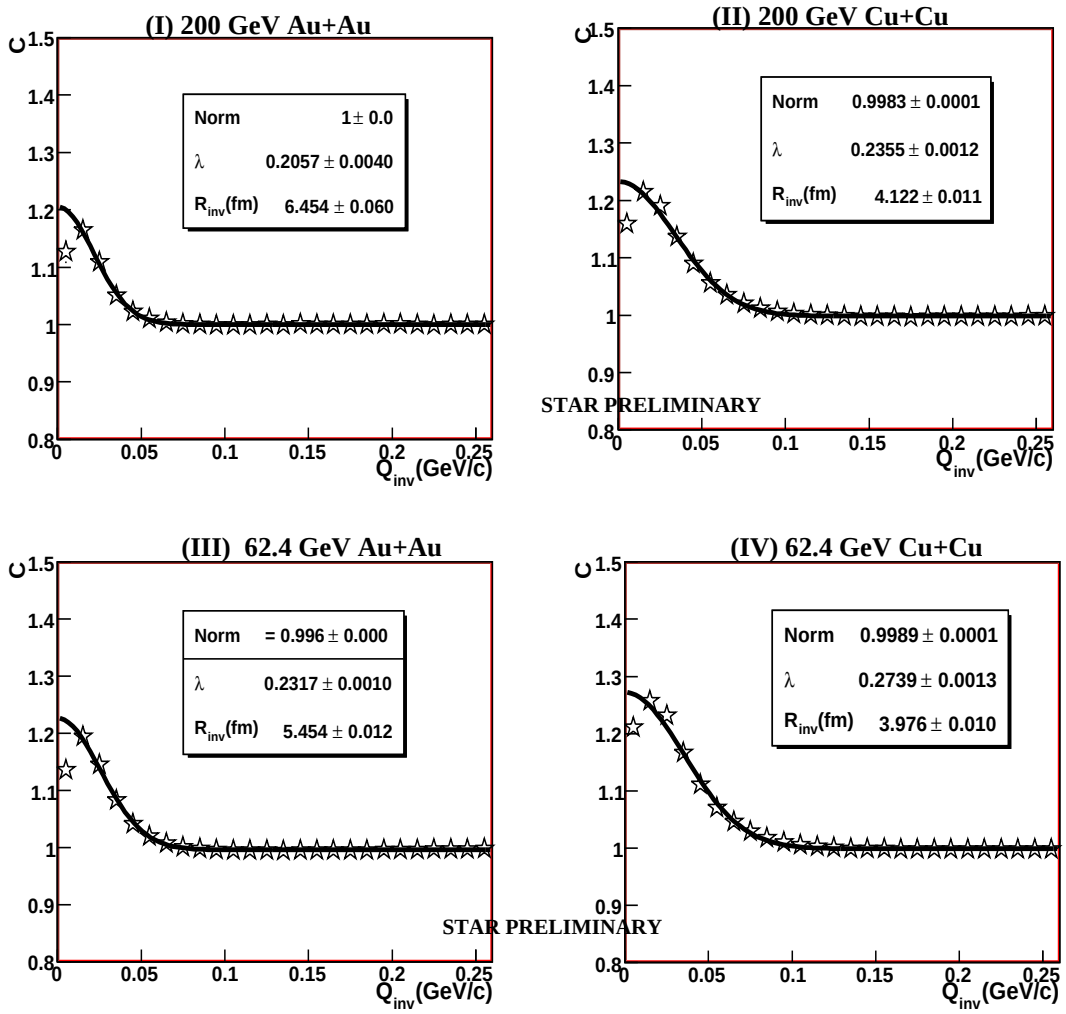

Figure 6.7: 1-dimensional distribution as a function of Q_{inv} for charged pions fitted with Eq. (5.5), in Au+Au and Cu+Cu collisions at $\sqrt{s_{\rm NN}} = 62.4$ GeV and 200 GeV.

we have followed the procedure described for our previous analysis at $\sqrt{s_{\rm NN}} = 200$ GeV [153].

For an azimuthally integrated analysis, at mid-rapidity in the longitudinal co-moving system (LCMS) frame the correlation function in Eq. (6.1) can be decomposed with the Bertsch-Pratt parametrization [123, 147] and using the Bowler-Sinyukov procedure is fitted to :

$$C(q_{out}, q_{side}, q_{long}) = (1 - \lambda) + \lambda K_{coul}(Q_{inv})(1 + e^{(-q_{out}^2 R_{out}^2 - q_{side}^2 R_{side}^2 - q_{long}^2 R_{long}^2)}) \tag{6.3}$$

normalized to unity for large $\overrightarrow{q}$, and K_{coul} is the squared Coulomb wave-function integrated over the full source. We have considered a spherical Gaussian source of 5 fm radius for Au+Au collisions at $\sqrt{s_{\rm NN}} = 62.4$ GeV, whereas a 3 fm radius is used for Cu+Cu collisions at $\sqrt{s_{\rm NN}} = 62.4$ and 200 GeV in the present analysis. The first term $(1 - \lambda)$ of Eq.(6.3) is for those pairs which do not interact and the second term for those pairs where both (Bose-Einstein and Coulomb) interactions are present [153].

The underlying assumption of HBT is that pions are produced from a completely chaotic source or in other words a source in which the hadronized pions have random production phases. The λ parameter is called the incoherence or chaoticity parameter which depends on k_T. The correlation function interpolates between the case of a coherent source $\lambda = 0$ and the case of a completely chaotic source with $\lambda = 1$. The observational measurements of $\lambda \neq 1$ are mainly attributed to long-lived resonances along with the particle mis-identification which can cause reduction in λ [123, 153]. Besides that Coulomb corrections for final-state interactions (FSI) also influences the values of λ [52]. A better understanding of the source chaoticity or particle contamination which affects the value of λ can be

effectively estimated by three-particle correlations [200].

6.6.3 Associated systematics

The associated changes in the fitted HBT source parameters with the application of FMH cut, Coulomb approximations and purity corrections are essential for the understanding of systematic uncertainties.

6.6.3.1 With Pair Cuts

The maximum Fraction Of Merged Hits (FMH) cut is explained in Section 6.5. We observe from the Figure (6.6), that the nature of the correlation functions are very close for FMH $< 20\%$ and FMH $< 10\%$. Study of the systematic changes observed in the HBT radii with FMH values are hence required, since such a cut differentiates against low momentum pairs, thus affecting the correlation signal. Here we have considered three conditions of FMH less than 5%, 10% and 20%.

The mean of the fitted source parameter (*i.e* the corresponding out, side and long radii) considering the applied conditions of FMH is calculated as,

$$R_{i\,=\,o,s,l_{[Mean]}} = \frac{(R_{i\,=\,o,s,l_{(FMH\,<\,5\%)}} + R_{i\,=\,o,s,l_{(FMH\,<\,10\%)}} + R_{i\,=\,o,s,l_{(FMH\,<\,20\%)}})}{3}\,. \tag{6.4}$$

The systematic error (δR_{sys}) is estimated as the deviation (in %) from such above defined mean as,

$$\delta R_{sys} = \frac{(|R_{i=o,s,l} - R_{i\,=\,o,s,l_{[Mean]}}|)}{R_{i\,=\,o,s,l_{[Mean]}}} \tag{6.5}$$

which is calculated in all centrality and k_T bins.

The fitted R_{out}, R_{side} and R_{long} HBT radii parameters as a function of applied conditions of FMH ($< 5\%$, 10% and 20%) for all centralities and k_T bins (which

correspond to [150,250] MeV/c, [250,350] MeV/c, [350,450] MeV/c and [450,600] MeV/c) in Cu+Cu collisions at $\sqrt{s_{\rm NN}}$ = 200 GeV are presented in Figures (6.8), (6.9) and (6.10) respectively. The maximum deviations in δR_{sys} (calculated using Eq. (6.5)) are estimated to be 7% for R_{out}, 9% for R_{side} and 7% for R_{long}. The estimated systematic errors due to FMH cuts calculated according to this method are less than 10% in all centralities and k_T bins for the presented datasets.

6.6.3.2 With Coulomb approximations

The study of the fitted source parameters with different sets of Coulomb approximations is done for Eq.(6.3). Such studies will show the systematic uncertainties introduced by such approximations. So K_{coul}, the squared Coulomb wave function integrated over the whole source, which in our cases are spherical Gaussian sources of radii (I) 3fm and (II) 2fm respectively. Such studies in Cu+Cu collisions at $\sqrt{s_{\rm NN}}$ = 62.4 GeV (the smallest radii among the presently analysed heavy ion dataset) show no difference within statistical errors as presented in Figures (6.11) and (6.12) for central (0-10%) and peripheral (50 - 60%) collisions respectively. Figure (6.13) shows that radii values of 2,3 and 4 fm studied for Cu+Cu collisions at $\sqrt{s_{\rm NN}}$ = 62.4 GeV also confirm no difference within statistical errors and can be concluded that the associated uncertainties are negligible with Coulomb approximations.

6.6.3.3 With Pion Pair Purity effects

We have stated "particle misidentification" as a possible source for the reduction of the λ parameter (discussed in Section 6.6.2). To understand and estimate the pion purity in the analysed dataset (assuming that the non-pure pions are completely uncorrelated) the correlation function is constructed as [201],

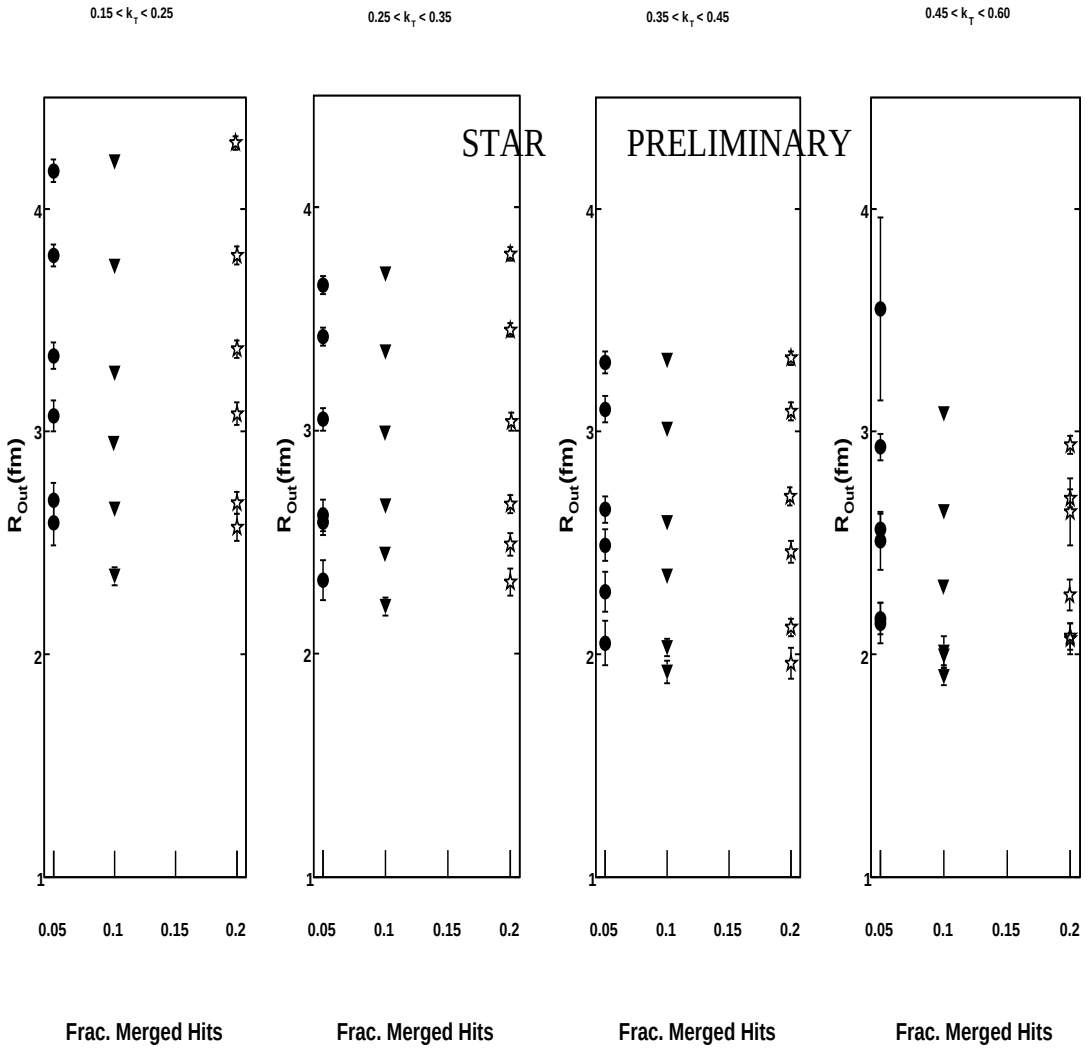

Figure 6.8: The fitted R_{out} parameters with FMH cuts less than 5%, 10% and 20% in Cu+Cu collisions at $\sqrt{s_{\rm NN}} = 200$ GeV.

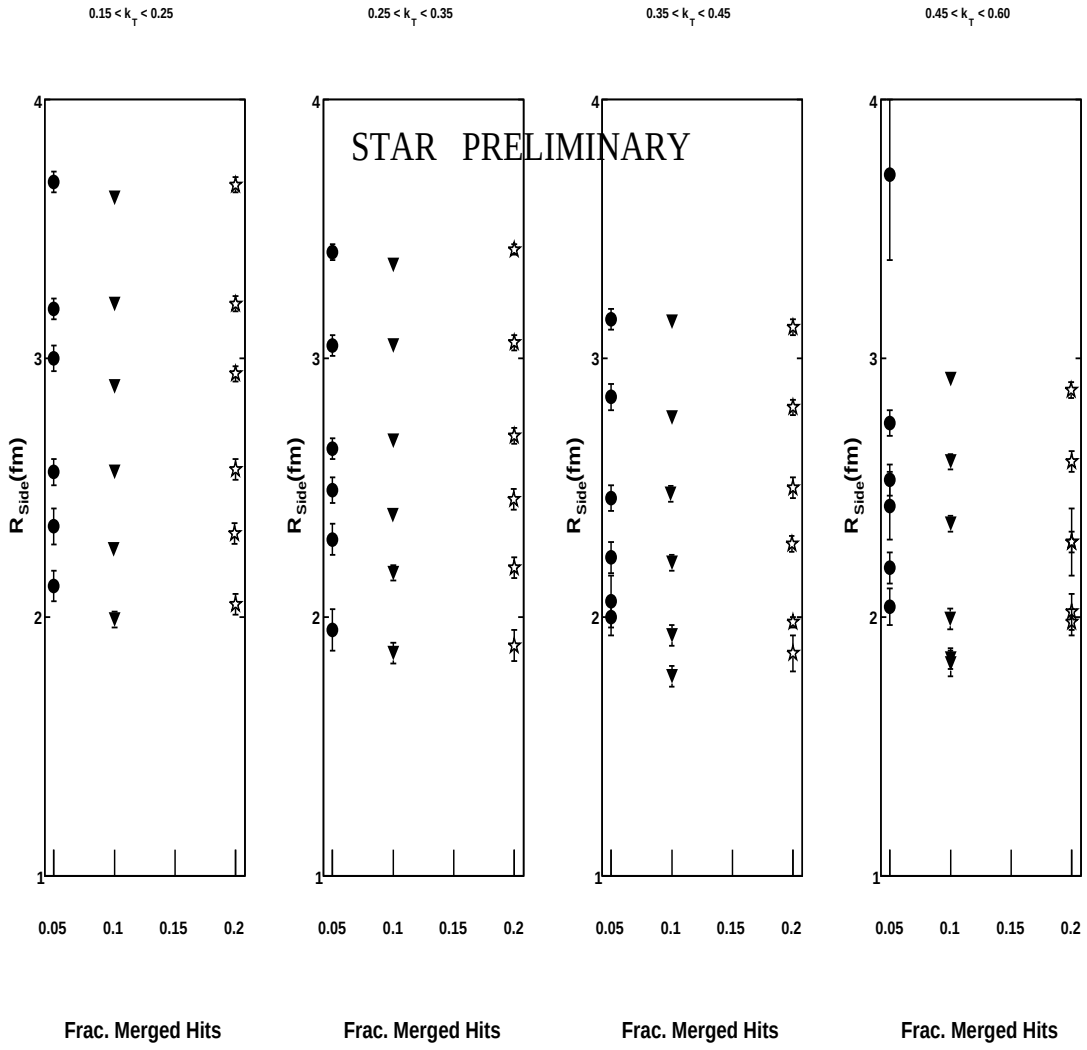

Figure 6.9: The fitted R_{side} parameters with FMH cuts less than 5%, 10% and 20% in Cu+Cu collisions at $\sqrt{s_{\rm NN}} = 200$ GeV.

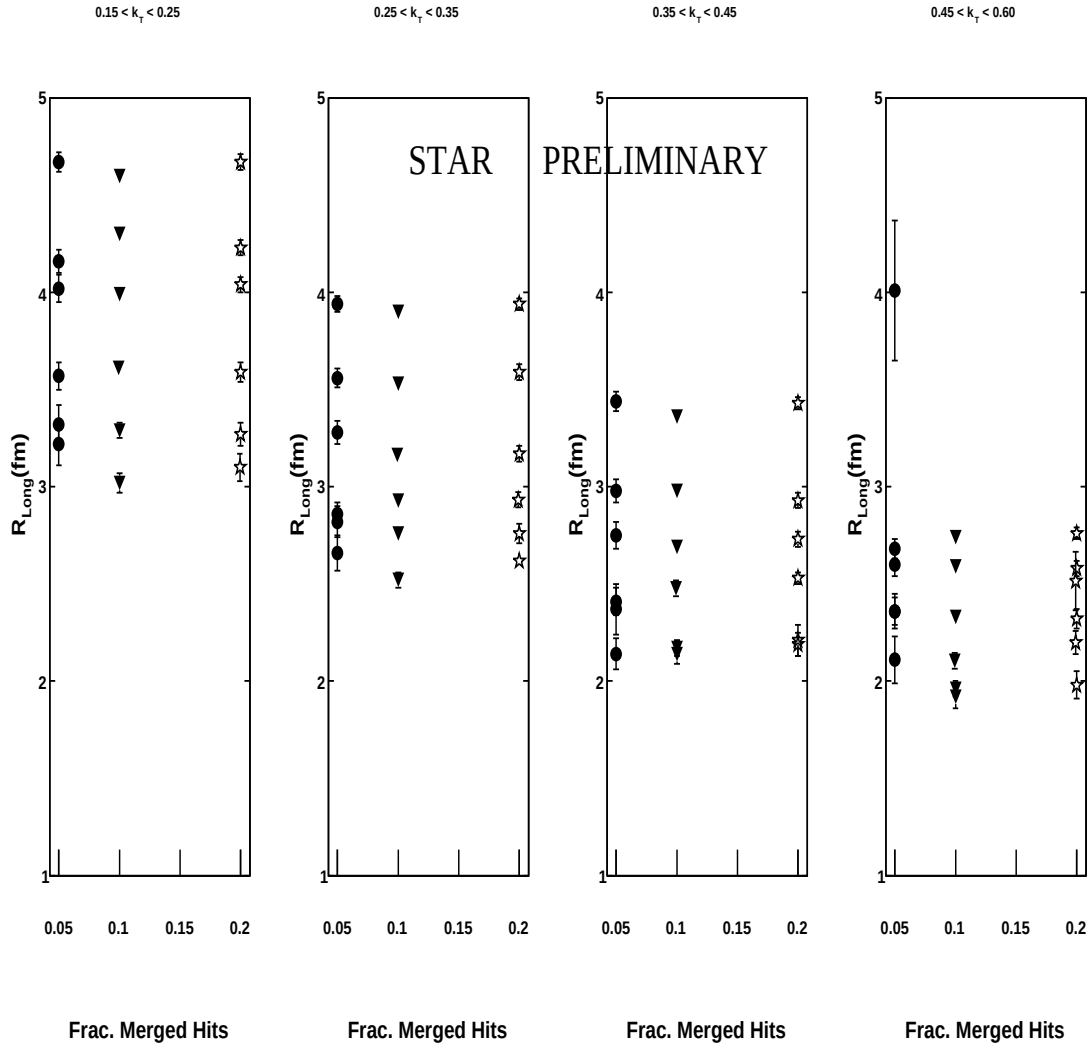

Figure 6.10: The fitted R_{long} parameters with FMH cuts less than 5%, 10% and 20% in Cu+Cu collisions at $\sqrt{s_{\rm NN}} = 200$ GeV.

$$C_{corrected} = \frac{C_{measured} - 1}{Purity(p)} + 1 \ . \tag{6.6}$$

The correlation function $C_{measured}$ can be further expressed as the ratio of numerator and denominator thus being identical to $C(\overrightarrow{q}, \overrightarrow{K})$ described in Eq. (6.1). The bin-by-bin correction is done using the known $C_{measured}$ distribution and average purity (p) in the bin to get the corrected correlation function ($C_{corrected}$) as explained in Eq. (6.6).

Comparative studies are done with and without purity corrections in Au+Au collisions at $\sqrt{s_{\rm NN}}$ = 200 GeV (where the same dataset is used as in STAR HBT analysis in Ref [153]). The Figures (6.14) and (6.15) however show that the purity correction pushes the λ parameter to higher values without affecting the HBT radii (R_{out}, R_{side} and R_{long}) which remain quite robust over centralities and k_T bins. So even though such purity corrections were not used in Ref [153], the present comparative studies with the same 200 GeV Au+Au dataset infer that the associated systematic errors are negligible.

6.7 Analysis Results for Pion Interferometry

6.7.1 Au+Au collisions at $\sqrt{s_{\rm NN}}$ = 62.4 GeV

The correlation function as described in Eq.(6.3) has been constructed for Au+Au collisions at $\sqrt{s_{\rm NN}}$ = 62.4 GeV for different centrality and m_T bins as defined earlier in Sections 6.3 and 6.5. The analysis is performed separately for $\pi^+\pi^+$ and $\pi^-\pi^-$ pairs. The final histograms for the like sign pairs are summed up in order to increase the statistics as they do not show appreciable differences. Figure (6.16) gives the results for R_{out}, R_{side}, R_{long}, λ and the ratio, R_{out}/R_{side}. The three HBT radii increase with increasing centrality, whereas the values of the λ parameter and

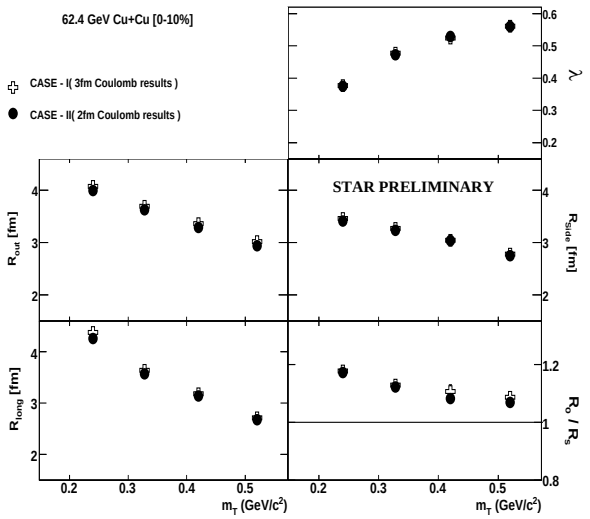

Figure 6.11: The comparative studies of source parameters with Coulomb approximations of 2fm and 3fm respectively for top centrality (0 - 10%) in Cu+Cu collisions at $\sqrt{s_{\rm NN}} = 62.4$ GeV show no difference within errors.

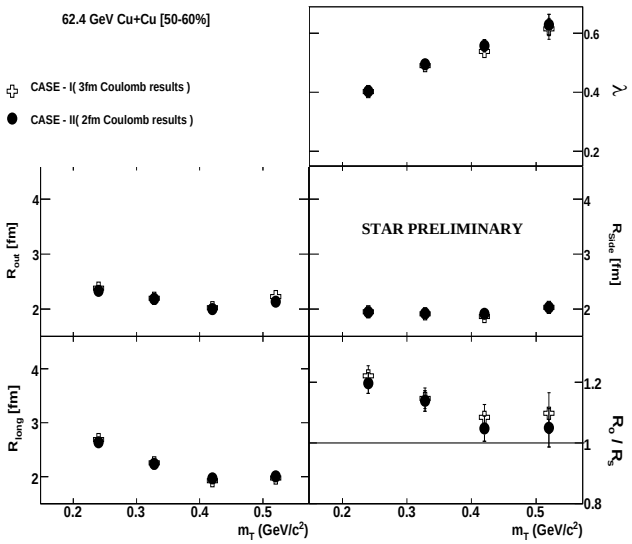

Figure 6.12: The comparative studies of source parameters with Coulomb approximations of 2fm and 3fm respectively for peripheral (50 - 60%) Cu+Cu collisions at $\sqrt{s_{\rm NN}} = 62.4$ GeV show no difference within errors.

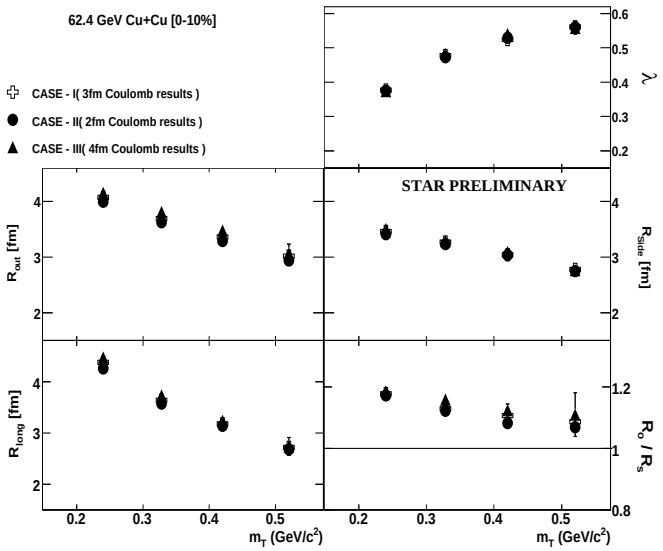

Figure 6.13: The comparative studies of source parameters with Coulomb approximations of 2,3 and 4 fm, for top centrality (0-10%) in Cu+Cu collisions at $\sqrt{s_{\rm NN}}$ = 62.4 GeV show no difference within errors.

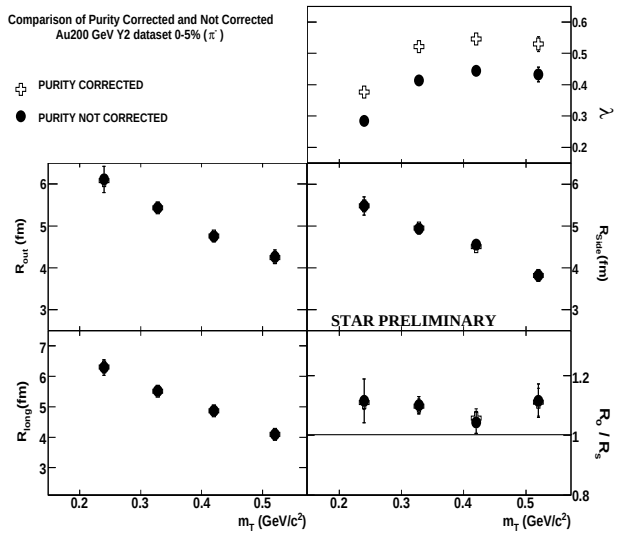

Figure 6.14: The effect of purity corrections on measured HBT parameters for 0-5% central Au+Au collisions at $\sqrt{s_{\rm NN}}$ = 200 GeV.

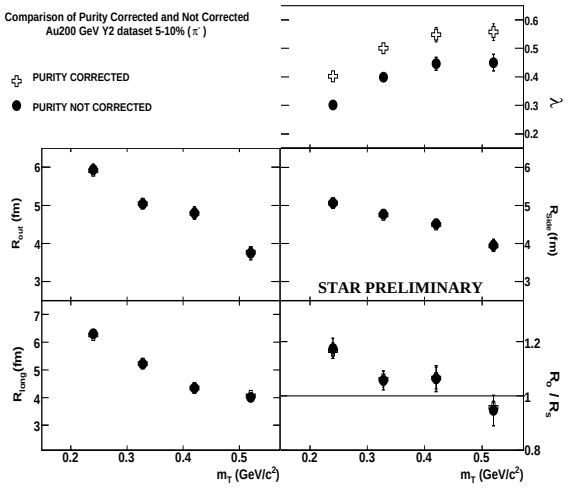

Figure 6.15: The effect of purity corrections on measured HBT parameters for 5-10% central Au+Au collisions at $\sqrt{s_{\rm NN}} = 200$ GeV.

R_{out}/R_{side} ratio exhibit no clear centrality dependence.

We observe that for all centralities, the three HBT radii decrease with the increase of the m_T bin, whereas the λ parameter increases with m_T bin. Such behaviour are consistent with the results obtained for Au+Au collisions at $\sqrt{s_{\rm NN}} =$ 200 GeV [153]. The increase of λ parameter with m_T is due to the decreasing contribution of pions produced from long-lived resonance decays at higher transverse momenta.

For comparison, in Figure (6.17), we show the results for Au+Au collisions at $\sqrt{s_{\rm NN}} = 62.4$ GeV and 200 GeV for the most central collisions. We observe that the R_{out} values are similar for both cases, but there is a difference in the values of R_{side} and R_{long}. The R_{out}/R_{side} ratio decreases with m_T, but the values are higher for $\sqrt{s_{\rm NN}} = 62.4$ GeV compared to the results for $\sqrt{s_{\rm NN}} = 200$ GeV.

The behaviour observed for the three HBT radii is qualitatively consistent with models with collective flow [202, 203, 204]. The collective expansion results

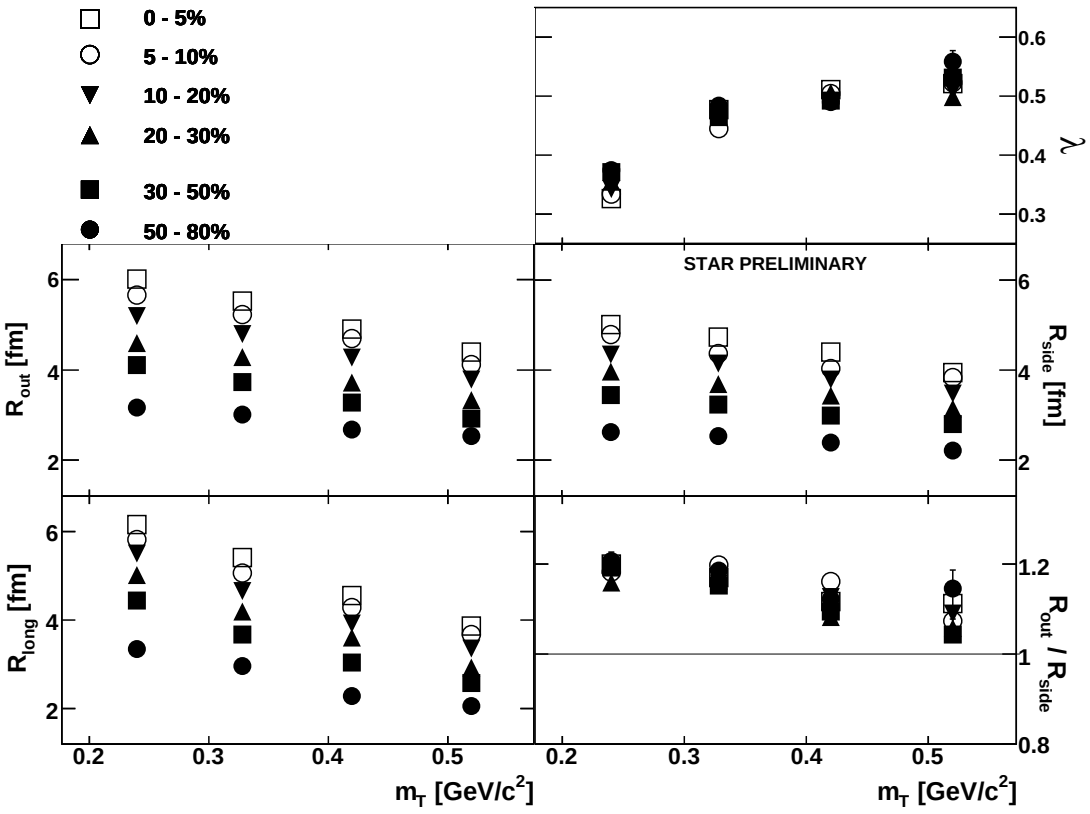

Figure 6.16: The HBT parameters *vs* m_T for 6 different centralities for Au+Au collisions at $\sqrt{s_{\rm NN}} = 62.4$ GeV. Only statistical errors are shown.

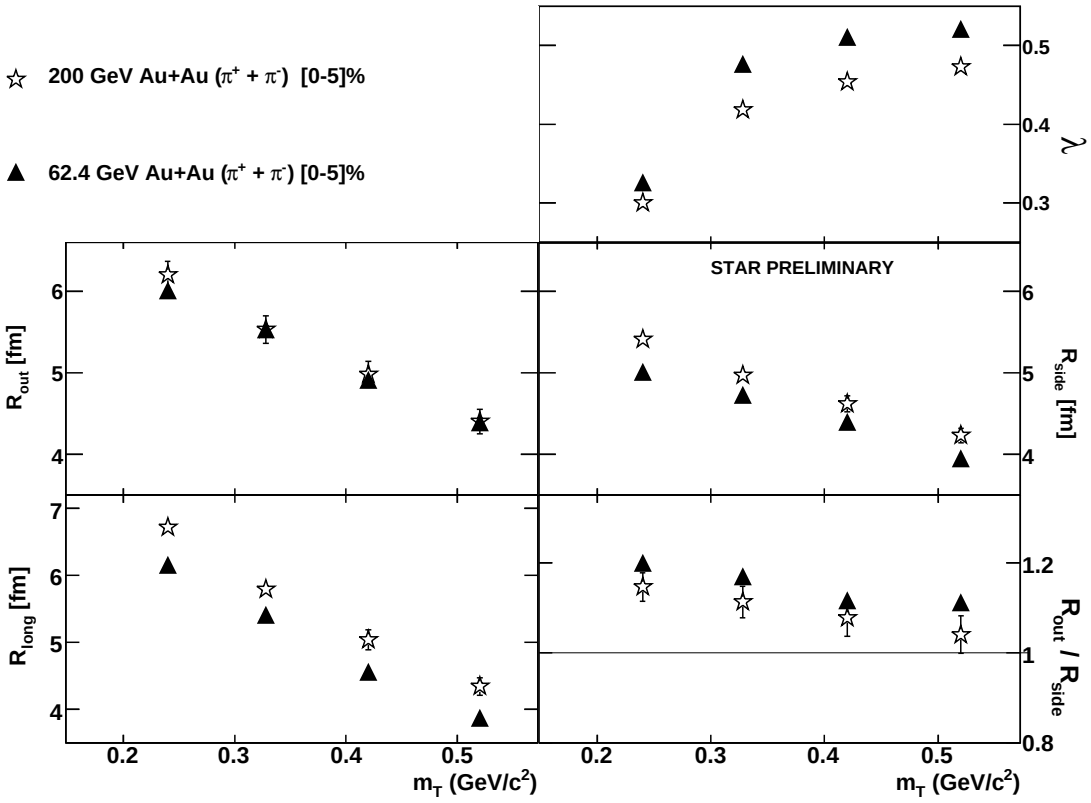

Figure 6.17: The comparison of HBT measurements of Au+Au collisions at $\sqrt{s_{\rm NN}}$ = 200 GeV and 62.4 GeV for 0-5% most central events. The 200 GeV results are from [153].

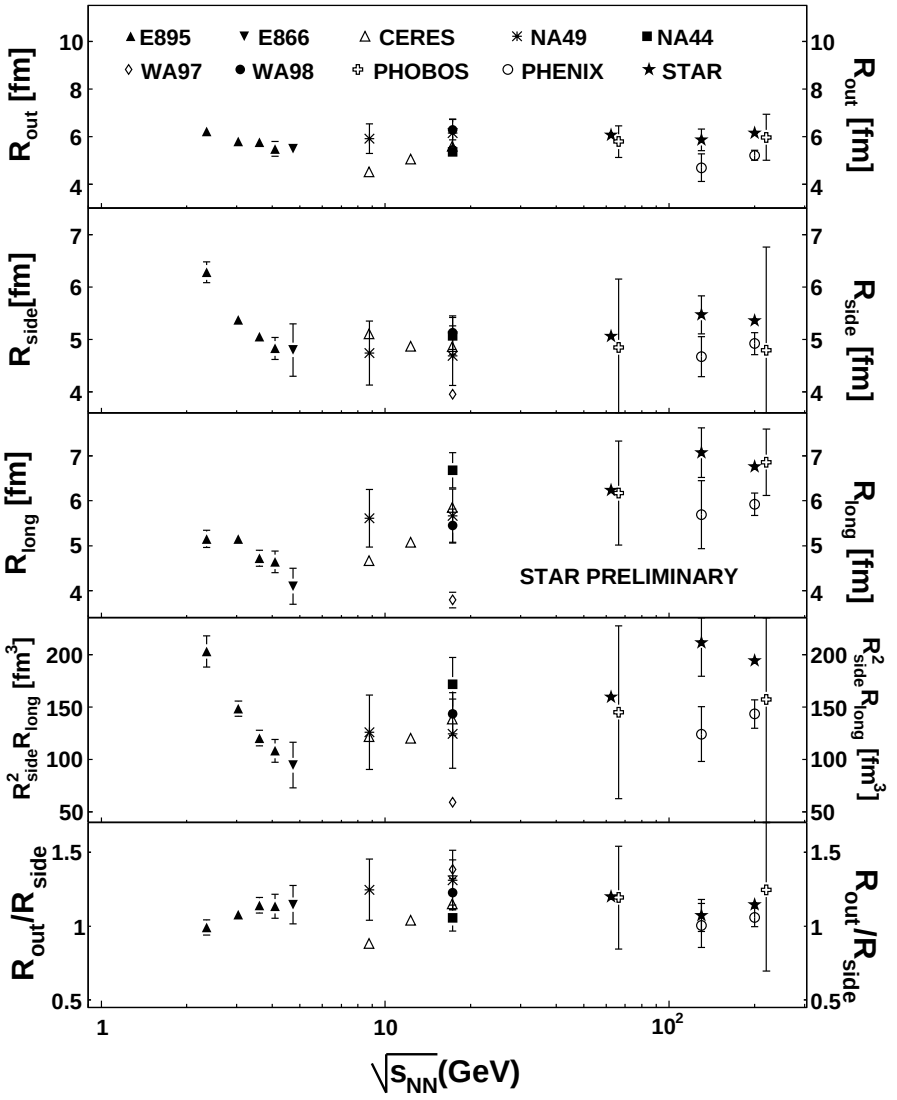

Figure 6.18: The energy dependence of π^- HBT parameters for AGS, SPS and RHIC experiments [153, 194, 195, 196, 198, 199, 209, 210, 211, 212, 213, 214, 215] for central Au+Au, Pb+Pb and Pb+Au collisions at mid-rapidity and $\langle k_T \rangle \approx 0.2$-0.3 GeV/c. Error bars on NA44, NA49, CERES, PHENIX, PHOBOS and STAR at $\sqrt{s_{\rm NN}} = 130$ and 200 GeV results include systematic uncertainties; error bars on other results are only statistical. The PHOBOS results from [209] for $\sqrt{s_{\rm NN}} =$ 62.4 and 200 GeV are slightly shifted horizontally to improve presentation.

in position-momentum correlations in both transverse and longitudinal directions. Pions of higher energy appear to come from a smaller source and the physical reason for this behaviour is that the faster pions are more likely to be emitted near the point on the source expanding with velocity in the direction of $\overrightarrow{K}$ which in turn generates a characteristic dependence of HBT radii on m_T [44, 128, 141, 148, 205, 206]. The presence of collective flow in the expanding system causes a decrease in HBT radii with m_T [123, 207, 208] where the fall-off of "out" and "side" components is caused due to transverse flow [128, 148, 153, 205] and for the "long" component due to the longitudinal flow [145, 148, 153, 206].

6.7.2 Energy dependence of HBT radii

In Figure (6.18), we present the energy dependence of the three HBT radii, the ratio of R_{out}/R_{side} for the available data from AGS, SPS and RHIC energies. The results are compiled for Au+Au, Pb+Pb and Pb+Au collisions at mid-rapidity and for $< k_T > \sim$ 0.2-0.3 GeV/c. With this we have included our measurements in Au+Au collisions at $\sqrt{s_{\rm NN}}$ = 62.4 GeV. The quality of the data and the error bars show significant improvement for the present STAR results compared to those obtained before for PHOBOS [209] at the same energy. The HBT radii do not show any sharp rise from SPS to RHIC energies.

Hydrodynamic calculations [58, 158] have predicted an enhancement in the ratio of R_{out}/R_{side} with the increase of beam energy. The observed experimental results show no such behaviour.

6.7.3 Cu+Cu collisions at $\sqrt{s_{\rm NN}}$ = 62.4 GeV and 200 GeV

The correlation functions have been constructed for Cu+Cu collisions at $\sqrt{s_{\rm NN}}$ = 62.4 GeV and 200 GeV. The extracted HBT radii, R_{out}, R_{side}, R_{long} along with the

λ parameter and the ratio, R_{out}/R_{side} have been presented in Figure (6.19) and Figure (6.20) for the cases of 62.4 GeV and 200 GeV, respectively. The results are presented for six different centralities and various m_T bins. For both the collision energies, the three HBT radii increase with increasing centrality whereas the λ parameter have a small dependence on centrality.

The m_T dependence of the HBT radii show similar behaviour as discussed for Au+Au collisions in Section 6.7.1. The decrease in HBT radii with respect to increasing of m_T at all observed centralities is attributed to collective expansion of the source as discussed earlier in Section 6.7.1. The R_{out}/R_{side} ratio exhibit no clear centrality dependence for both $\sqrt{s_{\rm NN}} = 62.4$ and 200 GeV analysis.

6.7.4 Comparison of HBT radii for Cu+Cu and Au+Au collisions

We include a comparative study in Figure (6.21) of the HBT source parameters, λ, R_{out}, R_{side}, R_{long} and the ratio, R_{out}/R_{side} for central (0-5%) Au+Au collisions at $\sqrt{s_{\rm NN}} = 200$ GeV [153] with central (0-10%) Cu+Cu collisions at same beam energy. As expected, the HBT radii for Cu+Cu collisions are smaller than Au+Au collisions at the same beam energy. The interesting fact is that the ratios of R_{out}/R_{side} give similar values.

In Figure (6.22), we extend the comparative studies of HBT source parameters for central (0-5%) Au+Au collisions at $\sqrt{s_{\rm NN}} = 62.4$ GeV with the central (0-10%) Cu+Cu collisions at $\sqrt{s_{\rm NN}} = 62.4$ GeV and 200 GeV. The HBT radii for Cu+Cu collisions at $\sqrt{s_{\rm NN}} = 62.4$ GeV are smaller than the Au+Au collisions at the same beam energy. The HBT radii for Cu+Cu central collisions are similar for both the energies. The ratio, R_{out}/R_{side} vary with m_T in a similar fashion for Au+Au and Cu+Cu collisions.

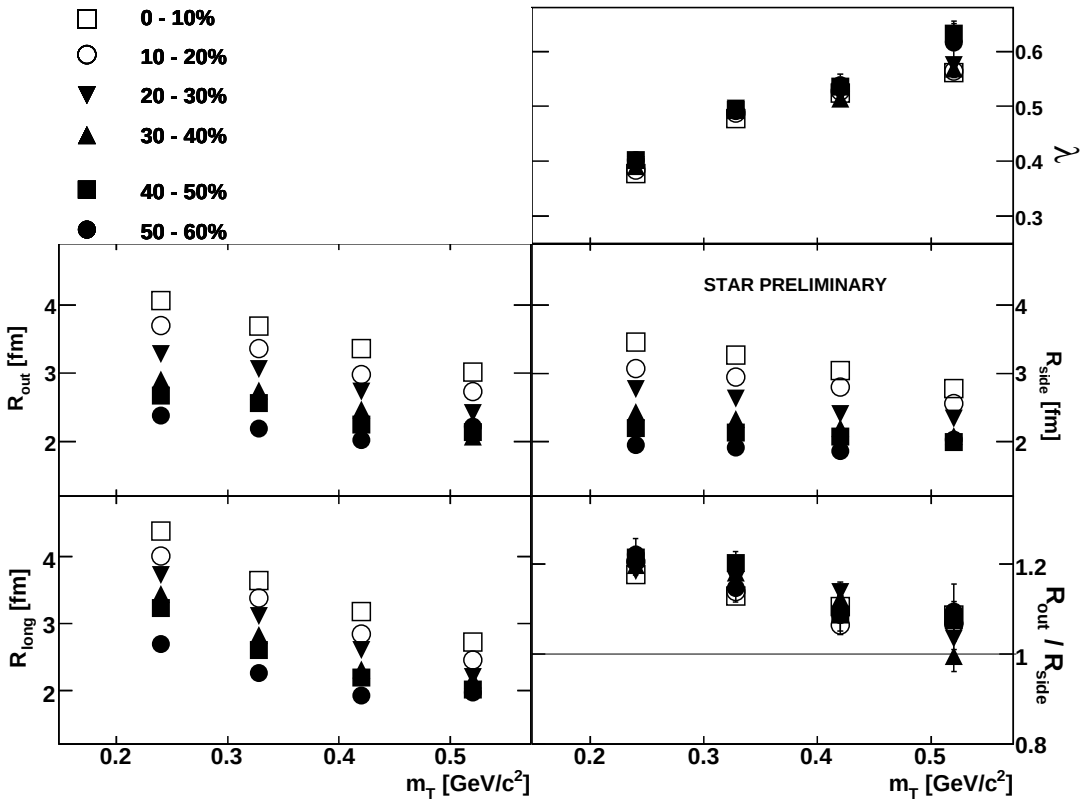

Figure 6.19: The HBT parameters *vs* m_T for 6 different centralities for Cu+Cu collisions at $\sqrt{s_{\rm NN}} = 62.4$ GeV. Only statistical errors are shown.

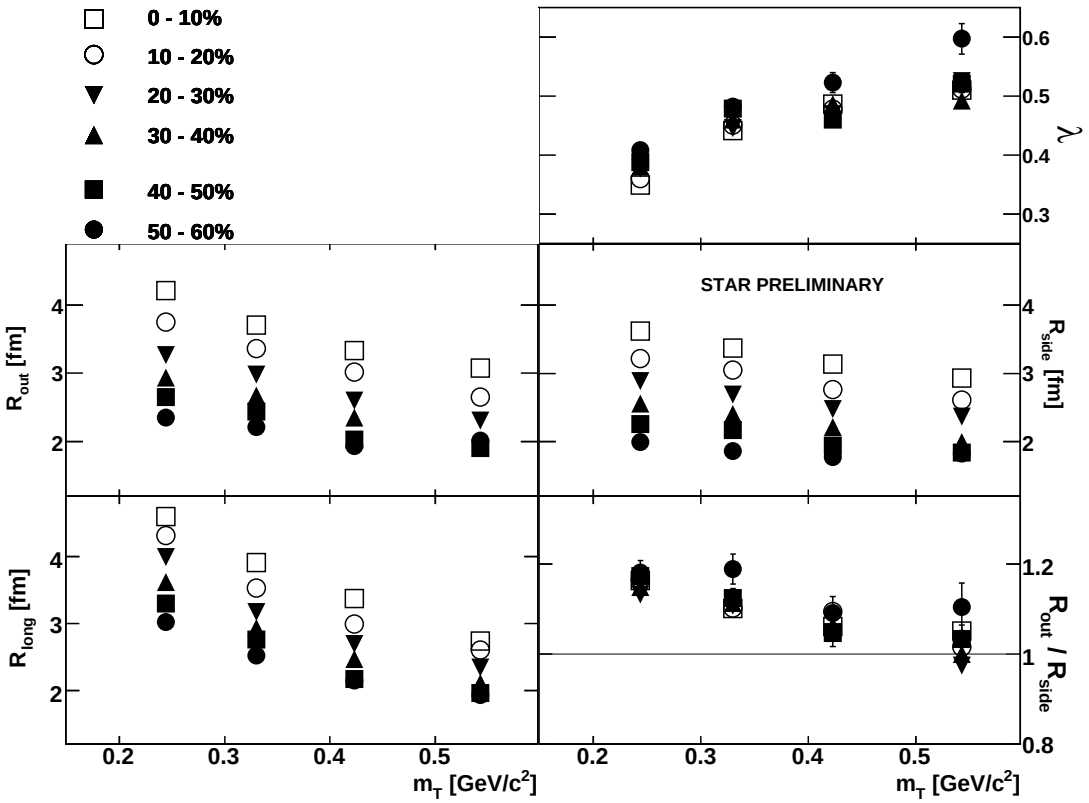

Figure 6.20: The HBT parameters *vs* m_T for 6 different centralities for Cu+Cu collisions at $\sqrt{s_{\rm NN}} = 200$ GeV. Only statistical errors are shown.

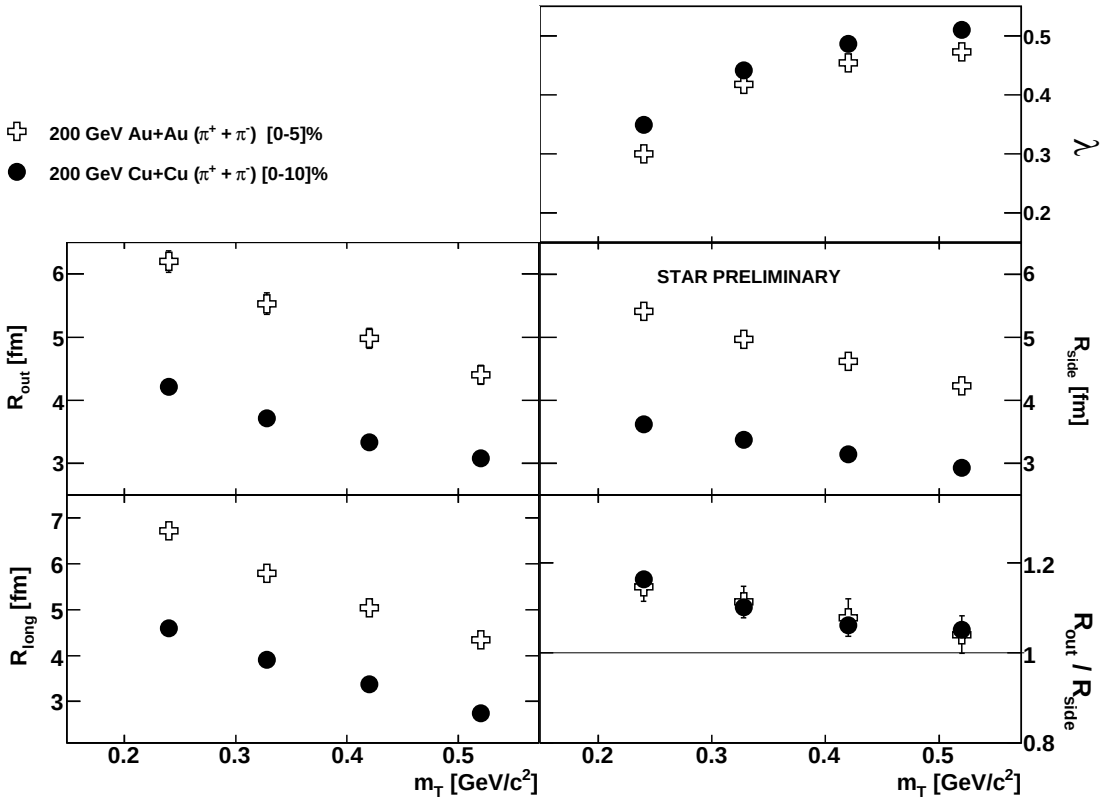

Figure 6.21: The comparison of HBT measurements of STAR Au+Au and Cu+Cu collisions at $\sqrt{s_{\rm NN}} = 200$ GeV. The Au+Au results are from previous STAR measurements [153].

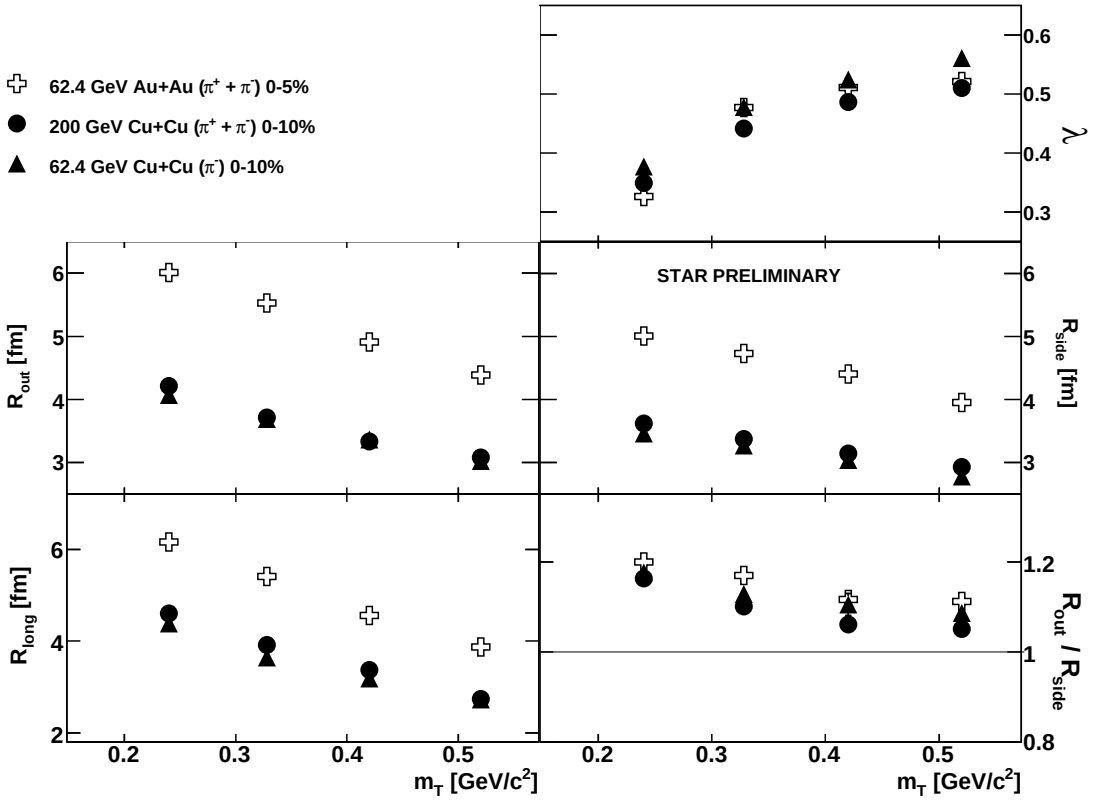

Figure 6.22: The comparison of HBT measurements of STAR Cu+Cu collisions at $\sqrt{s_{\rm NN}} = 200$ and 62.4 GeV and Au+Au collisions at $\sqrt{s_{\rm NN}} = 62.4$ GeV. Only statistical errors are shown.

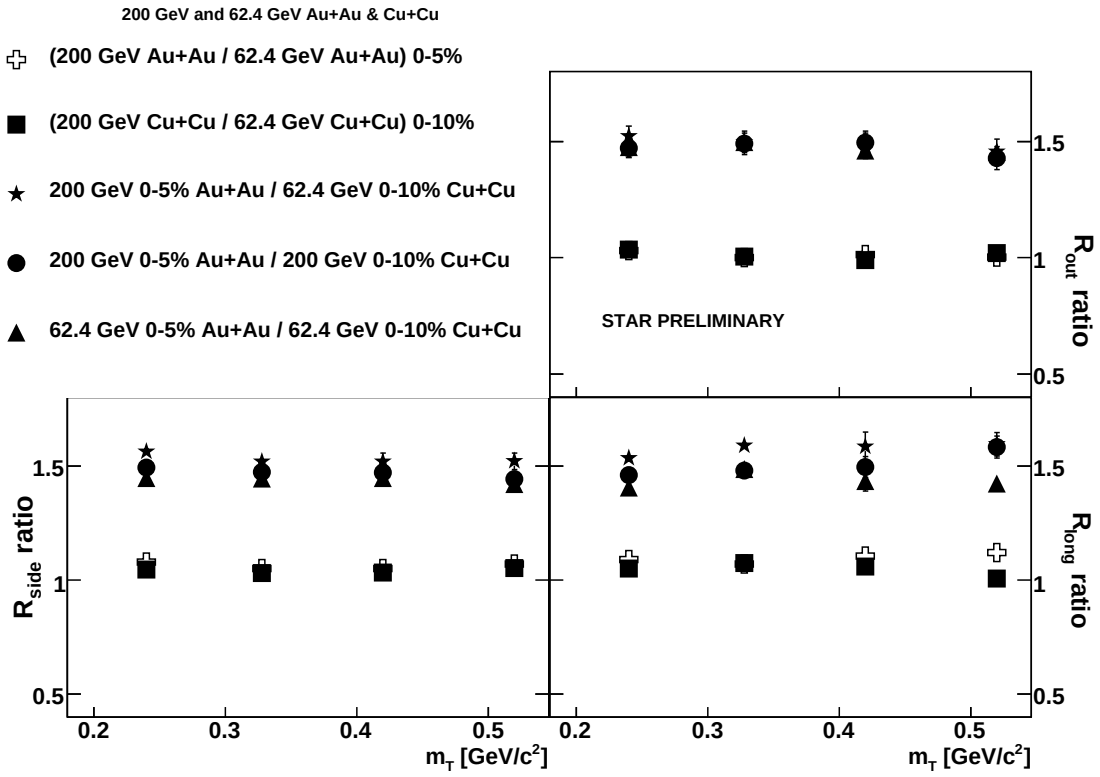

Figure 6.23: The HBT radii ratio at top centralities for Au+Au and Cu+Cu collisions at $\sqrt{s_{\rm NN}} = 200$ and 62.4 GeV with m_T.

In Figure (6.23), we present the ratios of HBT radii for top centralities with m_T in Au+Au and Cu+Cu collisions at $\sqrt{s_{\rm NN}} = 200$ GeV and 62.4 GeV. The ratios for similar colliding systems are close to unity whereas for dissimilar colliding systems are $\sim$1.5. Such similar variation of HBT radii for different colliding systems show a clear difference from the previously explained decrease with m_T observed for individual colliding species and particular energy.

6.7.5 Volume estimates and Multiplicity Scaling

The number of produced pions rise with the increase of beam energy. We can have an understanding of the freeze-out properties from the measured HBT radii through a pion freeze-out volume estimate using the expressions :

$$V_f \propto R_{side}^2 R_{long} \tag{6.7}$$

$$\propto R_{out} R_{side} R_{long} \tag{6.8}$$

where V_f is the freeze-out volume.

We have discussed in Sections (6.7.1 and 6.7.3) that the effects of collective expansion of the system lead to the m_T dependence fall-off on HBT radius parameters compared to the measured dimensions of source. As explained in Section(6.7.1) the HBT radii of such an expanding source correspond to the m_T(or k_T) dependent region of homogeneity which is smaller than the entire collision region. Henceforth the best volume estimates in Eqs. (6.7) and (6.8) are measured for lowest k_T bin which in our case corresponds to [150,250] MeV/c described in Section(6.5).

The fourth panel from top of Figure (6.18) shows the freeze-out volume V_f measurements using Eq. (6.7) as a function of $\sqrt{s}$. The comparative V_f measurements using Eqs. (6.7) and (6.8) as a function of $\sqrt{s}$, presented in Figure (6.24), show two distinct domains; the observed volumes decrease at the AGS and steadily rise with

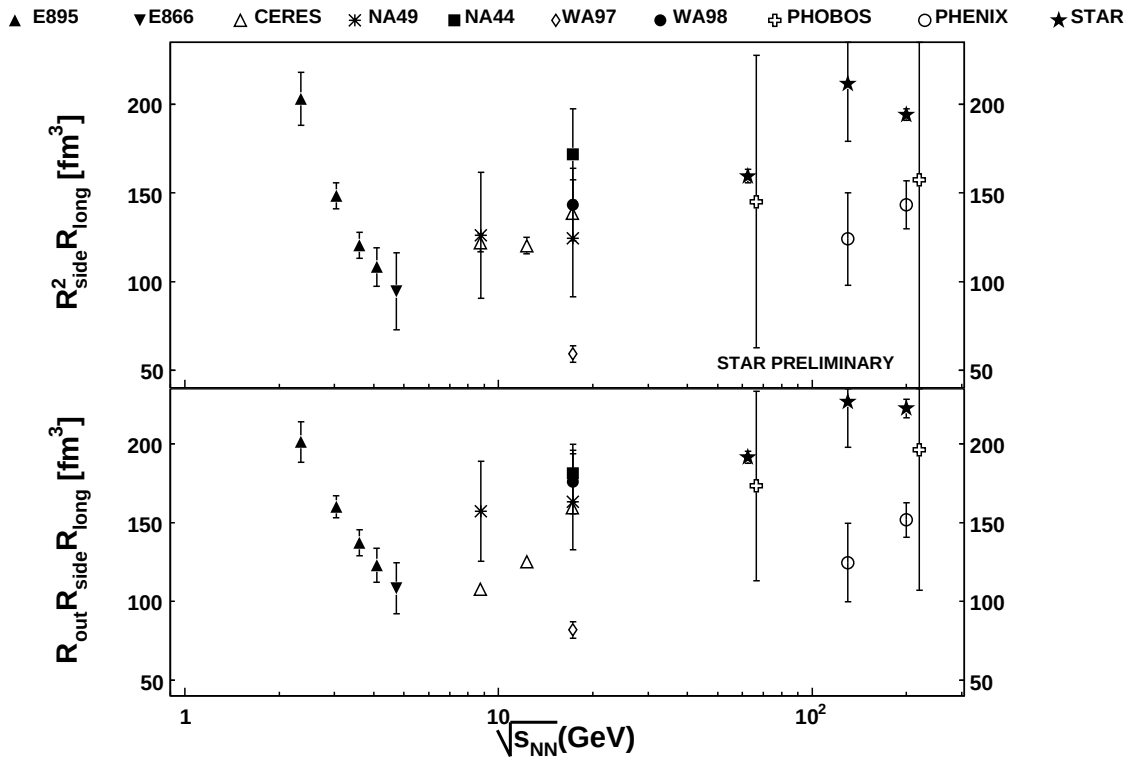

Figure 6.24: The energy dependence of pion freeze-out volume for AGS, SPS and RHIC as estimated using Eqs. (6.7) and (6.8). The references are as in Figure (6.18).

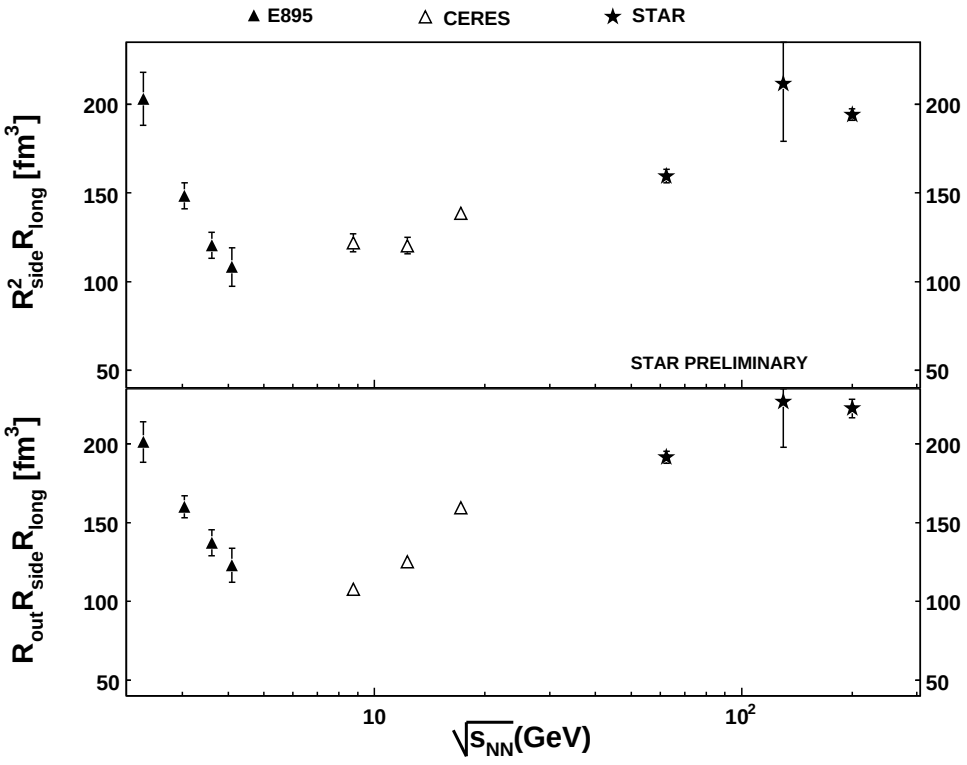

Figure 6.25: The energy dependence of pion freeze-out volume for AGS, SPS and RHIC as estimated using Eq. (6.7) and (6.8) with results from E895, CERES and STAR experiments. The references are as in Figure (6.18).

the SPS and RHIC energy regimes. The selected results from from E895, CERES and STAR experiments further strengthen the observation in Figure (6.25).

A detailed description of this non-trivial behaviour was suggested in Ref [216] where it was based on the hypothesis of constant mean free path of pions at freeze-out. The explanation provided in Ref [216] takes into account the definition of mean free path of pions, λ_f, defined as:

$$\lambda_f = \frac{1}{\rho_f \sigma} = \frac{V_f}{N\sigma} \tag{6.9}$$

where ρ_f is the freeze-out density. It can be expressed as the ratio of the freeze-out volume V_f and $N\sigma$. Here σ is the total cross-section of the pions with the surrounding medium and N is the number of particles in V_f.

The denominator $N\sigma$ can be expanded as the sum of the pion-pion and pion-nucleon cross-sections. At AGS energies pion-nucleon term dominates since the pion-proton cross-section is larger than pion-pion. Also the number of nucleons in such energies at mid-rapidity is more than the number of pions. Hence decrease in the number of mid-rapidity nucleons lead to a decrease in the observed freeze-out volume(V_f) as a function of $\sqrt{s}$. At SPS and RHIC energies due to copious pion production the pion-pion term dominates the denominator in Eq. (6.9) leading to an increase in the observed V_f. The drop in V_f for AGS energies followed by rise for SPS to RHIC is clearly presented in Figure (6.25). From this point of view in the pion dominated RHIC regime we do expect the volume estimates to show a linear dependence with charge particle multiplicity, which we observe in Figure (6.26) and Figure (6.27).

Figure (6.26) shows the comparative study of freeze-out volume estimates (using Eq. (6.7) and Eq. (6.8) as a function of the number of participants and charge particle multiplicity for Au+Au collisions at $\sqrt{s_{\rm NN}} = 62.4$ and 200 GeV. Measurements of Au+Au collisions at same centralities and different energies show different

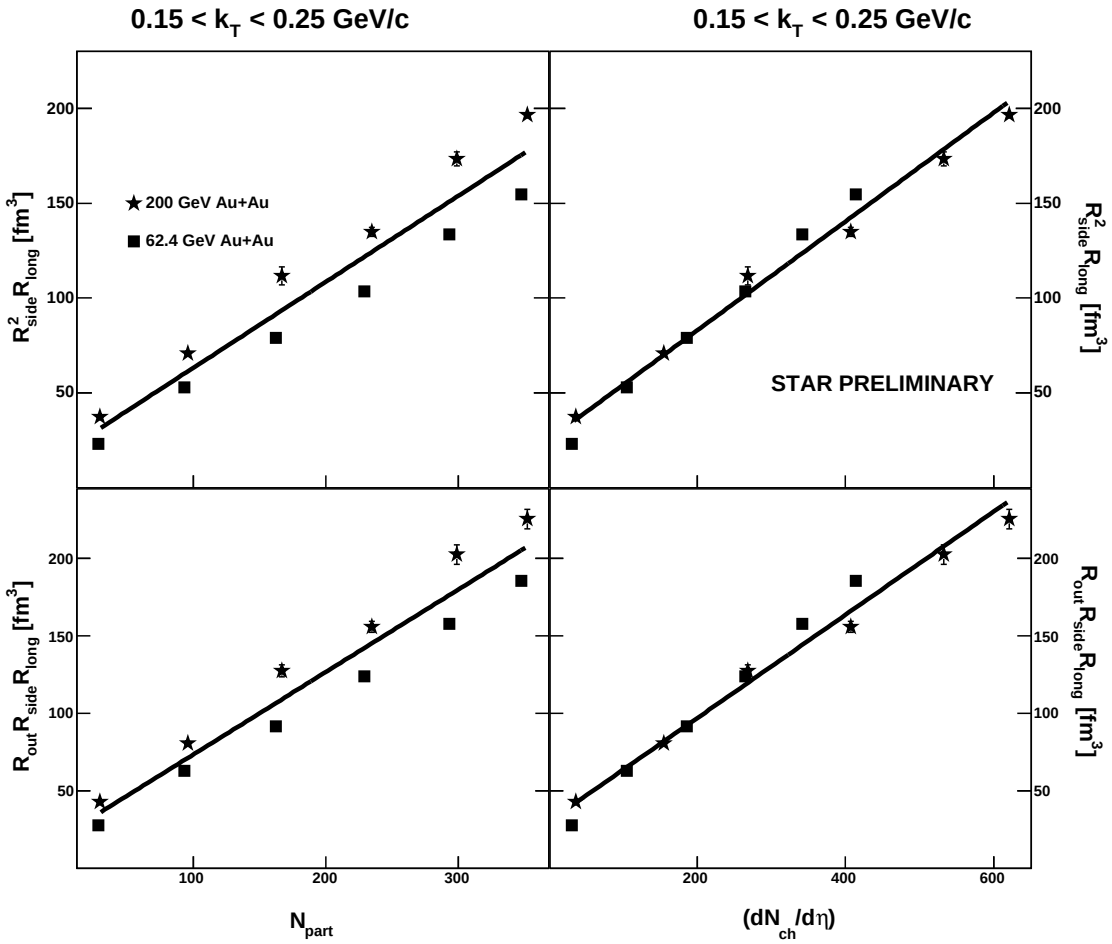

Figure 6.26: Pion freeze-out volume estimates as a function of number of participants and charged particle multiplicities for Au+Au at $\sqrt{s_{\rm NN}} = 200$ and 62.4 GeV. The Au+Au at $\sqrt{s_{\rm NN}} = 200$ GeV results from [153]. The lines are plotted to guide the eye and represent linear fits to data.

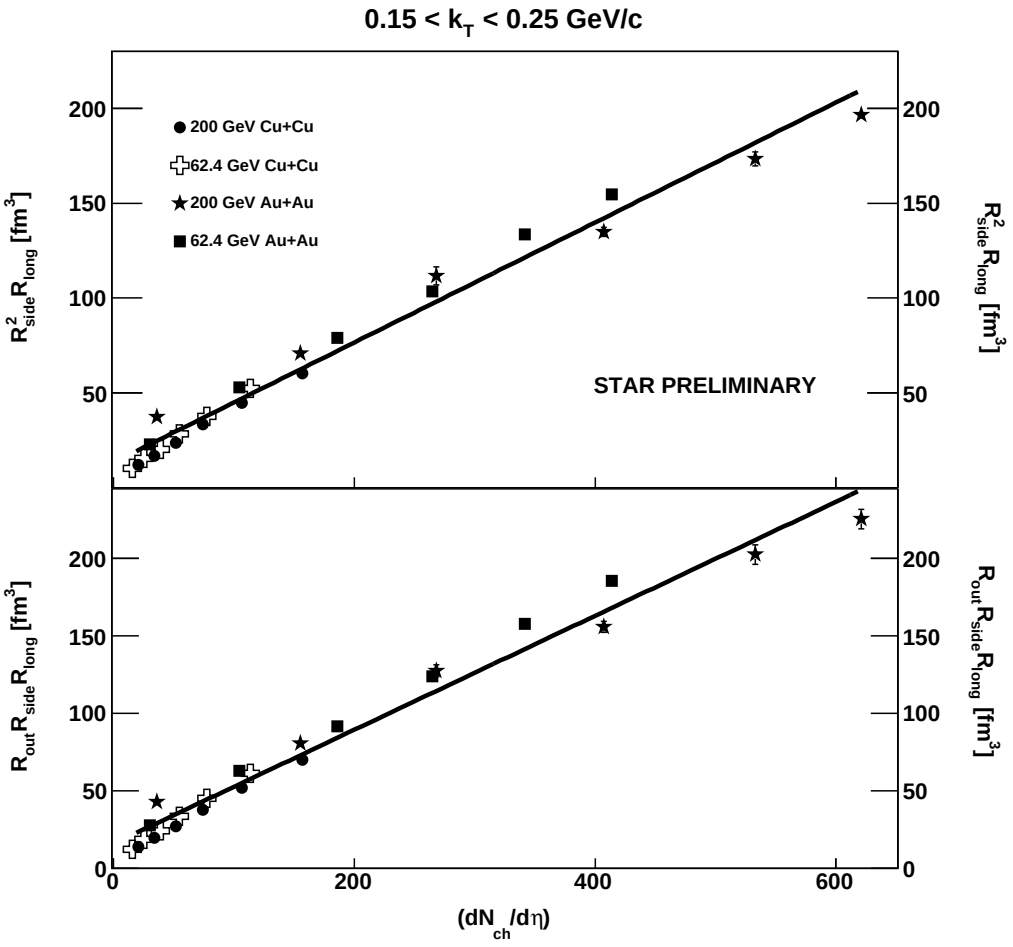

Figure 6.27: Pion freeze-out volume estimates as a function of charged particle multiplicity at mid-rapidity for Au-Au and Cu-Cu collisions for lowest k_T bin. The Au+Au collisions at $\sqrt{s_{\rm NN}} = 200$ GeV results from [153]. The lines are plotted to guide the eye and represent linear fits to data.

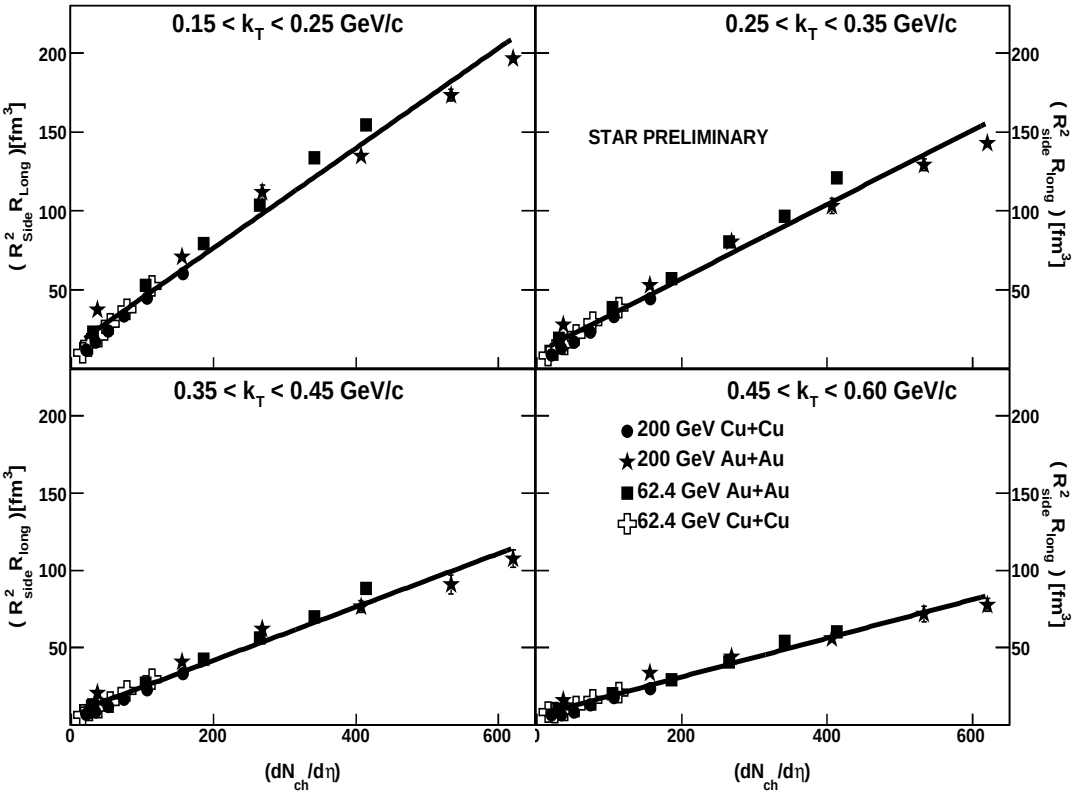

Figure 6.28: Pion freeze-out volume estimates using Eq. (6.7) as a function of charged particle multiplicity at mid-rapidity for Au-Au and Cu-Cu collisions for all four k_T bins described in Section 6.5. The Au+Au collisions at $\sqrt{s_{\rm NN}} = 200$ GeV results from [153]. The lines are plotted to guide the eye and represent linear fits to data.

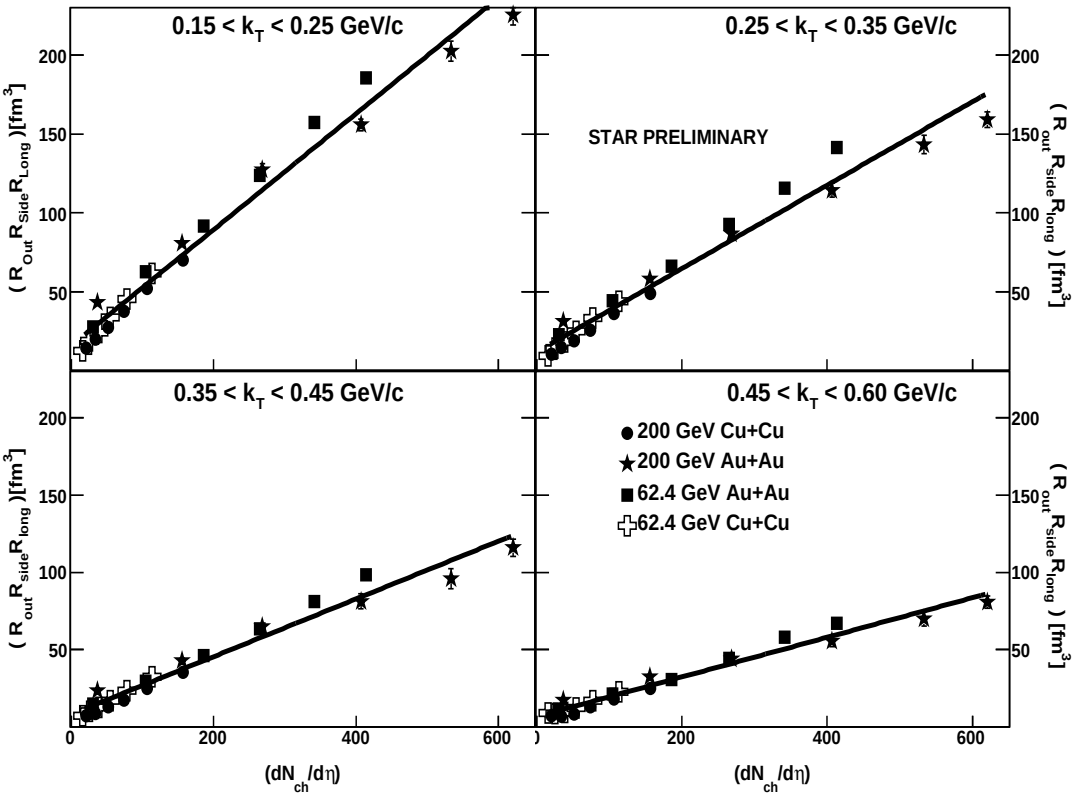

Figure 6.29: Pion freeze-out volume estimates using Eq. (6.8) as a function of charged particle multiplicity at mid-rapidity for Au-Au and Cu-Cu collisions for all four k_T bins described in Section 6.5. The Au+Au collisions at $\sqrt{s_{\rm NN}} = 200$ GeV results from [153]. The lines are plotted to guide the eye and represent linear fits to data.

freeze-out volume, which means that N_{part} is not a suitable scaling variable in this case. On the other hand charge particle multiplicity seems to be a better scaling variable.

The study of freeze-out volume estimates are presented in Figure (6.27) for Au+Au and Cu+Cu collisions at $\sqrt{s_{\rm NN}}$ = 62.4 and 200 GeV as a function of charge particle multiplicity for the lowest k_T bin. The freeze-out volume estimates for measured systems show a linear dependence as a function of charge particle multiplicity. Such linear dependences are also observed in all the analysed k_T bins which correspond to [150,250] MeV/c, [250,350] MeV/c, [350,450] MeV/c and [450,600] MeV/c as presented in Figures (6.28) and (6.29) using the volume estimates of Eq. (6.7) and Eq. (6.8) respectively.

The linear dependence of HBT radii with $(dN_{ch}/d\eta)^{1/3}$ for Au+Au and Cu+Cu collisions at $\sqrt{s_{\rm NN}}$ = 62.4 and 200 GeV is exhibited in Figure (6.30) for lowest k_T bin. Figures (6.31), (6.32) and (6.33) show linear dependence of HBT radii with $(dN_{ch}/d\eta)^{1/3}$ for all measured k_T bins in R_{out}, R_{side} and R_{long} respectively. Such dependences are naturally expected within a framework of constant mean free-path of pions suggested in [216, 217].

6.7.6 Discussions

We have presented systematic measurements of two-pion correlation functions in Au+Au collisions at $\sqrt{s_{\rm NN}}$ = 62.4 GeV and Cu+Cu collisions at $\sqrt{s_{\rm NN}}$ = 62.4 and 200 GeV using the data from STAR experiment. We have analysed both one dimensional invariant relative momentum distributions and three dimensional studies using Bertsch-Pratt parametrization. The expected increase of the invariant radii from lighter systems like Cu+Cu to heavier ones like Au+Au provide an estimate of the space-time extent of the source. The three-dimensional Bertsch-Pratt (or "out-side-long") convention provided a much detail understanding of the

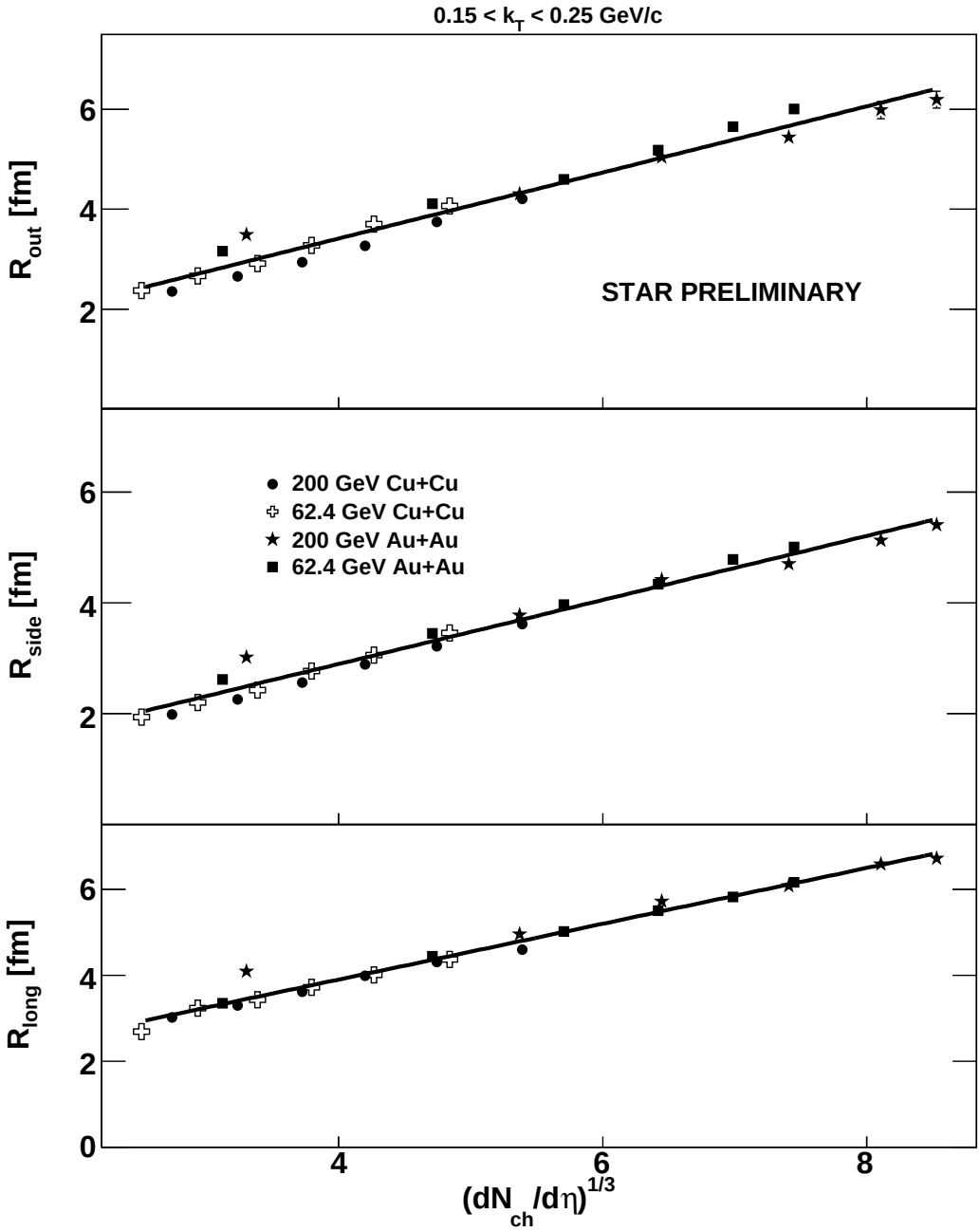

Figure 6.30: The pion source radii dependence on charged particle multiplicity for Au+Au and Cu+Cu collisions for lowest k_T bin. The Au+Au at $\sqrt{s_{\rm NN}} = 200$ GeV results from [153]. The lines are plotted to guide the eye and represent linear fits to the data.

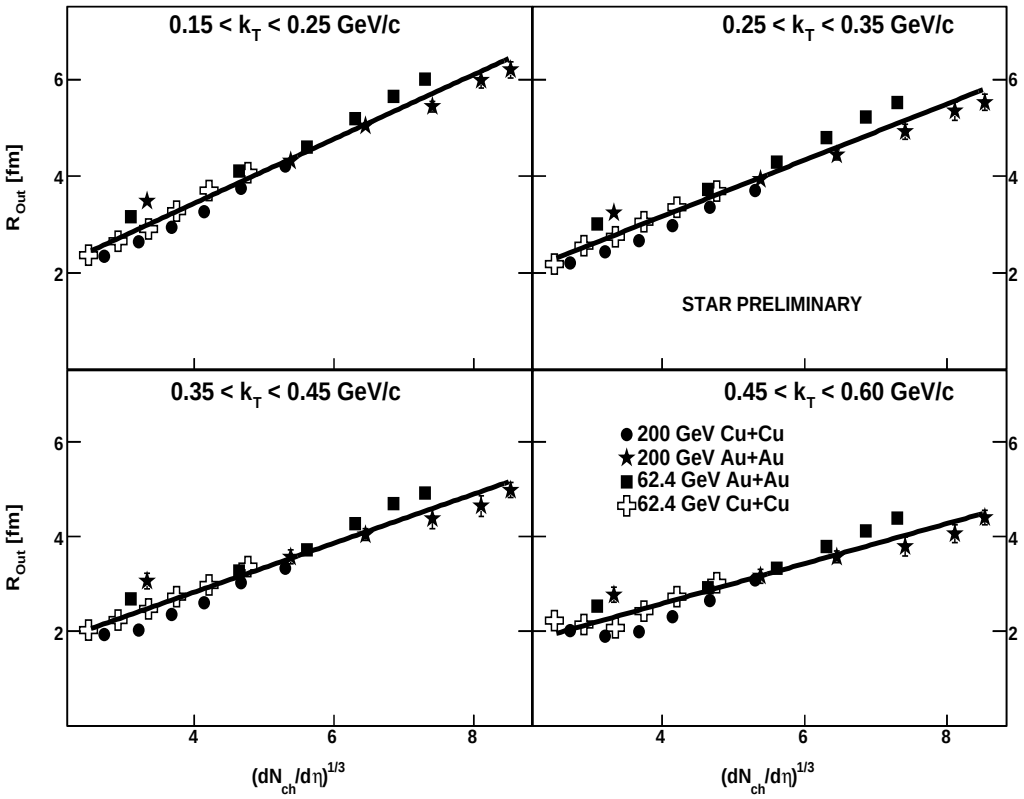

Figure 6.31: The pion source radii, R_{out}, dependence on charged particle multiplicity for Au+Au and Cu+Cu collisions for all four k_T bins described in Section 6.5. The Au+Au at $\sqrt{s_{\rm NN}} = 200$ GeV results from [153]. The lines are plotted to guide the eye and represent linear fits to the data.

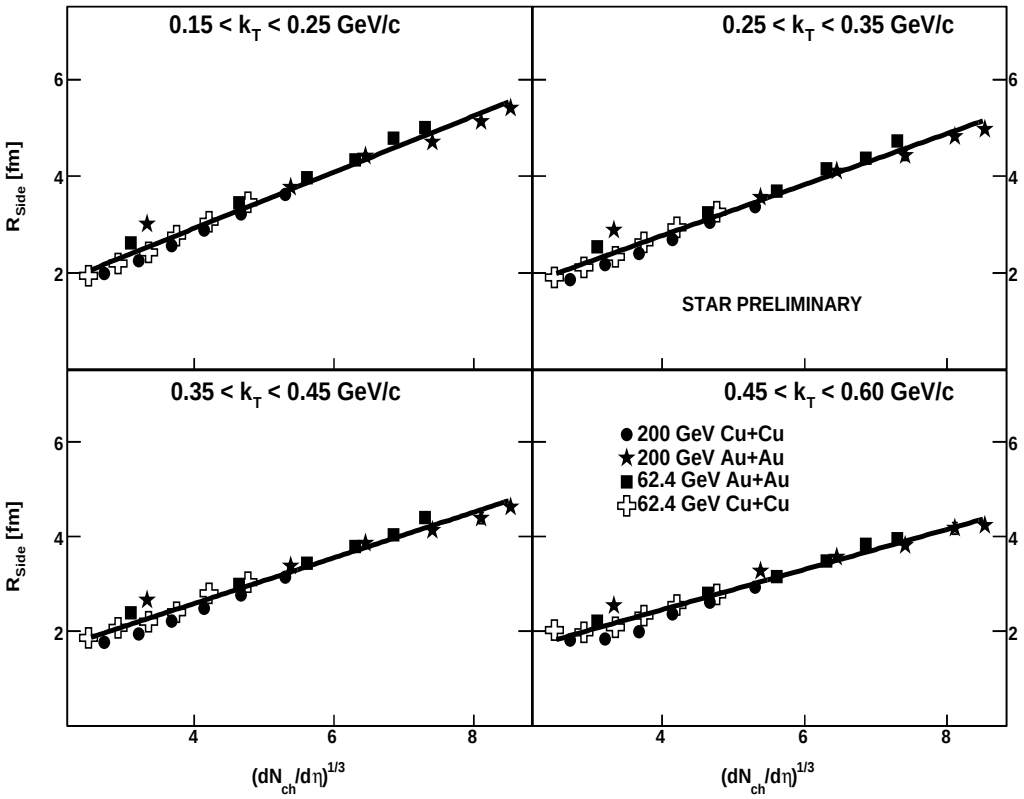

Figure 6.32: The pion source radii, R_{side}, dependence on charged particle multiplicity for Au+Au and Cu+Cu collisions for all four k_T bins described in Section 6.5. The Au+Au at $\sqrt{s_{\rm NN}} = 200$ GeV results from [153]. The lines are plotted to guide the eye and represent linear fits to the data.

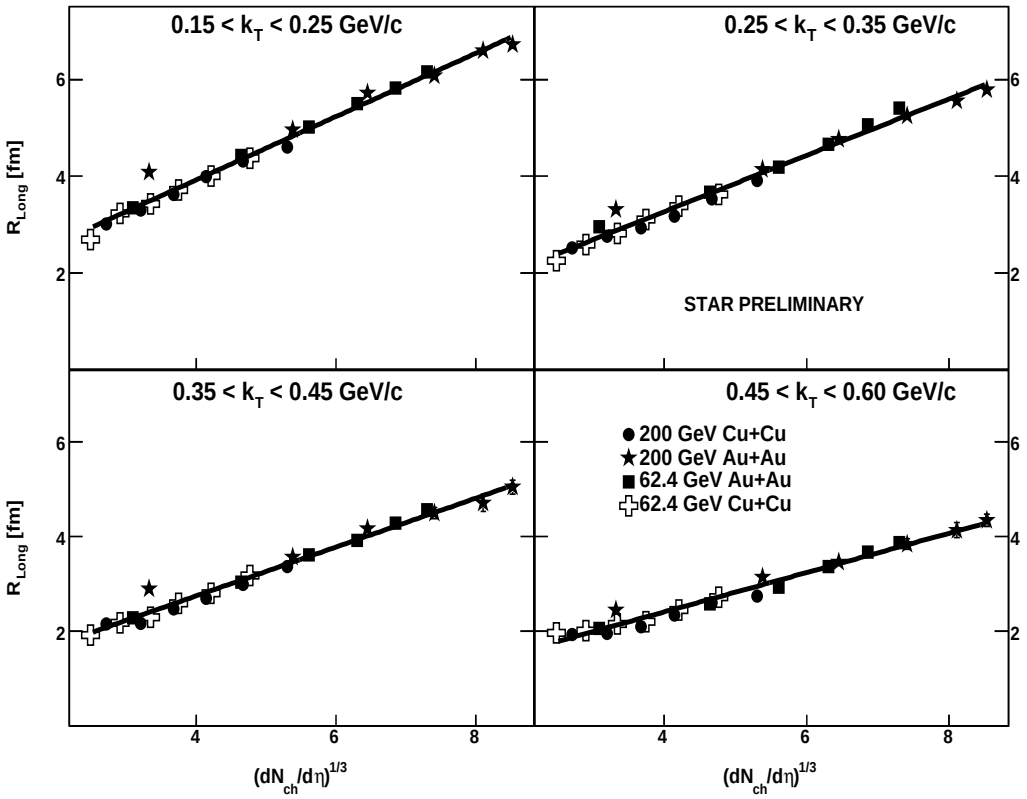

Figure 6.33: The pion source radii, R_{long}, dependence on charged particle multiplicity for Au+Au and Cu+Cu collisions for all four k_T bins described in Section 6.5. The results of Au+Au collisions at $\sqrt{s_{\rm NN}} = 200$ GeV are from Ref [153]. The lines are plotted to guide the eye and represent linear fits to the data.

features of the dynamic source.

The three HBT radii (R_{out},R_{side} and R_{long}) increase with centrality (or event multiplicity), whereas the values of the λ parameter and R_{out}/R_{side} ratio exhibit no clear centrality dependence. For all centralities, the three HBT radii decrease with the increase of the m_T bin, whereas the λ parameter increases with m_T bin. Such behaviour are consistent with the results of Au+Au collisions at $\sqrt{s_{\rm NN}} = 200$ GeV [153] compared with the present datasets. The increase of λ parameter with m_T is attributed to the decreasing contribution of pions produced from long-lived resonance decays at higher transverse momenta.

The presence of collective flow in the expanding system causes a decrease in HBT radii with m_T. The ratios of HBT radii at top centralities for different colliding systems (Au+Au and Cu+Cu) at $\sqrt{s_{\rm NN}} = 62.4$ and 200 GeV show that the corresponding HBT radii vary with m_T in a similar manner.

Comparative studies with the world's dataset of π^- HBT correlation parameters for central Au+Au, Pb+Pb and Pb+Au collisions at mid-rapidity and $\langle k_T \rangle \approx 0.2$-0.3 GeV/c are necessary to look for nontrivial structures in the excitation function, which might arise from threshold behavior due to a phase transition [58]. The radius parameter R_{side} has the most direct correlation with the source geometry, whereas R_{out} encodes both geometry and time scale. Experimentally measured results show that, R_{side} has an initial decrease at AGS and then a significant rise with collision energy from SPS to RHIC. R_{long} does not show a significant increase with collision energy after the initial increase between AGS and SPS energies. For R_{out} the change is very small. The predicted rise of R_{out}/R_{side} ratio due to a phase transition [58] is found to be absent.

Collective effects of the individual HBT radii are observed with the freeze-out volume estimate (V_f) studies (using $R_{out}R_{side}R_{long}$ and $R^2_{side}R_{long}$) carried out as a function of $\sqrt{s}$. The comparative V_f measurements as a function of $\sqrt{s}$ show

two distinct domains; the observed volumes decrease at the AGS and steadily rise with the SPS and RHIC energy regimes. At AGS energies, decrease in the number of baryons at mid-rapidity nucleons leads to a decrease in the observed freeze-out volume(V_f) as a function of $\sqrt{s}$, after which copious pion production from SPS to RHIC cause the rise. From this point of view in the pion dominated RHIC regime we do expect the volume estimates to show a linear dependence with charge particle multiplicity.

The scaling of the apparent freeze-out volume with number of participants and charged particle multiplicity is studied. Measurements of Au+Au collisions at same centralities and different energies yield different freeze-out volumes, which means that N_{part} is not a suitable scaling variable. The freeze-out volume estimates for all presented systems show linear dependence as a function of charge particle multiplicity showing consistent behaviour with a universal mean-free-path at freeze-out.

For the systems studied, the multiplicity and k_T dependence of the HBT radii are consistent with previously-established trends at RHIC and lower energies. The radii scale with the collision multiplicity; in a static model, this is consistent with a universal mean-free-path at freeze-out. As in measurements at all other energies [123], the k_T dependence remains independent of $\sqrt{s_{\rm NN}}$, collision system, and multiplicity.

Chapter 7

Summary and Outlook

Statistical QCD predicts that strongly interacting matter should at sufficiently high density undergo a transition from hadronic matter to QGP. This deconfined state of quarks and gluons is believed to be the one in which the early universe existed one millionth of a second (a micro-second) after the "Big-Bang" which marked the beginning about 14 billion years ago.

The ultra-relativistic heavy ion collisions recorded and analysed by the STAR experiment at Relativistic Heavy Ion Collider at Brookhaven National Laboratory provide an opportunity to study the properties of the strongly interacting matter created under such extreme conditions of temperature and density. However the experimental study of the nature of the transition from hadronic phase to the QGP phase is complicated by the short lifetime (or transient nature) and small size of the produced system.

The produced and emitted particles from the collision environment comprise of photons, leptons and hadrons. Photons are produced in all the stages of the system created in heavy ion collisions. They do not interact strongly with the medium and hence carry information about the history of the collisions. The studies of hadrons provide an understanding of the evolutionary path of the system created

in the collision at the time of freeze-out.

The measurement of photons in high energy physics experiments have been traditionally carried out using calorimeters. Due to the large spatial density of produced particles in the forward rapidity region in relativistic nuclear collisions, and consequent overlap of showers, one cannot use calorimeters beyond a certain region. Under such conditions, a limited goal of photon study can be achieved using a preshower detector having a relatively thinner converter and also restricting the development of shower. The description of the detector details presented in this thesis explain the challenges imposed in photon multiplicity measurements at forward rapidity in STAR experiment with PMD.

The dynamical evolution of the collision fireball and its space-time structure is studied with two-photon and two-pion intensity interferometry techniques in STAR experiment. The information about the space-time structure of the emitting source can be extracted by the method of intensity interferometry techniques popularly known as Hanbury-Brown Twiss (HBT) correlations. Numerous experimental observables have been proposed as signatures of QGP creation in heavy-ion collisions. One of the predictions is based on the expectation that large number of degrees of freedom associated with deconfined state, manifests itself in an increased entropy of the system which should survive subsequent hadronization and freeze-out. This is expected to lead to an increased dimension and duration of particle emission, thus manifesting as one of the significant probes for QGP phase transition.

The Bose-Einstein correlations of the direct photons provide information about the various stages of heavy ion collisions. But it is difficult to extract the small yield of direct photons due to the large background of photons produced by electromagnetic decay of the hadrons (especially π^0's and η's). The development of analyses cuts for two-photon intensity interferometry measurements in Au+Au collisions at $\sqrt{s_{\rm NN}} = 62.4$ GeV using STAR BEMC are discussed. However such

correlations performed at same energy with Au+Au collisions, at mid-rapidity and low transverse momentum, using charged pions (the most abundantly produced hadron) from STAR TPC are measured to study the space-time extent of the dynamically evolving collision fireball at freeze-out. The invariant interferometric radii extracted from such correlations with direct photons and charged pions reveal comparable results.

The systematic analyses of two-pion intensity interferometry in Au+Au collisions at $\sqrt{s_{\rm NN}}$ = 62.4 GeV and Cu+Cu collisions at $\sqrt{s_{\rm NN}}$ = 62.4 and 200 GeV with charged pions show that the multiplicity and k_T dependence of the HBT radii are strongly consistent with previously-established trends at RHIC and lower energies. The predicted rise of R_{out}/R_{side} ratio due to phase transition is found to be absent.

The radii scale with the collision multiplicity; in a static model, this is consistent with a universal mean-free-path at freeze-out. As in measurements at all other energies, the k_T dependence remains independent of $\sqrt{s_{\rm NN}}$, collision system, and multiplicity. Furthermore, they establish the baseline systematics against which to compare future HBT studies at the LHC [218].

The scaling of the apparent freeze-out volume with number of participants and charged particle multiplicity is studied. Measurements of Au+Au collisions at same centralities and different energies (like 62.4 GeV and 200 GeV), yield different freeze-out volumes, which means that N_{part} is not a suitable scaling variable. The freeze-out volume estimates for all the presented systems (like Au+Au and Cu+Cu), show linear dependence as a function of charge particle multiplicity inferring consistent behaviour with a universal mean-free-path at freeze-out.

Bibliography

[1] I.S.Hughes, *Elementary particles*, Cambridge University Press (1991) .

[2] David Griffiths, *Introduction to Elementary Particles*, John Wiley and Sons (1987) .

[3] C.Y.Wong, *Introduction to High − Energy Heavy − Ion Collisions*, World Scientific(1994).

[4] Y.M.Yao *et al.* Journal of Physics G **33**, 1 (2006) (Review of Particle Physics) [http://www-theory.lbl.gov/∼ianh/alpha/alpha.html]

[5] Francis Halzen and Alan.D.Martin,
Quarks and Leptons : *An Introductory Course to Modern Particle Physics*, John Wiley and Sons (1984); Kohsuke Yagi, Tetsuo Hatsuda and Yasuo Miake, *Quark − Gluon Plasma* : *From Big Bang to Little Bang*, Cambridge University Press(2005).

[6] Bikash Sinha, Santanu Pal and Sibaji Raha (ed.),
Quark − gluon plasma : *Invited lectures of winter school Puri*, *Orissa*, *India*, *December 5 − 16*, *1989* Springer-Verlag (1990).

[7] B.P.Roe, *Particle Physics at the New Millennium*,
Springer-Verlag (1996).

[8] D. J. Gross and F. Wilczek, Phys. Rev. Lett. **30**, 1343 (1973).

[9] H. D. Politzer, Phys. Rev. Lett. **30**, 1346 (1973).

[10] F. Wilczek, arXiv:hep-ph/0003183.

[11] J. Berges, arXiv:hep-ph/9902419.

[12] H. Satz, Nucl. Phys. A **418**, 447C (1984).

[13] F. Karsch, Nucl. Phys. Proc. Suppl. **83**, 14 (2000) [arXiv:hep-lat/9909006].

[14] J. C. Collins and M. J. Perry, Phys. Rev. Lett. **34**, 1353 (1975).

[15] K. Adcox *et al.* [PHENIX Collaboration], Nucl. Phys. A **757**, 184 (2005) [arXiv:nucl-ex/0410003].

[16] E. V. Shuryak, Phys. Rept. **61**, 71 (1980).

[17] F. Karsch, Lect. Notes Phys. **583**, 209 (2002) [arXiv:hep-lat/0106019]. F. Karsch, Nucl. Phys. A **698**, 199 (2002) [arXiv:hep-ph/0103314].

[18] H. Satz, arXiv:hep-ph/9706342.

[19] S. Hands, Contemp. Phys. **42**, 209 (2001) [arXiv:physics/0105022].

[20] P. Braun-Munzinger, Nucl. Phys. A **681**, 119 (2001) [arXiv:nucl-ex/0007021].

[21] P. Braun-Munzinger, I. Heppe and J. Stachel, Phys. Lett. B **465**, 15 (1999) [arXiv:nucl-th/9903010].

[22] L. D. McLerran and B. Svetitsky, Phys. Lett. B **98**, 195 (1981).

[23] B. Muller and J. L. Nagle, arXiv:nucl-th/0602029.

[24] I. Arsene *et al.* [BRAHMS Collaboration], Nucl. Phys. A **757**, 1 (2005) [arXiv:nucl-ex/0410020].

[25] B. B. Back *et al.* [PHOBOS Collaboration], Nucl. Phys. A **757**, 28 (2005) [arXiv:nucl-ex/0410022].

[26] J. Adams *et al.* [STAR Collaboration], Nucl. Phys. A **757**, 102 (2005) [arXiv:nucl-ex/0501009].

[27] R. Hagedorn, Nuovo Cim. Suppl. **3**, 147 (1965).

[28] B. Tomasik, arXiv:nucl-th/0610042.

[29] J. D. Bjorken, Phys. Rev. D **27**, 140 (1983).

[30] G. Baym, B. L. Friman, J. P. Blaizot, M. Soyeur and W. Czyz, Nucl. Phys. A **407**, 541 (1983).

[31] P. Braun-Munzinger, K. Redlich and J. Stachel, arXiv:nucl-th/0304013.

[32] P. Braun-Munzinger and J. Stachel, Nucl. Phys. A **638**, 3 (1998) [arXiv:nucl-ex/9803015].

[33] P. Aurenche, arXiv:hep-ph/0201011.

[34] F. Arleo *et al.*, arXiv:hep-ph/0311131.

[35] N. Xu and M. Kaneta, Nucl. Phys. A **698**, 306 (2002) [arXiv:nucl-ex/0104021].

[36] A. Andronic, P. Braun-Munzinger and J. Stachel, Nucl. Phys. A **772**, 167 (2006) [arXiv:nucl-th/0511071].

[37] J. Cleymans, H. Oeschler, K. Redlich and S. Wheaton, J. Phys. G **32**, S165 (2006) [arXiv:hep-ph/0607164].

[38] D. Prorok, arXiv:nucl-th/0702042.

[39] S. A. Voloshin, J. Phys. Conf. Ser. **50**, 111 (2006) [arXiv:nucl-ex/0505003].

[40] S. A. Voloshin, Nucl. Phys. A **749**, 287 (2005) [arXiv:nucl-th/0410024].

[41] B. B. Back *et al.* [PHOBOS Collaboration], Phys. Rev. C **74**, 011901 (2006) [arXiv:nucl-ex/0603026].

[42] R. L. Ray [STAR Collaboration], J. Phys. Conf. Ser. **27** (2005) 108.

[43] T. Csorgo, J. Phys. Conf. Ser. **50**, 259 (2006) [arXiv:nucl-th/0505019].

[44] S. Pratt, Phys. Rev. D **33**, 1314 (1986).

[45] J. W. Harris and B. Muller, Ann. Rev. Nucl. Part. Sci. **46**, 71 (1996) [arXiv:hep-ph/9602235].

[46] R. A. Fini [ALICE Collaboration], Nucl. Phys. A **749**, 325 (2005).

[47] H. A. Gustafsson *et al.*, Phys. Rev. Lett. **52**, 1590 (1984).

[48] K. H. Ackermann *et al.* [STAR Collaboration], Phys. Rev. Lett. **86**, 402 (2001) [arXiv:nucl-ex/0009011].

[49] C. Adler *et al.* [STAR Collaboration], Phys. Rev. Lett. **87**, 182301 (2001) [arXiv:nucl-ex/0107003].

[50] T. K. Nayak, J. Phys. G **32**, S187 (2006) [arXiv:nucl-ex/0608021].

[51] G. Goldhaber, S. Goldhaber, W. Y. Lee and A. Pais, Phys. Rev. **120**, 300 (1960).

[52] U. A. Wiedemann and U. W. Heinz, Phys. Rept. **319**, 145 (1999) [arXiv:nucl-th/9901094].

[53] R. Hanbury Brown and R. Q. Twiss, Phil. Mag. **45**, 663 (1954). R. Hanbury Brown and R. Q. Twiss, Nature **178**, 1046 (1956).

[54] U. A. Wiedemann, Nucl. Phys. A **661**, 65C (1999) [arXiv:nucl-th/9907048].

[55] F. Karsch and E. Laermann, arXiv:hep-lat/0305025.

[56] U. W. Heinz, J. Phys. Conf. Ser. **50**, 230 (2006) [arXiv:nucl-th/0504011].

[57] C. M. Hung and E. V. Shuryak, Phys. Rev. Lett. **75**, 4003 (1995) [arXiv:hep-ph/9412360].

[58] D. H. Rischke and M. Gyulassy, Nucl. Phys. A **608**, 479 (1996) [arXiv:nucl-th/9606039].

[59] P. Aurenche, Nucl. Phys. Proc. Suppl. **96**, 179 (2001) [arXiv:hep-ph/0009015].

[60] C. Gale, arXiv:hep-ph/0102214.

[61] V. Koch, Acta Phys. Polon. B **29**, 3233 (1998) [arXiv:nucl-th/9706069].

[62] J. Alam, B. Sinha and S. Raha, Phys. Rept. **273**, 243 (1996).

[63] P. Aurenche, arXiv:hep-ph/0610218.

[64] T. Peitzmann and M. H. Thoma, Phys. Rept. **364**, 175 (2002) [arXiv:hep-ph/0111114].

[65] K. Reygers [PHENIX Collaboration], Eur. Phys. J. C **43**, 393 (2005) [arXiv:nucl-ex/0502018].

[66] C. Adler *et al.* [STAR Collaboration], Phys. Rev. Lett. **90**, 082302 (2003) [arXiv:nucl-ex/0210033].

[67] J. W. Harris, Eur. Phys. J. C **43**, 445 (2005) [arXiv:nucl-ex/0503014].

[68] J. Adams *et al.* [STAR Collaboration], Phys. Rev. Lett. **91**, 072304 (2003) [arXiv:nucl-ex/0306024].

[69] H. Satz, Nucl. Phys. A **590**, 63C (1995) [arXiv:hep-ph/9502322].

[70] S. S. Adler *et al.* [PHENIX Collaboration], Phys. Rev. C **69**, 014901 (2004) [arXiv:nucl-ex/0305030].

[71] T. Matsui and H. Satz, Phys. Lett. B **178**, 416 (1986).

[72] R. Arnaldi *et al.* [NA60 Collaboration R Arnaldi], Nucl. Phys. A **783**, 261 (2007) [arXiv:nucl-ex/0701033].

[73] J. Rafelski and B. Muller, Phys. Rev. Lett. **48**, 1066 (1982) [Erratum-ibid. **56**, 2334 (1986)].

[74] B. Sinha, Phys. Lett. B **135**, 169 (1984).

[75] P. Koch, B. Muller and J. Rafelski, Z. Phys. A **324**, 453 (1986).

[76] J. Letessier and J. Rafelski, Phys. Rev. C **75**, 014905 (2007) [arXiv:nucl-th/0602047].

[77] B. Mohanty and J. Serreau, Phys. Rept. **414**, 263 (2005) [arXiv:hep-ph/0504154].

[78] S. A. Bass, B. Muller and D. K. Srivastava, Phys. Rev. Lett. **93**, 162301 (2004) [arXiv:nucl-th/0404050].

[79] A. Timmermann, U. Ornik, M. Plumer and R. Weiner, *Prepared for 25th International Symposium on Multiparticle Dynamics, Stara Lesna, Slovakia, 12-16 Sep 1995*

[80] R. M. Weiner, arXiv:hep-ph/9809202.

[81] T. Ludlam, Nucl. Instrum. Meth. A **499**, 428 (2003).

[82] M. Harrison, T. Ludlam and S. Ozaki, Nucl. Instrum. Meth. A **499**, 235 (2003).

[83] I. Alekseev *et al.*, Nucl. Instrum. Meth. A **499**, 392 (2003).

[84] M. Adamczyk *et al.* [BRAHMS Collaboration], Nucl. Instrum. Meth. A **499**, 437 (2003).

[85] K. Adcox *et al.* [PHENIX Collaboration], Nucl. Instrum. Meth. A **499**, 469 (2003).

[86] B. B. Back *et al.* [PHOBOS Collaboration], Nucl. Instrum. Meth. A **499**, 603 (2003).

[87] K. H. Ackermann *et al.* [STAR Collaboration], Nucl. Instrum. Meth. A **499**, 624 (2003). (STAR homepage:) [http://www.star.bnl.gov]

[88] H. S. Matis, R. L. Brown, W. Christie, W. R. Edwards, R. Jared, B. Minor and P. Salz, Nucl. Instrum. Meth. A **499**, 802 (2003) [arXiv:nucl-ex/0205008].

[89] D. Reichhold *et al.* [STAR Collaboration], Nucl. Instrum. Meth. A **499**, 792 (2003).

[90] F. Bergsma *et al.* [STAR Collaboration], Nucl. Instrum. Meth. A **499**, 633 (2003).

[91] R. Bellwied *et al.* [STAR-SVT Collaboration], Nucl. Instrum. Meth. A **400**, 279 (1997).

[92] R. Bellwied *et al.* [STAR-SVT Collaboration], Nucl. Instrum. Meth. A **377**, 387 (1996).

[93] M. Anderson *et al.*, Nucl. Instrum. Meth. A **499**, 659 (2003) [arXiv:nucl-ex/0301015].

[94] L. Kochenda *et al.* [STAR Collaboration], Nucl. Instrum. Meth. A **499**, 703 (2003).

[95] W. J. Llope *et al.*, Nucl. Instrum. Meth. A **522**, 252 (2004) [arXiv:nucl-ex/0308022].

[96] M. Beddo *et al.* [STAR Collaboration], Nucl. Instrum. Meth. A **499**, 725 (2003).

[97] K. H. Ackermann *et al.*, Nucl. Instrum. Meth. A **499**, 713 (2003) [arXiv:nucl-ex/0211014].

[98] C. E. Allgower *et al.* [STAR Collaboration], Nucl. Instrum. Meth. A **499**, 740 (2003).

[99] (STAR FPD documents) [http://www.star.bnl.gov/STAR/fpd/index.html]

[100] M. M. Aggarwal *et al.*, Nucl. Instrum. Meth. A **499**, 751 (2003) [arXiv:nucl-ex/0212006].

[101] F. S. Bieser *et al.* [STAR Collaboration], Nucl. Instrum. Meth. A **499**, 766 (2003).

[102] J. M. Landgraf, M. J. LeVine, A. Ljubicic, D. Padrazo, J. M. Nelson and M. W. Schulz [STAR Collaboration], Nucl. Instrum. Meth. A **499**, 762 (2003).

[103] C. Adler *et al.* [STAR Collaboration], Nucl. Instrum. Meth. A **499**, 778 (2003).

[104] C. Adler, A. Denisov, E. Garcia, M. J. Murray, H. Strobele and S. White, Nucl. Instrum. Meth. A **470**, 488 (2001) [arXiv:nucl-ex/0008005].

[105] (STAR Trigger documents) [http://www.star.bnl.gov/STAR/html/trg_l/]

[106] Y. P. Viyogi *et al.* [WA93 Collaboration.], Nucl. Phys. A **566**, 623C (1994).

[107] V. P. Viyogi *et al.* [WA93 Collaboration], Nucl. Phys. A **590**, 503C (1995).

[108] M. M. Aggarwal *et al.*, Nucl. Instrum. Meth. A **372**, 143 (1996).

[109] M. M. Aggarwal *et al.*, Nucl. Instrum. Meth. A **424**, 395 (1999) [arXiv:hep-ex/9807026].

[110] "A Preshower PMD for STAR Experiment", STAR Note 310 (1997).

[111] J. Adams *et al.* [STAR Collaboration], Phys. Rev. Lett. **95**, 062301 (2005) [arXiv:nucl-ex/0502008].

[112] M. M. Aggarwal *et al.*, Nucl. Instrum. Meth. A **488**, 131 (2002) [arXiv:nucl-ex/0112016].

[113] "Photon Multiplicity Detector for STAR:Technical Proposal", VECC Internal Report VECC/EQG/00-04, May 2000, revised:Jan. 2001.

[114] M.R.Dutta Majumder,Debasish Das,T.K.Nayak and Y.P.Viyogi Proceedings of DAE-BRNS Symposium on Nuclear Physics, Mumbai Vol **50** 2005 (437).

[115] Debasish Das *et al.*
Proceedings of DAE-BRNS Symposium on Nuclear Physics, Mumbai Vol **46B** 2003 (520).

[116] M. R. Dutta Majumdar, D. Das and T. K. Nayak, arXiv:physics/0512227.

[117] J. C. Santiard and K. Marent [ALICE Collaboration], CERN-ALICE-PUB-2001-49

[118] "ALICE HMPID Technical Design Report", CERN/LHCC 98-19 (1998).

[119] W-IE-NE-R Plein and Baus GmBH, "PCI-VME PCI to VME Interface. Users manual", June 1999; S.Pal, Proceedings of DAE-BRNS Symposium on Nuclear Physics, Tirunelveli Vol **45B** 2002 (428).

[120] "Indian detector stars at Brookhaven", CERN COURIER, Volume 44, Number 7.

[121] G. I. Kopylov and M. I. Podgoretsky, Sov. J. Nucl. Phys. **15**, 219 (1972) [Yad. Fiz. **15**, 392 (1972)].

[122] E. V. Shuryak, Phys. Lett. B **44**, 387 (1973).

[123] M. A. Lisa, S. Pratt, R. Soltz and U. Wiedemann, Ann. Rev. Nucl. Part. Sci. **55**, 357 (2005) [arXiv:nucl-ex/0505014].

[124] G. Bertsch, M. Gong and M. Tohyama, Phys. Rev. C **37**, 1896 (1988).

[125] L. D. McLerran, FERMILAB-CONF-88-068-T *Presented at Int. Conf. on Physics and Astrophysics of the Quark Gluon Plasma, Bombay, India, Feb 8-12, 1988*

[126] G. Baym, Acta Phys. Polon. B **29**, 1839 (1998) [arXiv:nucl-th/9804026].

[127] S. S. Padula, Braz. J. Phys. **35**, 70 (2005) [arXiv:nucl-th/0412103].

[128] U. W. Heinz, arXiv:nucl-th/9609029.

[129] U. W. Heinz and B. V. Jacak, Ann. Rev. Nucl. Part. Sci. **49**, 529 (1999) [arXiv:nucl-th/9902020].

[130] U. W. Heinz, Nucl. Phys. A **610**, 264C (1996) [arXiv:nucl-th/9608002].

[131] M. Gyulassy, S. K. Kauffmann and L. W. Wilson, Phys. Rev. C **20**, 2267 (1979).

[132] D. H. Boal, C. K. Gelbke and B. K. Jennings, Rev. Mod. Phys. **62**, 553 (1990).

[133] Y. Sinyukov, R. Lednicky, S. V. Akkelin, J. Pluta and B. Erazmus, "Coulombcorrections for interferometry analysis of expanding hadron Phys. Lett. B **432**, 248 (1998).

[134] M. G. Bowler, Z. Phys. C **39**, 81 (1988).

[135] M. G. Bowler, Phys. Lett. B **270**, 69 (1991).

[136] S. E. Koonin, Phys. Lett. B **70**, 43 (1977).

[137] M. Suzuki, Phys. Rev. D **35**, 3359 (1987).

[138] G. Baym and P. Braun-Munzinger, Nucl. Phys. A **610**, 286C (1996) [arXiv:nucl-th/9606055].

[139] L.I.Schiff, *Quantum Mechanics* . McGraw-Hill (1955).

[140] S. Pratt, Phys. Rev. D **33**, 72 (1986).

[141] S. Pratt, Phys. Rev. Lett. **53**, 1219 (1984).

[142] D. A. Brown and P. Danielewicz, Phys. Lett. B **398**, 252 (1997) [arXiv:nucl-th/9701010].

[143] P. Danielewicz and S. Pratt, Phys. Lett. B **618**, 60 (2005) [arXiv:nucl-th/0501003].

[144] Z. Chajecki, T. D. Gutierrez, M. A. Lisa and M. Lopez-Noriega [The STAR Collaboration], arXiv:nucl-ex/0505009.

[145] A. N. Makhlin and Y. M. Sinyukov, Z. Phys. C **39**, 69 (1988).

[146] B. Tomasik and U. A. Wiedemann, arXiv:hep-ph/0210250.

[147] S. Chapman, P. Scotto and U. W. Heinz, Phys. Rev. Lett. **74**, 4400 (1995) [arXiv:hep-ph/9408207].

[148] U. A. Wiedemann, Phys. Rev. C **57**, 266 (1998) [arXiv:nucl-th/9707046].

[149] S. Chapman, J. R. Nix and U. W. Heinz, Phys. Rev. C **52**, 2694 (1995) [arXiv:nucl-th/9505032].

[150] J. Adams *et al.* [STAR Collaboration], Phys. Rev. Lett. **93**, 012301 (2004) [arXiv:nucl-ex/0312009].

[151] M. A. Lisa *et al.* [E895 Collaboration], Phys. Lett. B **496**, 1 (2000) [arXiv:nucl-ex/0007022].

[152] S. A. Voloshin and W. E. Cleland, Phys. Rev. C **53**, 896 (1996) [arXiv:nucl-th/9509025].

[153] J. Adams *et al.* [STAR Collaboration], Phys. Rev. C **71**, 044906 (2005) [arXiv:nucl-ex/0411036].

[154] T. Csorgo and A. T. Szerzo, arXiv:hep-ph/9912220.

[155] T. Csorgo and S. Hegyi, Phys. Lett. B **489**, 15 (2000).

[156] T. Csorgo, S. Hegyi and W. A. Zajc, Eur. Phys. J. C **36**, 67 (2004) [arXiv:nucl-th/0310042].

[157] L. D. Landau, Izv. Akad. Nauk Ser. Fiz. **17**, 51 (1953).

[158] D. H. Rischke, Nucl. Phys. A **610**, 88C (1996) [arXiv:nucl-th/9608024].

[159] P. Huovinen and P. V. Ruuskanen, arXiv:nucl-th/0605008.

[160] Yu. M. Sinyukov, S. V. Akkelin and Y. Hama, Phys. Rev. Lett. **89**, 052301 (2002) [arXiv:nucl-th/0201015].

[161] T. Hirano and K. Tsuda, Phys. Rev. C **66**, 054905 (2002) [arXiv:nucl-th/0205043].

[162] U. W. Heinz and P. F. Kolb, arXiv:hep-ph/0204061.

[163] D. Zschiesche, S. Schramm, H. Stoecker and W. Greiner, Phys. Rev. C **65**, 064902 (2002) [arXiv:nucl-th/0107037].

[164] S. Soff, S. A. Bass and A. Dumitru, Phys. Rev. Lett. **86**, 3981 (2001) [arXiv:nucl-th/0012085].

[165] H. Sorge, H. Stoecker and W. Greiner, Nucl. Phys. A **498**, 567C (1989).

[166] T. J. Humanic, Nucl. Phys. A **715**, 641 (2003) [arXiv:nucl-th/0205053].

[167] T. J. Humanic, Phys. Rev. D **66**, 010001 (2002) arXiv:nucl-th/0203004.

[168] D. Molnar and M. Gyulassy, Phys. Rev. Lett. **92**, 052301 (2004) [arXiv:nucl-th/0211017].

[169] Z. w. Lin, C. M. Ko and S. Pal, Phys. Rev. Lett. **89**, 152301 (2002) [arXiv:nucl-th/0204054].

[170] X. N. Wang and M. Gyulassy, Phys. Rev. D **44**, 3501 (1991).

[171] J. G. Cramer, G. A. Miller, J. M. S. Wu and J. H. S. Yoon, Phys. Rev. Lett. **94**, 102302 (2005) [arXiv:nucl-th/0411031].

[172] B. B. Back *et al.* [PHOBOS Collaboration], arXiv:nucl-ex/0506008.

[173] G. A. Miller and J. G. Cramer, arXiv:nucl-th/0507004.

[174] D. Teaney, Phys. Rev. C **68**, 034913 (2003) [arXiv:nucl-th/0301099].

[175] P. Romatschke, arXiv:nucl-th/0701032.

[176] W. N. Zhang and C. Y. Wong, arXiv:hep-ph/0702120.

[177] J. e. Alam, B. Mohanty, P. Roy, S. Sarkar and B. Sinha, Phys. Rev. C **67**, 054902 (2003) [arXiv:nucl-th/0302054].

[178] U. Ornik, M. Plumer, A. Timmermann and R. M. Weiner, arXiv:hep-ph/9509367.

[179] L. V. Razumov and H. Feldmeier, arXiv:hep-ph/9508318.

[180] A. Timmermann, M. Plumer, L. Razumov and R. M. Weiner, Phys. Rev. C **50**, 3060 (1994) [arXiv:hep-ph/9405232].

[181] D. K. Srivastava, Phys. Rev. C **71**, 034905 (2005) [arXiv:nucl-th/0411041].

[182] D. K. Srivastava, Phys. Rev. D **49**, 4523 (1994).

[183] D. K. Srivastava and J. I. Kapusta, Phys. Rev. C **48**, 1335 (1993).

[184] D. K. Srivastava and J. I. Kapusta, Phys. Lett. B **307**, 1 (1993).

[185] D. Kumar Srivastava and C. Gale, Phys. Lett. B **319**, 407 (1993) [arXiv:hep-ph/9311267].

[186] D. Peressounko, AIP Conf. Proc. **828**, 581 (2006) [arXiv:hep-ph/0512110].

[187] D. Peressounko, Phys. Rev. C **67**, 014905 (2003).

[188] F. M. Marques, G. Martinez, T. Matulewicz, R. W. Ostendorf and Y. Schutz, Phys. Rept. **284** (1997) 91.

[189] R. Ostendorf *et al.*, Phys. Rev. Lett. **73**, 34 (1994).

[190] A. Badala *et al.*, Phys. Rev. Lett. **74**, 4779 (1995).

[191] K. Piasecki and T. Matulewicz, Acta Phys. Polon. B **37**, 175 (2006).

[192] M. M. Aggarwal *et al.* [WA98 Collaboration], Phys. Rev. Lett. **93**, 022301 (2004) [arXiv:nucl-ex/0310022].

[193] D. Das *et al.* [STAR Collaboration], [arXiv:nucl-ex/0511055 and Nukleonika,Vol 51, Suppl 3, Page : S55-S58]

[194] C. Adler *et al.* [STAR Collaboration], Phys. Rev. Lett. **87**, 082301 (2001) [arXiv:nucl-ex/0107008].

[195] K. Adcox *et al.* [PHENIX Collaboration], Phys. Rev. Lett. **88**, 192302 (2002) [arXiv:nucl-ex/0201008].

[196] S. S. Adler *et al.* [PHENIX Collaboration], Phys. Rev. Lett. **93**, 152302 (2004) [arXiv:nucl-ex/0401003].

[197] J. Adams *et al.* (STAR Collaboration), nucl-ex/0311017.

[198] L. Ahle *et al.* [E802 Collaboration], Phys. Rev. C **66**, 054906 (2002) [arXiv:nucl-ex/0204001].

[199] D. Adamova *et al.* [CERES collaboration], Nucl. Phys. A **714**, 124 (2003) [arXiv:nucl-ex/0207005].

[200] J. Adams *et al.* [STAR Collaboration], "Three-pion HBT correlations in relativistic heavy-ion collisions from the Phys. Rev. Lett. **91**, 262301 (2003) [arXiv:nucl-ex/0306028].

[201] B. I. Abelev *et al.* [STAR Collaboration], Phys. Rev. C **74**, 054902 (2006) [arXiv:nucl-ex/0608012].

[202] P. F. Kolb and U. W. Heinz, arXiv:nucl-th/0305084.

[203] F. Retiere and M. A. Lisa, Phys. Rev. C **70**, 044907 (2004) [arXiv:nucl-th/0312024].

[204] T. Hirano and K. Tsuda, Nucl. Phys. A **715**, 821 (2003) [arXiv:nucl-th/0208068].

[205] B. Tomasik, U. A. Wiedemann and U. W. Heinz, Nucl. Phys. A **663**, 753 (2000) [arXiv:nucl-th/9907075].

[206] U. A. Wiedemann, P. Scotto and U. W. Heinz, Phys. Rev. C **53**, 918 (1996) [arXiv:nucl-th/9508040].

[207] B. R. Schlei and N. Xu, Phys. Rev. C **54**, 2155 (1996) [arXiv:nucl-th/9608048].

[208] B. R. Schlei, U. Ornik, M. Plumer and R. M. Weiner, Phys. Lett. B **293**, 275 (1992).

[209] B. B. Back *et al.* [PHOBOS Collaboration], Phys. Rev. C **73**, 031901 (2006) [arXiv:nucl-ex/0409001].

[210] M. A. Lisa *et al.* [E895 Collaboration], Phys. Rev. Lett. **84**, 2798 (2000).

[211] I. G. Bearden *et al.* [NA44 Collaboration], Phys. Rev. C **58**, 1656 (1998).

[212] R. A. Soltz *et al.* [E866 Collaboration], Nucl. Phys. A **661**, 439 (1999).

[213] S. V. Afanasev *et al.* [NA49 Collaboration], Nucl. Phys. A **698**, 104 (2002).

[214] F. Antinori *et al.* [WA97 Collaboration], J. Phys. G **27**, 2325 (2001) [arXiv:hep-ex/0108049].

[215] M. M. Aggarwal *et al.* [WA98 Collaboration], Phys. Rev. C **67**, 014906 (2003) [arXiv:nucl-ex/0210002].

[216] D. Adamova *et al.* [CERES Collaboration], Phys. Rev. Lett. **90**, 022301 (2003) [arXiv:nucl-ex/0207008].

[217] D. Das [STAR Collaboration], arXiv:nucl-ex/0702047.

[218] B. Alessandro *et al.* [ALICE Collaboration], J. Phys. G **32**, 1295 (2006).